

University of New Mexico

UNM Digital Repository

Optical Science and Engineering ETDs

Engineering ETDs

Summer 5-26-2023

Filaments and their application to air lasing, spectroscopy, and guided discharge

Ali Rastegari

University of New Mexico - Main Campus

Follow this and additional works at: https://digitalrepository.unm.edu/ose_etds



Part of the [Atomic, Molecular and Optical Physics Commons](#), [Optics Commons](#), and the [Other Engineering Commons](#)

Recommended Citation

Rastegari, Ali. "Filaments and their application to air lasing, spectroscopy, and guided discharge." (2023). https://digitalrepository.unm.edu/ose_etds/95

This Dissertation is brought to you for free and open access by the Engineering ETDs at UNM Digital Repository. It has been accepted for inclusion in Optical Science and Engineering ETDs by an authorized administrator of UNM Digital Repository. For more information, please contact disc@unm.edu.

Ali Rastegari

Candidate

Optical Science and Engineering

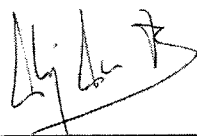
Department

This dissertation is approved, and it is acceptable in quality and form for publication:

Approved by the Dissertation Committee:



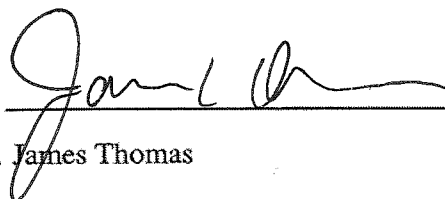
Dr. Jean-Claude Diels, Chair



Dr. Alejandro Aceves



Dr. Mark Gilmore



Dr. James Thomas

Filaments and their application to air lasing, spectroscopy, and guided discharge

by

Ali Rastegari

B.S., Physics, University of Tehran, 2007

M.S., Atomic and Molecular Physics, University of Tehran, 2010

M.S., Optical Science and Engineering, University of New Mexico, 2015

DISSERTATION

Submitted in Partial Fulfillment of the
Requirements for the Degree of

Doctor of Philosophy
Optical Science and Engineering

The University of New Mexico

Albuquerque, New Mexico

August, 2023

©2023, Ali Rastegari

<https://orcid.org/0000-0002-3628-9518>

All rights reserved except where otherwise noted

Acknowledgments

I consider myself extremely fortunate to be encircled by an amazing group of mentor, colleagues, friends, and family. It is thanks to these exceptional individuals that the contents of the forthcoming pages have come to fruition.

I would like to express my heartfelt gratitude to my academic advisor and mentor, Dr. Jean-Claude Diels, for graciously accepting me as a member of his esteemed research team and providing me with numerous opportunities to work on a variety of projects. His unwavering dedication to the field of science has been a profound source of inspiration, and even after all this time, I continue to glean new knowledge from his expertise. I am truly grateful for his exceptional patience in addressing the multitude of questions I have posed throughout these years.

I would like to express my sincere appreciation to Dr. Ladan Arissian for her invaluable help and unwavering support throughout my PhD journey. Her guidance has been instrumental in shaping my research endeavors, and I am truly grateful for her contributions. Additionally, I extend my thanks to Dr. Chengyong Feng for his exceptional assistance, particularly during the initial years of my PhD. I would also like to express my gratitude to Dr. Brian Kamer and Dr. Luke Horstman for their invaluable help on various projects during my PhD. Furthermore, I would like to extend my appreciation to the other members of our research team: Dr. Shermineh Rostami, Dr. Hanieh Afkhami, Dr. Ning Hsu, Dr. James Hemndrie, and Xiaobeng Xu. Their kind assistance and unwavering support have contributed greatly to the success of our collaborative endeavors. Collectively, I am deeply grateful to each of these individuals for their kind help and support throughout my PhD journey.

I am immensely grateful for the friendship and support of all my friends. I consider myself truly fortunate to have each and every one of them in my life. Their unwavering companionship and encouragement have been a constant source of joy and strength. Whether it's sharing laughter, lending a helping hand, or providing a listening ear, their presence has enriched my life in countless ways. I am profoundly thankful for their enduring friendship and the invaluable support they have provided me throughout my journey. I would like to express my deepest gratitude to my partner, Shakiba, for her unwavering support and kindness, especially during the past few months while I was immersed in working on my thesis. Her patience and understanding have been truly remarkable, and I am incredibly grateful for her presence by my side. Despite the demands and challenges of my thesis, she has provided unwavering encouragement and support, creating a nurturing environment that allowed me to focus on my work.

Finally, I would like to wholeheartedly express my deepest appreciation to my parents and sister for their unwavering support and kindness throughout my life. Their presence

and assistance have played a pivotal role in shaping the person I am today. Without their unwavering support and guidance, I would not have been able to achieve the milestones and successes that I have. Their constant belief in me and their unconditional love have been a constant source of strength and inspiration. I am forever grateful for their presence in my life and for the profound impact they have had on my personal and academic journey.

To each of these individuals and to the countless others who have contributed to my growth and success, I offer my heartfelt thanks. Your support and presence have made an indelible mark on my life, and I am eternally grateful.

Filaments and their application to air lasing, spectroscopy, and guided discharge

by

Ali Rastegari

B.S., Physics, University of Tehran, 2007

M.S., Atomic and Molecular Physics, University of Tehran, 2010

M.S., Optical Science and Engineering, University of New Mexico, 2015

Ph.D. Optical Science and Engineering, University of New Mexico, 2023

Abstract

Laser filamentation is a fascinating phenomenon that occurs when an intense laser beam travels through transparent materials, in particular air. At sufficiently high power (TW in the near IR, GW in the UV), instead of spreading out like a regular laser beam, something remarkable happens: the laser beam becomes tightly focused, creating a thin and intense column of light called a laser filament. Laser filamentation is characterized by two main properties: (I) a high-intensity core that remains narrow over long distances beyond the Rayleigh range and (II) a low-density plasma channel within the core. In recent years, laser filamentation has gained significant attention due to its unique properties and wide range of applications.

This dissertation will provide an introduction to laser filamentation and discuss beam profile measurements related to UV filaments. Additionally, the results of experiments involving the applications of laser filaments will be presented. It has been demonstrated

that UV filaments can be utilized for laser breakdown spectroscopy, leading to higher resolution and accuracy. Furthermore, the phenomenon of air lasing induced by both UV and IR laser filaments was investigated. Finally, the potential application of UV filaments for guiding and triggering electrical discharges is studied.

Contents

List of Figures	xiv
List of Tables	xxx
1 Laser filamentation	1
1.1 Introduction	1
1.1.1 Diffraction	2
1.1.2 Self focusing	2
1.1.3 Plasma Defocusing	5
1.1.4 Self-induced waveguide versus moving focus	6
1.2 Trends of filamentation versus wavelength	8
1.2.1 Multiphoton versus Tunnel ionization	8
1.2.2 From photoionization to avalanche ionization	10
1.2.3 Filament stability versus order of ionization	11
1.2.4 Single filament propagation versus wavelength	12

Contents

1.3	Physical parameters relevant to UV filaments formation	14
1.3.1	Conditions particular to long UV pulse	14
1.3.2	Determination of $\sigma^{(3)}$, β_{ep} and γ	16
1.4	Outline	20
	References	25
2	UV laser filaments	31
2.1	Introduction	31
2.2	Laser source	32
2.3	Beam preparation	33
2.3.1	Introduction	33
2.3.2	The aerodynamic window	35
2.4	UV Filament Spatial Profile Measurements	38
2.4.1	3 m Lens	39
2.4.2	9 m Lens	41
2.5	Hydrodynamic waveguiding with filaments	42
2.5.1	Transient imaging of UV filaments via shadowgraphy	43
2.5.2	Hydrodynamic waveguiding	47
2.6	High-repetition laser source	48
2.6.1	Thermal Lensing Measurements	53

Contents

2.7	Velocity map imaging (VMI) setup	55
2.7.1	Introduction	55
2.7.2	Overview of the developed VMI setup	58
2.7.3	Detection system	64
2.8	Future Work	67
	References	68
3	Measurement of delayed fluorescence in N_2^+ with a streak camera	75
3.1	Introduction	75
3.2	Experimental techniques	78
3.2.1	Streak Camera	78
3.2.2	Experimental setup	80
3.2.3	Optical synchronization	83
3.2.4	Determination of an accurate time origin for temporal measurements	85
3.3	Experimental Results	86
3.3.1	De-convolution	86
3.3.2	Time resolved measurements in selected spectral bands	88
3.4	Is 800 nm a "magic wavelength"?	95
3.5	Conclusion	98
3.6	Future work	99

Contents

References	100
4 High-resolution spectroscopy induced with UV filaments	105
4.1 Introduction	105
4.1.1 Self-absorption	109
4.2 Experimental Setup	111
4.3 Experimental Results	113
4.3.1 Wavelength dependence	113
4.3.2 Enhanced resolution through the utilization of self-absorption	115
4.3.3 Temporal evolution of self absorption and emission profile	120
4.4 Investigation of the plume generated in LIBS process induced by a ps UV laser	126
4.5 Conclusion	128
4.6 Future Work	130
References	131
5 Investigation of laser-induced discharge via UV filaments	139
5.1 Introduction	139
5.2 Experimental setup	142
5.2.1 High voltage laboratory	142

Contents

5.2.2	Laser sources	145
5.3	Experimental results	148
5.3.1	UV filament induced discharges	148
5.3.2	Combination of the UV filament with two other lasers	150
5.3.3	Filament Conductivity Measurements	154
5.3.4	Shadowgraphy measurements	158
5.4	Conclusion	161
5.5	Future work	162
	References	163
	A Matlab code for data analysis of chapter 3	169
A.1	Analyzing the data	169
A.2	De-convolution	182
	B Matlab code for data analysis of chapter 4	189
	C Matlab code for data analysis of chapter 5	198

List of Figures

1.1	Diagrams illustrating the basic principle behind (a) self-focusing and (b) plasma defocusing. (c) Diagram illustrating the filamentation dynamics.	3
1.2	(a) Sketch of the cw filamentation observed in suspensions of dielectric spheres. (b) Moving focus model.	7
1.3	(a) Multiphoton ionization: at short wavelengths, the relatively high energy photons stack themselves out of the potential well of the molecule. (b) Tunnel ionization dominates at lower photon energies. While the electron remains near the bottom of the well, the potential surface gets tilted by the field, creating a narrowing potential wall through which the electron can tunnel.	8
1.5	Trend in the wavelength range from 248 to 800 nm for single filaments. Second column: intensity range. Third column: range of energy/filamenting pulse. Fourth column: dominant loss mechanism. Fifth column: some references.	14
1.7	Setup of absorption measurement	18
2.1	Schematic diagram of the UV laser.	33

List of Figures

2.2 (a) Profile of the super-Gaussian 266 nm beam. (b) Filament pattern produced by the profile (a) in air (Aerodynamic window is not operational). (c) Far field profile as produced in vacuum with the operational aerodynamic window (hence in the absence of nonlinear effect) at the focus of a lens. (d) Single filament profile taken at 2 m from the exit of the aerodynamic window. 35

2.3 (a) Profile of the aerodynamic window nozzle and expansion chamber, cut in an aluminum bloc. The cut is 20 mm deep. The arrow indicate the direction of propagation of the light from vacuum to atmosphere. The light passes through a 3 mm diameter hole, or in another realization a 3 mm × 20 mm slot. (b) Setup for investigation of the stability of the beam profile of a He-Ne laser going through the aerodynamic window. 36

2.4 Comparison between the centroid (left) and the beam waist (right) of the beam profile of a He-Ne laser (for 49 successive images), with and without an aerodynamic window. The expanded He-Ne laser beam is focused with a 3 m lens. 38

2.5 Experimental setup which is used for observing the spatial profile of the UV filaments. The beam is linearly attenuated by a grazing incidence plate (fused silica, 15 mm thickness, 150 mm diameter coated for maximum reflectivity at 355 nm (normal incidence). The beam is thereafter further attenuated by neutral density filters before being recorded by a CCD. 39

List of Figures

2.6 (a) and (b) UV filament beam profile for the case of focusing with a 3 m lens in vacuum (operational aerodynamic window). The UV filament has a FWHM of about 375 μm . This is measured using the setup described in Fig. 2.5. The CCD is 2 m away from the exit point of the aerodynamic window. (c) Calibration image of the focused UV laser beam at very low power, exiting the aerodynamic window, taken with an image intensifier and a CCD. The 13 μm waist is a few cm before the exit plane of the window. (d) Image of the filament taken with the image intensifier and a CCD, showing a FWHM of about 300 μm 40

2.7 The beam profiles of UV filaments at different distances from the 9 m focusing lens. These beam profiles are captured by a digital camera recording the impact of the UV filament on a piece of paper. Different colors correspond to the fluorescent emission from the paper which is changing based on the impacted beam intensity. The white dots in the figure are related to multiple filaments. 42

2.8 (a) Picture of the shadowgraphy setup. (b) Schematic diagram of the shadowgraphy setup. 43

2.9 Shadowgraphs of UV filament vs time. (Top) Focused with a 1m lens. (Bottom) Focused with a 3m lens. The low density tube and shock-waves are demonstrated by white arrows and dashed lines respectively. 44

2.10 Image of the plasma channels taken with a digital camera from the side for the filaments generated with three focusing lenses of (a) 0.6 m, (b) 1 m, and (c) 3 m. The initial beam diameter is the same for all three pictures. The Rayleigh range is approximately 1 mm for (c), hence much smaller than the plasma length. 45

List of Figures

2.11 Propagation distance R of the shock-wave versus time. a) In the first regime the shock-wave propagation follows the Sedov formula for cylindrical symmetry ($d = 2$). b) In the second regime the shock-wave propagates at constant velocity. 46

2.12 Right) Schematic of the new cooling system of the Ti:sapphire crystal. Left) Picture of the new regenerative amplifier Ti:sapphire crystal chamber. 49

2.13 Top) Topological configuration of the regenerative amplifier. The s-polarized 800 nm seed pulse is reflected from the surface of the Ti:sapphire gain crystal (as it is cut at Brewster angle) towards the end mirror of the cavity. Then going through the Pockels cell it is switched to p-polarization to be trapped in the cavity. After a number of round-trips, the amplified pulse is extracted by rotating its polarization to s by the second Pockels. The s-polarized pulse is reflected by the thin film polarizer (TPF). With all focal lengths being equal, the ABCD matrix of this cavity is -1, implying that the beam size will adjust to the size of the gain volume in the crystal. Bottom) The focusing is performed with mirrors at an angle such that astigmatism introduced by the Brewster rod is compensated. 51

2.14 Picture of the regenerative amplifier cavity. Green: the path of the pump beam. Red: the path of the 800 nm pulses. 52

2.15 Schematic of the thermal lensing measurement setup. 53

List of Figures

2.16	Pictures from the beam profiler. (a) He-Ne profile at 32 cm from the Ti:sapphire crystal, with pump off. (b) He-Ne profile at 32 cm from the Ti:sapphire crystal, with 70 W 532 nm pump. (c) and (d): measurements corresponding to (a) and (b), except at 56.5 cm from the crystal. (e) He-Ne beam profile at 32 cm from the crystal, when the pump is focused on the axis with a 60 cm focal distance lens. (f) He-Ne beam profile at 32 cm from crystal, when the pump is focused by a $R = 1$ m mirror at an angle of incidence of 6° . (g) The effective waist provided by the beam profiler program vs distance from the center of the crystal. For both sets of measurements, the crystal temperature has been sustained at -3°C	54
2.17	Schematic representation of the detection mechanism of a velocity-map imaging setup.	56
2.18	Overview of the velocity map imaging technique. Electrons/ions emitted created by the interaction of laser pulses with matter are projected by the electric field of the electrostatic lenses onto the detector. As the result, a 2D projection of the velocity and momentum distribution is created on the detector.	57
2.19	Overall picture of the assembled VMI setup.	59
2.20	Schematic drawing of the VMI setup showing different parts and connections. .	60
2.21	(a) The schematic design of the gas feeding system including the <i>gas manipulator</i> . The input gas flow is controlled by a high-speed solenoid valve from <i>Parker</i> . A skimmer is placed at the output flange of the <i>second chamber</i> just before the 8" valve. A nozzle is placed at the end of the input gas tube which is intended to eject gas in a coherent stream toward the skimmer. (b) The schematic design of the <i>mirror manipulator</i> and the mirror mount. The mirror is a 1" on-axis parabolic mirror with a 1" focal length from <i>SORL</i> that has been specially coated to be highly reflective for 266 nm and 800 nm laser filaments.	61

List of Figures

2.22 Schematics of the pumping circuit are presented. Each chamber is pumped by its own turbomolecular pump (from *Pfeiffer*). The molecular jet is injected into the VMI setup through the *second chamber* which has the largest pump flow capacity. The *Hipace 300* turbomolecular pump is cooled by air. On the other hand, the *Hipace 1500* turbomolecular pump needs to be cooled by water. The chiller for this purpose is located outside of the lab in the chase. A vacuum better than 10^{-8} torr is achieved in the main chamber. The input of both turbomolecular pumps is connected to a dry scroll pump via a solenoid valve. (*Adixen ACP 28*). 62

2.23 (c) Image of the detection assembly. The laser beam and the gas jet cross at a right angle in the center of the space between the repeller and the first electrode. Below the electrode assembly, one can distinguish the multichannel plate (MCP) to amplify the two-dimensional electron image, which produces a visible image on a fluorescent plate. The latter is imaged on a fast CCD camera (*Andor Zyla*) through the window of the flange. (d) Schematics of different feedthrough electrodes are shown. This schematic can be used to identify different voltage inputs on the feedthrough for the 5 electrostatic lenses and the MCP assembly. V_A : Voltage on the phosphor screen, V_I : Input voltage of the MCP, V_O : Output voltage of MCP, 1 to 5: Electrostatic lenses as labeled in (c). Red numbers 1-3 correspond to the numbering marked in black on the outside of the flange that can be used for identification purposes. 65

2.24 (a) Simulated trajectories of electrons with initial velocities directed at 90° azimuthal angle are presented. Each trajectory corresponds to different initial energies ranging from 10 eV to 250 eV. For each trajectory 100 electrons which are randomly distributed in a sphere with $r=150 \mu\text{m}$ are simulated. From bottom to top the energies are 10, 25, 50, 100, 150, 200, and 250 eV. (b) The position (R) on MCP vs square root of the energy ($E^{1/2}$). 66

List of Figures

2.25	Simulations for electrons at azimuthal angle pairs of 30°-150°, 45°-135°, and 60°-120°. For each trajectory 100 electrons which are randomly distributed in a sphere with $r=150 \mu\text{m}$ are simulated. (a) For 50 eV initial energy and (b) for 200 eV initial energy.	66
3.1	Schematic diagram of nitrogen cations energy-levels. The transitions between $B^2\Sigma_g^+$ (upper) and $X^2\Sigma_g^+$ (lower) states are indicated with corresponding lasing wavelengths.	77
3.2	Operating principle of a streak camera.	79
3.3	Operation timing of a streak camera at the time of sweep.	80
3.4	Top) From left to right, the image of the plasma induced by focusing 800 nm laser pulses with 10 cm and 40 cm focusing lenses, and the image of the Rayleigh scattering. Bottom) Picture of the streak camera fluorescence detection setup showing different elements of the setup.	81
3.5	Sketch of the streak camera fluorescence detection. The side emission of the plasma created by the focused main beam (thick red line) is imaged onto the streak camera. A weak beam split off from the main beam (dashed red line) provides a temporal reference spot on each frame of the streak camera. The streak camera slit is parallel to the main beam (z direction) and is used at its minimum possible opening for best time resolution. A typical image taken with infrared filter is presented in the inset. The abscissa is the propagation axis, and the ordinate is time. The image is integrated over the transverse dimension as a function of z (coordinate along the beam). The trace of the plasma radiation is recorded. The reference light (on the left) is used for timing reference and correction of spatial jitter. BP represents the band-pass filter. A nebulizer is used to measure the Rayleigh scattering from the focused beam for a weak non-ionizing pulse.	82

List of Figures

- 3.6 The blue area is a typical average of 1000 frames, that captured the reference (turquoise spot in the middle-top of the figure) and the scattering of a diffuser (turquoise spot in the middle left). The ordinate is a spatial coordinate, the abscissa time. The total width of the image is swept in 100 ps. The spacing between pixels corresponds to 2.88 ps. The inserted graphs below reference and scattering spots are space integrated recordings of intensity versus time. For ideal resolution, the reference (top) and the image have the same intensity. Note that they have the same width. 83
- 3.7 (a) In yellow: the reference pulse obtained by sending the low intensity laser beam through a dispersed mist. Green: reference pulse obtained with a solid diffuser surface. The center of gravity of the yellow reference will be used as the time of arrival of the fs pulse. (b) Typical averaged streak camera frame. . . 86
- 3.8 Spatially integrated emission of the nitrogen cation at 391 nm. The fitted function (Equation 3.1) to the fast decay section of the raw data is represented by the green dashed line, and the de-convoluted data is represented by a black line. . . 87

List of Figures

3.9 Spatially integrated emission versus time. (a) and (b) show the normalized emission of the nitrogen cation at 391 nm (a) and at 428 nm (b), respectively for the case of focusing with a 10 cm lens. (c) and (d) show the normalized emission of the nitrogen cation at 391 nm (c) and at 428 nm (d), respectively for the case of focusing with a 40 cm lens. The dashed line indicates the center of gravity of the yellow reference, which is the Rayleigh scattering measured separately at low power as shown in Fig. 3.7(a). The raw data for both 391 nm 428 nm cases are shown in blue and red respectively. The green dotted curve is the fit to data in proximity of the peak. The de-convoluted fast decaying emissions of 391 and 428 are calculated using the instrument response function of the Rayleigh scattering of the femtosecond pulse shown with black curve. There are two time constants for the ion emission known as “fast” and “slow” decay. 88

3.10 Table summarising delay times and fast decay times for 391 nm and 428 nm emissions for both focusing case. 89

3.11 The 391 nm and 428 nm emission and broadband IR emission ($\lambda > 750$ nm) are plotted without normalization for focusing with 10 cm (a) and 40 cm (b). There are two time constants for the ion emission known as “fast” and “slow” decay. 90

3.12 Normalized integrated IR emission from selected spatial regions of the plasma labeled as “A” , “B”, and “C” as shown in the legend. The inset shows the relative intensity along the filament for different slices. 92

3.13 Comparing fast decay and built up time of the emission at 391 nm from the selected spatial regions of the plasma labeled as “A” , “B”, and “C” as shown in the legend. 94

List of Figures

- 3.14 Schematic diagram of the setup for the detection of N_2^+ emissions induced by the UV filaments. UV laser pulses are focused using a 3 m lens into the vacuum chamber connected to the aerodynamic window. Measurements have been performed in both cases of the operational and non-operational aerodynamic window. The side fluorescence emission was collected by an aspheric lens with a focal length of 32 mm. The collected light is then imaged on the entrance slit of a monochromator. A high-gain Photo Multiplier Tube (PMT) is placed at the exit slit of the monochromator. The PMT is connected to an oscilloscope in order to measure its output voltage which is proportional to the light intensity. 96
- 3.15 The 391 nm (a) and 428 nm (b) emission lines for a UV filament are plotted. Results for both cases of the operational and non-operational aerodynamic window are plotted. Each point in the plots is calculated by averaging 64 laser shots. The gain voltages for the detection of 391 nm and 428 nm emission were 1.480 kV. The monochromator's best achievable resolution was not enough to separate the rotational bands (P and R branches) of N_2^+ , hence only the envelope can be observed in the measurements. The general shape of the envelopes are in general agreement with previously reported fluorescence emission lines of N_2^+ 97
- 3.16 The intensity of the 391 nm emission line along the UV filament is measured. The 3 m geometrical focal point of the lens is represented with a black dashed line. In (a) The blue lines correspond to measurements in which 1.4 kV was the applied gain on the PMT. As the standard deviation on the intensity measurements at the beginning and the end of the scan range for this gain was too high, measurements in these respective positions were repeated with a higher gain of 1.7 kV applied to the PMT which is plotted in red. (b) Schematics of the experimental setup. 98

List of Figures

4.1	Left) Schematic of the laser-induced breakdown process. Right) Schematics illustrating the plasma evolution in time, in which the timing of the laser pulse, the intensity of background radiation, delay time, and gate width have been depicted.	107
4.2	(a) An image of a typical spectrum of a uranium sample measured by <i>DEMON</i> . The self-absorption dip is present for both uranium lines of 385.464 nm and 385.957 nm. The experiments were performed with UV filaments created by 266 nm laser pulses of 200 ps duration and with energy of 105 mJ per pulse. The gate width is 500 ns, and the delay is 325 nm. (b) A schematic diagram showing the self-absorption mechanism. The temperature gradient is depicted, indicating a hot central region and a colder outer region.	110
4.3	Right) Schematics of the LIBS setup. A photograph of the plume produced with natural uranium is shown on top. Different laser sources have been used for the LIBS experiments. Most of the experiments were performed with UV filaments created by 266 nm laser pulses of 200 ps duration and with energies up to 200 mJ. Other sources were: 1. Laser pulses at 1064 nm with 10 ns pulse width, 2. Laser pulses at 532 nm with 240 ps pulse width, and 3. IR filaments created by laser pulses at 800 nm with 50 fs pulse width with 1 mJ energy. The emitted light is collected with a 5 cm aspheric lens and coupled into a fiber. The spectrum is observed with a fiber coupled <i>DEMON</i> spectrometer. Left) The picture of the LIBS setup.	112

List of Figures

4.4 (a) The LIBS spectrum of aluminum (Transition from $3s^23p \ J = 3/2$ state to $3s^24s \ J = 1/2$ at 396.152 nm) using a 10 ns pulse at 1064 nm focused by a 40 cm lens is shown for gate delays of 3, 5, 5.5, and 6 μs . The first delay time of 0.5 μs shows the continuum emission rather than emission from the spectral line. The self absorption dip is only recognized at the latest gate delay. (b) LIBS spectrum taken with a 266 nm pulse of 200 ps duration, 200 mJ energy, focused by a 40 cm lens is taken for much shorter delays of 225,525, 725 and 925 ns. 114

4.5 The LIBS was performed via the UV filament at atmospheric pressures. (a) The lithium (6Li) transition line of 670.791 nm is represented. The gate width for this measurement was 1 μs and the delay time was 25 ns. The self-absorption dip has an FWHM of about 289 pm which is much narrower than the emission line. (b) The Aluminum (${}^{27}Al$) transition line of 396.152 nm is represented. The gate width for this measurement was 500 ns and the delay time was 725 ns. The self-absorption dip has an FWHM of about 18 pm which is much narrower than the emission line. (c) and (d) show three transition lines of uranium (${}^{238}U$), with wavelengths of 393.098 and 393.202 nm for (c), and 385.957 nm for (d). The gate width for this measurement was 500 ns and the delay time was 725 ns and 425 ns for (c) and (d) respectively. The self-absorption dips have FWHM values of approximately 8 and 9 pm for (c) and 10 pm for (d) which are much narrower than the emission lines. 117

List of Figures

- 4.6 Left) LIBS spectrum of steel taken with a 200 ps pulse of 200 mJ energy, focused by a lens of 40 cm focal distance at gate delays of 1, 3, and 5 μ s. A broad emission structure can be seen between 301.44 nm and 301.54 nm, which includes three chromium transitions from the $3d^4 4s^2$ [$J = 1, 2, 3$] ground state to the $3d^4(^5D)4s4p(^1P^\circ)$ [$J = 2, 3, 0$] levels at 301.476 (A), 301.491 nm (B), and 301.520 nm (C). Emission lines labeled D (chromium transition from $3d^4(a^3F)4s$ $J = 7/2$ to $3d^4(a^3F)4p$ $J = 7/2$ at 301.550 nm) and E (iron transition from $3d^6 4s^2$ $J = 5$ to $3d^7(^2H)4p$ $J = 4$ at 301.592 nm), do not show a re-absorption dip. Right) LIBS spectra of the two isotopes of Lithium. The transition lines for these two isotopes are at 670.830 nm (Li7) and 670.849 nm (Li6) which indicates an isotopic shift of 19 pm. The emission line extends far beyond the boundaries of the figure. Samples are irradiated by a UV filament at atmospheric pressure. UV laser pulse is a 200 ps pulse of 200 mJ energy, focused by a lens of 40 cm focal distance. 120
- 4.7 The time evolution of the emission spectra for the 424.166 nm transition line of a uranium (^{238}U) sample is shown for delay times ranging from 25 ns to 1025 ns. For all the spectra the gate width is 500 ns. 121
- 4.8 LIBS spectrum of the uranium line (Transition from $5f^3(4I^\circ)6d7s^2$ state to $5f^3 6d7p$ at 385.957 nm), for gate delay of 425 ns, and 40 cm focalization.. The stars are the data points, the solid green line the fit consisting in a Gaussian line (red dotted line) subtracted from the Lorentzian fit (dashed line). 122

List of Figures

4.9 (a) LIBS spectra of the uranium line at 385.957 nm, for gate delays of 425, 925 and 1625 ns, and 40 cm focalization. The solid thick lines are the Lorentzian-Gaussian fits to the data. The solid thin lines are the Lorentzian fits. Triangles, squares, and stars are the data point for respective delays. The vertical arrows pointing to the peaks of the Lorentzians fits show a linewidth and Stark shift decreasing with delay. The dashed line shows the center of the re-absorption dips, emphasizing the absence of Stark shift in the absorption feature. (b) LIBS spectra of the aluminum line (transition from $3s^23p J = 3/2$ state to $3s^24s J = 1/2$ at 396.152 nm), for gate delays of 225, 525, and 925 ns. The stars, diamonds, and triangles are the data points, and the solid thick lines are the complete fits. The dotted lines indicate the Lorentzian parts of the fit. 123

4.10 Comparison of the emission and re-absorption, as analyzed through the fits of Fig. 4.8 versus gate delay. (a) Wavelength of the emission (at the peak of the Lorentzian) and of the re-absorption (at the peak of the Gaussian fit). The 50 pm stark shift of the emission (solid line) rejoins the absorption dip wavelength (dashed line) for delays in excess of 1 μ s. (b) Decrease of the width of the absorption dip versus delay. (c) The broader width of the emission line exhibits a faster decay rate, indicating a faster cooling/expansion of the excited region. (d) Total integrated absorption (area under the Gaussian) versus delay. (e) Total integrated emission (area under the Lorentzian) versus delay. (f) Ratio of (d) to (e). 125

4.11 Schematics of the shadowgraphy setup. 126

4.12 Shadowgraphs of the plume for the first regime. Top: 180 mJ Bottom: 300 mJ. 127

4.13 Shadowgraphs of the plume for the second regime. Top: 180 mJ Bottom: 300 mJ. 128

4.14 a) Shock-wave radius vs time for the first regime. b) Shock-wave radius vs time for the second regime. 129

List of Figures

5.1 (a) High voltage lab and mirrors on the roof. The path of the laser beam(s) is shown by red arrows. (b) and (c) are showing the guiding optics. M9-10: 45° 1064 and 532 and 266 nm HR mirrors; L1: Fused silica Lens with 9 m focal length. For the complete schematics of the optical elements please refer to Fig. 5.4. D: The optical detector which is used to monitor the UV filament arrival time. Filters have been located in front of the detector to ensure that only the UV beam is detected by the detector. 143

5.2 a) Experimental setup. (b) Schematic diagram of the circuit. 144

5.3 Simulation results showing the electric field on the walls of the Faraday cage and also for the electrodes and power supply toroids. Simulations were performed with the assistance of J. Elizondo at Sandia National Lab. 146

5.4 Combination and propagation of three laser beams into the high voltage lab on the roof; M1-2: 45° 266 nm HR (High Reflection) mirrors; M3-5: 45° 1064 nm HR mirrors; M6-7: 45° 1064 and 532 nm HR mirrors; M8-10: 45° 1064 and 532 and 266 nm HR mirrors; M11: HR 532 nm and HT (High Transmission) 1064 nm beam combining mirror; M12: HR 266 nm and HT 1064 and 532 nm beam combining mirror; L1: Fused silica Lens with 9 m focal length; TL1: Telescope with a magnification of 2.7; TL2: Near afocal telescope with a magnification of 1.13; TL3: Telescope with a magnification of 7; All the telescope lenses are uncoated fused silica. The propagation distance of the UV laser up to the middle of the two electrodes is approximately 30 meters. 147

5.12 The beam profiles of UV filaments at different distances from the 9 m focusing lens. These beam profiles are captured by a digital camera recording the impact of the UV filament on a piece of paper. Different colors correspond to the fluorescent emission from the paper which is changing based on the impacted beam intensity. The white dots in the figure are related to multiple filaments. 158

List of Figures

5.13 (a) The two electrodes are charged at 250 kV and their distance is 16 cm. The filament passes through two 3 mm diameter holes in each electrode. The shadow of the electrical discharge and associated shock-wave is projected onto a screen and recorded by a CCD camera. (b) The *Surelite* laser (Continuum), synchronized with a discharge triggering/guiding UV filament emits a 10 ns 100 mJ pulse, expanded, and aimed at the discharge. (c) Schematic diagram of the shadowgraphy setup; M: 45° mirrors, and SHG: Second Harmonic Generation crystal. 159

5.14 Top left: picture of a guided and unguided discharge. In the blue background: shadows of discharge taken at successive times after the UV filament pulse. . . 160

5.15 a) Shock-wave radius vs time for the first regime. b) Shock-wave radius vs time for the second regime. 161

5.16 a) Electric field evolution in atmospheric pressure air following photoionization by a fs UV pulse. At t=0 electrons a(dotted line). The simulation shows the field enhancement at the extremities of the plasma. b) The schematic of the proposed setup for electric field measurements. 163

List of Tables

5.1	Comparison of the self-breakdown voltage and the breakdown voltage in the presence of the UV filament for different gap distances. d : Gap distance between the electrodes; V_B : Self-breakdown voltage; V_{UV} : Breakdown voltage in the presence of the UV filament.	149
-----	--	-----

Chapter 1

Laser filamentation

1.1 Introduction

Laser filamentation is a form of nonlinear propagation that is characterized by two main properties: (i) a high-intensity core that remains narrow over long distances beyond the Rayleigh range, and (ii) a low-density plasma channel that exists within the core. Although the idea of a self-trapped beam of light was first proposed 1960s [1,2], laser filamentation gained significant attention with the development and availability of high-power ultrashort laser pulses. Even though the formation of laser filaments in liquids and solids has been reported [3–5], interest in laser filamentation was limited until 1995. In 1995 formation of laser filaments induced by both 800 nm [6] and 248 nm [7] laser sources was experimentally demonstrated for the first time. Filamentation was defined by Akhmanov [2] as a self-guiding phenomenon that can occur in transparent media with an intensity-dependent index of refraction. If the non-linearity of the medium is positive at moderate intensities (self-focusing), and saturates or turns over (self-defocusing) at higher intensity, a stable waveguide can be formed, which can exist for distances exceeding the Rayleigh range. Laser filamentation has many applications including remote sensing [8–10], laser guided

electrical discharges [11–15], and air lasing [16–20].

1.1.1 Diffraction

During the propagation of a laser beam, diffraction takes place inevitably (even in a vacuum resulting in the transverse broadening of the beam). For Gaussian beams, a parameter that can be used to quantify this divergence is called Rayleigh length. The Rayleigh range is the distance over which the width of a Gaussian beam (with initial flat spatial phase) increases by a factor of $\sqrt{2}$ during propagation. The diameter of a Gaussian beam after propagating over distance Z can be defined as a function of Rayleigh length Z_R :

$$\omega = \omega_0 \sqrt{1 + \left(\frac{Z}{Z_R}\right)^2} \quad \left(Z_R = \frac{\pi\omega_0^2}{\lambda}\right) \quad (1.1)$$

In this equation λ is the laser wavelength, and ω_0 is the beam waist of the Gaussian beam.

1.1.2 Self focusing

If the intensity of a light beam passing through a transparent medium (gas, liquid, or solid) is sufficiently high, the polarization of the medium cannot be assumed to be linearly proportional to the electric field, and nonlinear effects must be considered as represented in Eq. 1.2. In this equation \vec{E} is the electric field and $\chi^{(n)}$ is the electric susceptibility of the order of n [21].

$$\vec{P} = \varepsilon_0 (\chi^{(1)}\vec{E} + \chi^{(2)}\vec{E}^2 + \chi^{(3)}\vec{E}^3 + \dots) \quad (1.2)$$

Air is a centrosymmetric medium and its $\chi^{(2)}$ is equal to zero, and the first estimation for the \vec{P} is only dependent on $\chi^{(1)}$ and $\chi^{(3)}$. The nonlinear index of refraction can be then written as:

$$n = n_0 + n_2 I \quad \left(I = |\vec{E}|^2, \quad n_2 = \frac{3\chi^{(3)}}{4c\varepsilon_0 n_0^2}\right) \quad (1.3)$$

Chapter 1. Laser filamentation

In this equation I is the intensity of the electric field, n_0 is the linear index of refraction, n_2 is the nonlinear index of refraction, and c is the speed of light. As seen in Eq. 1.3 the presence of the high-intensity light beam has modified the index of refraction of the medium which is now dependent on the intensity of the electric field. This phenomenon is referred to as the Kerr effect [22–24]. The value of n_2 for air is approximated to be equal to $\approx 3 \times 10^{-19} \text{cm}^2/\text{W}$ for $\lambda = 800 \text{ nm}$, which is much smaller compared to n_0 for air at the same wavelength [25]. This explains the necessity of the presence of the high-intensity laser pulses to observe a substantial difference in the propagation of laser pulses in air.

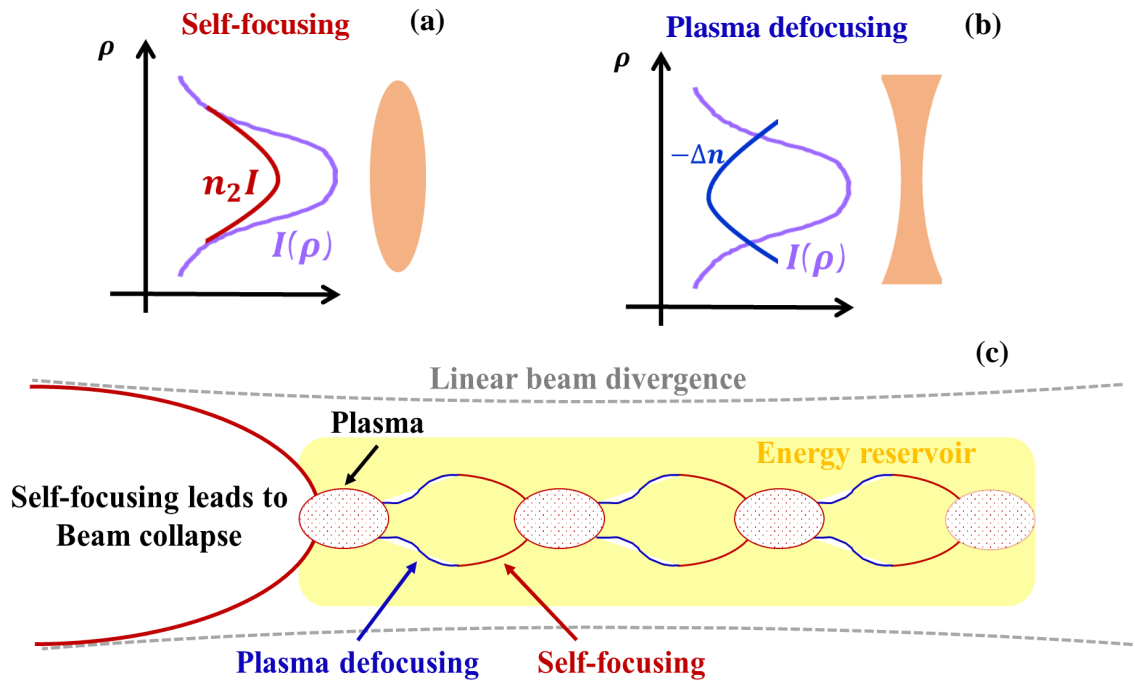


Figure 1.1: Diagrams illustrating the basic principle behind (a) self-focusing and (b) plasma defocusing. (c) Diagram illustrating the filamentation dynamics.

The self-focusing of intense laser beams during propagation is a significant outcome of the Kerr effect. When a Gaussian beam travels through air, it encounters a region of higher index around its center, which causes the wavefront to deform and the beam to converge, similar to the effect of a positive lens as depicted in Fig. 1.1(a). On the other words, the

Chapter 1. Laser filamentation

medium will behave as a converging lens for the beam as it propagates. This self-focusing effect exhibits a cumulative characteristic: as the pulse propagates, it becomes increasingly focused, leading to higher intensity, which in turn enhances the Kerr effect and results in stronger focusing, and so forth [6, 22, 26–28].

As previously stated, a laser beam undergoing diffraction will spread out and diverge. The competition between diffraction and the Kerr self-focusing effect can be defined by a threshold known as the critical power for self-focusing (P_{cr}). When the power of the beam is below P_{cr} , diffraction dominates and causes the beam to continuously diverge. However, when the power exceeds P_{cr} , the Kerr self-focusing effect outweighs diffraction and the beam self-focuses as it travels. The critical power for a Gaussian beam at a wavelength λ_0 can be expressed as [1, 23, 24, 28]:

$$P_{cr} = \frac{3.77\lambda_0^2}{8\pi n_0 n_2} \quad (1.4)$$

If the power of a beam exceeds P_{cr} , it will experience the self-focusing cumulative effect and converge towards a theoretical point of infinite intensity. The distance that a beam of power P needs to travel to reach this point is determined by the formula developed by Marburger [24, 29, 30]:

$$Z = \frac{0.367Z_R}{\sqrt{\left(\sqrt{\frac{P}{P_{cr}}} - 0.852\right)^2 - 0.0219}} \quad (1.5)$$

In the above formula, Z_R is the Rayleigh length of the Gaussian laser beam and the distance Z is measured from the beam waist of the Gaussian beam. In a laboratory setting, the self-focusing distance may be excessively long depending on the beam's size and power. To mitigate this, it is common practice to use optics with a focal length to focus the beam. This modification reduces the self-focusing distance. Although the emergence of a singularity of infinite intensity is predicted, it is not a physical phenomenon and has never been observed. The increasing intensity triggers new processes that prevent its appearance. These processes will be addressed in the following section.

1.1.3 Plasma Defocusing

When the self-focusing of a beam significantly reduces its size, the electric field within the beam becomes strong enough to ionize the air it passes through. The main effect that will take place to hinder the collapse of the beam is the ionization of the medium by the laser field that happens at high intensity. The ionization mechanism is discussed in detail in Section 1.2. The ionization of air will result in the generation of plasma. The under-dense generated plasma is believed to have the same number of free electrons and ions. Since free electrons are only minimally affected by the restoring force during their interaction with the incident electromagnetic field, their motion can be modeled using the Drude model. Using this model, the refractive index of the plasma can be expressed as [6, 23]:

$$n = n_0 - \frac{e^2 \rho^2}{m_e \epsilon_0 \omega^2} \quad (1.6)$$

In Eq. 1.6 ρ is the electron density in the plasma, m_e is the mass of the electron, c is the speed of the light, and ω is the laser frequency. For a Gaussian laser beam, the intensity profile is non-uniform, with greater intensity at the center. Since ionization effects depend on intensity, more electrons will be created at the beam center than at the edges. According to Eq. 1.6, this higher electron density will reduce the optical index, resulting in the plasma acting as a diverging lens as depicted in Fig. 1.1(b). This effect becomes more significant as intensity increases, opposing self-focusing and preventing the occurrence of the infinite intensity singularity [22, 23, 31].

During the propagation of a high-power laser pulse, diffraction, self-focusing, and plasma defocusing are going to compete with each other. A simplified explanation of this competition is as follows. Initially, the beam intensity is too weak to ionize the air and self-focusing occurs, gradually increasing the intensity. At a certain threshold, the intensity becomes high enough to generate a plasma, which causes plasma defocusing that surpasses the Kerr self-focusing and reduces the intensity. With the intensity decreased, self-focusing takes over again, refocusing the beam for a second time, and so on. These

cycles can repeat over a considerable distance, as shown in Fig. 1.1(c). These cycles of focusing and defocusing results in the formation of a thin light channel of high intensity that keeps a constant diameter over a long distance. This phenomenon is called laser filamentation. It should be emphasized that in reality laser filament is a continuous plasma channel, and there is no switching between zones with and without plasma, as the competition eventually reaches a quasi-equilibrium between the three effects [6, 26–28, 31].

1.1.4 Self-induced waveguide versus moving focus

In the case of femtosecond mid-IR filaments, multiple observations of a well-defined clamping intensity have clearly established [32] that these filaments involve a balance between Kerr focusing, diffraction, and plasma defocusing. There have been persistent claims that self-induced waveguide does not exist in the case of a longer pulse, invoking the moving focus model [33, 34]. Perhaps the most convincing example of a self-induced waveguide has been achieved with low power CW light. In that demonstration sketched in Fig. 1.2(a), a laser beam is focused in a cell containing a suspension of dielectric spheres. The dipolar force on the spheres being proportional to the gradient of the field, spheres of higher index of refraction than the liquid migrate towards the center of the beam, creating a focusing effect similar to Kerr lensing. The Brownian motion counterbalances the light-induced concentration, akin to plasma defocusing in the case of fs filaments. The dielectric spheres are either latex spheres of the order of 100 nm diameter, or oil spheres of 40 nm in micro-emulsions. This experiment can be seen as a scaling up in time and space of the optical filaments in air. The electrons responsible for the nonlinearity in air are replaced by microscopic spheres. Interestingly, the giant nonlinearity of the micro-emulsion has a time constant of the order of minutes, and one can observe in real-time the collapse and channeling of the beam as it enters the liquid cell.

It remains that the moving focus model has explained satisfactorily the filament-like

Chapter 1. Laser filamentation

rosary of glass beads produced by self-focusing of a Q-switched pulse in a transparent material [33, 35]. The "moving focus" model is explained by the sketch of Fig. 1.2(b) by decomposing the laser pulse in successive temporal slices of different intensities. As the intensity increases along the leading edge of the pulse, it reaches the critical intensity (Eq. (1.4), leading to self-focusing. The subsequent slices will reach focal points closer to the source as the intensity increases. The fourth slice corresponding to the peak intensity in the figure will focus at the shortest distance.

One may wonder whether the moving focus model should apply to the UV filament, which is closer to nanosecond than femtosecond. The experimental answer to this question is to enter the nonlinear medium with a beam focused down to the diameter of the filament. There is no possibility of moving focus if at the edge of the nonlinear medium the beam has already been focused. This experiment is described in Section 2.3, where the beam is focused in vacuum, and launched into the atmosphere through an aerodynamic window.

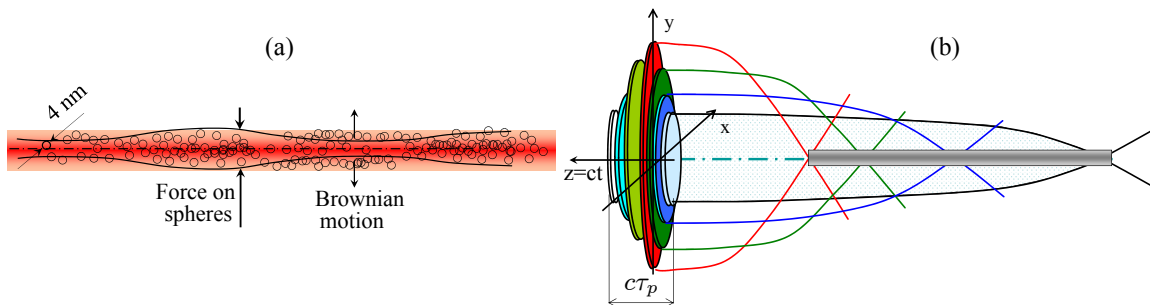


Figure 1.2: (a) Sketch of the cw filamentation observed in suspensions of dielectric spheres [5]. (b) Moving focus model.

1.2 Trends of filamentation versus wavelength

1.2.1 Multiphoton versus Tunnel ionization

In the description of matter by an “index of refraction” or a “polarization”, one tends to forget that the nature of light-matter interaction is simply re-radiation of electrons driven by a combination of the applied electromagnetic field of the light and the field of other particles. The moving electrons radiate a field that adds to that of the light, resulting in phase and amplitude changes of the optical field.

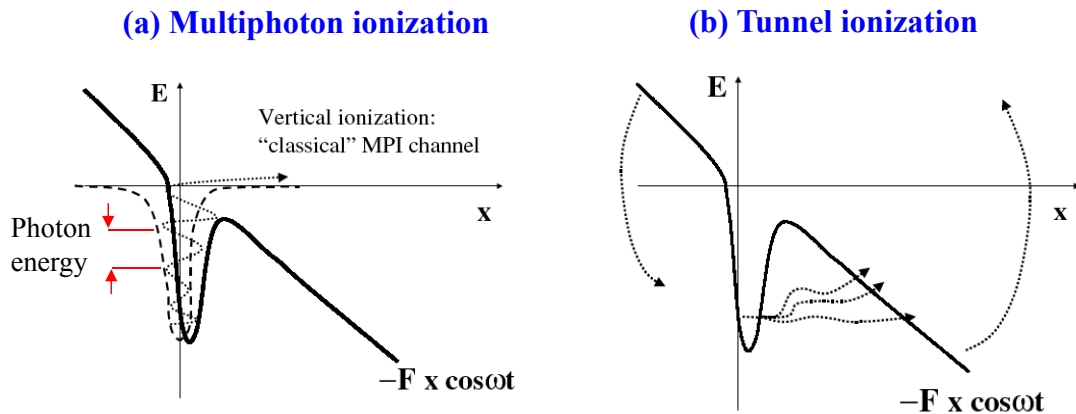


Figure 1.3: (a) Multiphoton ionization: at short wavelengths, the relatively high energy photons stack themselves out of the potential well of the molecule. (b) Tunnel ionization dominates at lower photon energies. While the electron remains near the bottom of the well, the potential surface gets tilted by the field, creating a narrowing potential wall through which the electron can tunnel.

The nature of the ionization process and the electron trajectories following ionization are quite dependent on the wavelength. At the UV wavelength the photon energy is a small fraction of the ionization potential of the gas molecules, and the electron plasma is created through multiphoton ionization. If N is the minimum number of photons of energy $\hbar\omega$ required to exceed the ionization potential I_p , the photoelectron production rate is proportional to the N^{th} power of the light pulse intensity I . The electrons are created with

Chapter 1. Laser filamentation

a kinetic energy equal to the excess energy $N\hbar\omega I_p$. The electron energy spectrum after ionization shows peaks corresponding to ‘‘Above Threshold Ionization’’ (ATI) at energies of $(N + m)\hbar\omega - I_p$ corresponding to the absorption of $N + m$ photons.

At longer wavelengths, the intensity required for N photons to stack themselves out of the potential well of the gas molecule gets comparable to the intensity required to tunnel out of the potential wall created by the distorted potential surface. In contrast to the case of multiphoton ionization, the tunneled electron is released at the other side of the wall with zero velocity.

The distinction between multiphoton and tunnel ionization is quantified by the ‘‘Keldish parameter’’ γ [36]:

$$\gamma = \sqrt{\frac{I_p}{2U_p}}, \quad (1.7)$$

where U_p is the ponderomotive energy or the the average kinetic energy of a free electron oscillating in the laser field. If e and m_e are the charge and mass of the electron; ω the (angular) frequency of the light field of amplitude E :

$$U_p = \frac{e^2 E^2}{4m_e \omega^2}. \quad (1.8)$$

U_p expressed in eV as a function of the light intensity I_ℓ in W/cm² and the wavelength λ in microns is:

$$U_p = 9.33 \cdot 10^{-14} I_\ell \lambda^2 \quad (1.9)$$

In the ‘‘quasistatic limit’’ of $\gamma < 1$ the dressed Coulomb barrier is essentially static as seen by the electrons and the method of releasing the electrons is dominated by *tunneling*. For $\gamma > 1$ the electron release is most likely described by photon absorption, and *multiphoton* features are more dominant [37]. The difference between tunneling and multiphoton is experimentally recognized in measurements of velocity mapping imaging (VMI) where the electron momentum distribution following ionization is measured [38]. These

measurements show that at 800 nm where $\gamma \approx 1$, the electron is released with approximately zero velocity and there is no evidence of ATI. One concludes therefore that tunnel ionization corresponds to $\gamma \leq 1$. A tunneled electron leaves its parent atom/molecule instantaneously along the direction of light polarization, at the moment of ionization, with zero velocity [39]. The electrons leave the atom from a Rydberg state that typically has an orbit radius one order of magnitude larger than the atomic radius. Formulae can be found in the literature for the tunneling rate and the ratio of electron production for various polarizations [40, 41]. The trajectory of the electron released near a peak alternate of the laser field can be calculated classically. In the case of linear polarization, it is easily seen that the released electron remains in the vicinity of the molecule, which implies that recollision is possible, leading to attosecond pulse generation [42]. In the case of circular polarization, the electron drifts away from the parent molecule.

1.2.2 From photoionization to avalanche ionization

As a high-intensity beam above critical power starts to focus in the atmosphere, it creates a low density plasma by multiphoton ionization. In the intense light field, the photoelectrons will gain energy by inverse Bremsstrahlung [43]. The rate of energy gain dW/dt depends on the optical frequency, being proportional to the square of the wavelength. The accelerated electrons can collide with neutral molecules, thereby increasing the plasma density by collisional ionization. This is the avalanche process leading to full ionization of the medium. The additional influx of electron will perturb the delicate balance between self-focusing and defocusing that leads to a filament. A filament equilibrium between self-focusing and defocusing by photoionized electrons is possible before the electron density gets dominated by collision ionization. A characteristic parameter is the time required for the electron energy to reach the the ionization energy of oxygen.

The electron-ion collision rate being $\nu_{ei} = 1.07 \times 10^{11} \text{ s}^{-1}$ [44], an electron will gain

Chapter 1. Laser filamentation

an energy U_p in the time interval $1/\nu_{ei}$ between collisions. The energy gain dW in a time interval dt due to inverse Bremsstrahlung can be estimated as:

$$\frac{dW}{dt} \approx U_p \nu_{ei} \approx \cdot 10^{-2} I_\ell \lambda^2 \quad (1.10)$$

where we have used the units of Eq. (1.9), and expressed the collision time in ps. A rough estimate for the time Δt needed to reach the ionization potential of 12.2 eV (oxygen) is

$$\Delta t = \frac{1.22 \cdot 10^{15}}{I_\ell \lambda^2} \quad (1.11)$$

For the typical 50 TW/cm² at 800 nm, Eq. (1.11) indicates that the pulse duration should be small compared to 40 ps to prevent collisional ionization from affecting the balance between self-focusing and plasma self-defocusing. This limit increases to 40 ns for a 0.5 TW/cm² at 250 nm.

In the case of fs near IR filaments, a number of phenomena can contribute to balancing the self-focusing effect: creation of an electron plasma, energy loss due to pulse-splitting or conical emission, and higher order nonlinearities. In the case of long-pulse UV filaments, this balance is entirely provided by the creation of electrons due to multiphoton ionization which is a purely intensity-dependent mechanism. Knowing that UV filaments consume 40 μ J per meter of propagation [45] one should be able to increase the length of UV filaments by increasing the pulsewidth of the UV laser beam.

1.2.3 Filament stability versus order of ionization

To have a stabilizing effect on the beam (or filament) diameter, the plasma self-defocusing should have an intensity dependence of higher order than the Kerr effect. It is clear from the theory of Section 1.3 that three-photon ionization is the lower order possible. The wavelength dependence of filamentation has been studied in ZnSe [46]. The wavelength was varied from a condition of three-photon excitation of the conduction band to five

photons. The spectral bandwidth of the filamented pulses as well as the length of the fluorescence track was seen to increase with the order of ionization. Multiphoton absorption was cited as a major contributing factor for increased losses at low order. The situation is different in dry air where an energy loss of only $40 \mu\text{J}/\text{m}$ was measured [45] for 248 nm filaments with pulses of 1 ps duration. These measurements were made in the 5% humidity atmosphere of New Mexico. The situation is different in humid air, where a two-photon resonance enhanced ionization was identified [47]. The initial excitation proceeds via the two-photon resonant transition in water vapor $\tilde{C}^1B_1 \leftarrow \tilde{X}^1A_1$. This excitation is followed by single photon ionization from the \tilde{C}^1B_1 , the rate of which is enhanced by a resonance with the molecular-ionic transition $^2A_1(3a_1^{-1}) \leftarrow \tilde{C}^1$ [47].

1.2.4 Single filament propagation versus wavelength

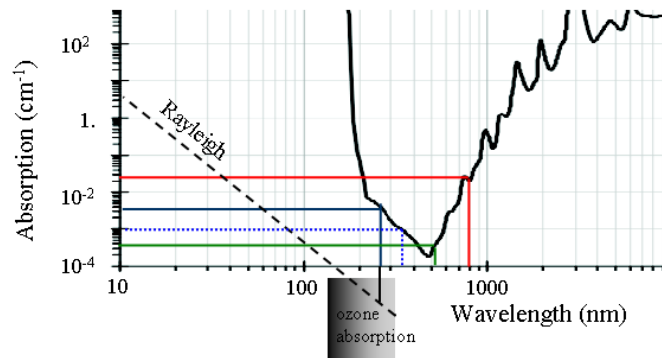


Figure 1.4: Attenuation lengths for various atmospheric factors. Solid line: water absorption. Dashed line: Rayleigh scattering. The red, green, dotted blue, and solid dark blue lines indicate wavelengths of 800 nm, 532 nm, 355 nm, and 266 nm, respectively.

Linear optical properties of the atmosphere should be a factor in choosing the wavelength that would propagate with the least attenuation. The attenuation length corresponding to various phenomena is plotted in Fig. 1.4. The solid line shows water absorption, with a minimum near 400 nm. Closest to this minimum is the second harmonic of Nd:YAG at

Chapter 1. Laser filamentation

532 nm. This wavelength is indicated by the green lines in Fig. 1.4. Attempts of filamentation were made with Nd:YAG laser pulses that are frequency doubled and compressed down to 200 ps, at an energy of 1.2 J. The peak power was clearly above the self-trapping critical power. Plasma beads created by avalanche ionization were observed, indicating that 200 ps duration at that wavelength is too long for stable filament formation. At the wavelength of 266 nm indicated in the figure by the dark blue line, ozone absorption, water absorption, and Rayleigh scattering are present. These factors are negligible at the third harmonic of the Nd:YAG laser of 355 nm, indicated by the dotted line.

Because of the plasma defocusing, the intensity of a single filament is clamped. Consequently, a 800 nm filament of about 100 fs will have its energy typically clamped around 1 mJ. Because of the high intensity in the filament core, it loses its energy through non-linear effects (in particular by generation of broadband conical emission). These energy losses limit the propagation distance of the single 800 nm filament to a distance of the order of a meter. The “brute force” method to extend the range of filaments is to use a high energy pulse as an initial condition. For instance, a pulse of 1 J energy will generate approximately 10^3 filaments distributed over the initial beam diameter and covering a distance that can exceed 100 m. An approach to extend the *range* of filaments, proposed initially for UV pulses [44], is to downchirp the initial pulse so that it can be compressed by propagating through the atmosphere which has positive dispersion. This method of postponing the start point of a filament is well adapted to broadband fs pulses and has been demonstrated over a distance of 1 km [48] with 800 nm pulses. While the dispersion of the atmosphere is larger in the UV, the narrow bandwidth of a 100 ps pulse precludes the application of this technique of temporal focusing to long UV pulses.

There has not been a systematic study of filament properties versus wavelength, because of limited access to high-power sources in multiple wavelength ranges. Figure 1.5 attempts to give a rough idea of the trend for filament parameters versus wavelength. The longer the wavelength, the shorter the pulse duration required to prevent avalanche, and

Chapter 1. Laser filamentation

λ (nm)	I TW/cm ²	τ ps	Energy mJ	Losses	References
248	1	10,000	10,000	Linear Ozone Rayleigh	Zhao 1995, Smetanin 2016, Zvorykin 2015
266					
355					
400	50	1	1	Nonlinear Conical Emission	Daigle 2010
800					

Figure 1.5: Trend in the wavelength range from 248 to 800 nm for single filaments. Second column: intensity range. Third column: range of energy/filamenting pulse. Fourth column: dominant loss mechanism. Fifth column: some references. Zhao 1995 = [7]; Smetanin 2016 = [49]; Zvorykin 2015 = [50]; Chalus 2008 = [51]; Daigle 2010 = [52]; Braun 1995 = [6].

the intensity required for creating the defocusing plasma is higher. Because of intensity clamping, the energy of the filamented pulse decreases by 3 orders of magnitude between the UV and infrared. Losses are mostly linear in the UV (ozone absorption, Rayleigh scattering) and nonlinear in the infrared due to the high intensity [53].

1.3 Physical parameters relevant to UV filaments formation

1.3.1 Conditions particular to long UV pulse

The time to reach avalanche being of the order of tens of ns, as shown by Eq. (1.11), one might search for a condition where the interaction of light with air reaches a steady state. Under constant electric field of the light, the dynamics of the evolution of the electron

Chapter 1. Laser filamentation

density depends on the ionization cross section $\sigma^{(3)}$, the recombination rate β_{ep} , and the rate of attachment of electrons to oxygen γ . In the approximation that the number of electrons remains small compared to the number of neutrals, the equation for the generation of electrons is:

$$\frac{dN_e}{dt} = N_0\sigma^{(3)}I^3 - \beta_{ep}N_e^2 - \gamma N_e, \quad (1.12)$$

where I is the laser field intensity and N_0 is the density of oxygen molecules in air. Measurement and calculation of the parameters $\sigma^{(3)}$, β_{ep} and γ are presented in Section 1.3.2 that follows.

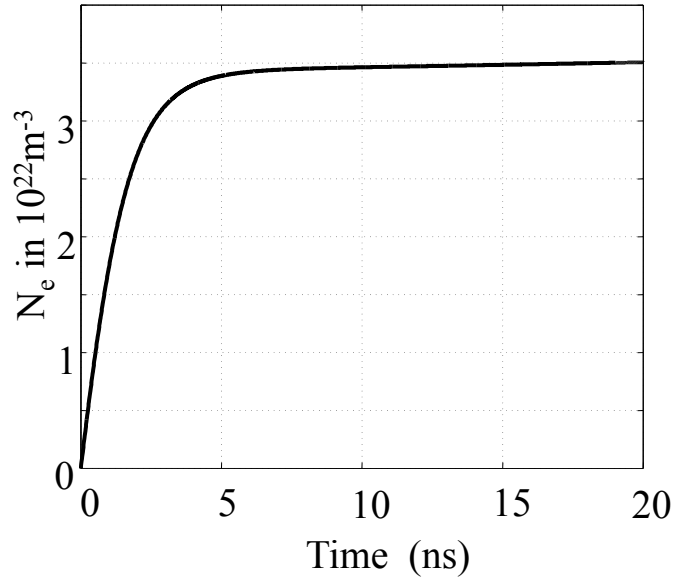


Figure 1.6: Evolution of the electron density N_e as a function of time for a step-function irradiation of intensity $I = 0.54 \text{ TW/cm}^2$ [54].

Figure 1.6 shows the temporal evolution of the density of electrons as a function of time, for a step-function intensity of 0.5 TW/cm^2 (intensity measured in UV filaments [45,

51, 55]). The asymptotic value is:

$$\begin{aligned} N_{eq} &= \frac{-\gamma + \sqrt{\gamma^2 + 4\beta_{ep}N_O\sigma^{(3)}I^3}}{2\beta_{ep}} \\ &= \frac{\sqrt{4\beta_{ep}N_O\sigma^{(3)}I^3}}{2\beta_{ep}} \left[1 + \frac{1}{2} \frac{\gamma^2}{(4\beta_{ep}N_O\sigma^{(3)}I^3)} \right] - \frac{\gamma}{2\beta_{ep}}. \end{aligned} \quad (1.13)$$

The last term of this expansion contains no field dependence, and will be ignored since it contributes only to the linear polarization. Figure 1.6 indicates that 75% of this value is reached after 2 ns. This justifies using a steady state approach for calculating the energy density when pulses have a duration between 2 and 40 ns.

The nonlinear polarization amplitude contribution from the electron plasma is:

$$P_{NL} = \epsilon_0 \frac{\omega_p^2}{\omega^2} E = \frac{\epsilon_0 N_e e^2}{\omega^2 m_e \epsilon_0} E, \quad (1.14)$$

where ω_p is the plasma frequency and m_e the electron mass. One notes that, with a three-photon absorption, the nonlinear index due to the plasma is only proportional to the power 1.5 of the intensity. Three photon ionization is the lowest order multiphoton process to create a plasma stabilizing the $n_2 I$ of Kerr self-focusing. If the attachment coefficient to oxygen γ is neglected, the nonlinear polarization of Eq. (1.14) corresponds to a nonlinear index

$$\Delta n = \frac{\omega_p^2}{\omega^2} = \frac{N_e e^2}{\omega^2 m_e \epsilon_0} \approx \frac{\sqrt{\beta_{ep} N_O \sigma^{(3)} I^3}}{2\beta_{ep}} \frac{e^2}{m_e \epsilon_0 \omega^2} \quad (1.15)$$

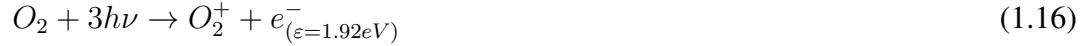
Neglecting the attachment coefficient to oxygen will lead to a simple eigenvalue equation for the UV steady-state pulse, an extension of the Townes soliton.

1.3.2 Determination of $\sigma^{(3)}$, β_{ep} and γ

A self-defocusing associated with the photoelectron plasma is crucial in preventing the collapse of the beam through Kerr self-focusing. The ionization energy of oxygen being

Chapter 1. Laser filamentation

12.2 eV, at the wavelength of 266 nm (4.66 eV), three photons are needed to extract the electron from the oxygen:



At wavelengths shorter than 300 nm, the density of electrons is critically dependent on three parameters: the three-photon ionization cross-section of oxygen $\sigma^{(3)}$, the recombination rate of electrons β_{ep} , and the attachment coefficient γ of electrons to neutral oxygen to form a negative ion.

Negative oxygen ions

The negative oxygen ion (O^-) plays an important role in reducing the number of photo-electrons created by the ionizing pulse. It can be created by simple inelastic collision of the oxygen molecule with an electron of energy >6.5 eV:



This two-body attachment requires that the plasma has been heated up to ≈ 6.5 eV by inverse Bremsstrahlung. A second process that results in the creation of O^- at low electron temperatures consists in a cascade of two reactions: a two-photon dissociation of O_2 in two oxygen atoms, followed by the attachment of the previously formed electron with one oxygen atom. This latter reaction, unlike the attachment of the electron with O_2 , requires only an electron with kinetic energy of 1.5 eV. The the reaction sequence is:



Pump-probe experiments on O^-

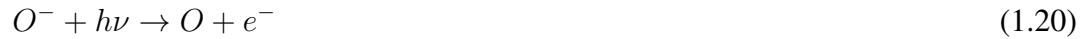
Attachment to oxygen

The conventional approach to photo-ionization measurements is to irradiate the molecules

Chapter 1. Laser filamentation

in a low pressure cell, and to measure the charges collected on electrodes. Since the parameters are needed to model filaments *in air*, the approach chosen here is to study oxygen at a pressure as close as possible to atmospheric pressure [55].

In the experimental set-up sketched in Fig. 1.7, the concentration of O^- is monitored through the absorption of a He-Ne laser beam. The single photon photodetachment spectrum of O^- indicates an absorption cross section of $6 \cdot 10^{-18} \text{ cm}^2$ [56] in the wavelength range from 350 nm to 620 nm. The photodetachment reaction is:



In the experimental setup sketched in Fig. 1.7(a), a 4.5 m cell filled with up to 2 atm of

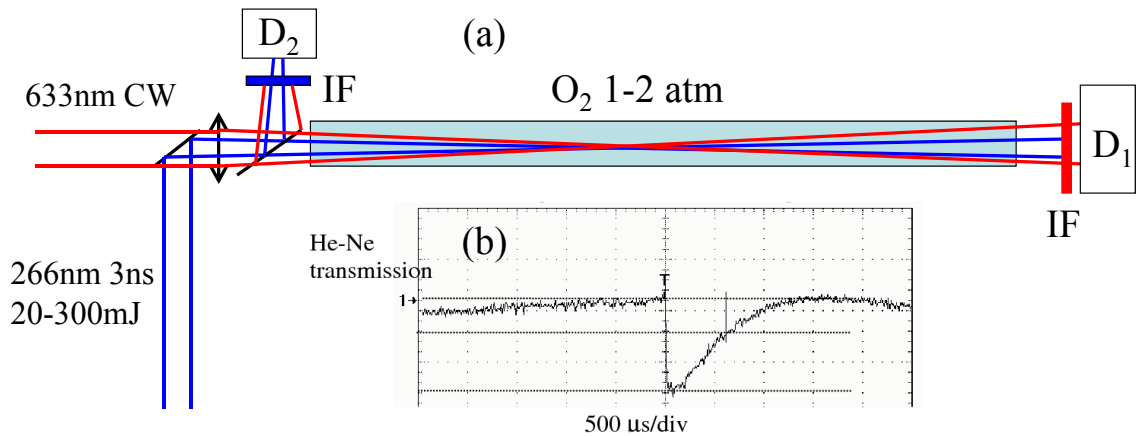


Figure 1.7: (a) Setup for measurement of absorption by O^- ($D_{1,2}$ =Detectors, IF=Interference filter). (b) Induced absorption trace on the He-Ne beam [55].

pure oxygen is used ¹. An ionizing pulse is provided by the fourth harmonic (266 nm) of a Nd:YAG laser, with a pulse duration of 3 ns and an energy from 20 to 300 mJ at 2 Hz. The 633 nm intensity is monitored at the same time as the energy of the UV pulse with detectors D_1 and D_2 , respectively, after passing through corresponding interference filters, and for two different pressures (1 and 2 atmospheres). In the presence of ionizing

¹More experimental details can be found in [55].

radiation, the induced absorption coefficient $\alpha(t)$ can be recorded as a function of time:

$$\alpha(t) = -\frac{1}{L} \ln \frac{D_1}{D_2} \approx \frac{1}{L} \left(1 - \frac{D_1}{D_2} \right), \quad (1.21)$$

where L is the length of interaction region between the focused He-Ne laser beam and the plasma. The measurement of the absorption coefficient α at the He-Ne wavelength leads to the concentration in O^- ions since $\alpha = \sigma N_{O^-}$, where $\sigma = 5.8 \cdot 10^{-18} \text{ cm}^2$ [56]. At 1 atmosphere, with an ionizing laser power of 10MW (intensity of $2.5 \cdot 10^{11} \text{ W/cm}^2$), an attenuation of 34% of the probe He-Ne laser is measured. This leads to an estimate of $N_{O^-} = 5.6 \cdot 10^{16} \text{ cm}^{-3}$ for the density of O^- .

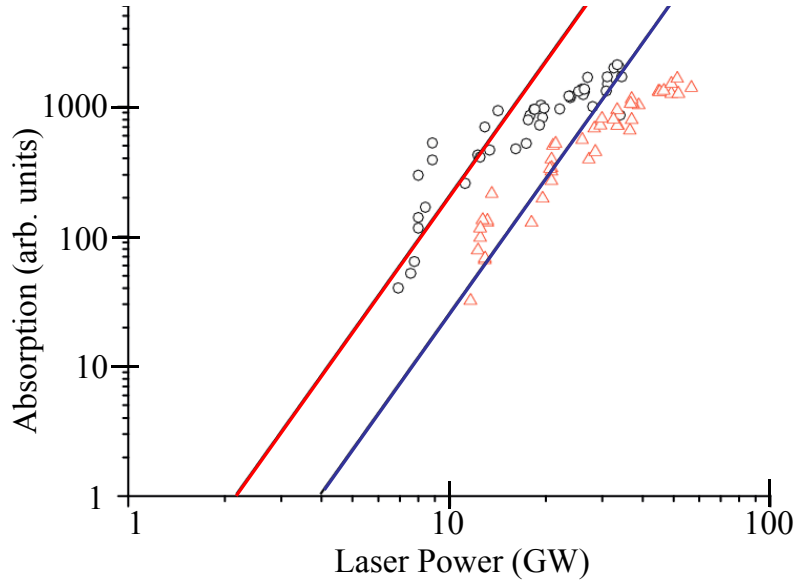


Figure 1.8: Absorption at 633 nm is induced by the recombination of electrons with oxygen. The absorption coefficient is proportional to the concentration of O^- ions, which is proportional to the number of photoelectrons. Circles: 2 atm pressure, Triangles: 1 atm pressure. The straight lines indicate the slope corresponding to the (UV laser power)³ [55].

A typical oscilloscope trace of the probe transient absorption is shown in Fig. 1.7(b), indicating a $1/e$ decay of $620 \mu\text{s}$. After deconvolution for the response time of the detection, the lifetime of the O^- is found to be $\tau_o = 590 \mu\text{s}$. At electron energies below 6.5 eV, the two-body attachment process of Eqs. (1.18) and (1.19) dominates. Three body attachment reactions involving nitrogen and oxygen can also be considered but are negligible

Chapter 1. Laser filamentation

above 1 eV electron temperature [55]. The contribution of the two-body attachment to the decay of the electron population is $\gamma = \eta_{att}[O_2]$ where $[O_2]$ is the concentration of oxygen and η_{att} is given by [57]:

$$\eta_{att} = 2.75 \times 10^{-10} T_e^{-0.5} e^{-\frac{5}{T_e}} \text{cm}^3 \text{s}^{-1} \quad (1.22)$$

where T_e is the temperature of the electrons expressed in eV. Choosing $T_e = 2$ eV leads to $\gamma = 1.5 \cdot 10^8$.

Photoionization cross section

The induced absorption, plotted versus the intensity of the UV beam, shows the expected cubic dependence (Fig 1.8). The induced absorption is proportional to the concentration of oxygen and photoelectrons. Since $N_e \geq N_{O_2}$ one can use the measurement of Fig 1.8 to get a rough upper estimate of the 3-photon ionization cross section of oxygen. That estimate gives $\sigma^{(3)} = 4.1 \times 10^{-41} \text{m}^6 \text{s}^2 / \text{J}^3$, close to the theoretical value of $3.0 \times 10^{-29} \text{cm}^6 \text{s}^2 \text{J}^{-3}$ [36] and published experimental data [45, 53, 58].

Summary of the parameters used for the plasma defocusing

parameter	$\sigma^{(3)}$	β_{ep}	γ
value	$3 \cdot 10^{-41}$	$1.3 \cdot 10^{-14}$	$1.5 \cdot 10^8$
Unit	$\text{m}^6 \text{s}^2 \text{J}^{-3}$	$\text{m}^3 \text{s}^{-1}$	s^{-1}

1.4 Outline

In this section, the outline of the next chapters of the dissertation is introduced. Chapter 2 focuses primarily on UV filaments and their corresponding measurements. UV filaments are generated by UV laser pulses with a duration of 200 ps and an energy of up to 300 mJ, operating at a wavelength of 266 nm. The chapter explores the impact of different

Chapter 1. Laser filamentation

beam preparation scenarios on UV filamentation. Beam preparation by focusing in vacuum and launching into the atmosphere through an aerodynamic window establishes the existence of filaments as self-guided non-diffracting entities. Aerodynamic window is a tool in which a supersonic flow of air is forced through a narrow nozzle. As the air flows through a curved expansion chamber, it creates a pressure gradient from vacuum to atmospheric pressure which results in the effective separation of the low vacuum chamber (pressure of about 10 torr) from atmosphere. Furthermore, focusing through the aerodynamic window transforms the initial super-Gaussian beam profile into a parabolic shape at the edge of the nonlinear medium (air). The impulsive heating of gas by UV filaments creates shock-waves of cylindrical symmetry which propagate outward from the center line, leaving a low-density channel behind. The shock-waves generated by the UV filaments are examined using shadowgraphy techniques. Analysis of the shadowgraphy data reveals that the low-density channel forms within 300 ns and maintains stability and uniformity for up to 200 μ s. At sufficiently high repetition rates, it becomes possible to sustain this low-density channel, creating a stationary waveguide that can be utilized for optical guiding purposes. Following the investigation of UV filamentation, the chapter proceeds to discuss the progress made in developing a new high repetition (up to 20 kHz) laser source. Towards the end of the chapter, a comprehensive description is provided for the design and various components of the developed Velocity Map Imaging (VMI) setup which is adapted to the study of filaments.

In the next chapter, the application of laser filamentation towards “Air Lasing” will be studied. “Air Lasing” is a phenomenon that was first proposed in 2003 based on the observation of amplified emissions in a femtosecond laser filament. Since then, it has garnered significant attention due to its potential applications. The concept of air lasing differs from that of conventional lasers, as it enables remote mirrorless (no-cavity) optical amplification in ambient conditions. The mechanism behind the generated gain in this phenomenon is still the subject of heated debate. Various air constituents have been proposed and investigated as potential gain media for air lasing. Among these candidates, the transitions

Chapter 1. Laser filamentation

of the nitrogen cation N_2^+ are of particular interest, with two transitions corresponding to wavelengths of 391 nm and 428 nm being investigated. In this study, we employed a streak camera to measure the time- and space-resolved dynamics of N_2^+ emission from a self-seeded femtosecond 800 nm filament. The measurements were conducted on 800 nm laser filaments prepared using two different focusing lenses, with focal lengths of 10 cm and 40 cm. The Rayleigh scattering, which is enhanced by small water droplets, provided an accurate time origin for temporal measurements. To eliminate the effect of the response function of the streak camera, a de-convolution process was performed using MATLAB. Our unique capability of sub-picosecond timing resolution, along with absolute timing measurement using Rayleigh scattering, enables us to report accurate measurements of the timing and temporal profile of the N_2^+ emissions. It has been observed that these emissions exhibit a delay with respect to the ionizing 800 nm laser filament. Our study suggests that the fast decay and high peak gain observed in air lasing are due to the collective emission introduced by Dicke in 1954. The temporal behavior of the pulse as a function of density agrees with the predictions of superfluorescence. Therefore, it can be concluded that the collective emission and spatial distribution of the plasma need to be considered for applications in remote source design using N_2^+ as a gain medium.

Chapter 4 investigates Laser Induced Breakdown Spectroscopy (LIBS) via UV filaments. After providing an initial overview of LIBS, the chapter investigates the intriguing self-absorption phenomenon in LIBS, shedding light on its mechanisms and implications for achieving enhanced detection precision. Self-absorption occurs when the emitted radiation from the hotter core of the laser-induced plasma is absorbed by the outer colder layers of the plasma, leading to a decrease in the intensity of the emitted spectral lines. Due to the lower electron number density in the outer layers compared to the plasma core, the absorption line profile is not affected by Stark broadening and is narrower than the emission profile, creating an absorption dip in the emission line. Importantly, self-absorption dips are more likely to occur at higher pressures, including atmospheric pressures, due to the greater confinement of the plasma, resulting in an inhomogeneous plasma. The

Chapter 1. Laser filamentation

chapter investigates LIBS spectra from multiple samples at atmospheric pressures and demonstrates that self-absorption dips exhibit a significantly smaller Full Width at Half Maximum (FWHM) compared to the typically broad emission lines observed under these conditions. It has been shown that by utilizing the narrower self-absorption dip, it becomes possible to resolve isotopic shifts on the order of tens of picometers, which is typically not achievable via emission lines at atmospheric pressures. Moreover, in contrast to the emission lines, the self-absorption dip is not Stark shifted, offering better accuracy in LIBS measurements. The effect of laser wavelength on the self-absorption dip is also examined, revealing that when using UV filaments, the self-absorption dips appear at much shorter delays relative to the ionizing laser pulses compared to IR laser pulses. Furthermore, this chapter quantitatively studies the temporal evolution of the self-absorption dip in a selected line of Uranium. The evolution of the plume and the propagation of the created shock-waves are also investigated using the shadowgraphy technique. Overall, our findings demonstrate that by harnessing self-absorption dips in LIBS through the use of UV filaments, we can achieve higher resolution and improved accuracy in measurements. This provides promising opportunities for precise elemental analysis and quantitative measurements in LIBS.

The final chapter of the thesis focused on the study of triggering and guiding high-voltage electrical discharges by UV filaments. Since their invention, researchers have investigated lasers as potential candidates for guiding and triggering electrical discharges. The effectiveness of UV filaments in triggering and guiding electrical discharges over different gap distances, ranging from 5 cm to 38 cm, was investigated. It was concluded that UV filaments produce transient conductivity twice as large as 800 nm filaments, and they achieve laser-induced discharge at less than half the self-breakdown voltage compared to a 20-30% reduction for IR filaments. The development time of guided discharges over long distances ranges from tens to hundreds of μs , depending on the gap, while the plasma's lifetime is on the order of tens of ns. Therefore, it can be concluded that rather than being guided by the conductivity of the plasma, the guiding mechanism in filament-induced dis-

Chapter 1. Laser filamentation

charges is the air rarefaction through the low-density channel left behind after the filament-generated shock-wave propagates outwards. In an attempt to achieve plasma-guided discharge, we combined UV filaments with two other laser pulses. A 10 ns frequency doubled Nd:YAG laser at 532 nm was chosen for photodetaching O^- , and a Nd:YAG laser at 1064 nm for plasma heating. The study measured two main factors to investigate the contribution of adding the two laser pulses: the discharge probability and the delay between the discharge and the arrival of the UV filament. However, the high-power photodetaching nanosecond laser pulses at 532 nm and the plasma heating pulses at 1064 nm had no effect on the discharge probability and the delay of discharge with respect to the UV laser filament. Additionally, the study investigated the effect of absolute humidity on laser-induced discharges, concluding that the discharge probability and average delay are dependent on the absolute humidity. As the humidity increases, the discharge probability increases, and the average delay decreases.

References

- [1] R. Y. Chiao, E. Garmire, and C. H. Townes. Self-trapping of optical beams. *Physics Review Letter*, 13:479–482, 1964.
- [2] S. A. Akhmanov, A. P. Sukhorukov, and R. V. Khokhlov. Self focusing and self trapping of intense light beams in a nonlinear medium. *Sov. Phys JETP*, 23:1025–1033, 1966.
- [3] Michael M. T. Loy and Y. R. Shen. Small-scale filaments in liquids and tracks of moving foci. *Phys. Rev. Lett.*, 22:994–997, May 1969.
- [4] George N. Steinberg. Filamentary tracks formed in transparent optical glass by laser beam self-focusing. i. experimental investigation. *Phys. Rev. A*, 4:1182–1194, Sep 1971.
- [5] E. Freysz, M. Afifi, A. Ducasse, B. Pouligny, and J. R. Lallane. Giant optical nonlinearities of critical micro-emulsions. *J. Physique Lett.*, 46:181–187, 1985.
- [6] A. Braun, G. Korn, X. Liu, D. Du, J. Squier, and G. Mourou. Self-channeling of high-peak-power femtosecond laser pulses in air. *Optics Lett.*, 20:73–75, 1995.
- [7] Xin Miao Zhao, Patrick Rambo, and Jean-Claude Diels. Filamentation of femtosecond UV pulses in air. In *QELS, 1995*, volume 16, page 178 (QThD2), Baltimore, MA, 1995. Optical Society of America.
- [8] Matthieu Baudelet, Myriam Boueri, Jin Yu, Samuel S. Mao, Vincent Piscitelli, Xianglei Mao, and Richard E. Russo. Time-resolved ultraviolet laser-induced breakdown spectroscopy for organic material analysis. *Spectrochimica Acta Part B: Atomic Spectroscopy*, 62(12):1329–1334, 2007. A Collection of Papers Presented at the 4th International Conference on Laser Induced Plasma Spectroscopy and Applications (LIBS 2006).
- [9] K. Stelmaszczyk, P. Rohwetter, G. Méjean, J. Yu, E. Salmon, J. Kasparian, R. Ackermann, J. P. Wolf, and L. Wöste. Long-distance remote laser-induced breakdown spectroscopy using filamentation in air. *Appl. Phys. Lett.*, 85:3977–3979, 2004.
- [10] Ali Rastegari, Matthias Lenzner, Jean-Claude Diels, Kristen Peterson, and Ladan Arissian. High-resolution remote spectroscopy and plasma dynamics induced with UV filaments. *Opt. Lett.*, 44(1):147–150, Jan 2019.
- [11] Thomas Produit, Pierre Walch, Clemens Herkommer, Amirhossein Mostajabi, Michel Moret, Ugo Andral, Antonio Sunjerga, Mohammad Azadifar, Yves-Bernard André, Benoît Mahieu, Walter Haas, Bruno Esmiller, Gilles Fournier, Peter Krötz,

References

- Thomas Metzger, Knut Michel, André Mysyrowicz, Marcos Rubinstein, Farhad Rachidi, Jérôme Kasparian, Jean-Pierre Wolf, and Aurélien Houard. The laser lightning rod project. *Eur. Phys. J. Appl. Phys.*, 93(1):10504, 2021.
- [12] Francis Théberge, Jean-François Daigle, Jean-Claude Kieffer, François Vidal, and Marc Châteauneuf. Laser-guided energetic discharges over large air gaps by electric-field enhanced plasma filaments. *Scientific Reports*, 7(1):40063, Jan 2017.
- [13] Ali Rastegari, Elise Schubert, Chengyong Feng, Denis Mongin, Brian Kamer, Jerome Kasparian, Jean-Pierre Wolf, Ladan Arissian, and Jean-Claude Diels. Beam control through nonlinear propagation in air and laser induced discharges. In *Laser resonators and beam control XVIII, Photonics West, Conference 9727-51*, pages 9727–51, San Francisco, CA, 2016. SPIE.
- [14] Elise Schubert, Ali Rastegari, Chengyong Feng, Denis Mongin, Brian Kamer, Jerome Kasparian, Jean-Pierre Wolf, Ladan Arissian, and Jean-Claude Diels. HV discharge acceleration by sequences of UV laser filaments with visible and near-infrared pulses. *New Journal of Physics*, 19(12):123040, 2017.
- [15] A. Houard, C. D’Amico, Y. Liu, Y. B. Andre, M. Franco, B. Prade, A. Mysyrowicz, E. Salmon, P. Pierlot, and L.-M. Cleon. High current permanent discharges in air induced by femtosecond laser filamentation. *Applied Physics Letters*, 90(17):171501, 2007.
- [16] Q. Luo, W. Liu, and S.L. Chin. Lasing action in air induced by ultra-fast laser filamentation. *Applied Physics B*, 76(3):337–340, Mar 2003.
- [17] Ladan Arissian, Brian Kamer, Ali Rastegari, D. M. Villeneuve, and Jean-Claude Diels. Transient gain from N_2^+ in light filaments. *Phys. Rev. A*, 98:053438, Nov 2018.
- [18] Mathew Britton, Marianna Lytova, Patrick Laferrière, Peng Peng, Felipe Morales, Dong Hyuk Ko, Maria Richter, Pavel Polynkin, D. M. Villeneuve, Chunmei Zhang, Misha Ivanov, Michael Spanner, Ladan Arissian, and P. B. Corkum. Short- and long-term gain dynamics in N_2^+ air lasing. *Phys. Rev. A*, 100(4):013406, 2019.
- [19] A. Mysyrowicz, R. Danylo, A. Houard, V. Tikhonchuk, X. Zhang, Z. Fan, Q. Liang, S. Zhuang, L. Yuan, and Y. Liu. Lasing without population inversion in N_2^+ . *APL Photonics*, 4(11):110807, 2019.
- [20] Jean-Claude Diels, Ali Rastegari, Alejandro Aceves, and Nicolas Bagley. Filaments 2022: Fast and slow dynamics and the challenges they present in understanding filamentation. In *International Conference on Laser Filamentation (COFIL)*, 2022.

References

- [21] W. Boyd. *Nonlinear Optics*. Academic Press, New York, 1991.
- [22] A. Couairon and A. Mysyrowicz. Femtosecond filamentation in transparent media. *Physics Reports*, 441(2):47 – 189, 2007.
- [23] S. L. Chin, S. A. Hosseini, W. Liu, Q. Luo, F. Théberge, N. Aközbek, A. Becker, V.P. Kandidov, O.G. Kosareva, and H. Schroeder. The propagation of powerful femtosecond laser pulses in optical media: physics, applications, and new challenges. *Can. J. Phys.*, 83:863 – 905, 2005.
- [24] V P Kandidov, S A Shlenov, and O G Kosareva. Filamentation of high-power femtosecond laser radiation. *Optics Lett.*, 39:205–228, 2009.
- [25] E. T. J. Nibbering, G. Grillon, M. A. Franco, B. S. Prade, and A. Mysyrowicz. Determination of the inertial contribution to the nonlinear refractive index of air, N₂, and O₂ by use of unfocused high-intensity femtosecond laser pulses. *J. Opt. Soc. Am.*, B14:650–660, 1997.
- [26] E. T. J. Nibbering, P. F. Curley, G. Grillon, B. S. Prade, M. A. Franco, F. Salin, and A. Mysyrowicz. Conical emission from self-guided femtosecond pulses in air. *Opt. Lett.*, 21:62–64, 1996.
- [27] B. La Fontaine, F. Vidal, Z. Jiang, C. Y. Chien, D. Comtois, A. Desparois, T. W. Johnston, J.-C. Kieffer, and H. Pepin. Filamentation of ultrashort pulse laser beams resulting from their propagation over long distances in air. *Physics of Plasmas*, 6:1615–1621, 1999.
- [28] Jean-Claude Diels, editor. *Light Filaments: Structures, challenges and applications*. Electromagnetic Waves. Institution of Engineering and Technology, 2021.
- [29] J.H. Marburger. Self-focusing: Theory. *Progress in Quantum Electronics*, 4:35–110, 1975.
- [30] J. H. Marburger. Self-focusing. In J. H. Sanders and S. Stenholm, editors, *Progr. Quantum Electron.*, volume 4, pages 35–110. Pergamon, Oxford, 1977.
- [31] Pierre Walch. *Study of the filamentation of high-speed laser pulses for the development of a laser lightning rod*. PhD thesis, Institut polytechnique de Paris, 2022.
- [32] H. R. Lange, G. Grillon, J.-F. Ripoche, M. A. Franco, B. Lamouroux, B. S. Prade, A. Mysyrowicz, E. T. J. Nibbering, and A. Chiron. Anomalous long-range propagation of femtosecond laser pulses through air: moving focus or pulse self-guiding? *Optics Letters*, 23:120–122, 1998.

References

- [33] Y. R. Shen. *The Principles of Nonlinear Optics*. John Wiley & Sons, New York, 1984.
- [34] A. Brodeur, C. Y. Chien, F. A. Ilkov, S. L. Chin, O. G. Kosareva, and V. P. Kandidov. Moving focus in the propagation of ultrashort laser pulses in air. *Optics Lett.*, 22:304–306, 1997.
- [35] Y. R. Shen and M. M. Loy. Theoretical interpretation of small-scale filaments of light originating from moving focal spots. *Physical Review A*, 3:2099–2105, 1971.
- [36] L. V. Keldysh. Ionization in the field of a strong electromagnetic wave. *Soviet Physics JET*, 20(5):1307–1314, 1965.
- [37] V. S. Popov. Tunnel and multiphoton ionization of atoms and ions in a strong laser field (kelysh theory). *Phys.-Usp*, 47:855, 2004.
- [38] L. Arissian, C. Smeenk, F. Turner, C. Trallero, A. V. Sokolov, D. Villeneuve A. Staudte, and P B Corkum. Direct test of laser tunneling with electron momentum imaging. *Physical Review Letters*, 105:133002, 2010.
- [39] M. Y. Ivanov, M. Spanner, and O. Smirnova. Anatomy of strong field ionization. *J. Mod.Phys*, 52:165–184, 2005.
- [40] V. P. Krainov. Ionization rates and energy and angular distributions at the barrier-suppression ionization of complex atoms and atomic ions. *J. Opt. Soc. Am. B*, 14:425, 1997.
- [41] L. Arissian and J.-C. Diels. Ultrafast electron plasma index; an ionization perspective. *Journal of Lasers, Optics & Photonics*, 1:107–111, 2014.
- [42] P. B. Corkum. Plasma perspective on strong-field multiphoton ionization. *Phys. Rev. Lett.*, 71:1994–1997, 1993.
- [43] Yu P. Raizer. Breakdown and heating of gases under the influence of a laser beam. *Soviet Physics Uspekhi*, 8(5):650–673, 1966.
- [44] Xin Miao Zhao, Jean-Claude Diels, Cai Yi Wang, and Juan Elizondo. Femtosecond ultraviolet laser pulse induced electrical discharges in gases. *IEEE J. Quantum Electr.*, 31:599–612, 1995.
- [45] J. Schwarz, P. K. Rambo, J.-C. Diels, M. Kolesik, E. Wright, and J. V. Moloney. UV filamentation in air. *Optics Comm.*, 180:383–390, 2000.
- [46] M. Durand, A. Houard, K. Lim, A. Durécu, O. Vasseur, and M. Richardson. Study of filamentation threshold in zinc selenide. *Optics Express*, 22:5852–5858, 2014.

References

- [47] A. V. Shutov, N. N. Ustinovskii, I. V. Smetanin, D. V. Mokrousova, S. A. Goncharov, S. V. Ryabchuk, E. S. Sunchugasheva, L. V. Seleznev, A. A. Ionin, and V. D. Zvorykin. Major pathway for multiphoton air ionization at 248 nm laser wavelength. *Journal of Chem. Phys.*, 64:1733–1740, 1975.
- [48] Magali Durand, Aurélien Houard, Bernard Prade, André Mysyrowicz, Anne Durécu, Bernard Moreau, Didier Fleury, Olivier Vasseur, Hartmut Borchert, Karsten Diener, Rudiger Schmitt, Francis Théberge, Marc Chateaneuf, Jean-François Daigle, and Jacques Dubois. Kilometer range filamentation. *Opt. Express*, 21(22):26836–26845, Nov 2013.
- [49] I.V. Smetanin, A.O Levchenko, A. V. Shutov, N.N. Ustinovskii, and V. D. Zvorykin. Role of coherent resonant nonlinear processes in the ultrashort KrF laser pulse propagation and filamentation in air. *Nuclear instruments and methods in physics research B*, 369:87–91, 2016.
- [50] V. D. Zvorykin, A. A. Ionin, A. O. Levchenko, L. V. Seleznev, D. V. Sinitsyn, I. V. Smetanin, N. N. Ustinovskii, and A. V. Shutov. Extended plasma channels created by UV laser in air and their application to control electric discharges. *Plasma physics repots*, 41:112–146, 2015.
- [51] Olivier J. Chalus, A. Sukhinin, A. Aceves, and J.-C. Diels. Propagation of non-diffracting intense ultraviolet beams. *Optics Communication*, 281:3356–3360, 2008.
- [52] J.-F. Daigle, A. Jacon-Becker, S. Hosseiniand T.-J. Wang, Y. Kamali, G. Roy, A. Becker, and S. L. Chin. Intensity clamping measurement of laser filaments in air at 400 and 800 nm. *Physical Review A*, 82:023405, 2010.
- [53] Ali Rastegari, Alejandro Aceves, and Jean-Claude Diels. UV filaments. *Light Filaments: Structures, Challenges and Applications*, page 31, 2021.
- [54] Olivier CHALUS, Alexey SUKHININ, Alain BOURDIER, Daniel MIRELL, Alejandro ACEVES, and Jean-Claude DIELS. Simulation of the propagation of a uv filament in the air. In *Conference on Lasers and Electro-Optics/Quantum Electronics and Laser Science Conference and Photonic Applications Systems Technologies*, page JWA70. Optica Publishing Group, 2007.
- [55] Olivier Chalus. *Study of Nonlinear Effects of Intense UV Beams in the Atmosphere*. PhD thesis, University of New Mexico and University Louis Pasteur, Strasbourg, 2007.
- [56] L. M. Branscomb, D. S. Burch, S. J. Smith, and S. Geltman. Photodetachment cross section and the electron aknity of atomic oxygen. *Phys. Rev.*, 111:504–513, 1958.

References

- [57] A. W. Ali. The electron avalanche ionization of air and a simple air chemistry model. Nrl memorandum report 4794, Naval Research Laboratory, April 1982.
- [58] J. Schwarz and J.-C. Diels. Analytical solution for UV filaments. *Phys. Rev. A*, 65:013806–1—013806–10, 2001.

Chapter 2

UV laser filaments

2.1 Introduction

Laser filamentation is a phenomenon that has caught a lot of attention during the past decades and has many applications including remote sensing [1–4], laser guided electrical discharges [5–10], and air lasing [11–15]. Filamentation was defined by Akhmanov [16] as a self-guiding phenomenon that can occur in transparent media with an intensity dependent index of refraction. If the non-linearity of the medium is positive at moderate intensities (self-focusing), and saturates or turns over (self-defocusing) at higher intensity, a stable waveguide can be formed, which can exist for distances exceeding the Rayleigh range. Such stable waveguides were observed in liquids at very low optical powers, exploiting the nonlinearity of micro-emulsions [17]. One requirement for observing non-linear collapse and filamentation is that the beam power exceeds the critical power for self-focusing [18, 19]. Since the power required in air is in excess of 12 GW at 800 nm, atmospheric filamentation was first demonstrated with femtosecond pulses of several mJ energy from amplified Ti:sapphire lasers [20]. Since the critical power for self-focusing is much lower in the UV (13 MW at 250 nm [21], filamentation in air was also observed

Chapter 2. UV laser filaments

with sub-mJ pulses of 1 ps at 248 nm [22]. Another requirement for filamentation is that the pulse duration be shorter than the time required to heat the photo-excited electrons by inverse Bremsstrahlung to the ionization potential. This time being in the ns range at 250 nm and in the ps range at 800 nm makes it possible to carry much higher energies in UV filaments than in IR filaments [10, 23]. For the same amount of loss, the larger reservoir of energy in the shorter wavelength pulse will take longer distances to be depleted by losses. The length of a single-Near Infra-Red (NIR) filament is mainly limited by nonlinear losses (for instance generation of conical emission). In the case of the less intense UV filaments, a loss of $60 \mu\text{J}/\text{m}$ was measured [4, 23], which is a very small fraction of the tens of mJ energy of the 170 ps UV pulse that are investigated here.

The UV laser source is briefly introduced in Section 2.2. Different beam preparation techniques leading to different filamentation are presented in Section 2.3. Measurement of beam profiles presented in Section 2.4 involve either high-power linear attenuators, shadowgraphy, or impact measurements.

2.2 Laser source

Most ultrashort/intense laser pulse sources start from an oscillator generating fs pulses that are subsequently stretched to ps for amplification. In an effort to create a more robust laser source, we start with a Q-switched ns oscillator-amplifier Nd:YAG system, a workhorse of the laser industry. A Q-switched injected-seeded Nd:YAG oscillator generates single longitudinal mode, 10 ns pulses with a repetition rate of 1.25 Hz [24]. After amplification through a 6-stage single-pass Nd:YAG amplifier, the energy of the 1064 nm pulses increases up to about 3.5 J. These pulses are frequency doubled to 532 nm through a LBO crystal (*Laser Cristal*, France) [25]. The 532 nm pulses with energy of up to 2.4 J are compressed by stimulated Brillouin backscattering in two water cells arranged in an oscillator-amplifier configuration [26, 27]. The phonon lifetime limit of water at 532 nm

is about $\tau_{ph} = 295$ ps. With a 10 ns input pulse of 2.4 J energy, a minimum compressed pulse duration of 180 ps ($0.6\tau_{ph}$) and output energy of 1.2 J (at 532 nm) is achieved in a SBS amplifier cell. Details can be found in [27]. The compressed green pulses are thereafter frequency doubled in a KDP crystal, with an efficiency limited to only 10 to 20% by two-photon absorption. The resulting pulses at 266 nm are 200 ps in duration and have 300 mJ energy per pulse [4, 28].

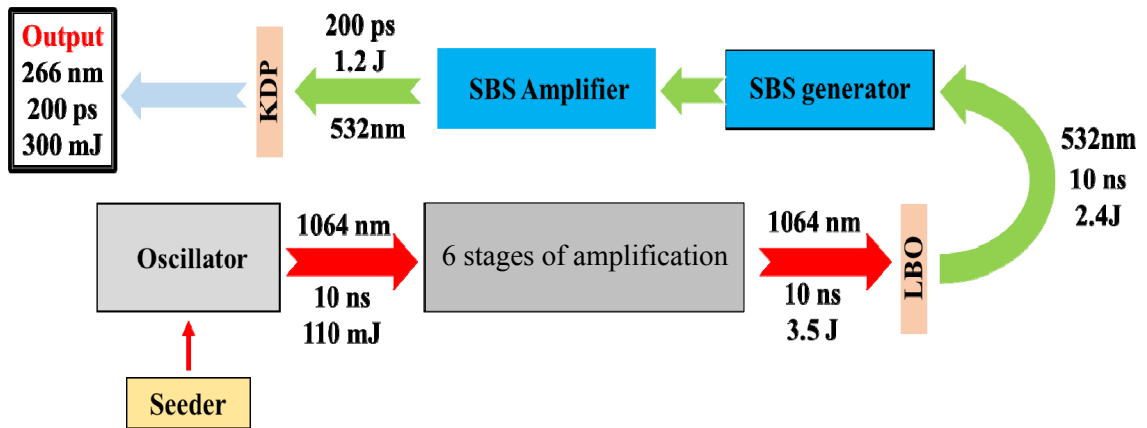


Figure 2.1: Schematic diagram of the UV laser.

2.3 Beam preparation

2.3.1 Introduction

For the purpose of filamentation the source presented in the previous section presents two major challenges. First, the unstable cavity of the oscillator creates a super-Gaussian beam profile. Second, the spatio-temporal energy profile of the beam issued from the oscillator and amplifier is curved. The latter results in an undesirable energy spread along the propagation direction in a focused beam.

Chapter 2. UV laser filaments

The supergaussian profile is ideal for obtaining high energy from the oscillator and amplifiers, as well as for harmonic generation. It is well known however that such a beam results in the formation of multiple filaments distributed along a circle [29]. This filament configuration remains the same for all focusing geometry, because the nonlinear lensing dominates before the far field pattern from diffraction is achieved.

A typical profile of the 266 nm beam is shown in Fig. 2.2(a). Figure 2.2(b) shows the circle of filaments created by this flat-top profile. If focused in vacuum, in the absence of nonlinearity, the beam profile will be the Fraunhofer diffraction of the supergaussian shown in Fig. 2.2(c). This far field diffraction having a parabolic profile on axis is favorable for the formation of a single filament, as shown in Fig. 2.2(d). The challenge here is not to focus the beam in vacuum, but to launch the focused spot in air through a window that can withstand the high intensity of the beam. It is shown in the next subsection that an “air window” can be created in the expansion chamber of a supersonic nozzle. Another property of this window is that it does not introduce beam pointing instabilities and turbulence that would perturb the nonlinear focusing, defocusing and guiding.

The purpose of using a focused beam in vacuum as initial condition is twofold. First it serves at eliminating the high spatial frequencies prior to entering the nonlinear medium. Second, it serves to establish the existence of filaments as self-guided non-diffracting entities, as opposed to a moving focus. The latter phenomenon relates to damage tracks produced in transparent solids by intense nanosecond pulses [30]. As the pulse power increases beyond the critical power along the leading edge of the pulse, the self focus recedes from infinity to a shortest distance reached at the peak of the pulse. There is no possibility of moving focus if the initial condition at the edge of the nonlinear medium is a waist of the size of the observed filament.

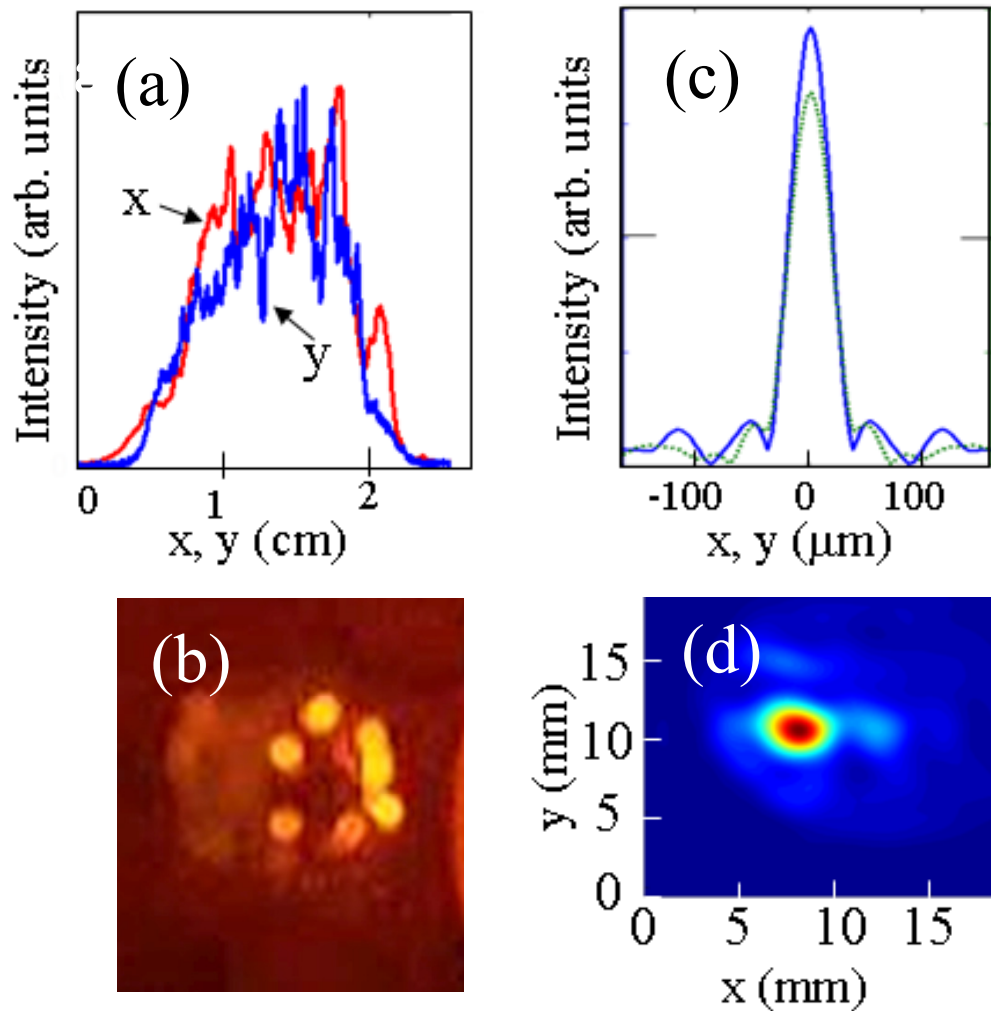


Figure 2.2: (a) Profile of the super-Gaussian 266 nm beam. (b) Filament pattern produced by the profile (a) in air (Aerodynamic window is not operational). (c) Far field profile as produced in vacuum with the operational aerodynamic window (hence in the absence of nonlinear effect) at the focus of a lens. (d) Single filament profile taken at 2 m from the exit of the aerodynamic window.

2.3.2 The aerodynamic window

Aerodynamic windows were first developed in the 70's as windows for very high power CO₂ lasers [31]. In an aerodynamic window a supersonic flow of air is forced through a narrow nozzle. As the air flows through a curved expansion chamber, it creates a pressure

Chapter 2. UV laser filaments

gradient from vacuum to atmospheric pressure which results in the effective separation of the low vacuum chamber (pressure of about 10 torr) from atmosphere [31, 32]. The profile of the air channel cut in an aluminum block is shown in Fig. 2.3(a). The red arrow indicates the direction of propagation of light, entering from the right (vacuum side) through a hole or slit, and exiting at atmospheric pressure to the left. A setup for the investigation of the optical quality of the window is shown in Fig. 2.3(b). The pressure distribution in the expansion chamber of the aerodynamic window is shown by the color coded profile. The supersonic flow is generated by an air compressor providing a flow of up to $10 \text{ m}^3/\text{min}$ at a pressure of $8 \text{ kg}/\text{cm}^2$. The aerodynamic window provides a high damage threshold barrier between the atmosphere and the vacuum chamber, enabling linear propagation of the intense pulse up to the boundary of the nonlinear medium (air in this case).

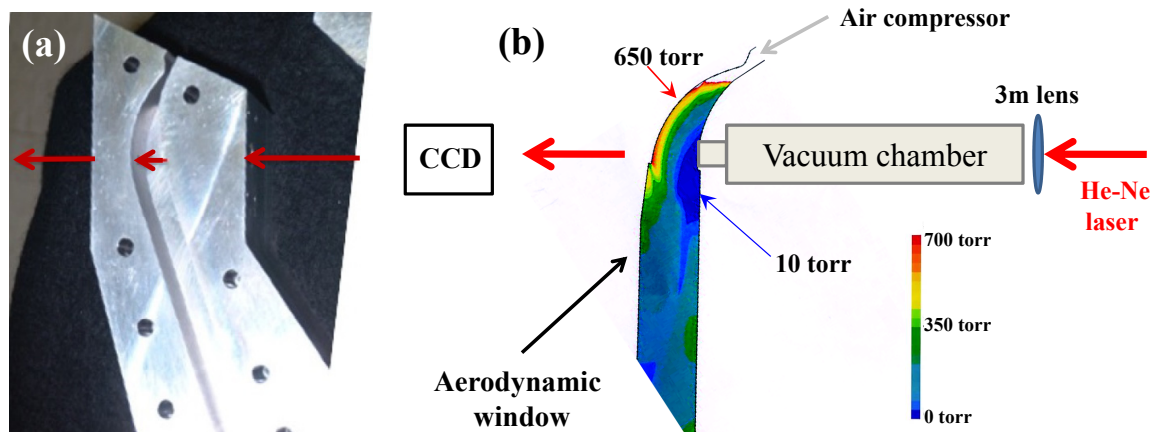


Figure 2.3: (a) Profile of the aerodynamic window nozzle and expansion chamber, cut in an aluminum bloc. The cut is 20 mm deep. The arrow indicate the direction of propagation of the light from vacuum to atmosphere. The light passes through a 3 mm diameter hole, or in another realization a 3 mm \times 20 mm slot. (b) Setup for investigation of the stability of the beam profile of a He-Ne laser going through the aerodynamic window.

Beam pointing stability

The fact that a supersonic air flow is used to generate the pressure gradient in an aerodynamic window may rise suspicion about the stability of a laser beam going through such a window. In order to address this issue an expanded He-Ne laser focused with a 3 m lens is used to investigate the beam pointing stability through the aerodynamic window [Fig 2.3(b)]. Successive images of the beam profile of the He-Ne laser are captured at 2.4 m from the exit point of the aerodynamic window by a high resolution camera and saved for further processing. We compare the centroid or the center of gravity (\bar{x}) and the beam size (w) Mean Square deviation (MSQ) [33, 34] of the He-Ne laser in two cases of operational and non-operational aerodynamic window. All other conditions are kept the same. For the center of gravity along x :

$$\bar{x} = \frac{\sum_{i,j=0}^N x_i I(x_i, y_j)}{\sum_{i,j=0}^N I(x_i, y_j)}$$

while the beam waist along the x direction is defined as:

$$w_x = \sqrt{\frac{\sum_{i,j=0}^N (x_i - \bar{x})^2 I(x_i, y_j)}{\sum_{i,j=0}^N I(x_i, y_j)}}$$

These quantities are calculated and plotted in Fig 2.4 for 48 successive images. Surprisingly, the fluctuations are reduced when the aerodynamic window is operating, indicating that the beam is more disturbed by the turbulence in the stagnant air of the 3 m tube, than by the window. The calculated standard deviation of the data sets for the measurement of the centroid of the beam in the cases of operational versus non-operational aerodynamic window are 1.84 and 7.52 pixels respectively (one pixel is $15\mu\text{m}$). In addition the calculated standard deviation of the data sets for the measurement of the beam waist in the cases of operational versus non-operational aerodynamic window are 0.015 and 0.024 mm respectively. Since all other conditions are the same, we can conclude that the stability of the laser beam going through the vacuum tube terminated by the operational aerodynamic

Chapter 2. UV laser filaments

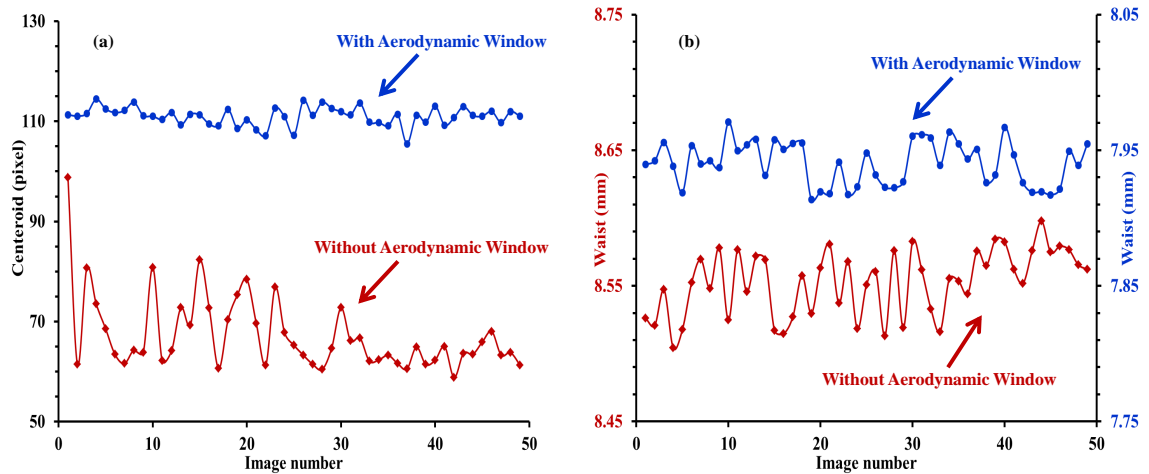


Figure 2.4: Comparison between the centroid (left) and the beam waist (right) of the beam profile of a He-Ne laser (for 49 successive images), with and without an aerodynamic window. The expanded He-Ne laser beam is focused with a 3 m lens.

window is improved and the beam profile has fewer fluctuations both in the location of its centroid and its beam waist [4, 10].

2.4 UV Filament Spatial Profile Measurements

It has been established that properties of filaments such as length and plasma density are dependent on the focusing conditions used for the initiation of the filament [35, 36]. Thus, various lenses with focal lengths from 0.5 m up to 9 m have been used for filament experimental generation and detection. Results of the investigation of spatial profiles of the filaments generated by the 3 m and 9 m lenses are presented in Section 2.4.1 and 2.4.2.

Measuring the beam profile of a 300 mJ pulse of less than 200 ps in a sub-millimeter cross section is a challenge. The solution found to attenuate *linearly* the beam is to use a 15 cm diameter grazing incidence coated fused silica plate [32]. Because one linear dimension of the filament is stretched over 15 cm, the intensity can be kept below the damage threshold of the coating. A 355 nm coating at normal incidence is a standard

Chapter 2. UV laser filaments

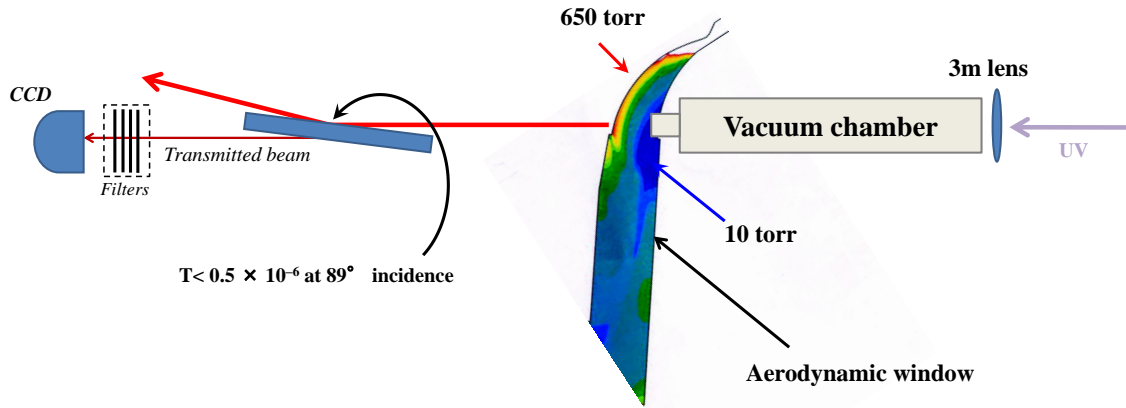


Figure 2.5: Experimental setup which is used for observing the spatial profile of the UV filaments. The beam is linearly attenuated by a grazing incidence plate (fused silica, 15 mm thickness, 150 mm diameter coated for maximum reflectivity at 355 nm (normal incidence). The beam is thereafter further attenuated by neutral density filters before being recorded by a CCD.

coating for an excimer laser. The reflectivity of such a coating for s-polarization at 8 different wavelengths close to 266 nm was measured to be $0.5 \cdot 10^{-6}$ (Fig. 2.5).

2.4.1 3 m Lens

The spatial profiles of the UV filaments generated with a 3 m lens is compared for two different schemes of focusing in air and in vacuum (operational aerodynamic window). The distance between the 3m lens and the entrance window of the vacuum chamber is chosen in a way that the geometrical focus is located a few millimeters before the beam crosses the expanding flow of the aerodynamic window. As mentioned before, by using the aerodynamic window it is possible to focus the UV pulse in vacuum before the onset of the UV filament, resulting in a different initial preparation phase for the filament [4, 10].

In Fig 2.6(a) and Fig. 2.6(b), the beam profile of the UV filament for the case of focusing in vacuum using a 3 m lens (operational aerodynamic window) is represented.

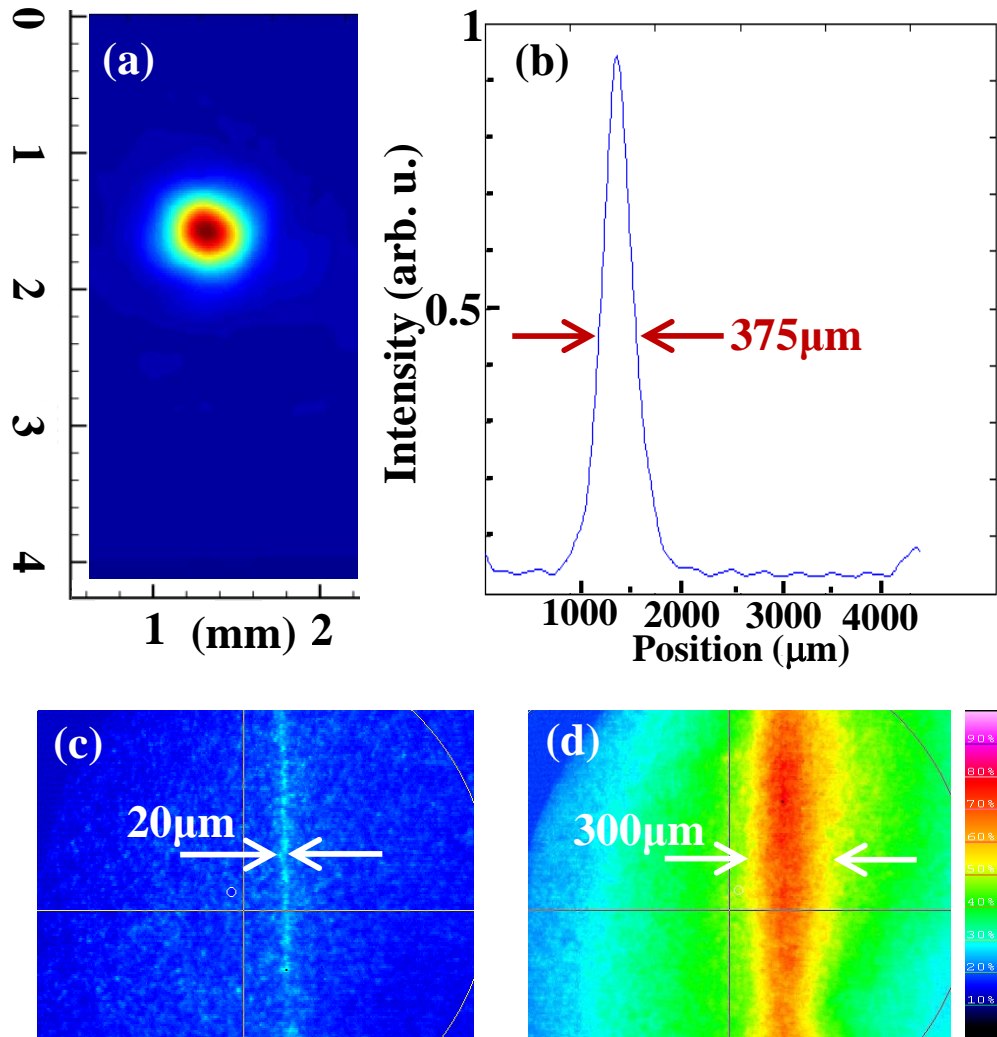


Figure 2.6: (a) and (b) UV filament beam profile for the case of focusing with a 3 m lens in vacuum (operational aerodynamic window) [37]. The UV filament has a FWHM of about $375 \mu\text{m}$. This is measured using the setup described in Fig. 2.5. The CCD is 2 m away from the exit point of the aerodynamic window. (c) Calibration image of the focused UV laser beam at very low power, exiting the aerodynamic window, taken with an image intensifier and a CCD. The $13 \mu\text{m}$ waist is a few cm before the exit plane of the window. (d) Image of the filament taken with the image intensifier and a CCD, showing a FWHM of about $300 \mu\text{m}$.

The UV filament has a FWHM of about $375 \mu\text{m}$ which is measured at the distance of 2 m from the exit of the aerodynamic window. A transverse image of a weak beam (sufficiently attenuated not to induce any nonlinear effect) is shown in Fig. 2.6(c). The $20 \mu\text{m}$ indicated

Chapter 2. UV laser filaments

on the figure corresponds to the beam size at the exit plane of the window, a few cm after the waist of $w = 13$ mm, hence the initial condition for the filamenting beam exiting the aerodynamic window at the end of the 3 m vacuum tube. The transverse image of the UV filament which is taken using an image intensifier for the same experimental conditions is shown in figure 2.6(d). It can be seen that the FWHM of the filament in this image is $300\mu\text{m}$, which is in good agreement with beam profile measurements. Figure 2.6 is another demonstration that the moving focus model [38] does not apply, even for these sub-nanosecond pulses. It is a rare example of a filament starting from a $13\mu\text{m}$ waist to evolve into the quasi-steady state filament shown in Fig. 2.6(d).

Filaments obtained by focusing in vacuum have smaller diameters compared to the ones obtained by direct focusing in air [37, 39]. In the case of focusing in air diameters in the range of $300\text{-}400\mu\text{m}$ have been measured for different distances up to 4 m with respect to the exit of the aerodynamic window. These distances are more than 2 orders of magnitude larger than the Rayleigh range. Similar measurements for the case of focusing in air resulted in a diameter of the order of 1 mm [37]. The probability of forming a filament is also reduced in the case of focusing in air, as compared to the case of focusing in vacuum. This is explained by the fact that the nonlinear losses during the initial self-focusing phase are prevented, and, as shown in Section 2.3.2, wavefront distortion by air turbulence is avoided in the 3 m vacuum tube. The measured beam profiles are in good agreement with the previous theoretical calculations [21].

2.4.2 9 m Lens

The beam profiles are recorded without the use of the aerodynamic window, outside of the laboratory. The laser beam is sent through a periscope to a 9 m focusing lens at 30 m of the source. The multiple reflections account for an attenuation of about 30% in the energy of the beam. Figure 2.7 shows pictures of successive beam profiles as a function of the

Chapter 2. UV laser filaments

distance from the 9 m lens. The initially super-Gaussian profile has diffracted, propagating through turbulent air, until reaching the 9 m focal lens (beam diameter 20 cm). Multiple filaments are generated, as been reported in similar focusing conditions ($f = 10$ m) with near infrared filaments [40]. The distance over which the filaments are observed is about 2 m, which is much longer than the Rayleigh range (approximately 1 mm) for this focusing scheme.

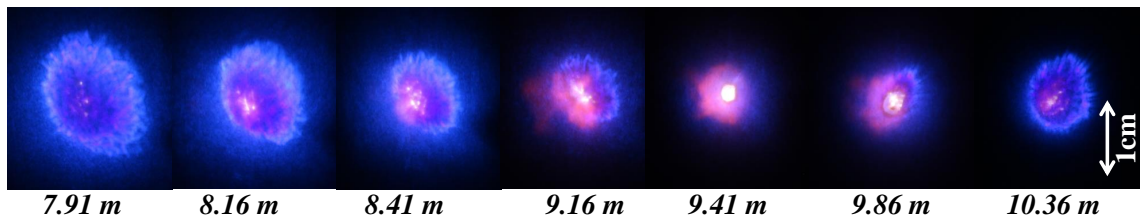


Figure 2.7: The beam profiles of UV filaments at different distances from the 9 m focusing lens. These beam profiles are captured by a digital camera recording the impact of the UV filament on a piece of paper. Different colors correspond to the fluorescent emission from the paper which is changing based on the impacted beam intensity. The white dots in the figure are related to multiple filaments.

2.5 Hydrodynamic waveguiding with filaments

Sudden heating of a gas with a high intensity UV filament will create a low-density plasma channel. The impulsive heating of gas creates shock-waves of cylindrical symmetry which propagate outward from the center line, leaving the low-density channel behind [41]. Initially, the shock-waves propagate with velocities much larger than the speed of sound, i.e. supersonic, but their velocity rapidly decreases to the speed of sound as they propagate. The diameter of the low-density tube is determined by the deposited energy and the gas pressure [42, 43].

2.5.1 Transient imaging of UV filaments via shadowgraphy

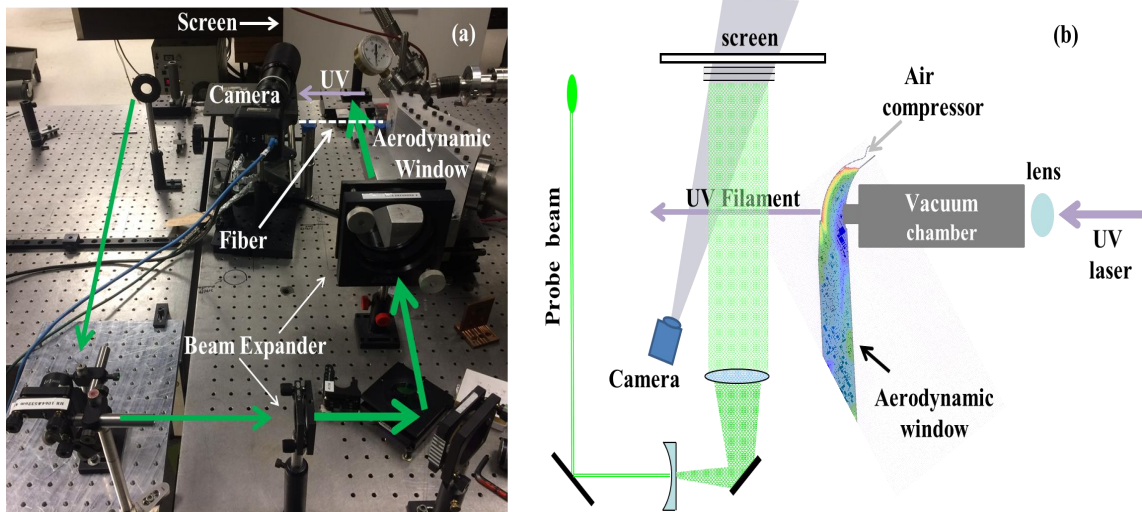


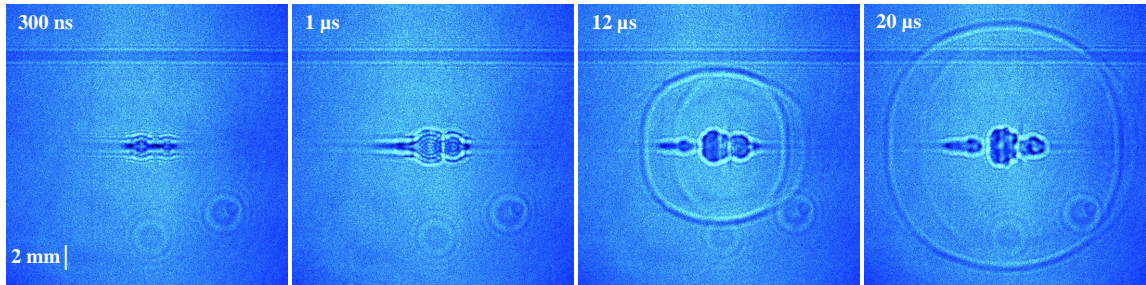
Figure 2.8: (a) Picture of the shadowgraphy setup. (b) Schematic diagram of the shadowgraphy setup.

Shadowgraphy is an optical technique that can be used for the investigation of small amplitude changes in refractive index in transparent materials, which in the case of UV filaments is a consequence of the change in air density [44, 45]. Shadowgraphy technique is used to investigate the characteristics of the mentioned low-density tube and shock-waves created by the UV filaments. The probe beam is a collimated and expanded (about 6 cm) green (532 nm) laser pulse with 10 ns temporal width. This probe beam is sent perpendicular to the UV filament and is imaging the area of interest on a screen located at a 1 m distance from the filament (Fig. 2.8).

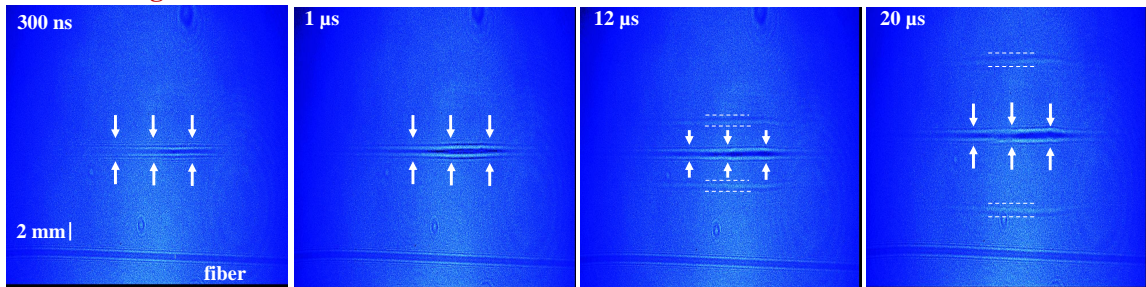
A CCD camera is used to capture the shadowgrams on the screen. An optical fiber is placed just below the UV filament, providing a reference for the size of shadowgrams. A master clock is used to synchronize the UV laser, the green laser, and the camera. A delay generator controls the relative delay times between the probe beam and the UV laser, making it possible to investigate the temporal evolution of the shock-waves and the low-density channel. The shadowgrams of UV filaments in different focusing schemes

Chapter 2. UV laser filaments

50 cm focusing



1 m focusing



3 m focusing

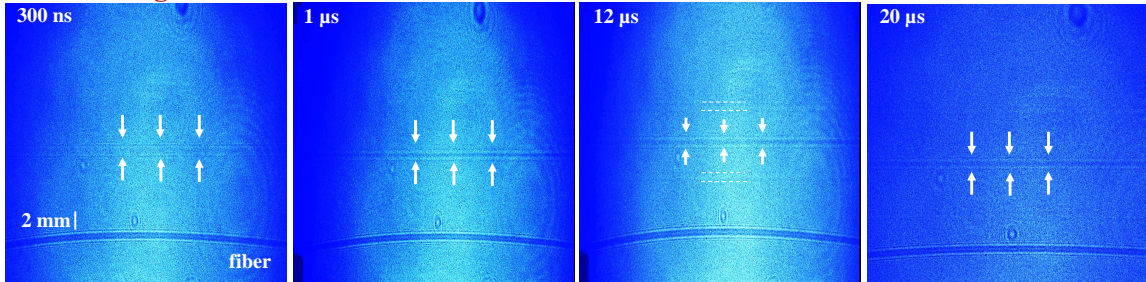


Figure 2.9: Shadowgrams of UV filament vs time. (Top) Focused with a 1m lens. (Bottom) Focused with a 3m lens. The low density tube and shock-waves are demonstrated by white arrows and dashed lines respectively.

were investigated. The results of focusing with 1 m and 3 m lenses are presented here. In Fig. 2.9, selected shadowgrams of UV filaments are displayed for different time delays between the UV laser and the probe beam for both focusing schemes.

From the shadowgrams we can conclude that, as expected, the filament length is longer when focusing with a 3 m lens. In this case the low density tube is present all over the probe beam. This fact is also evident in Fig. 2.10, which is a direct image of the plasma

Chapter 2. UV laser filaments

channel of the filament taken with a digital camera [46].

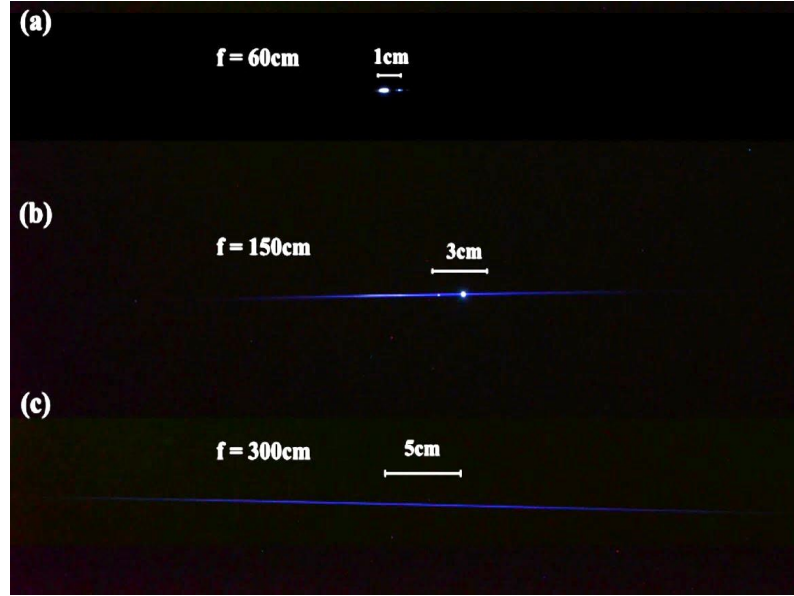


Figure 2.10: Image of the plasma channels taken with a digital camera from the side for the filaments generated with three focusing lenses of (a) 0.6 m, (b) 1 m, and (c) 3 m [39]. The initial beam diameter is the same for all three pictures. The Rayleigh range is approximately 1 mm for (c), hence much smaller than the plasma length.

The shock-waves created from tighter focusing are more intense. This is also expected since in tighter focusing higher plasma electron densities are created. The higher intensity deposited by the filament [47, 48] affects the width of the low-density tube. The widths of the low-density channels in both cases are measured using the image of the fiber as a reference. These widths are $485 \mu\text{m}$ and $420 \mu\text{m}$ for the 3 m and 1 m lenses, respectively [4, 10]. The width of these channels is in agreement with the UV filament FWHM reported in Section 2.4.

Different focusing geometries lead to different plasma densities. Focusing lenses of 50 cm, 1 m, and 3 m focal distances were used to produce the filaments. Figure 2.9 shows the shadowgrams taken at different delays following the filament excitation, for the three focusing geometries. The low-density tube and shock-waves are indicated by white

arrows and dashed lines, respectively. Two-speed regimes are observed with respect to the propagation of the shock-waves generated by the filament.

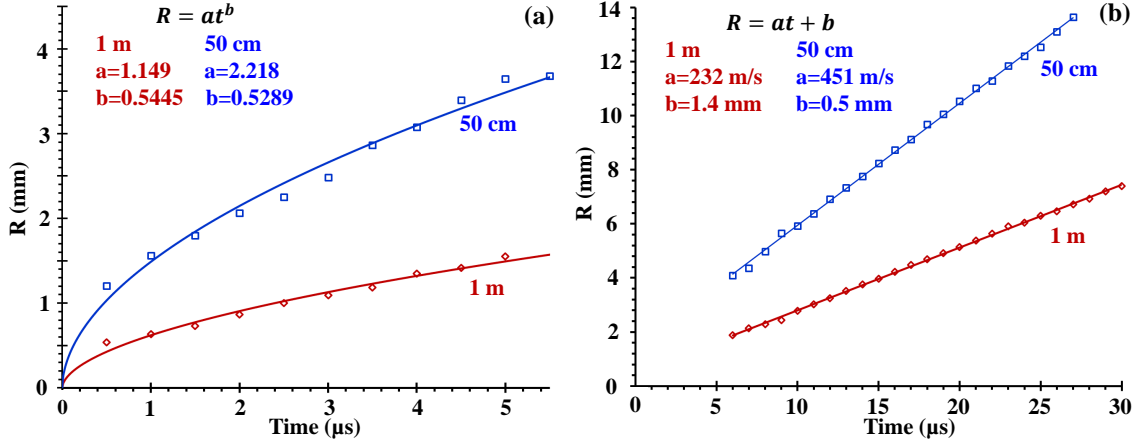


Figure 2.11: Propagation distance R of the shock-wave versus time. a) In the first regime the shock-wave propagation follows the Sedov formula [49] for cylindrical symmetry ($d = 2$). b) In the second regime the shock-wave propagates at constant velocity.

Initially, the shock-waves propagate with supersonic velocities, but their velocity decreases to reach a constant speed after $6 \mu\text{s}$. The shock-wave is not a monochromatic wave, but a wave packet, akin to an ultrashort optical pulse. Its linear propagation velocity is therefore a *group velocity* which is dependent on the acoustic spectral content of the shock-wave. It is expected that the 50 cm focusing (as compared to 1 m) creates a shock-wave more localized in space-time, with higher frequency components. Consistent with the acoustic dispersion data of [50], the higher frequencies in air should correspond to smaller delays, i.e. higher velocities, as is observed in Fig. 2.11(b). The fitted group velocities are 451 m/s and 232 m/s for the 50 cm focusing and 1 m focusing, respectively [51].

The first regime of the expansion of the plasma lasts up to about $6 \mu\text{s}$. In this regime, from the initiation point the shock-wave moves with time t a distance R given by the Sedov formula [49]: $R = \left[\left(\frac{E}{\rho} \right)^{\frac{1}{2+d}} \right] t^{\frac{2}{2+d}}$. In this formula, E is the total energy transferred to the plasma, ρ is the air density, and $d = 1, 2, 3$ for planar, cylindrical, and spherical propagation respectively. Our data presented in Fig. 2.11(a) fit remarkably well to the

Sedov formula for cylindrical symmetry ($d = 2$), even in the case of short focusing ($f = 50$ cm). The fitting curves in Fig. 2.11(a) correspond to $d = 1.67$ for 50 cm focusing, and $d = 1.78$ for the case of 1 m focusing. In the 3 m focusing regime, the shock-waves being very weak, it was not possible to analyze their propagation with good accuracy.

2.5.2 Hydrodynamic waveguiding

Another observation from the shadowgraphy data is that the generated waveguide is formed within 300 ns and remains stable and uniform up to 200 μ s [4, 10]. As a result, a series of ionizing laser pulses will lead to the production of heat bursts, and each heat burst will create a shock-wave that does not decay before the arrival of the next pulse. The generation of this waveguide based on the shock-wave being long-lived, can possibly result in a stationary waveguide at sufficiently high repetition rates. The stationary waveguides mentioned in this section can be used for optical guiding of another filamenting laser pulse [52–55]. This can have possible applications for remote sensing [1–3], directed energy applications [56, 57], and triggering and guiding of electrical discharges [?, 5, 6, 8, 9].

In [52] the authors have investigated waveguides generated by fs IR filaments. Their experiments in the single filament scenario have shown that an initial density hole will grow for tens of nanoseconds as a shock-wave propagates outwards. Later after approximately 1-2 μ s the pressure inside the waveguide reaches equilibrium. This generated leaky waveguide will decay in ms time scales. These and also measurements reported in [41] are in agreement with our shadowgraphy study using UV filaments reported in this section. Positive index profiles — hence dielectric waveguides — were achieved with multiple IR filaments forming a symmetric four-lobed pattern which created a long-lived, of the order of ms, waveguide in air. It was also reported that the length of these waveguides depended only on the propagation distance of the inducing fs array of filaments [52]. A probe laser beam used to investigate the guiding property of the positive pressure waveguide indicated

a peak guiding efficiency of 70% at $\simeq 600 \mu\text{s}$ which decreased to 15% at $\simeq 2 \text{ ms}$. In their latest publication [53] the authors reported successful guiding over lengths of up to 30 cm. In applications to remote sensing, the generated waveguide can not only be used for guiding a second high peak power filament to irradiate a sample, but it has also been shown that these air waveguides can act as a broadband collection optics that enhance the returning signal from the sample which will improve the sensitivity in remote sensing [54].

2.6 High-repetition laser source

As mentioned in section 2.5.2 the generated waveguide is formed within 300 ns and remains stable and uniform up to approximately 200 μs . As a result, at repetition rates above 5 kHz a stationary waveguide can be formed. To achieve a higher repetition rate we decided to upgrade an existing Ti:sapphire laser system. This laser system had a regenerative amplifier operating at 1 kHz, followed by a 10 Hz amplifier boosting the energy to 50 mJ/pulse.

The initial step was to replace the 532 nm pump laser of the regenerative amplifier (*Evolution* from *Coherent*) with a high power and high repetition rate *Lee* laser. *Lee* laser is a Q-switched laser at 532 nm with 10 ns pulse width which is capable of working up to 50 kHz. The current output power of the *Lee* laser is 70 W at 10 kHz (70 % of the advertised power) and 50 W at 50kHz repetition rates. Three *Lee* lasers were recovered from the *Starfire* optical range of the AFRL (Airforce Research Lab) in Albuquerque. Because they had been left in the open, none were operational. All cooling parts were cracked, brittle tubings had to be replaced, electronics replaced, etc. By cannibalizing all three lasers I was able to reconstruct an operational laser. Originally maintenance of this laser was a problem, as cooling parts weakened by past harsh exposure to weather burst periodically flooding the hygroscopic nonlinear LBO crystal, and/or the diode pump. So I gradually made changes to the original designs of the cooling system resulting in the much

Chapter 2. UV laser filaments

more stable operation of the laser.

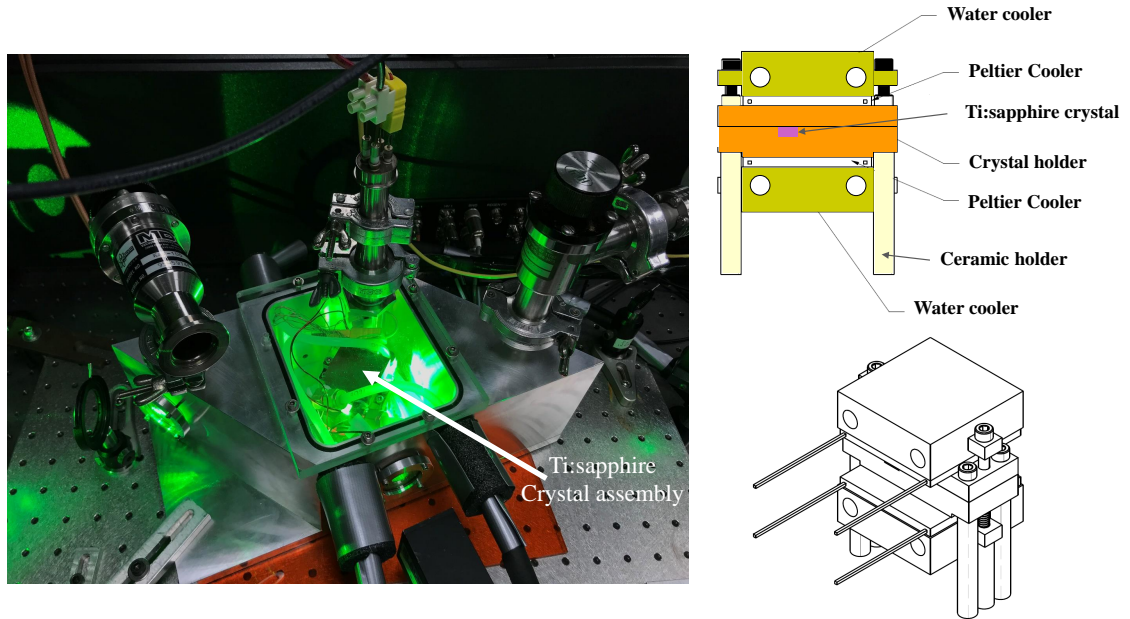


Figure 2.12: Right) Schematic of the new cooling system of the Ti:sapphire crystal. Left) Picture of the new regenerative amplifier Ti:sapphire crystal chamber.

The high average power of the pump laser called for a complete re-design of the regenerative amplifier. The original KDP Pockel's cells needed to be replaced with acquired Beta Barium Borate (BBO) Pockel's cells with appropriate drives that are capable of operating at new high repetition rates. KDP Pockel's cells will not provide good contrast at the higher repetition rate due to piezoelectric resonances.

The new higher average power of the pump laser brings two technical difficulties: 1. Evacuating 70 W of heat from the Ti:sapphire crystal, 2. The higher power of the pump laser will lead to thermal lensing that will affect the cavity and needs to be addressed. The solution to both these problems was to redesign the cooling system of the crystal. The crystal holder went through numerous redesign and modifications. In the latest design, the copper crystal holder is sandwiched between two Peltier coolers as demonstrated in Fig. 2.12(Right). Each thermoelectric cooler is type PC7-16-F1-4040-TART- W6 of Laird

Chapter 2. UV laser filaments

thermal systems. The “hot” side of the Peltier coolers is maintained at a low temperature by two copper heat exchangers in which a mixture of 35 % methanol in water circulates. Each copper heat exchanger is connected to a separate chiller as the heat exchange capacity of one chiller was not sufficient. The reason for using a mixture of Methanol and water for a cooling solution is that the needed temperature of the cooling mixture to achieve the desired temperatures in the crystal is -20°C .

Both to avoid condensation of water vapor on the crystal and also to increase the efficiency of the Peltier coolers the whole cooling system of the crystal needed to be in a vacuum. The focused high-power pump beam’s interaction with small particles of dust will lead to the generation of occasional sparks that can potentially cause damage on the surface of the crystal and keeping the crystal in a vacuum will also prevent this. The latest regenerative amplifier crystal holder chamber is made of aluminum as illustrated in Fig. 2.12(Left). This chamber is designed to provide the needed vacuum. In the latest design in order to achieve the desired temperatures it was necessary to isolate the cooling parts from the aluminum body and to isolate the latter from the optical table. The 532 nm laser is p-polarized, so in order to achieve zero reflection the aluminum chamber is designed in a way that the entrance window is at the Brewster angle with respect to the incident pump laser beam. Also to minimize losses, the Ti:sapphire crystal is cut at Brewster angle. The temperature of the Ti:sapphire crystal is monitored using a K-type thermocouple which is located on the top of the crystal. Various combinations of chiller temperature and Peltier cooler current have been tested in order to investigate the lowest achievable temperature on the Ti:Sapphire crystal. The best lowest temperature was achieved when two Peltier coolers are operated in series with a current of 5.66 A and a voltage of 18.3 V. The chillers temperature is -20°C . With the pump laser operating at 68.5 W (power at 10 kHz repetition rate), a stable equilibrium temperature of -3°C is maintained.

The topological configuration of the regenerative amplifier is represented in Fig. 2.13. Focusing of the 532 nm pump into the Ti:sapphire crystal is made with a concave mirror

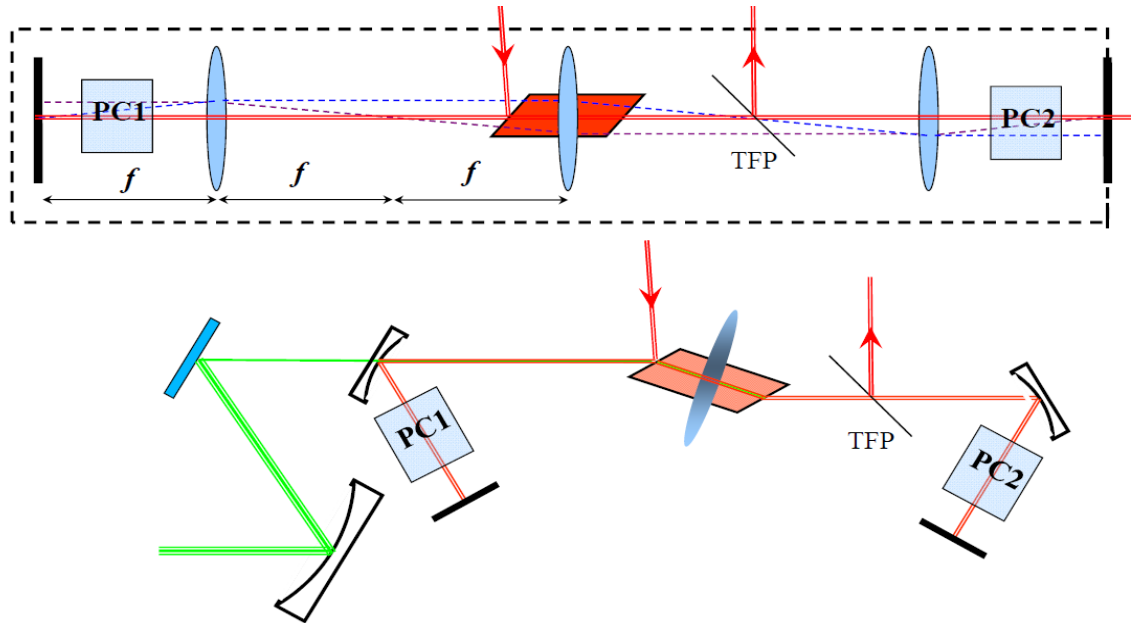


Figure 2.13: Top) Topological configuration of the regenerative amplifier. The s-polarized 800 nm seed pulse is reflected from the surface of the Ti:sapphire gain crystal (as it is cut at brewster angle) towards the end mirror of the cavity. Then going through the Pockels cell it is switched to p-polarization to be trapped in the cavity. After a number of round-trips, the amplified pulse is extracted by rotating its polarization to s by the second Pockels. The s-polarized pulse is reflected by the thin film polarizer (TFP). With all focal lengths being equal, the ABCD matrix of this cavity is -1, implying that the beam size will adjust to the size of the gain volume in the crystal. Bottom) The focusing is performed with mirrors at an angle such that astigmatism introduced by the Brewster rod is compensated.

with a radius of curvature of $R = 1$ m and at an angle of incidence of 6° . This angle was selected for astigmatism compensation by the Brewster angle crystal [58]. The s-polarized 800 nm seed pulse enters the aluminum chamber through the third window. Then it is reflected from the surface of the Ti:sapphire gain crystal (as it is cut at brewster angle) towards the end mirror of the cavity. Then going through the Pockels cell it is switched to p-polarization to be trapped in the cavity. After a number of round-trips, the amplified pulse is extracted by rotating its polarization to s by the second Pockels. The s-polarized pulse is reflected by the thin film polarizer (TFP) leaving the regen cavity. An image of the regen cavity is shown in Fig. 2.14.

Chapter 2. UV laser filaments

Ideally, the mode of the cavity should match the pump spot size. With the nonlinearities due to thermal lensing combined with Kerr focusing, it is not possible to predict the pump spot size in the Ti:sapphire. Therefore, we choose a cavity configuration where the ABCD matrix is minus one:

$$\begin{vmatrix} -1 & 0 \\ 0 & -1 \end{vmatrix}$$

In such a cavity, the size of the waist is totally undetermined (0/0) and adjusts itself to the pump volume. The thermal lensing measurements provided an approximate 30 cm value for the focal point of the thermal lens at -3°C (see section 2.6.1). Hence, two concave mirrors with focal points equal to 30 cm are chosen as end mirrors. When the cavity length is equal to 6 times the focal length of the thermal lens (30 cm) this cavity will have a ABCD matrix equal to -1 (Fig. 2.13(top)).

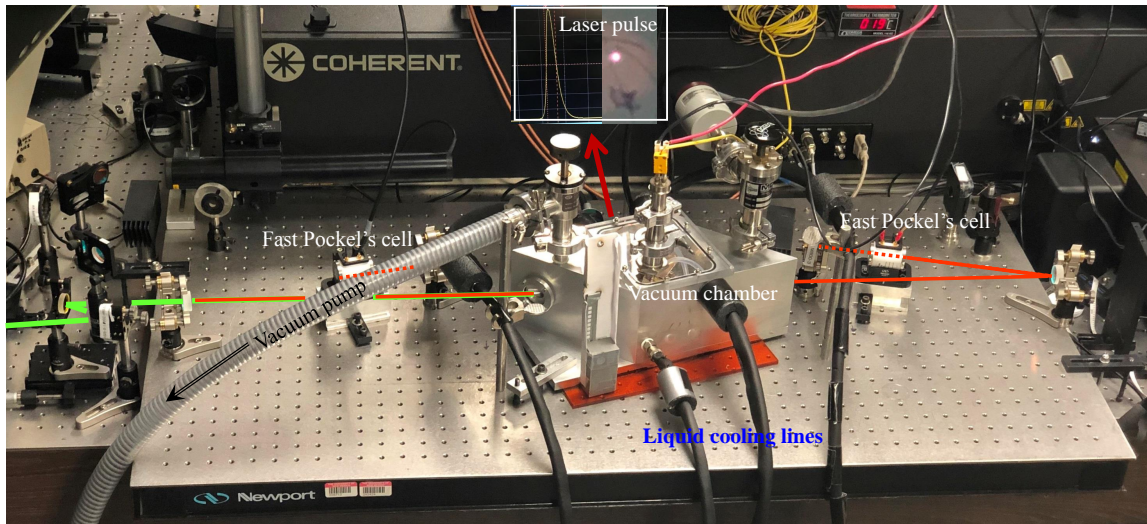


Figure 2.14: Picture of the regenerative amplifier cavity. Green: the path of the pump beam. Red: the path of the 800 nm pulses.

2.6.1 Thermal Lensing Measurements

As mentioned before the 70 W power of the pumping laser will result in the creation of a thermal lens inside the Ti:sapphire crystal [59, 60]. In order to build a working cavity it is important to measure the focal point of this thermal lens. The setup to measure thermal lensing is shown in Fig. 2.15. A He-Ne laser beam is sent through the Ti:sapphire crystal and analyzed with a beam profiler at various distances from the crystal. A highly reflective 532 nm mirror at 45° has been used to filter out the remaining pump beam that passes through the crystal. The effect of the thermal lens can be seen in Fig. 2.16(a) to (d), as the He-Ne probe beam is clearly affected by the presence of the thermal lens whenever the pump laser is present. The Ti:sapphire crystal temperature for these measurements was -3°C .

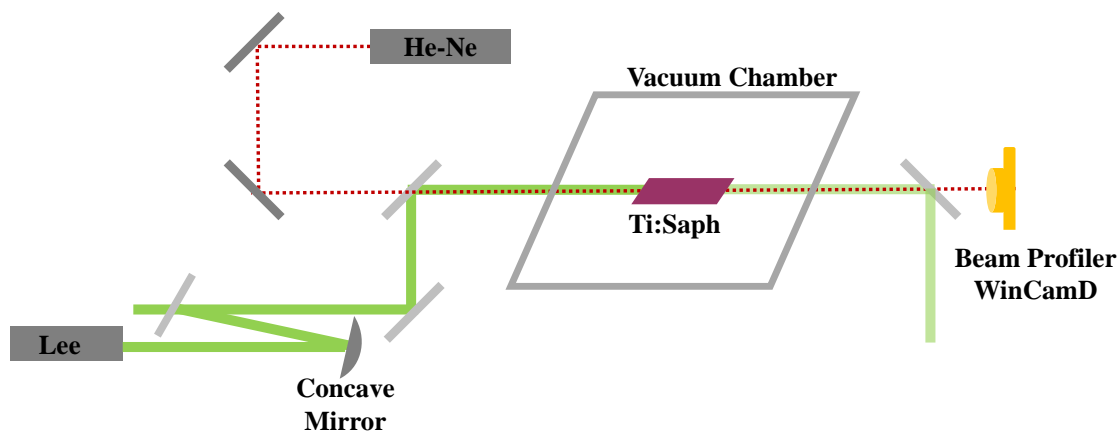


Figure 2.15: Schematic of the thermal lensing measurement setup.

It should be mentioned that when focusing the 532 nm pump beam with a 60 cm lens astigmatism affects its beam evolution. This can be seen in Fig. 2.16(e) illustrating the He-Ne beam profile at 32 cm from the crystal, when the pump is focused on the axis with a 60 cm focal distance lens. To correct that astigmatic illumination affecting the thermal lensing, focusing of the pump into the Ti:sapphire crystal is made with a curved mirror with a radius of curvature of $R = 1\text{ m}$ and at an angle of incidence of 6° . This angle was

selected for astigmatism compensation by the Brewster angle crystal [58]. The resulting beam profile is shown in Fig. 2.16(f). The effective waist of the He-Ne probe beam vs

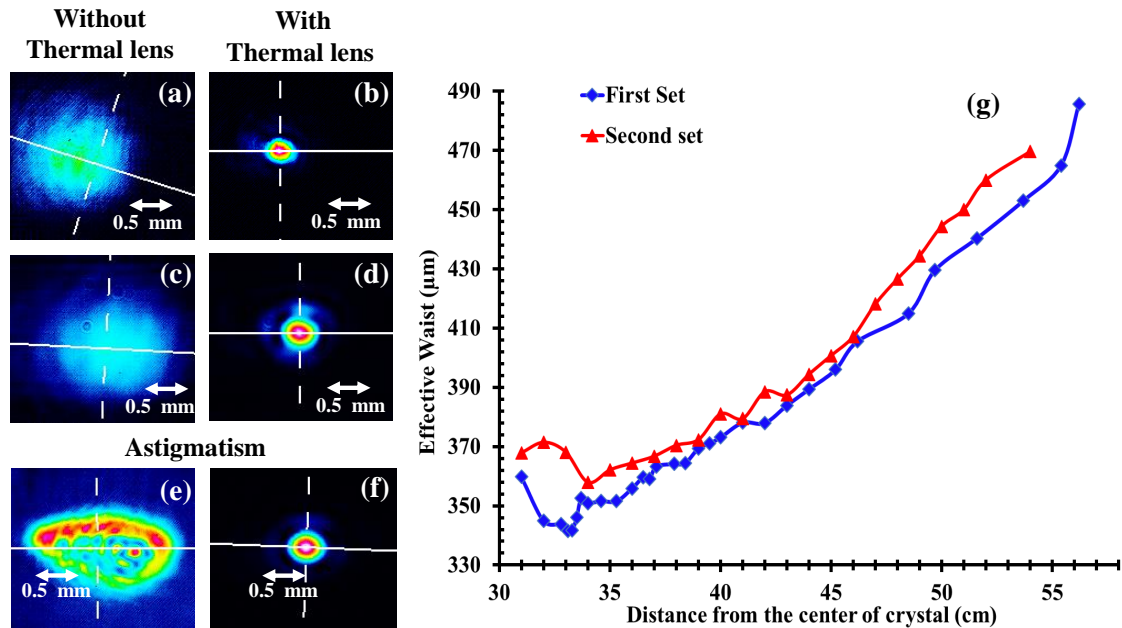


Figure 2.16: Pictures from the beam profiler. (a) He-Ne profile at 32 cm from the Ti:sapphire crystal, with pump off. (b) He-Ne profile at 32 cm from the Ti:sapphire crystal, with 70 W 532 nm pump. (c) and (d): measurements corresponding to (a) and (b), except at 56.5 cm from the crystal. (e) He-Ne beam profile at 32 cm from the crystal, when the pump is focused on the axis with a 60 cm focal distance lens. (f) He-Ne beam profile at 32 cm from crystal, when the pump is focused by a $R = 1$ m mirror at an angle of incidence of 6° . (g) The effective waist provided by the beam profiler program vs distance from the center of the crystal. For both sets of measurements, the crystal temperature has been sustained at -3°C .

distance from the center of the crystal provided is illustrated in Fig. 2.16(g) for two different sets of measurements. For both sets of measurements, the crystal temperature has been sustained at -3°C . Shorter distances of 30 cm can not be measured due to technical restrictions. The effective beam waist is provided by the beam profiler program. Although these measurements are not able to provide the exact results, it can be concluded that the focal distance of the thermal lens is approximately 33 cm. A genetic evolution algorithm was initially applied to the problem of locating the focus, given the lens position, and vari-

ous profiles. The results of these calculations were not also conclusive, please refer to [61] for detailed information on these calculations.

2.7 Velocity map imaging (VMI) setup

2.7.1 Introduction

The trajectory of the electrons under the applied field determines the reaction of the electrons to the applied field [62]. The study of electron currents is a key to the analysis of radiative phenomena associated with filaments, and to modeling the difference of response in linear or circular polarization. For direct experimental verification of the theory, we have constructed a Velocity Map Imaging (VMI) setup adapted to the study of filaments. The main objective is to measure the distribution of energy and momenta of the electrons under the influence of the field of the filament. Hence providing information not only on the charged particles but also on the filamented field. I completed successfully the construction of the VMI. Unfortunately, funding limitations and shifting sponsor priorities prevented us from completing the planned experiments. Details of the construction and operation are included for the benefit of graduate student(s) that might take over this research.

Velocity Map Imaging (VMI) is a powerful experimental technique used in physics and physical chemistry research to investigate gas ionization, fragmentation dynamics, and photoelectron spectroscopy. VMI provides details on the velocity and momentum distribution of electrons and ions generated resulting from the interaction of laser pulses and matter. It offers more complete information compared to many standard ion imaging and spectrometry techniques preceding it. Velocity Map imaging is a technique that was proposed for the first time in 1997 [64]. A schematic diagram of a VMI setup is illustrated in Fig. 2.17 [63]. The original design includes three metallic circular electrodes that are con-

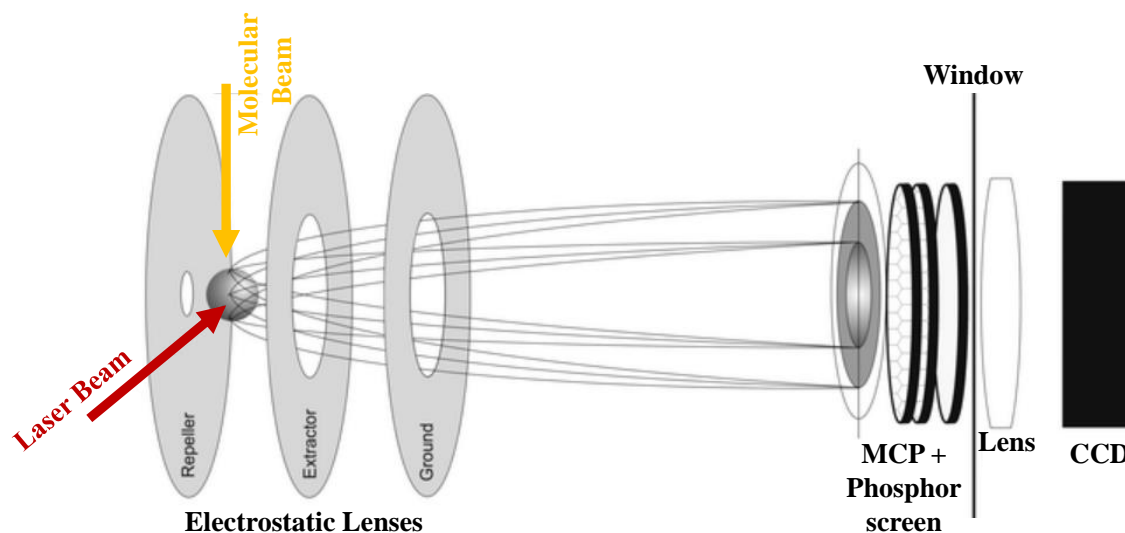


Figure 2.17: Schematic representation of the detection mechanism of a velocity-map imaging setup [63].

nected to high-voltage sources. The laser and molecular beams intercept each other in the center of the space between the first two electrodes shown in Fig. 2.17. These three electrodes act like electrostatic lenses, which similar to optical lenses, image electrons/ions created in the interaction area on the detector. The detector consists of a Micro Channel Plate (MCP) and a phosphor screen attached to it. MCP is an electron multiplier that is used for the detection of charged particles, UV radiation, X-rays, etc. MCPs can have linear gains up to 1000 and one of their advantages is that they preserve the spatial resolution of the original input radiation as they generate the output two-dimensional electron image. Immediately at the back of MCP, there is a phosphor screen that converts electrons that have been multiplied several thousand times in the MCP, into light upon their impact on it. The image created by the phosphor screen is then imaged on a fast CCD camera. By tuning the voltage on the repeller and extractor the electrostatic lens system which focuses the charged particles onto the MCP detector. The electrons/ions are mapped onto the detector based on their kinetic energy (proportional to the magnitude of velocity) and initial velocity distribution. The VMI setup is basically capable of measuring both

Chapter 2. UV laser filaments

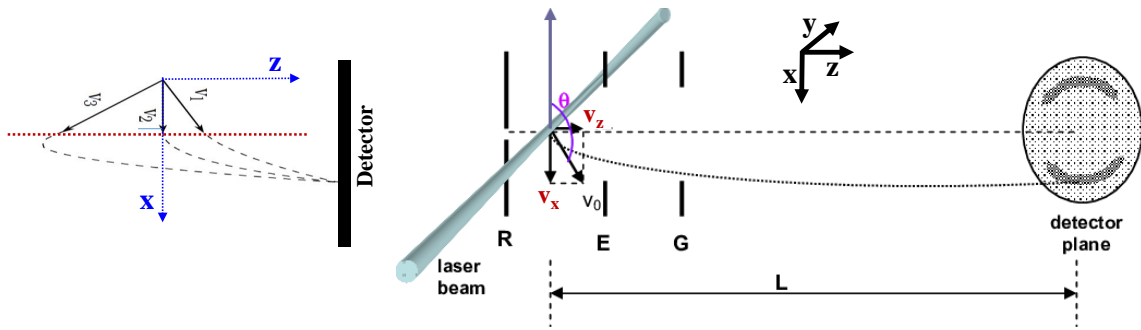


Figure 2.18: Overview of the velocity map imaging technique. Electrons/ions emitted created by the interaction of laser pulses with matter are projected by the electric field of the electrostatic lenses onto the detector. As the result, a 2D projection of the velocity and momentum distribution is created on the detector [65].

the direction and magnitude of the velocity of all the particles created during the interaction. The position at which the electrons/ions hits the detector is directly proportional to the electron's/ion's initial velocity in the YX plane as seen in Fig. 2.18. In Fig. 2.18(left) three velocity vectors having different magnitudes but the same V_x components are shown. The electric field created by the electrostatic lenses integrates over the V_y component and focuses every charged particle with a similar V_x component onto an identical location in the detector plane. Another way of looking at this is that the difference in the velocity magnitude along the Z direction will affect the time at which the electrons/ions reach the detector but not the position at which they reach the detector. The V_y velocity difference between the particles will result in the generation of the circular/semi-circular patterns on the detector. Consequently, in a standard VMI setup, the measured 2-D momentum spectrum is a projection of the 3-D distribution onto the detector creating a *velocity map image* [63–67].

In order to recover the 3D map of the momentum distribution from its measured 2D projection several different methods have been suggested in the literature. The most common approach to recovering the 3-D distribution in VMI experiments is to exploit initial symmetries present in the original distribution. For instance, in experiments where the

ionizing laser is linearly polarized, the momentum distribution is cylindrically symmetric about the polarization axis [66, 68, 69]. Then it is possible to mathematically extract the 3D distribution from its 2D projection using the inverse Abel transform [67, 70]. If cylindrical symmetry is not present more general techniques are needed. Another technique is to record the Time of Flight (TOF) using a high-speed shutter mechanism in addition to the 2D x-y projection. By combining TOF and the 2D image it is possible to recover the complete 3-D distribution [71]. This method is applicable to ions as due to their larger mass they have TOF of the order of microseconds [66]. On the other hand, this method is not suitable for lighter electrons as their TOF is much smaller. Another approach called slice imaging uses electrostatic fields to isolate a slice of the momentum distribution before pulsing an MCP detector [72–74].

2.7.2 Overview of the developed VMI setup

Vacuum chambers

An image of the assembled VMI setup is illustrated in Fig. 2.19. The VMI setup has two chambers that are both made of non-magnetic stainless steel and are separated by a large 8” valve. These two chambers are labeled as the *main chamber* and *second chamber* as shown in Fig. 2.19. Both chambers are going to be kept on ultra-high vacuum of the order of 10^{-8} torr by utilizing two turbo-molecular vacuum pumps. The *main chamber* has 6 symmetric flanges as represented in schematics of Fig. 2.20. The laser filament is going to enter the *main chamber* through a fused silica 3” window which is mounted on one of the flanges. Then passing through the chamber it is focused at the center of the *main chamber* with a parabolic mirror which is mounted on another flange directly across the entering flange. The mirror is a 1” on-axis parabolic mirror with a 3” focal length from *SORL* that has been custom-designed to be highly reflective for 266 nm and 800 nm laser filaments. A parabolic mirror is used in our design to avoid aberrations that are present when using

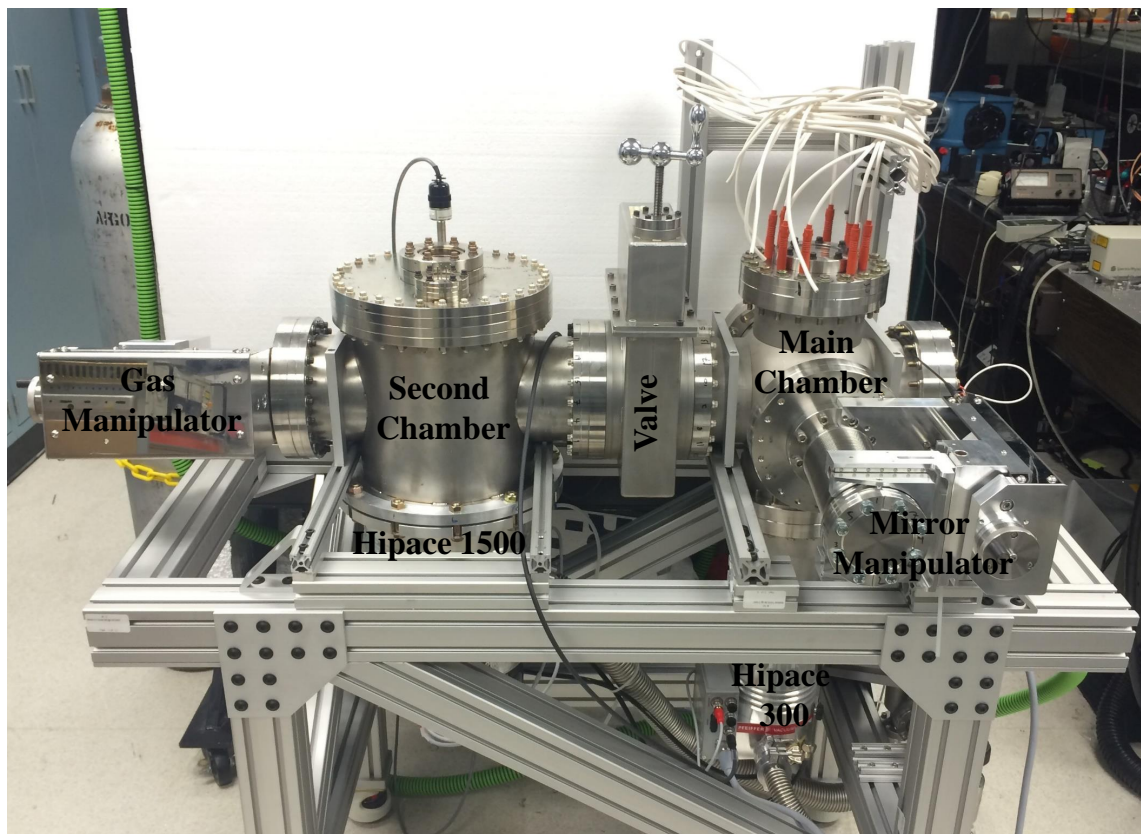


Figure 2.19: Overall picture of the assembled VMI setup.

spherical mirrors or lenses. The mirror mount is connected to a micro-manipulator that is going to be used for alignment purposes as it can move along XYZ axes without affecting the vacuum. The mirror mount attached to the *mirror manipulator* is designed in a way that when the manipulator is in the middle of its' Z range, the geometrical focal point of the parabolic mirror is located in the middle of the *main chamber* (Fig. 2.21(b)). An ion gauge is connected to another flange of the main chamber to monitor the vacuum. On the top flange of the *main chamber*, a feedthrough with 8 electrodes is mounted. In the middle of the feedthrough flange, there is a 3" fused silica window. A high-speed CCD camera (*Andor Zyla*) is mounted on top of this window. Inside the *main chamber* the electrostatic lensing apparatus is connected to the bottom of this feedthrough. For more information on electrostatic lensing apparatus please refer to 2.7.3. On the bottom flange

Chapter 2. UV laser filaments

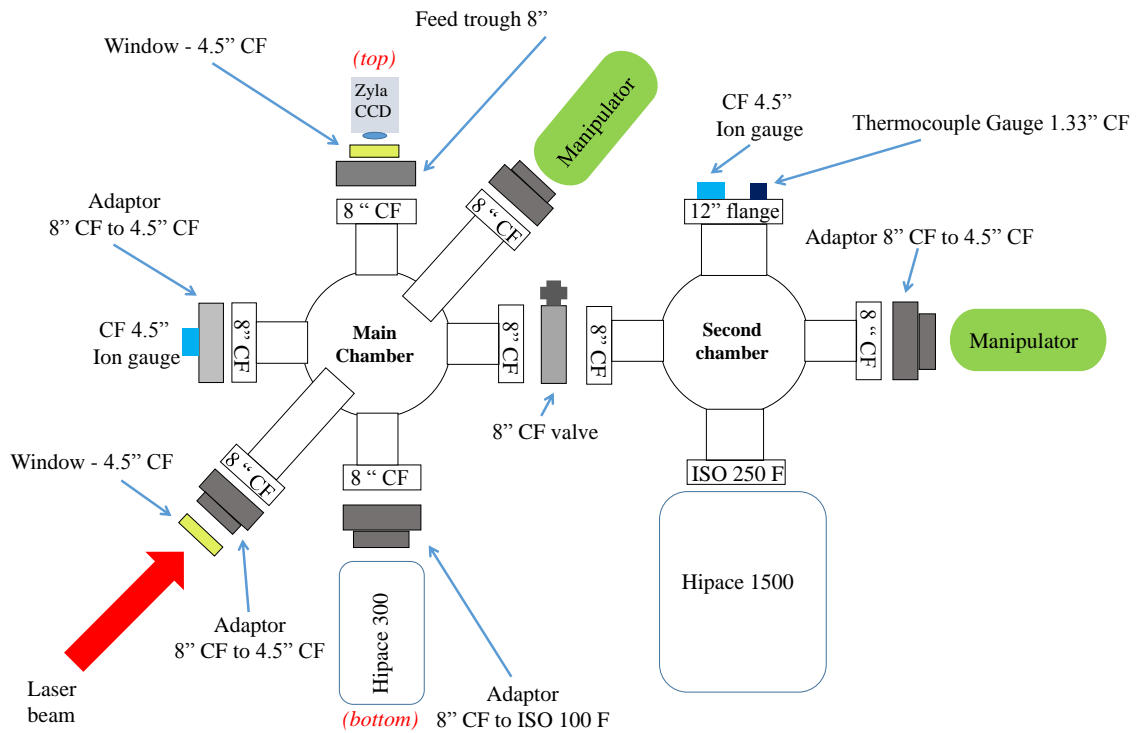


Figure 2.20: Schematic drawing of the VMI setup showing different parts and connections.

of the *main chamber*, the *Hipace 300* turbomolecular vacuum pump is mounted. Finally, the last remaining flange is connected through a valve to the *second chamber*.

The *second chamber* has 4 symmetric flanges. The bottom flange is connected directly to the *Hipace 1500* turbomolecular vacuum pump. To monitor the pressure inside the chamber a thermocouple gauge and a second ion gauge are mounted on the top flange. There is also an 8" fused silica window at the center of the top flange for potential monitoring purposes. The other flange of the *second chamber* is connected to the second micro-manipulator. As it is demonstrated in Fig. 2.21(a) the *gas manipulator* serves as the gas input for the VMI. The input gas flow is controlled by a high-speed solenoid valve from *Parker* (Model: 009-0100-900) with response times of less than 6 ms which is controlled by a 12 V DC power supply. Both sides of the valve are connected to flexible tubes resulting in the smooth movement of the manipulator in XYZ directions (Fig. 2.21(a)). A

Chapter 2. UV laser filaments

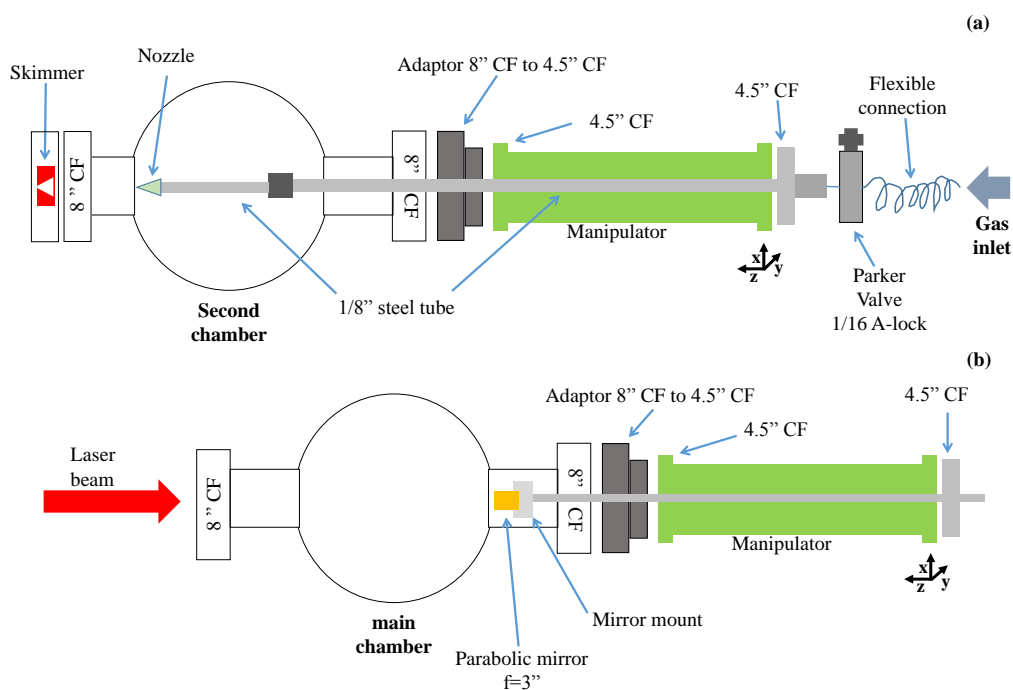


Figure 2.21: (a) The schematic design of the gas feeding system including the *gas manipulator*. The input gas flow is controlled by a high-speed solenoid valve from *Parker*. A skimmer is placed at the output flange of the *second chamber* just before the 8" valve. A nozzle is placed at the end of the input gas tube which is intended to eject gas in a coherent stream toward the skimmer. (b) The schematic design of the *mirror manipulator* and the mirror mount. The mirror is a 1" on-axis parabolic mirror with a 1" focal length from *SORL* that has been specially coated to be highly reflective for 266 nm and 800 nm laser filaments.

skimmer is placed at the output flange of the *second chamber* just before the 8" valve. A nozzle is placed at the end of the input gas tube which is intended to eject gas in a coherent stream toward the skimmer. The presence of the nozzle and the skimmer results in the creation of a very narrow molecular beam that enters the *main chamber* through the 8" valve. By aligning the *gas manipulator* in all 3 axes of XYZ it is possible to ensure that the created molecular beam enters the *main chamber* in the desired direction.

Ultra-high Vacuum

As mentioned before, VMI setups need an ultra-high vacuum in order to provide accurate measurements of the Momenta and kinetic energy of the electrons/ions. The created electrons in the VMI chamber need long free collision-less paths until they reach the detection part. Hence, to significantly reduce the number of collisions achieving ultra-high vacuum is a necessity. The ultra-high vacuum of the order of 10^{-8} have been achieved by the implementation of the two turbomolecular vacuum pumps; *Hipace 300 and 1500*. The chambers are made from stainless steel and all the connections are suitable connections for sustaining the high vacuum. The whole setup has gone through a 48-hour constant baking in order to accelerate the process of outgassing and removing any impurities. The best-achieved pressure was 7.2×10^{-9} torr.

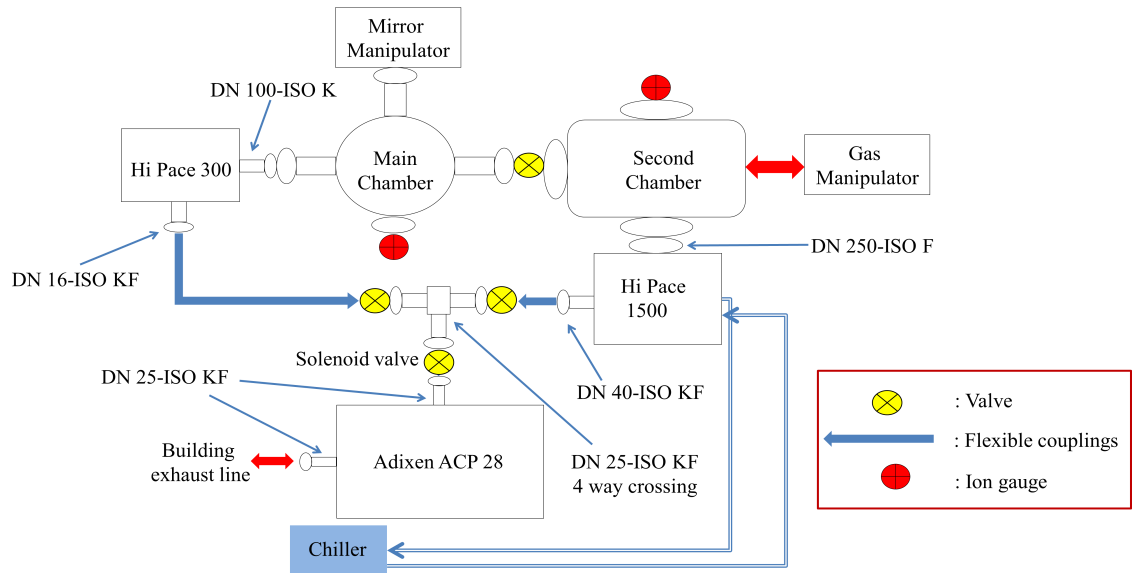


Figure 2.22: Schematics of the pumping circuit are presented. Each chamber is pumped by its own turbomolecular pump (from Pfeiffer). The molecular jet is injected into the VMI setup through the *second chamber* which has the largest pump flow capacity. The *Hipace 300* turbomolecular pump is cooled by air. On the other hand, the *Hipace 1500* turbomolecular pump needs to be cooled by water. The chiller for this purpose is located outside of the lab in the chase. A vacuum better than 10^{-8} torr is achieved in the main chamber. The input of both turbomolecular pumps is connected to a dry scroll pump via a solenoid valve. (*Adixen ACP 28*).

Chapter 2. UV laser filaments

A schematic of the pumping circuit of the VMI setup is represented in Fig. 2.22. It should be mentioned that initial vacuum of the order of 10^{-3} torr are necessary before the turbomolecular vacuum pumps can be operational. So the input of these pumps is connected to a dry scroll pump (*Adixen ACP 28*) which is acting as a backing pump. So initially the backing pump is going to be turned on and only after the desired pressures in the VMI setup are achieved the turbomolecular pumps can be operated. The *Hipace 300* is air-cooled, but the higher capacity *Highpace 1500* is water-cooled by a chiller. The pressure inside the VMI setup is measured by a thermocouple gauge and two ion gauges which are connected to the same controller unit. The thermocouple gauge is going to be used to measure low vacuum up to 10^{-3} torr, and higher vacuum are measured by the ion gauges. Ion gauges can be only operated at pressures of 10^{-4} torr and lower. A solenoid valve is placed between the backing pump and the input of the turbomolecular pumps as a safety measure. This valve will immediately close as soon as an emergency such as electrical power loss occurs sustaining the ultra-high vacuum.

In order to perform accurate measurements using the VMI technique the amount of the gas entering the *main chamber* needs to be as small as possible. Besides the high vacuum generated by the pumps, this is achieved by using both the high-speed pulsed input valve and also the skimmer. The high-speed valve should be synchronized with the incoming laser filament preferably by the use of a delay generator. Also, the presence of the skimmer will result in a narrow molecular beam which leads to a small interaction cross-section between the laser filament and the molecular beam increasing the accuracy of the measurements. In case of an operational MCP caution should be made during the alignment of the laser filament into the chamber making sure that the full-power laser filament will not hit any of the electrodes. As if the laser filament hits any of the electrodes by creating an intense plasma, a large number of electrons will be accelerated through the electrostatic lens toward the MCP which can cause damage to the MCP.

2.7.3 Detection system

In order to expand the dynamic range of this imaging we extended the imaging lenses to 5 from the classical 3-lens VMI setups. Similar to imaging objects in the configuration space, here having multiple lenses expands the dynamic range and magnification. In the VMI setup, the plates are fixed in position and only voltages are adjustable. The cylindrical spacer between electrodes is made of ceramic. In Fig. 2.23(a) the 2D schematics of the geometry of the electrostatic lens are demonstrated. A picture of the detection setup which is assembled on the feedthrough is presented in Fig. 2.23(c). In Fig. 2.23(d) the schematics of different feedthrough electrodes are shown. This schematic can be used to identify different voltage inputs on the feedthrough for the 5 electrostatic lenses and the MCP assembly. The parameters in the figure correspond to the following voltages: V_A : Voltage on the phosphor screen, V_I : Input voltage of the MCP, V_O : Output voltage of MCP, 1 to 5: Electrostatic lenses as labeled in Fig. 2.23(c). Red numbers 1-3 corresponds to the numbering marked in black on the outside of the flange which can be used for identification purposes. As mentioned before both the molecular beam and the focused laser filament are going to interact in the center of the *main chamber* by the use of the two manipulators. The detection assembly is designed in a way that the exact center point between the two first electrostatic lenses (labeled 5 and 4 in Fig. 2.23(c)) is also located in the center of the *main chamber*. This point is represented with a black dot in Fig. 2.23(a).

Simulations with *SIMION* have been performed to evaluate the proposed 5-lens system. *SIMION* is a software package primarily used to calculate electric fields and the trajectories of charged particles in those fields when given a configuration of electrodes with voltages and particle initial conditions, including optional RF (quasistatic), magnetic field, and collisional effects. In a VMI setup, the positions at which the particles hit the MCP (R) have a linear relation with respect to the square root of the initial energies of the particles ($E^{1/2}$) [64, 75]. In Fig. 2.24(a) simulated trajectories of electrons in the detection system for the mentioned voltages in Fig. 2.23(b) are represented. The initial velocities

Chapter 2. UV laser filaments

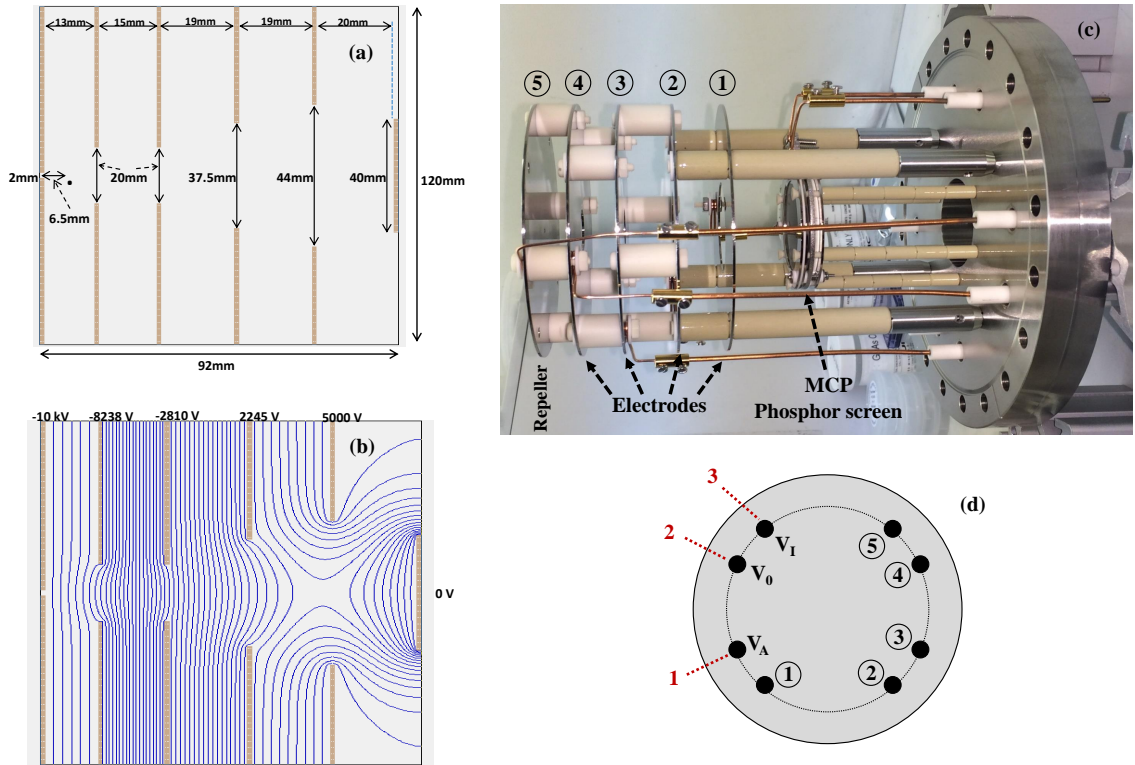


Figure 2.23: (c) Image of the detection assembly. The laser beam and the gas jet cross at a right angle in the center of the space between the repeller and the first electrode. Below the electrode assembly, one can distinguish the multichannel plate (MCP) to amplify the two-dimensional electron image, which produces a visible image on a fluorescent plate. The latter is imaged on a fast CCD camera (*Andor Zyla*) through the window of the flange. (d) Schematics of different feedthrough electrodes are shown. This schematic can be used to identify different voltage inputs on the feedthrough for the 5 electrostatic lenses and the MCP assembly. V_A : Voltage on the phosphor screen, V_I : Input voltage of the MCP, V_O : Output voltage of MCP, 1 to 5: Electrostatic lenses as labeled in (c). Red numbers 1-3 correspond to the numbering marked in black on the outside of the flange that can be used for identification purposes.

of electrons are directed at 90° azimuthal angle. Each trajectory corresponds to different initial energies ranging from 10 eV to 250 eV. For each trajectory 100 electrons which are randomly distributed in a sphere with $r=150 \mu\text{m}$ are simulated. From bottom to top the energies are 10, 25, 50, 100, 150, 200, and 250 eV. In Fig. 2.24(b) the positions at which these electrons hit the MCP vs $E^{1/2}$ are plotted. The relation is linear as it is expected.

Chapter 2. UV laser filaments

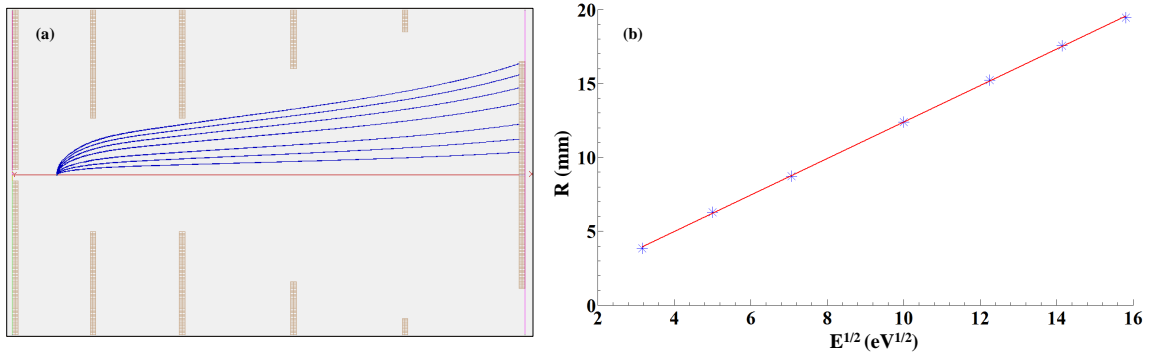


Figure 2.24: (a) Simulated trajectories of electrons with initial velocities directed at 90° azimuthal angle are presented. Each trajectory corresponds to different initial energies ranging from 10 eV to 250 eV. For each trajectory 100 electrons which are randomly distributed in a sphere with $r=150 \mu\text{m}$ are simulated. From bottom to top the energies are 10, 25, 50, 100, 150, 200, and 250 eV. (b) The position (R) on MCP vs square root of the energy ($E^{1/2}$).

Simulated trajectories of electrons at azimuthal angle pairs of 30° - 150° , 45° - 135° , and 60° - 120° are represented in Fig. 2.25. Similar to before, for each trajectory 100 electrons which are randomly distributed in a sphere with $r=150 \mu\text{m}$ are simulated. The initial energies of electrons are 50 eV and 200 eV for Fig. 2.25(a) and (b) respectively. The electron pairs that have similar initial velocity projections on the X-axis are going to be mapped on the same position on the MCP.

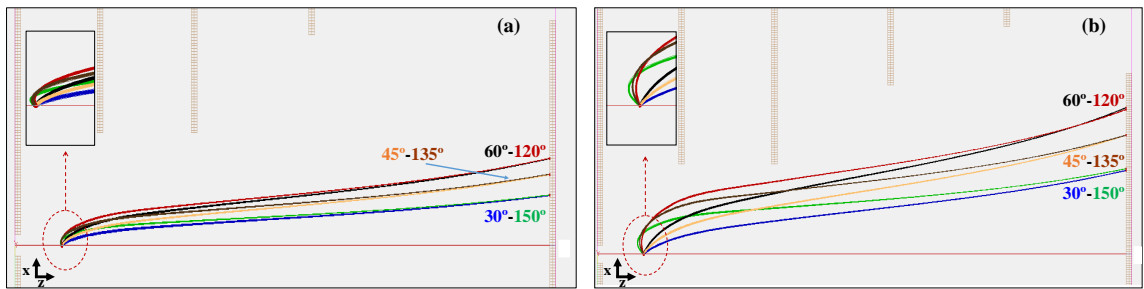


Figure 2.25: Simulations for electrons at azimuthal angle pairs of 30° - 150° , 45° - 135° , and 60° - 120° . For each trajectory 100 electrons which are randomly distributed in a sphere with $r=150 \mu\text{m}$ are simulated. (a) For 50 eV initial energy and (b) for 200 eV initial energy.

2.8 Future Work

Development of the high-repetition source needs to be completed. Afterwards experimental investigation of the laser filaments generated by this new laser source should be performed. This includes study of the waveguide generated by this source using the shadowgraphy technique. The initial testing of the VMI setup should be performed for calibration purposes. Next step is going to be investigation of the electron momentum distribution generated by the interaction of the laser filament and the gas.

Acknowledgement

This research has been supported by the Army Research office (ARO:W911NF-19-1-0272) and U.S. Department of Energy (DOE:DESC0011446).

References

- [1] Matthieu Baudelet, Myriam Boueri, Jin Yu, Samuel S. Mao, Vincent Piscitelli, Xianglei Mao, and Richard E. Russo. Time-resolved ultraviolet laser-induced breakdown spectroscopy for organic material analysis. *Spectrochimica Acta Part B: Atomic Spectroscopy*, 62(12):1329–1334, 2007. A Collection of Papers Presented at the 4th International Conference on Laser Induced Plasma Spectroscopy and Applications (LIBS 2006).
- [2] K. Stelmaszczyk, P. Rohwetter, G. Méjean, J. Yu, E. Salmon, J. Kasparian, R. Ackermann, J. P. Wolf, and L. Wöste. Long-distance remote laser-induced breakdown spectroscopy using filamentation in air. *Appl. Phys. Lett.*, 85:3977–3979, 2004.
- [3] Ali Rastegari, Matthias Lenzner, Jean-Claude Diels, Kristen Peterson, and Ladan Arissian. High-resolution remote spectroscopy and plasma dynamics induced with UV filaments. *Opt. Lett.*, 44(1):147–150, Jan 2019.
- [4] Ali Rastegari and Jean-Claude Diels. Investigation of UV filaments and their applications. *APL Photonics*, 6(6):060803, 2021.
- [5] Thomas Produit, Pierre Walch, Clemens Herkommer, Amirhossein Mostajabi, Michel Moret, Ugo Andral, Antonio Sunjerga, Mohammad Azadifar, Yves-Bernard André, Benoît Mahieu, Walter Haas, Bruno Esmiller, Gilles Fournier, Peter Krötz, Thomas Metzger, Knut Michel, André Mysyrowicz, Marcos Rubinstein, Farhad Rachidi, Jérôme Kasparian, Jean-Pierre Wolf, and Aurélien Houard. The laser lightning rod project. *Eur. Phys. J. Appl. Phys.*, 93(1):10504, 2021.
- [6] Francis Théberge, Jean-François Daigle, Jean-Claude Kieffer, François Vidal, and Marc Châteauneuf. Laser-guided energetic discharges over large air gaps by electric-field enhanced plasma filaments. *Scientific Reports*, 7(1):40063, Jan 2017.
- [7] Ali Rastegari, Elise Schubert, Chengyong Feng, Denis Mongin, Brian Kamer, Jerome Kasparian, Jean-Pierre Wolf, Ladan Arissian, and Jean-Claude Diels. Beam control through nonlinear propagation in air and laser induced discharges. In *Laser resonators and beam control XVIII, Photonics West, Conference 9727-51*, pages 9727–51, San Francisco, CA, 2016. SPIE.
- [8] Elise Schubert, Ali Rastegari, Chengyong Feng, Denis Mongin, Brian Kamer, Jerome Kasparian, Jean-Pierre Wolf, Ladan Arissian, and Jean-Claude Diels. HV discharge acceleration by sequences of UV laser filaments with visible and near-infrared pulses. *New Journal of Physics*, 19(12):123040, 2017.

References

- [9] A. Houard, C. D’Amico, Y. Liu, Y. B. Andre, M. Franco, B. Prade, A. Mysyrowicz, E. Salmon, P. Pierlot, and L.-M. Cleon. High current permanent discharges in air induced by femtosecond laser filamentation. *Applied Physics Letters*, 90(17):171501, 2007.
- [10] Ali Rastegari, Alejandro Aceves, and Jean-Claude Diels. UV filaments. *Light Filaments: Structures, Challenges and Applications*, page 31, 2021.
- [11] Q. Luo, W. Liu, and S.L. Chin. Lasing action in air induced by ultra-fast laser filamentation. *Applied Physics B*, 76(3):337–340, Mar 2003.
- [12] Ladan Arissian, Brian Kamer, Ali Rastegari, D. M. Villeneuve, and Jean-Claude Diels. Transient gain from N_2^+ in light filaments. *Phys. Rev. A*, 98:053438, Nov 2018.
- [13] Mathew Britton, Marianna Lytova, Patrick Laferrière, Peng Peng, Felipe Morales, Dong Hyuk Ko, Maria Richter, Pavel Polynkin, D. M. Villeneuve, Chunmei Zhang, Misha Ivanov, Michael Spanner, Ladan Arissian, and P. B. Corkum. Short- and long-term gain dynamics in N_2^+ air lasing. *Phys. Rev. A*, 100(4):013406, 2019.
- [14] A. Mysyrowicz, R. Danylo, A. Houard, V. Tikhonchuk, X. Zhang, Z. Fan, Q. Liang, S. Zhuang, L. Yuan, and Y. Liu. Lasing without population inversion in N_2^+ . *APL Photonics*, 4(11):110807, 2019.
- [15] Ali Rastegari, Jean-Claude Diels, Brian Kamer, Lee R. Liu, and Ladan Arissian. Measurement of delayed fluorescence in N_2^+ with a streak camera. *Opt. Express*, 30(17):31498–31508, Aug 2022.
- [16] S. A. Akhmanov, A. P. Sukhorukov, and R. V. Khokhlov. Self focusing and self trapping of intense light beams in a nonlinear medium. *Sov. Phys JETP*, 23:1025–1033, 1966.
- [17] E. Freysz, M. Afifi, A. Ducasse, B. Pouligny, and J. R. Lalanne. Giant optical nonlinearities of critical micro-emulsions. *J. Physique Lett.*, 46:181–187, 1985.
- [18] R. Y. Chiao, E. Garmire, and C. H. Townes. Self-trapping of optical beams. *Physics Review Letter*, 13:479–482, 1964.
- [19] J. H. Marburger. Self-focusing. In J. H. Sanders and S. Stenholm, editors, *Progr. Quantum Electron.*, volume 4, pages 35–110. Pergamon, Oxford, 1977.
- [20] A. Braun, G. Korn, X. Liu, D. Du, J. Squier, and G. Mourou. Self-channeling of high-peak-power femtosecond laser pulses in air. *Optics Lett.*, 20:73–75, 1995.

References

- [21] Olivier J. Chalus, A. Sukhinin, A. Aceves, and J.-C. Diels. Propagation of non-diffracting intense ultraviolet beams. *Optics Communication*, 281:3356–3360, 2008.
- [22] Xin Miao Zhao, Patrick Rambo, and Jean-Claude Diels. Filamentation of femtosecond UV pulses in air. In *QELS, 1995*, volume 16, page 178 (QThD2), Baltimore, MA, 1995. Optical Society of America.
- [23] J. Schwarz, P. K. Rambo, J.-C. Diels, M. Kolesik, E. Wright, and J. V. Moloney. UV filamentation in air. *Optics Comm.*, 180:383–390, 2000.
- [24] Xiaozhen Xu and J.-C. Diels. Stable single-axial-mode operation of injection-seeded Q-switched Nd:YAG laser by real-time resonance tracking method. *Applied Physics B*, 114:579, 2014.
- [25] Xiaozhen Xu. *High power UV source development and its applications*. PhD thesis, The University of New Mexico, Albuquerque, New Mexico, 2015.
- [26] Xiaozhen Xu, Chengyong Feng, and Jean-Claude Diels. Optimizing sub-ns pulse compression for high energy application. *Optics Express*, 22:13904–13915, 2014.
- [27] Chengyong Feng, Xiaozhen Xu, and Jean-Claude Diels. High-energy sub-phonon lifetime pulse compression based on stimulated Brillouin scattering in liquids. *Optics Express.*, 25:12421–12434, 2017.
- [28] Chengyong Feng, Xiaozhen Xu, and Jean-Claude Diels. Generation of 300 ps laser pulse with 1.2 J energy by stimulated Brillouin scattering in water at 532 nm. *Opt. Lett.*, 39(12):3367–3370, 2014.
- [29] T.D. Grow, A. A. Ishaaya, L. T. Vuong, A. L. Gaeta, R. Gavish, and G. Fibich. Collapse dynamics of super-Gaussian beams. *Optics Express*, 14:5468–5475, 2006.
- [30] Y. R. Shen and M. M. Loy. Theoretical interpretation of small-scale filaments of light originating from moving focal spots. *Physical Review A*, 3:2099–2105, 1971.
- [31] E. M. Parmentier and R. A. Greenberg. Supersonic flow aerodynamic windows for high-power lasers. *AIAA Journal*, 11(7):943–949, 1973.
- [32] J.-C. Diels, J. Yeak, D. Mirell, R. Fuentes, S. Rostami, D. Faccio, and P. di Trapani. Air filaments and vacuum. *Laser Physics*, 20:1101–1106, 2010.
- [33] T. S. Ross. *Laser beam quality metrics*. SPIE, 2013.
- [34] Yongzhao Du, Yuqing Fu, and Chaoying Zheng. Beam quality M^2 factor matrix for non-circular symmetric laser beams. *Laser Physics*, 27(2):025001, dec 2016.

References

- [35] K. Lim, M. Durand, M. Baudelet, and M. Richardson. Transition from linear- to nonlinear-focusing regime in filamentation. *Science Reports*, 4:7217, 2014.
- [36] Francis Théberge, Weiwei Liu, Patrick Tr. Simard, Andreas Becker, and See Leang Chin. Plasma density inside a femtosecond laser filament in air: Strong dependence on external focusing. *Phys. Rev. E*, 74:036406, Sep 2006.
- [37] Olivier Chalus. *Study of Nonlinear Effects of Intense UV Beams in the Atmosphere*. PhD thesis, University of New Mexico and University Louis Pasteur, Strasbourg, 2007.
- [38] A. Brodeur, C. Y. Chien, F. A. Ilkov, S. L. Chin, O. G. Kosareva, and V. P. Kandidov. Moving focus in the propagation of ultrashort laser pulses in air. *Optics Lett.*, 22:304–306, 1997.
- [39] Chengyong Feng. *Sub-nanosecond UV filaments and their applications for remote spectroscopy and high-voltage discharges*. PhD thesis, University of New Mexico, Albuquerque, NM, 2016.
- [40] Takashi Fujii, Megumu Miki, Naohiko Goto, Alexei Zhidkov, Tetsuo Fukuchi, Yuji Oishi, and Koshichi Nemoto. Leader effects on femtosecond-laser-filament-triggered discharges. *Physics of Plasmas*, 15(1):013107, 2008.
- [41] Y.-H. Cheng, J. K. Wahlstrand, N. Jhajj, and H. M. Milchberg. The effect of long timescale gas dynamics on femtosecond filamentation. *Opt. Express*, 21:4740, 2013.
- [42] M. N. Plooster. Shock waves from line sources. numerical solutions and experimental measurements. *Phys. Fluids*, 13:2665–2675, 1970.
- [43] K. Kremeyer, K. Sebastian, and C.-W Shu. Computational study of shock mitigation and drag reduction by pulsed energy lines. *AIAA J.*, 44:1720–1731, 2006.
- [44] P. K. Panigrahi and K. Muralidharl. *Schlieren and Shadowgraph methods in heat and mass transfer. Chap.2: Laser Schlieren and Shadowgraph*. Springer, 2012.
- [45] Gary S Settles and Michael J Hargather. A review of recent developments in schlieren and shadowgraph techniques. *Measurement Science and Technology*, 28(4):042001, feb 2017.
- [46] Ali Rastegari, Chengyong Feng, and Jean-Claude Diels. Investigation of the waveguide generated by uv filamentation. In *CLEO: 2018*, page JTu2A.161, San Jose, CA, 2018. Optical Society of America.

References

- [47] Xiao-Long Liu, Xin Lu, Xun Liu, Ting-Ting Xi, Feng Liu, Jing-Long Ma, and Jie Zhang. Tightly focused femtosecond laser pulse in air: from filamentation to breakdown. *Opt. Express*, 18(25):26007–26017, Dec 2010.
- [48] F V Potemkin, E I Mareev, A A Podshivalov, and V M Gordienko. Laser control of filament-induced shock wave in water. *Laser Physics Letters*, 11(10):106001, sep 2014.
- [49] Leonid Ivanovich Sedov and AG Volkovets. *Similarity and dimensional methods in mechanics*. CRC press, 2018.
- [50] Fernando J. Álvarez and Roman Kuc. Dispersion relation for air via Kramers-Kronig analysis. *The Journal of the Acoustical Society of America*, 124(2):EL57–EL61, 2008.
- [51] Ali Rastegari and Jean-Claude Diels. Investigation of shock-waves generated by ps UV filaments. In *Conference on Lasers and Electro-Optics*, page JW2A.82. Optica Publishing Group, 2023.
- [52] N. Jhajj, E.W. Rosenthal, R. Birnbaum, J. K. Wahlstrand, and H. M. Milchberg. Demonstration of long-lived high-power optical waveguides in air. *Physical Review X*, 4:011027, 2014.
- [53] B. Miao, L. Feder, J. E. Shrock, A. Goffin, and H. M. Milchberg. Optical guiding in meter-scale plasma waveguides. *Phys. Rev. Lett.*, 125:074801, Aug 2020.
- [54] E. W. Rosenthal, N. Jhajj, J. K. Wahlstrand, and H. M. Milchberg. Collection of remote optical signals by air waveguides. *Optica*, 1(1):5–9, Jul 2014.
- [55] Oren Lahav, Liad Levi, Itai Orr, Ron A. Nemirovsky, Jonathan Nemirovsky, Ido Kaminer, Mordechai Segev, and Oren Cohen. Long-lived waveguides and sound-wave generation by laser filamentation. *Phys. Rev. A*, 90:021801, Aug 2014.
- [56] Phillip Sprangle, Joseph Penano, and Bahman Hafizi. Optimum wavelength and power for efficient laser propagation in various atmospheric environments. *Journal of Directed Energy*, 2(1):71–95, 2006.
- [57] Phillip Sprangle, Bahman Hafizi, Antonio Ting, and Richard Fischer. High-power lasers for directed-energy applications. *Appl. Opt.*, 54(31):F201–F209, Nov 2015.
- [58] Jean-Claude Diels and Wolfgang Rudolph. *Ultrashort laser pulse phenomena*. Elsevier, 2006.
- [59] Walter Koechner. *Solid-state laser engineering*, volume 1. Springer, 2013.

References

- [60] Mukhtar Hussain, Tayyab Imran, and  Brzsny. Thermal lensing measurements of ti: sapphire crystal by an optical wavefront sensor. *Microwave and Optical Technology Letters*, 61(12):2901–2909, 2019.
- [61] Luke Jameson Horstman. *Intracavity Phase Interferometry Based Fiber Sensors*. PhD thesis, The University of New Mexico, 2022.
- [62] L. Arissian and J.-C. Diels. Ultrafast electron plasma index; an ionization perspective. *Journal of Lasers, Optics & Photonics*, 1:107–111, 2014.
- [63] James N Bull, Jason WL Lee, and Claire Vallance. Quantification of ions with identical mass-to-charge (m/z) ratios by velocity-map imaging mass spectrometry. *Physical Chemistry Chemical Physics*, 15(33):13796–13800, 2013.
- [64] Andr T. J. B. Eppink and David H. Parker. Velocity map imaging of ions and electrons using electrostatic lenses: Application in photoelectron and photofragment ion imaging of molecular oxygen. *Review of Scientific Instruments*, 68(9):3477–3484, 1997.
- [65] Angela Marcela Coroiu. *Photoinduced dynamics in NO2 and Tetrakis molecules using Velocity Map Imaging*. PhD thesis, [SI: sn], 2005.
- [66] Christopher Smeenk. *Imaging atoms and molecules with strong laser fields*, 2013.
- [67] C. Smeenk, L. Arissian, A. Staudte, D. Villeneuve, and P B Corkum. Tomographic imaging of the three dimensional momentum distribution in velocity map imaging experiments. *Journal of Physics B: At. Mol. Opt. Phys*, 42:185402, 2009.
- [68] Marc J. J. Vrakking. An iterative procedure for the inversion of two-dimensional ion/photoelectron imaging experiments. *Review of Scientific Instruments*, 72(11):4084–4089, 2001.
- [69] Gustavo A. Garcia, Laurent Nahon, and Ivan Powis. Two-dimensional charged particle image inversion using a polar basis function expansion. *Review of Scientific Instruments*, 75(11):4989–4996, 2004.
- [70] Ronald Bracewell. *The Fourier transform and its applications*. McGraw-Hill New York, 3rd edition, 2000.
- [71] L. Dinu, A. T. J. B. Eppink, F. Rosca-Pruna, H. L. Offerhaus, W. J. van der Zande, and M. J. J. Vrakking. Application of a time-resolved event counting technique in velocity map imaging. *Review of Scientific Instruments*, 73(12):4206–4213, 2002.

References

- [72] Christoph R. Gebhardt, T. Peter Rakitzis, Peter C. Samartzis, Vlassis Ladopoulos, and Theofanis N. Kitsopoulos. Slice imaging: A new approach to ion imaging and velocity mapping. *Review of Scientific Instruments*, 72(10):3848–3853, 2001.
- [73] Dave Townsend, Michael P. Minitti, and Arthur G. Suits. Direct current slice imaging. *Review of Scientific Instruments*, 74(4):2530–2539, 2003.
- [74] Jim J. Lin, Jingang Zhou, Weicheng Shiu, and Kopin Liu. Application of time-sliced ion velocity imaging to crossed molecular beam experiments. *Review of Scientific Instruments*, 74(4):2495–2500, 2003.
- [75] N G Kling, D Paul, A Gura, G Laurent, S De, H Li, Z Wang, B Ahn, C H Kim, T K Kim, I V Litvinyuk, C L Cocke, I Ben-Itzhak, D Kim, and M F Kling. Thick-lens velocity-map imaging spectrometer with high resolution for high-energy charged particles. *Journal of Instrumentation*, 9(05):P05005, may 2014.

Chapter 3

Measurement of delayed fluorescence in N_2^+ with a streak camera

3.1 Introduction

“Air Lasing” is a phenomenon that was first proposed in 2003 from the observation of amplified emissions in a femtosecond laser filament and since then has caught lots of attention as it has many potential applications [1, 2]. It has been demonstrated that a population inversion can be created for some of the ionized molecules/atoms inside the plasma generated by the laser filament, inversion which can result in amplification of coherent or incoherent light [1–4]. The concept of air lasing is different from the concept of conventional lasers as it enables remote mirrorless (no-cavity) optical amplification in ambient conditions. This phenomenon holds 3 unique properties: 1. Remote generation of optical gain in air molecules. 2. There is no cavity required for optical amplification, and 3. A coherent directional radiation is generated in both forward and backward directions with respect to the pump laser [2]. Since in air high-intensity laser filaments are hardly disturbed even in adverse environments [5, 6] and also because of their capability

of being projected at a far distance, air lasing can be implemented for the creation of a high-brightness source in the atmosphere, which has many potential applications including remote detection of gases and atmospheric studies [7–10]. Two decades after its first experimental observation, even though air lasing has been investigated in many studies both theoretically and experimentally, the physical mechanism behind it is still under hot debate.

Different air constituents are proposed and investigated as the gain medium for air lasing. Among these candidates the transitions of the nitrogen cation N_2^+ are of particular interest for this application [1] as their emission has been observed in a wide range of pressures and gas mixtures. High gain and fast decay is observed [11–13], with a timescale orders of magnitude shorter than the 67 nanoseconds natural lifetime of the excited state [14]. We have studied two transitions of the N_2^+ : $B^2\Sigma_u^+(\nu = 0) \rightarrow X^2\Sigma_g^+(\nu = 0, \nu = 1)$. These two transitions correspond to 391 nm ($\nu = 0$) and 428 nm ($\nu = 1$) as represented in Fig. 3.1 [15–17].

The mechanism of this gain is still under debate. Some argue that an inversion is created by the ultrashort pulse [18]; others propose a transient gain driven by rotational coherence [19] or lasing without inversion [20] involving coherence in a three level system (the $A^2\Pi_u$ state coupled to the $B^2\Sigma_u^+ \rightarrow X^2\Sigma_g^+$ transition), and finally some propose that the gain is achieved via superradiance [13, 21].

In most experiments, the dynamics of the emission is studied by varying the time delay between an ultrashort “pump” pulse at 800 nm, followed by an ultrashort “probe” pulse which resonantly seeds the single photon transition [11–13, 21–25]. This induces measurable changes in plasma radiation depending on the pump-probe delay, from which the temporal dynamics are inferred. However, this inevitably conflates unknown dynamics induced by the probe with the dynamics of interest. In addition, at each delay the reported measurement is integrated over the lifetime of the emission. In a typical pump-probe study the emission spectrum is integrated over the lifetime of the emission. The probe is known to seed the emission after a certain delay from the ionizing pulse which usually

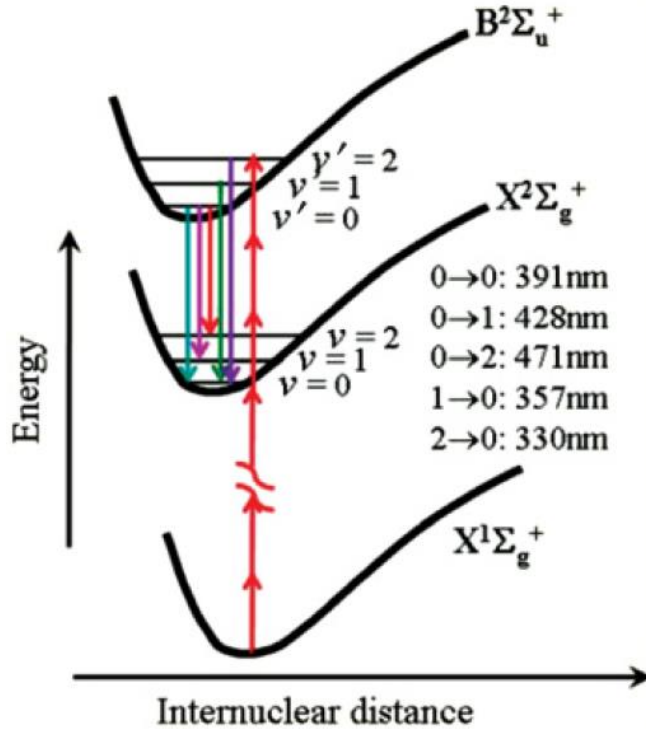


Figure 3.1: Schematic diagram of nitrogen cations energy-levels. The transitions between $B^2\Sigma_u^+$ (upper) and $X^2\Sigma_g^+$ (lower) states are indicated with corresponding lasing wavelengths [3].

does not create any ion emission by itself. In most cases the time delay scan of probe provides an insight on the wavepacket and plasma dynamics and not the time dependent emission. In some pump-probe studies a cross correlation with a third reference pulse provides a time-dependent emission at a particular seed delay. Our streak camera study (which is spatially integrated) can only be compared with the time-dependent emission at zero probe delay using a third pulse. A streak camera provides spatial imaging and real time information that are not available in pump-probe techniques. The streak camera is used to time-resolve the fluorescence emitted from the side of the plasma, originating from the $B^2\Sigma_u^+(\nu = 0) \rightarrow X^2\Sigma_g^+(\nu = 0, \nu = 1)$ transitions of N_2^+ . Particular care was taken to achieve an accurate reference for the excitation instant through an original technique detailed in Section 3.2.4. After deconvolution for the instrument response, these measure-

ments performed at atmospheric pressure show a delay between excitation and emission of tens of ps for both transitions, in contrast with what is generally assumed. For instance, some suggest an ‘instantaneous’ population inversion mechanism that may be achieved in molecular nitrogen ions at an ultrafast time scale comparable to the 800 nm pump pulse (abstract of ref. [12]). The interpretation is that “the population inversion can occur instantly with the ionization of inner-valence electrons” [3]. The measurement technique is described in Section 3.2. The jitter intrinsic to the streak camera electronic trigger is eliminated by using an optical reference point as detailed in Section 3.2.3. Subpicosecond resolution is achieved through a deconvolution technique presented in Section 3.3.1. The absolute timing of the cation emission, as well as the fluorescence decay time, are discussed in Section 3.2.4.

3.2 Experimental techniques

3.2.1 Streak Camera

A streak camera, despite being called a “camera”, differs significantly from conventional video and still cameras that we typically use to capture images of our surroundings. Its primary function is to measure ultra-fast light phenomena, providing intensity vs. time and position data. The term “streak” originates from the early days of high-speed rotating drum cameras, where reflected light was streaked onto film. The streak camera offers superior temporal resolution in directly detecting ultra-fast light phenomena compared to any other instrument. When used with appropriate optics, it can measure the time variation of incident light with respect to the position (time and space-resolved measurement). When combined with a spectroscope, it can measure the time variation of light intensity incident to the device relative to its wavelength (time-resolved spectroscopy) [26–28].

In Fig. 3.2 the operating principle of a streak camera is illustrated. The light that is being

Chapter 3. Measurement of delayed fluorescence in N_2^+ with a streak camera

measured enters the streak camera through the entrance slit of the camera. An image of the entrance slit is imaged via the optics inside the streak camera on the photocathode of the streak tube. For demonstration purposes, we assume that four optical pulses that are slightly varying in both space and time and also have different optical intensities are the inputs of the streak camera as shown in Fig. 3.2. In the photocathode, the four incident optical pulses are sequentially converted into electrons. The number of electrons is proportional to the intensity of these four pulses. The created electrons are accelerated toward the phosphor screen as they pass through a pair of accelerating/sweeping electrodes. As the electrons are passing through the pair of sweeping electrodes, time-varying high voltage which is in synchronization with the incident light is applied to the sweep electrodes (see Fig. 3.3 initiating a high-speed sweep of the electrons from top to bottom. During the

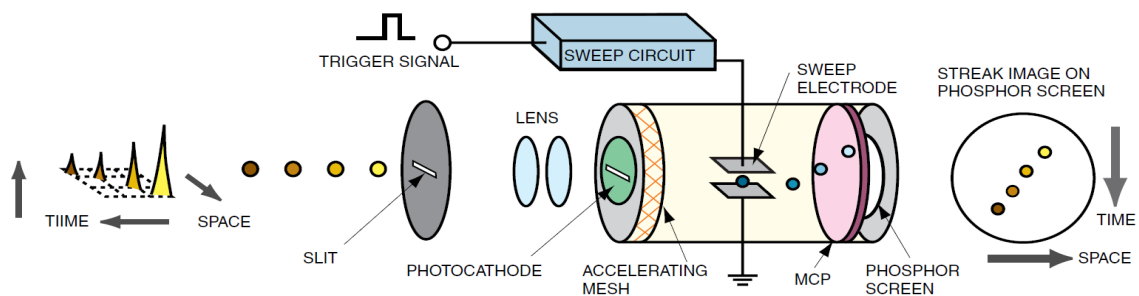


Figure 3.2: Operating principle of a streak camera [26].

high-speed sweep electrons arriving at slightly different times, are going to be deflected in slightly different angles in the vertical direction (perpendicular to the entrance slit of the streak camera), and as a result they would enter the Microchannel Plate (MCP) at different vertical positions. MCP is an electron multiplier that is used for the detection of charged particles, UV radiation, X-rays, etc. MCPs can have linear gains up to 1000 and one of their advantages is that they preserve the spatial resolution of the original input radiation as they generate the output two-dimensional electron image. Immediately at the back of MCP, there is a phosphor screen that converts electrons that have been multiplied several thousand times in the MCP, into light upon their impact on it [26–28].

The phosphor image that corresponds to the optical pulse arriving first is positioned at

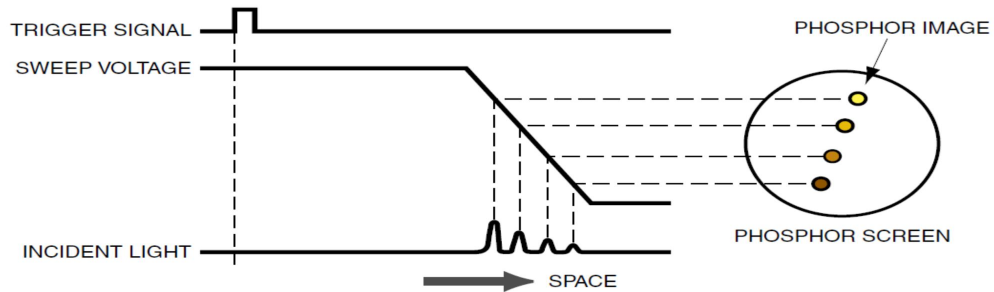


Figure 3.3: Operation timing of a streak camera at the time of sweep [26].

the top of the phosphor screen, while the remaining images follow in a sequential order from top to bottom. Essentially, the vertical direction on the phosphor screen functions as the time axis. In addition, the brightness of each phosphor image is directly proportional to the intensity of its corresponding incident optical pulse. The horizontal position of the phosphor image corresponds to the horizontal location of the incident light functioning as the space axis. Hence the optical intensity of the light is proportional to the intensity of the image created on the phosphor screen, and the temporal and spatial profile of the incident light is related to the position on the image of the phosphor screen [26–28].

3.2.2 Experimental setup

In our experiment, bandwidth-limited ultrashort pulses of 50 fs duration, 1 mJ energy, at 1 kHz repetition rate centered at 800 nm are focused in air. The measurements have been performed with 10 cm and 40 cm focusing lenses. In a tight focusing geometry, the peak intensity reaches $\approx 10^{14}$ Watt/cm² [29–31] generating a plasma that glows over one centimeter. The emission is self-seeded with the supercontinuum generated in the focused short pulse. Indeed, we observed the supercontinuum ring consisting of colorful rings covering the main beam in the far field.

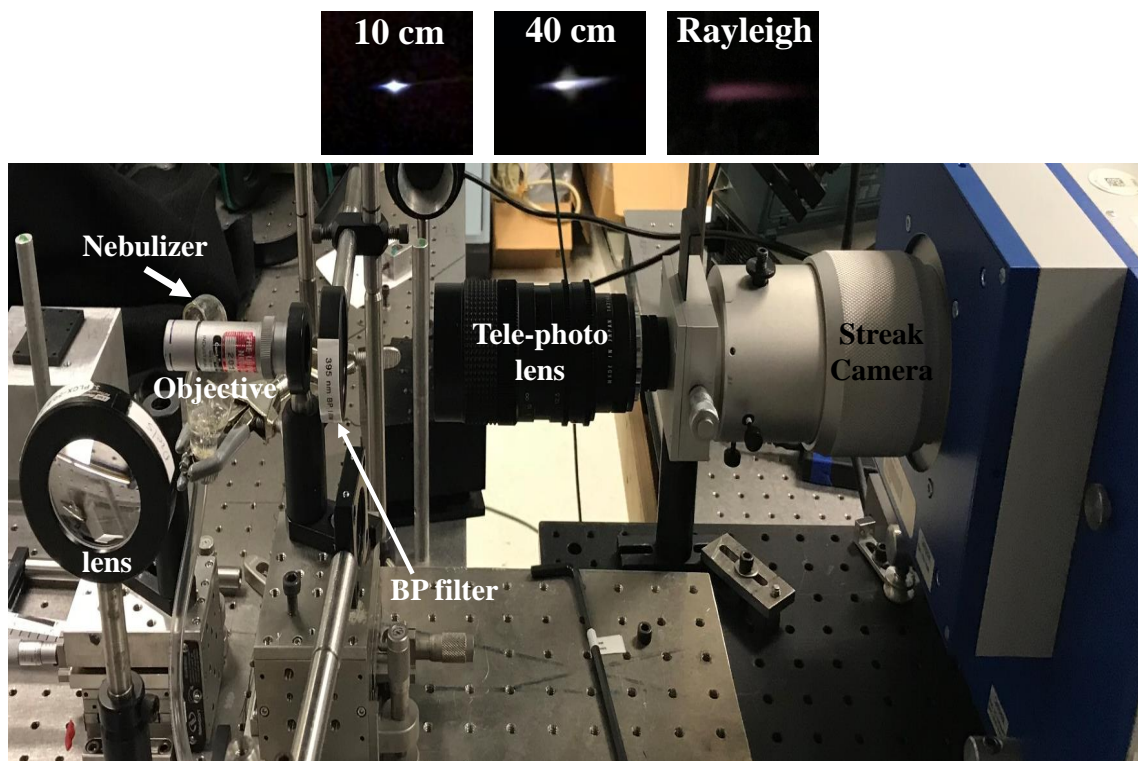


Figure 3.4: Top) From left to right, the image of the plasma induced by focusing 800 nm laser pulses with 10 cm and 40 cm focusing lenses, and the image of the Rayleigh scattering. Bottom) Picture of the streak camera fluorescence detection setup showing different elements of the setup.

The streak camera (Optronis 10C) captures emission from the side of the filament, as opposed to integrating the emission along its length [11–13, 21, 22, 24]. Thus, by making point by point measurements along the propagation direction, we access the “longitudinal emission profile” and can therefore monitor the effects of propagation. It should be mentioned that all the measurements presented in this paper have been taken with a sweep speed of 100 ps and the spacing between pixels corresponds to 2.88 ps.

In this configuration, our measurement is the signal collected from the cross section of the plasma and provides a different aspect of the emission, as opposed to integrating the radiation along the light propagation. Transient gain measurements have typically been performed at low pressures, while our observations are in air at atmospheric pressure

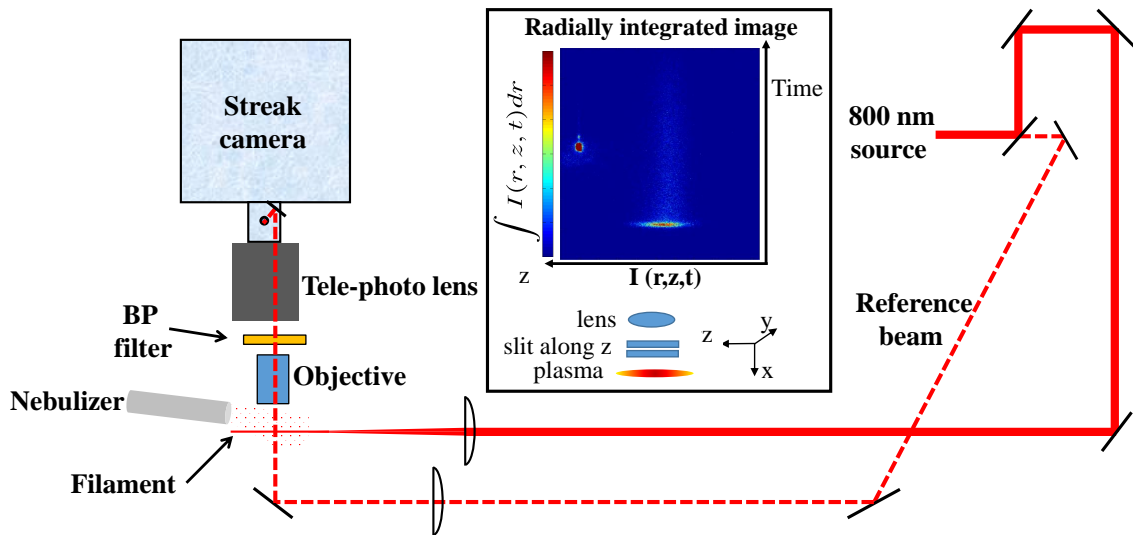


Figure 3.5: Sketch of the streak camera fluorescence detection. The side emission of the plasma created by the focused main beam (thick red line) is imaged onto the streak camera. A weak beam split off from the main beam (dashed red line) provides a temporal reference spot on each frame of the streak camera. The streak camera slit is parallel to the main beam (z direction) and is used at its minimum possible opening for best time resolution. A typical image taken with infrared filter is presented in the inset. The abscissa is the propagation axis, and the ordinate is time. The image is integrated over the transverse dimension as a function of z (coordinate along the beam). The trace of the plasma radiation is recorded. The reference light (on the left) is used for timing reference and correction of spatial jitter. BP represents the band-pass filter. A nebulizer is used to measure the Rayleigh scattering from the focused beam for a weak non-ionizing pulse.

(630 torr in Albuquerque). The emission of the plasma is very weak, corresponding to a plasma density of the order of 10^{17} cm^{-3} . In addition to being accumulated over a very short distance, the total signal is further decreased by the fact that we attempt to measure a number of photons emitted per picosecond time gate with spatial resolution over the length of the plasma. One of the most difficult challenges to address is to collect as efficiently as possible all the light that is emitted radially. Various focusing geometries have been tested. Best results were obtained with 10 cm and 40 cm focal distance lenses, and by using an objective lens and an achromatic telephoto lens to image the transverse emission onto the slit of the streak camera.

3.2.3 Optical synchronization

There are three elements that determine the time resolution of the system:

1. The accuracy of positioning the frames with respect to each other.
2. The intrinsic resolution of the streak camera.
3. The reproducibility of the event under observation.

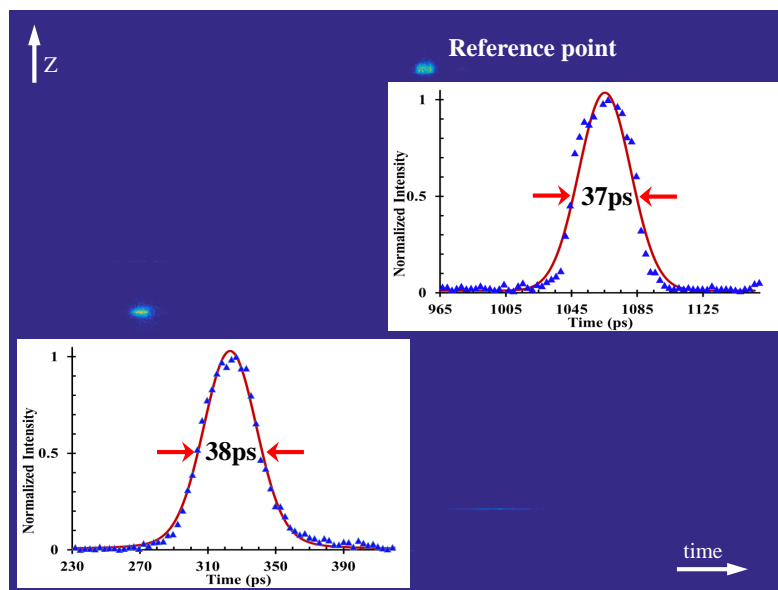


Figure 3.6: The blue area is a typical average of 1000 frames, that captured the reference (turquoise spot in the middle-top of the figure) and the scattering of a diffuser (turquoise spot in the middle left). The ordinate is a spatial coordinate, the abscissa time. The total width of the image is swept in 100 ps. The spacing between pixels corresponds to 2.88 ps. The inserted graphs below reference and scattering spots are space integrated recordings of intensity versus time. For ideal resolution, the reference (top) and the image have the same intensity. Note that they have the same width.

A delta function reference point

The streak camera is triggered electronically through the master clock of the laser system, thereby inheriting jitters of the laser electronics. In order to be unaffected by this jitter, each image is accurately timed by using a reference optical beam selected from the same pulse that creates the plasma, reference sent directly to the camera via a fixed path (Fig. 3.5). The path of the reference beam is such that it always illuminates the same point of the photo-cathode in the time frame of the camera streak, providing a temporal reference for every streak camera image. Mechanical and electronic jitters between frames are corrected by using the timing of the reference pulse in the Matlab reconstruction code [32]. The reference beam was sent directly through an optical port on top of the streak camera, which resulted in an order of magnitude better resolution than when using the fiber provided by the streak camera manufacturer.

Imaging the laser focal spot; time and space reference

The response to a delta function light pulse, obtained by scattering the filament off a ground glass diffuser, is extremely sensitive to the slit opening. In fact, it is only with the slit opened to its minimum (i.e. nearly closed) that the resolution quoted by the manufacturer is achieved. The signal is then so weak that it is reduced to a few scattered dots. In order to achieve the best resolution, it is necessary to accumulate and average between 1000 and 2500 frames. In doing so, the frames have to be synchronized as discussed in the previous paragraph. The intensity of the synchronization pulse should also be such that only 10 to 20 pixels are irradiated per frame.

The algorithm used takes the average of all the synchronization dots, excluding those that are outside of an area equal to 4 times the mean square deviation. This average is taken as reference for all frames. Fig. 3.6 shows an image of a filament scattered off ground glass (1000 frames are averaged). Both images of the reference and that of the scatterer have

the same width of 38 ps. This picture indicates that we can define the centroid and the rise time of the temporal sweep with a precision of a few ps.

3.2.4 Determination of an accurate time origin for temporal measurements

The reference pulse ensures temporal resolution by providing a common origin to the numerous frames being averaged. However, the objective is to measure the temporal profile of the UV emission, with respect to the 800 nm excitation *at the same location*. The problem is to ascertain with precision that exactly the same spot is being observed in both experiments. Using a diffuser plate — such as was done in the experiment to determine the instrumental resolution — puts one at the mercy of an error in positioning. An accurate time origin can be provided by Rayleigh scattering. However, Rayleigh scattering at 800 nm from air molecules is too weak to be observed (and time resolved) with the streak camera. Since we have achieved accurate timing of each frame with the reference pulse as demonstrated in Fig. 3.6, we can perform independent measurements to determine the arrival time of the 800 nm pulses.

The solution that we chose is to use Rayleigh scattering enhanced by aerosols. The aerosols are blown through the camera field of view along the path of the focused beam. The challenge here is to create droplets that enhance scattering without creating plasma and/or producing an optical resonance [33] in the droplet. The plasma is avoided by producing droplets of the order of 1 μm diameter with a nebulizer (mist generator based on Bernoulli principle). These droplets were sufficiently small as not to create any visible plasma or local illumination. The reference point accurately determined by recording Rayleigh scattering of the lowest density mist is shown in Fig. 3.7.

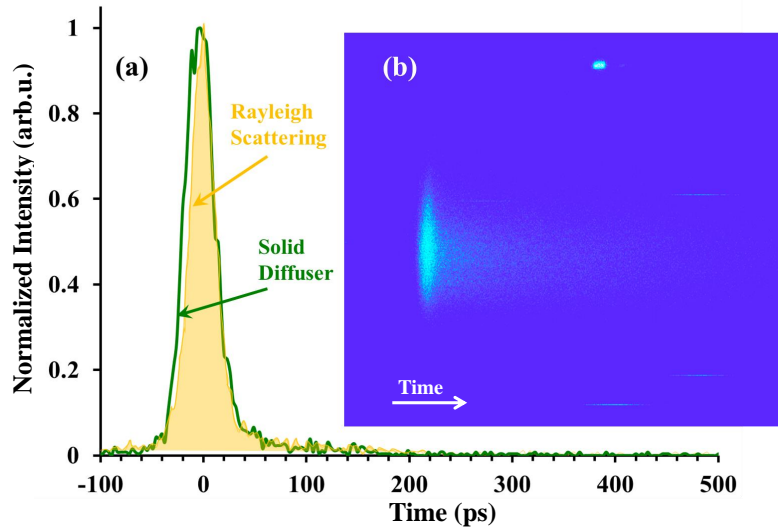


Figure 3.7: (a) In yellow: the reference pulse obtained by sending the low intensity laser beam through a dispersed mist. Green: reference pulse obtained with a solid diffuser surface. The center of gravity of the yellow reference will be used as the time of arrival of the fs pulse. (b) Typical averaged streak camera frame.

3.3 Experimental Results

3.3.1 De-convolution

As it can be seen in Fig. 3.6 for the selected slit opening of the streak camera the streaks of the fs laser pulse reflected from the diffuser and the reference optical beam extracted from the same fs laser pulse, have the same Full Width at Half Maximum (FWHM) of 40 ps. This width is orders of magnitude larger than the actual duration (≈ 50 fs) of the laser pulse. The 40 ps wide streak in the insets of Fig. 3.6 can be seen as the δ -function response of the streak camera for the particular slit opening used. The measured time delays and decay times that will be presented in section 3.3.2 have the same order of magnitude as this time resolution. The accurate knowledge of the δ -function response enables us to correct the measured response for the instrument response. The measured signal I_S is the convolution of the real signal S and the δ -function response R : $I_S = S \otimes R$ [34,

35]. By taking the Fourier transform we have: $\mathfrak{F}[I_S] = \mathfrak{F}[S] \times \mathfrak{F}[R]$. Hence, the actual signal can be calculated as: $S = \mathfrak{F}^{-1}[\mathfrak{F}[I_S]/\mathfrak{F}[R]]$. The Rayleigh scattering pulse and

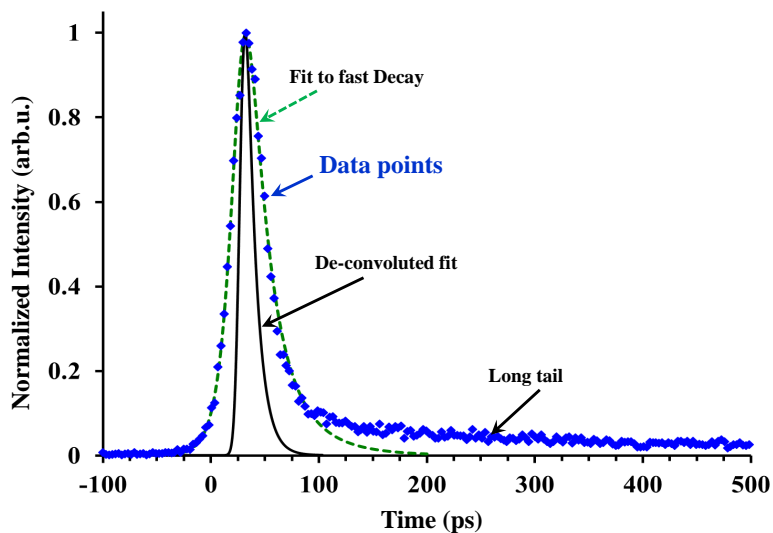


Figure 3.8: Spatially integrated emission of the nitrogen cation at 391 nm. The fitted function (Equation 3.1) to the fast decay section of the raw data is represented by the green dashed line, and the de-convoluted data is represented by a black line.

the reflected pulse from the diffuser have similar shapes, but the Rayleigh scattering has slightly smaller FWHM (Fig. 3.7) and consequently, the Rayleigh scattering pulse can be used to de-convolute the raw data and extract the true temporal profile of the fluorescence. A code in Matlab has been used to do the de-convolution process. The raw data has a long decay tail. In order to increase the precision of the Fast Fourier Transform (FFT), a custom function has been fitted to the fast decay section of raw data points using Origin:

$$\frac{1}{c \left[e^{(\sqrt{t-t_1})/T_1} + e^{(-t_2-t)/T_2} \right]} \quad (3.1)$$

where $t_1, t_2, T_1, T_2,$ and C are fitting constants. Fitting of the 391 nm emission is taken as an example in Fig. 3.8. The fitted function to the fast decay section of the raw data is represented by the green dashed line, and the de-convoluted data is represented by a black line. The same function, with different constants, has been used to deconvolute all the emission lines.

3.3.2 Time resolved measurements in selected spectral bands

We characterize the emission in three different spectral regions, selected by appropriate combination of filters: 391 ± 1 nm (corresponding to the $B^2\Sigma_u^+(\nu = 0) \rightarrow X^2\Sigma_g^+(\nu = 0)$ transition), 428 ± 1 nm (corresponding to the $B^2\Sigma_u^+(\nu = 0) \rightarrow X^2\Sigma_g^+(\nu = 1)$ transition), and $1\mu m > \lambda > 750$ nm that covers X to A transition. The time delay associated with each filter is accounted for. Note that the individual rotational transitions cannot be resolved.

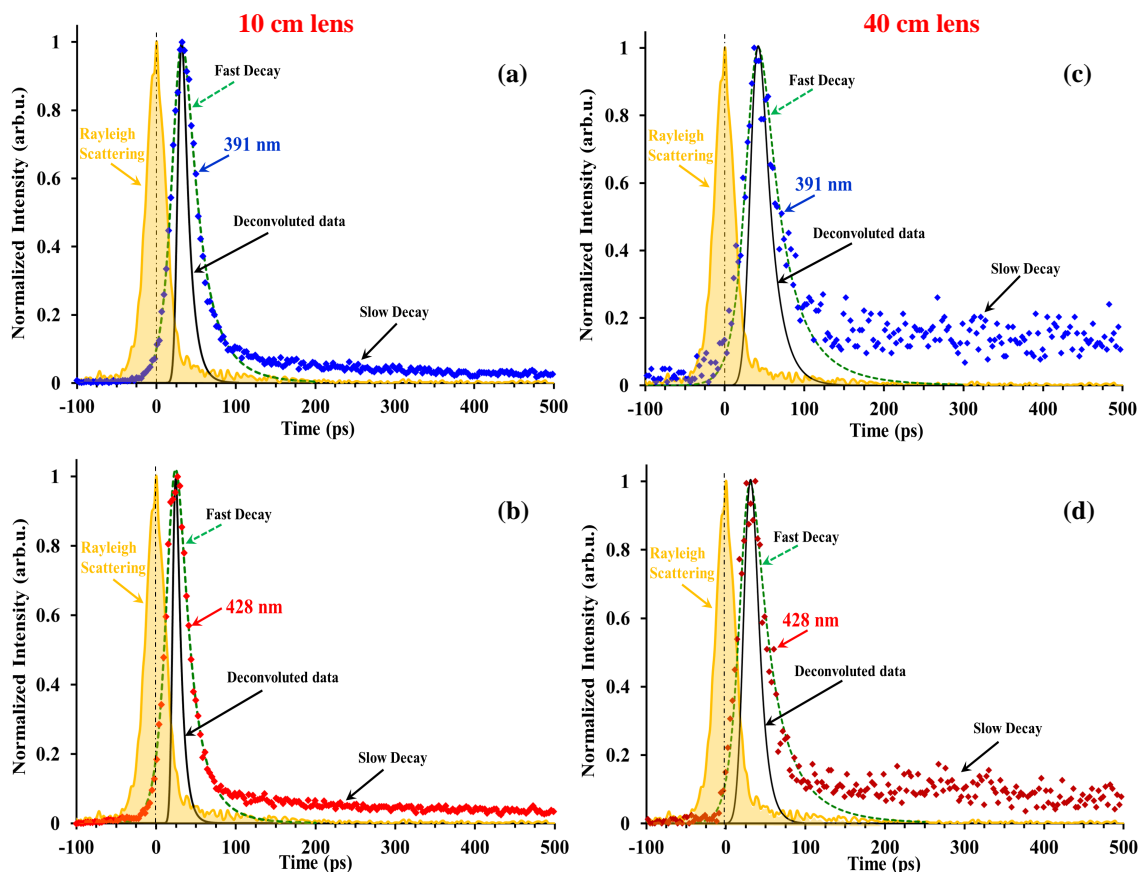


Figure 3.9: Spatially integrated emission versus time. (a) and (b) show the normalized emission of the nitrogen cation at 391 nm (a) and at 428 nm (b), respectively for the case of focusing with a 10 cm lens. (c) and (d) show the normalized emission of the nitrogen cation at 391 nm (c) and at 428 nm (d), respectively for the case of focusing with a 40 cm lens. The dashed line indicates the center of gravity of the yellow reference, which is the Rayleigh scattering measured separately at low power as shown in Fig. 3.7(a). The raw data for both 391 nm 428 nm cases are shown in blue and red respectively. The green dotted curve is the fit to data in proximity of the peak. The de-convoluted fast decaying emissions of 391 and 428 are calculated using the instrument response function of the Rayleigh scattering of the femtosecond pulse shown with black curve. There are two time constants for the ion emission known as “fast” and “slow” decay [25, 36].

Chapter 3. Measurement of delayed fluorescence in N_2^+ with a streak camera

The time dependence of the emission (integrated in space) of the plasma created by a focused 1 mJ pulse, is presented in the plots of Fig. 3.9 for both case of focusing with 10 cm and 40 cm lenses. The origin $t = 0$ is defined as the time of the Rayleigh scattering. Both raw and de-convoluted temporal emission profiles are plotted. The de-convoluted emission lines exhibit characteristic delays of 33 ± 0.3 ps at 391 nm (Fig.3.9(a)) and 25 ± 0.3 ps for 428 nm (Fig.3.9(b)) for 10 cm focusing lens, and 42 ± 0.3 ps at 391 nm (Fig.3.9(c)) and 31 ± 0.3 ps for 428 nm (Fig.3.9(d)) for 40 cm focusing lens. These delay times have been summarized in Table 3.10. Streak camera measurements performed with different experimental techniques that are made along the filament report a 5 ps delay between excitation and emission, which they attribute to the narrowness of the emission line [37]. In side emission measurements performed with streak camera by others, the emission is seen to start at the same time as the excitation [36, 38]. Unlike the Rayleigh

Wavelength (nm)	10 cm		40 cm	
	Delay (ps)	Width (ps)	Delay (ps)	Width (ps)
391	33	14	42	28
428	25	10	31	22

Figure 3.10: Table summarising delay times and fast decay times for 391 nm and 428 nm emissions for both focusing case.

scattering the emission profiles are asymmetric and two decay regimes are present in them; a “fast” decay regime, which is followed by a “slow” exponentially decaying tail. They exhibit short temporal widths of 14 ± 0.5 ps at 391 nm and 10 ± 0.5 ps at 428 nm in case of focusing with 10 cm lens and 28 ± 0.5 ps at 391 nm and 22 ± 0.5 ps at 428 nm for focusing with a 40 cm lens for the fast decay regime. These decay times have been summarized in table 3.10. De-convolution of time dependent signals requires an accurate knowledge of the instrument response function. Estimating a 5% accuracy in the Rayleigh signal, we calculate that a 5% increase in the instrument response changes the fast decay

Chapter 3. Measurement of delayed fluorescence in N_2^+ with a streak camera

of the 391 and 428 nm signals by 0.5 ps, leaving the rise time of the emission unchanged. The position of the peak is unchanged, confirming that the de-convolution process does not affect the time delay. To estimate the precision in the delay measurement, we take as error bar for the delay the width of the de-convoluted signal at 1% from its peak, or ± 0.3 ps. Using a streak camera "fast" and "slow" decays for the 391 nm emissions at much

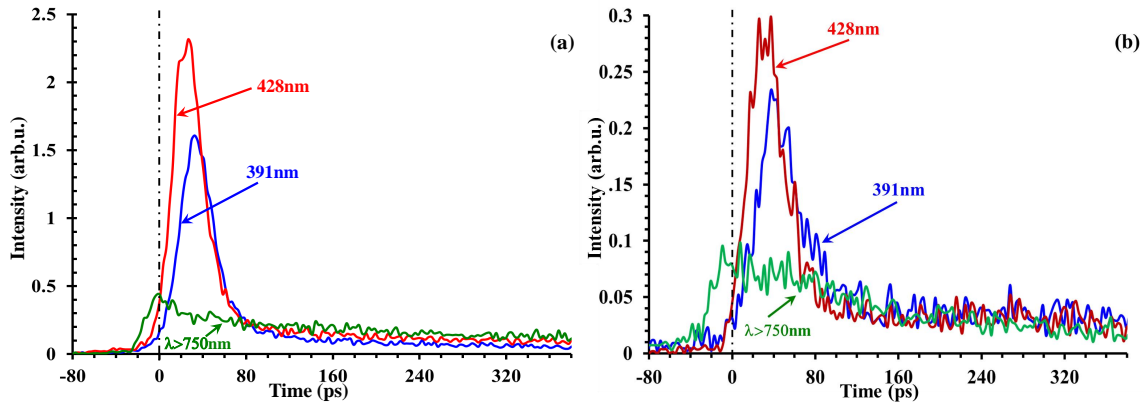


Figure 3.11: The 391 nm and 428 nm emission and broadband IR emission ($\lambda > 750$ nm) are plotted without normalization for focusing with 10 cm (a) and 40 cm (b). There are two time constants for the ion emission known as "fast" and "slow" decay [25, 36].

lower than atmospheric pressures have been observed [36]. In [36] the authors claim that the "fast" decay originates from the collision between the N_2^+ and free electrons. In this paper we have investigated simultaneously both the delay times between the ionizing laser filament and emissions, and the decay dynamics, which leads to a better understanding of the underlying phenomenon. As it is discussed in details below we believe that our observations suggest the involvement of Dicke superfluorescence [39] rather than attributing the delay to the narrowness of the emission line [37] or invoking the role of electron-cation collisions in fast decay mechanism [36].

Infrared emission at $\lambda > 750$ nm (green curve) is plotted in Fig. 3.11 for both cases of focusing with a 10 cm lens (a) and focusing with a 40 cm lens (b). The infrared emission has zero delay with respect to the Rayleigh scattering and decays exponentially with a time

Chapter 3. Measurement of delayed fluorescence in N_2^+ with a streak camera

constant of about 700 ps for both cases. It has a similar decay behavior as seen in both 391 and 428 nm emission profiles, suggesting the involvement of the A state in the dynamics [18]. The population exchange between X and A states affects the gain at the B to X transition wavelength. Such a long exponential tail has to be associated with N_2^+ , since it is not observed at low intensity as shown in Fig. 3.7(a). We can estimate this slow decay assuming it arises from population decay due to electron-cation collisions as $1/\rho v \sigma$, where ρ is the density of emitting dipoles, v is the velocity of electrons and σ is the collision cross section. $\rho = 0.01\rho_{air}$ based on an intensity of $\approx 10^{14}$ Watt/cm² [29–31] which yields an ionization rate [40] of one percent. The average energy of released electrons is 0.1 eV with the total electron cross section [41] of 5×10^{-16} cm². This yields a decay time of 700 picoseconds, in good agreement with the slow decay of the measured ion emission as well as the infrared emission in Fig. 3.9.

The concept of superradiance was first introduced in 1954 by Dicke [39]. Superradiance is a phenomenon of collective emission of a group of excited atoms, molecules or ions. The concept of superradiance can be understood by picturing each atom as a tiny antenna emitting electromagnetic waves. Excited atoms/molecules emit light randomly, and the emitted intensity is a function of the number of atoms/molecules, N . However, when the atomic “antennas” are coherently radiating in phase with each other, the net electromagnetic field is proportional to N , and therefore, the emitted intensity goes as N^2 . As a result, the atoms radiate their energy N times faster than for incoherent emission. It is this anomalous radiance that Dicke dubbed “superradiance” or “superfluorescence” [42]. For the impulsively excited dipoles to radiate in phase, there should be no dephasing collision between emitting ions between the instant of ionization and the peak emission. The length of the Dicke superradiant emission is limited by the mean free path between collisions, which, at atmospheric pressure, is of the order of the filament diameter. Dicke superradiance predicts that these delay and decay times should be inversely proportional to the number of dipole emitters involved in the emission [39, 43], which in turn is proportional to the time integral of the non-normalized emission profiles (Fig. 3.9). For the case of

Chapter 3. Measurement of delayed fluorescence in N_2^+ with a streak camera

focusing with a 10 cm lens, we find the ratio of the delay time for 391 nm emission to that of 428 nm to be 1.32 ± 0.02 , while the ratio of temporal widths is 1.4 ± 0.09 . Indeed, both these numbers are in close agreement with 1.4 ± 0.5 , the ratio of the number of emitters in the 428 nm to 391 nm emission profiles, obtained from their time integral. For the case of focusing with a 40 cm lens, we find the ratio of the delay time for 391 nm emission to that of 428 nm to be 1.35 ± 0.02 , while the ratio of temporal widths is 1.27 ± 0.09 . Both these numbers are in close agreement with 1.3 ± 0.5 the ratio of number of emitters in the 428 nm to 391 nm emission profiles, obtained from their time integral. Note that this collective emission does not require an inverted sample [44]. The higher gain of the 428 nm fluorescence can be due to higher inversion of the ($B^2\Sigma_u^+ \nu = 0 \rightarrow X^2\Sigma_g^+ \nu = 1$) transition due to unequal occupation of the $X^2\Sigma_g^+$ vibrational states following strong-field ionization [45].

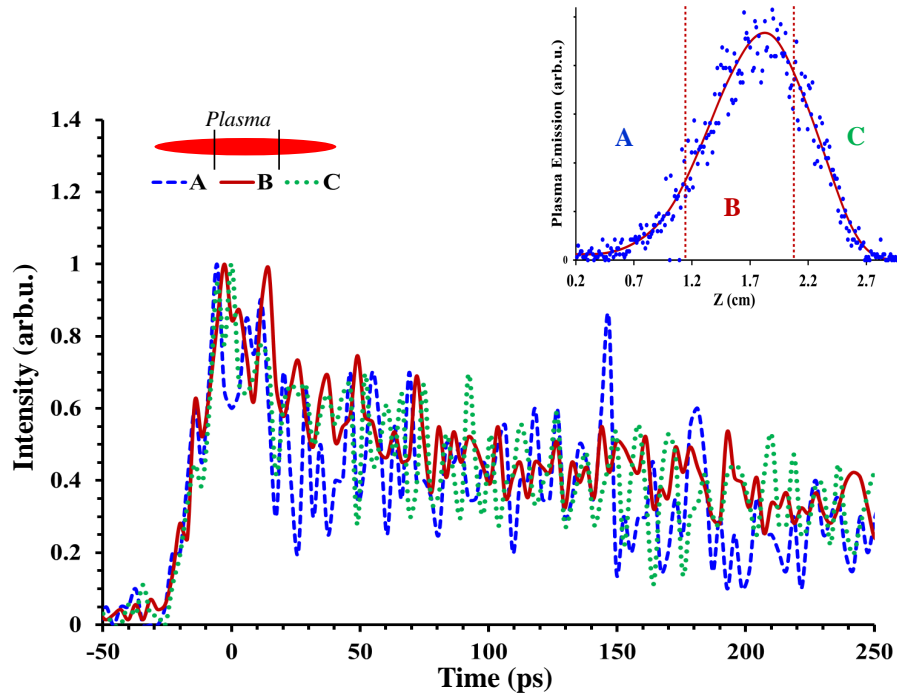


Figure 3.12: Normalized integrated IR emission from selected spatial regions of the plasma labeled as “A”, “B”, and “C” as shown in the legend. The inset shows the relative intensity along the filament for different slices.

Chapter 3. Measurement of delayed fluorescence in N_2^+ with a streak camera

In order to further investigate the collective contribution of emission, we analyze the spatial properties of the measured fluorescence. The emission is divided in three equal slices along the propagation direction as shown in the inset of Fig. 3.12. The emission is integrated in the radial direction over each section and plotted as a function of streak camera sweep. Fig. 3.12 shows the spectral emission with a long pass filter and the emission at 391 nm is represented in Fig. 3.13. The integrated signal in both IR and 391 nm is strongest in the central region of the plasma labeled as “B”, followed by “C” and “A”. The normalized emission in the IR shows that all regions have a comparable time dependent profile and no observable delay between regions could be measured in our system. IR emissions from the selected regions exhibit their maximum at the Rayleigh peak. However a measurable difference is recorded for the peak emission at 391 nm. The brightest region of the plasma has the least delay with respect to the Rayleigh peak, with a delay inversely proportional to the strength of the signal. The width of the emission increases as the total signal decreases. The 3 to 4.5 ps relative delay between emission originating from the center and sides of the plasma is much longer than the time it would take for light to travel between the sub-regions. We show that density of the emitters not only affect the strength of the signal but also the temporal profile of the emission. Altogether these observations suggest that it is important to include collective effects in modeling gain and propagation in air-lasing [15, 17, 46].

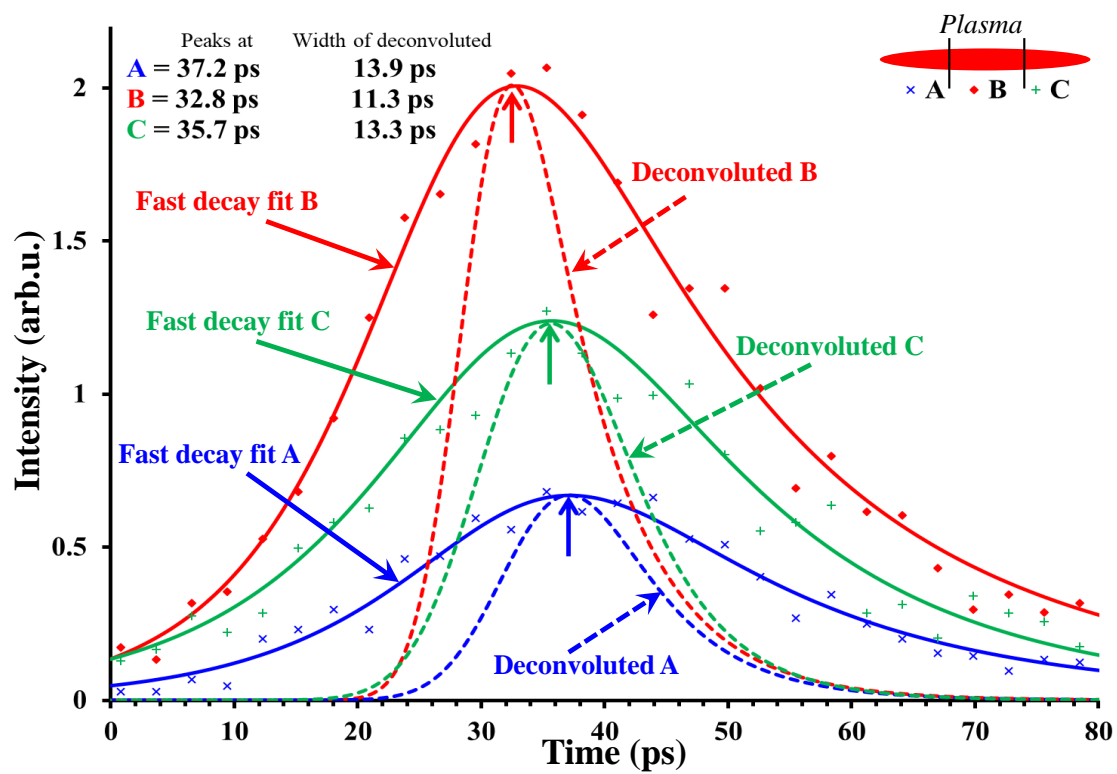


Figure 3.13: Comparing fast decay and built up time of the emission at 391 nm from the selected spatial regions of the plasma labeled as “A” , “B”, and “C” as shown in the legend.

3.4 Is 800 nm a "magic wavelength"?

It has been suggested that the fluorescence at 800 nm is associated with some resonance. To test this hypothesis, we investigate whether UV filaments at 266 nm lead also to fluorescence bands at 391 nm and 428 nm. Both 391 nm and 428 nm emissions have been detected from the side measurements of the UV filament. In Fig. 3.14 a schematic of the measurement setup is presented. UV laser pulses at 266 nm 200 ps in duration and 300 mJ energy [47, 48] are focused using a 3 m lens into the vacuum chamber connected to the aerodynamic window (Chapter 2). Measurements have been performed in both cases of operational and non-operational aerodynamic window. The side fluorescence emission was collected by an aspheric lens of 32 mm focal length. The collected light is then imaged on the entrance slit of a monochromator. To detect these emission bands it is necessary to use a high-gain Photo Multiplier Tube (PMT) at the exit slit of the monochromator due to the weak intensity of these emission lines. The PMT is connected to an oscilloscope in order to measure its output voltage which is proportional to the light intensity. The oscilloscope and the monochromator are connected to a Labview program that controls the wavelength scanning and also reads the voltage from the oscilloscope storing the data points on an Excel file. In Fig. 3.15 the results of some of the measurements for the mentioned two transitions are plotted. Each point in the plots is calculated by averaging 64 laser shots. The gain voltages for the detection of 391 nm and 428 nm emission were 1.480 kV. As it can be seen the presence of the aerodynamic window is not causing a significant change. For the 391 nm line, changing the polarization of the UV laser from linear to circular is not causing any change in the shape of the line, but, as expected, it is reducing the amplitude of the peak. The shapes of the lines are in general agreement with previously reported fluorescence emission lines of N_2^+ [3, 49, 50]. The monochromator's best achievable resolution was not sufficient to separate the rotational lines in the P and R branches of N_2^+ , hence only the envelope can be observed in the measurements [11, 49]. Measurement attempts with the high-resolution spectrometer *Demon* (Double Echelle MONochromator)

Chapter 3. Measurement of delayed fluorescence in N_2^+ with a streak camera

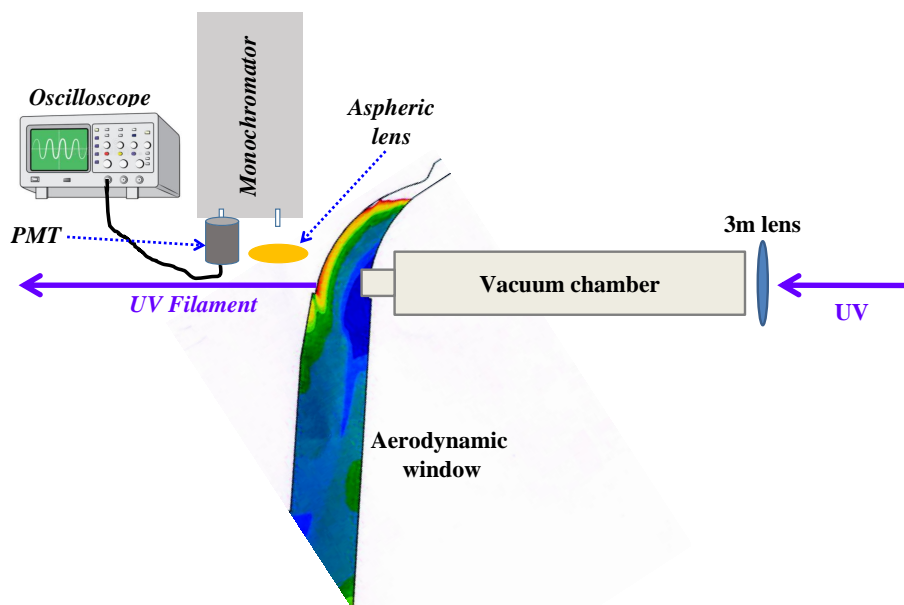


Figure 3.14: Schematic diagram of the setup for the detection of N_2^+ emissions induced by the UV filaments. UV laser pulses are focused using a 3 m lens into the vacuum chamber connected to the aerodynamic window. Measurements have been performed in both cases of the operational and non-operational aerodynamic window. The side fluorescence emission was collected by an aspheric lens with a focal length of 32 mm. The collected light is then imaged on the entrance slit of a monochromator. A high-gain Photo Multiplier Tube (PMT) is placed at the exit slit of the monochromator. The PMT is connected to an oscilloscope in order to measure its output voltage which is proportional to the light intensity.

were performed, but due to loss of intensity when coupling the scattered light into the input fiber of the *Demon* the experiments did not provide any results.

Measurements of the 391 nm emission along the Filament have been also performed. The results of these measurements are represented in Fig. 3.16. Scanning along the filament by moving all the detection parts was impractical. Instead the 3 m lens has been moved along the beam to scan the detection along the UV filament. Consequently, it was not possible to perform the measurement with the aerodynamic window being operational. The 3 m geometrical focal point of the lens is represented with a black dashed line in Fig. 3.16. The blue lines correspond to measurements in which 1.4 kV was the applied gain on the PMT. As the standard deviation on the intensity measurements at the

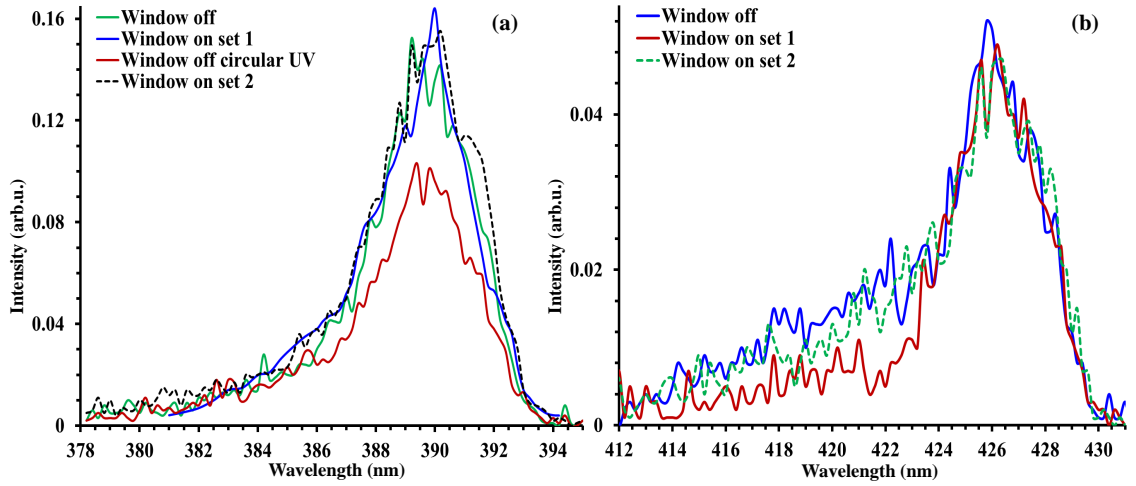


Figure 3.15: The 391 nm (a) and 428 nm (b) emission lines for a UV filament are plotted. Results for both cases of the operational and non-operational aerodynamic window are plotted. Each point in the plots is calculated by averaging 64 laser shots. The gain voltages for the detection of 391 nm and 428 nm emission were 1.480 kV. The monochromator's best achievable resolution was not enough to separate the rotational bands (P and R branches) of N_2^+ , hence only the envelope can be observed in the measurements. The general shape of the envelopes are in general agreement with previously reported fluorescence emission lines of N_2^+ [3, 49, 50].

beginning and the end of the scan range for this gain was too high, measurements in these respective positions were repeated with a higher gain of 1.7 kV applied to the PMT which is plotted in red in Fig. 3.16. The maximum gain applicable to the PMT is 1.85 kV, and in that case, the signal was present up to 50 cm from one end and 160 cm on the other end of the scanning distance, but the signal was really noisy with a big standard deviation. As expected the maximum intensity of the 391 nm emission is measured at the geometrical focus of the 3 m lens.

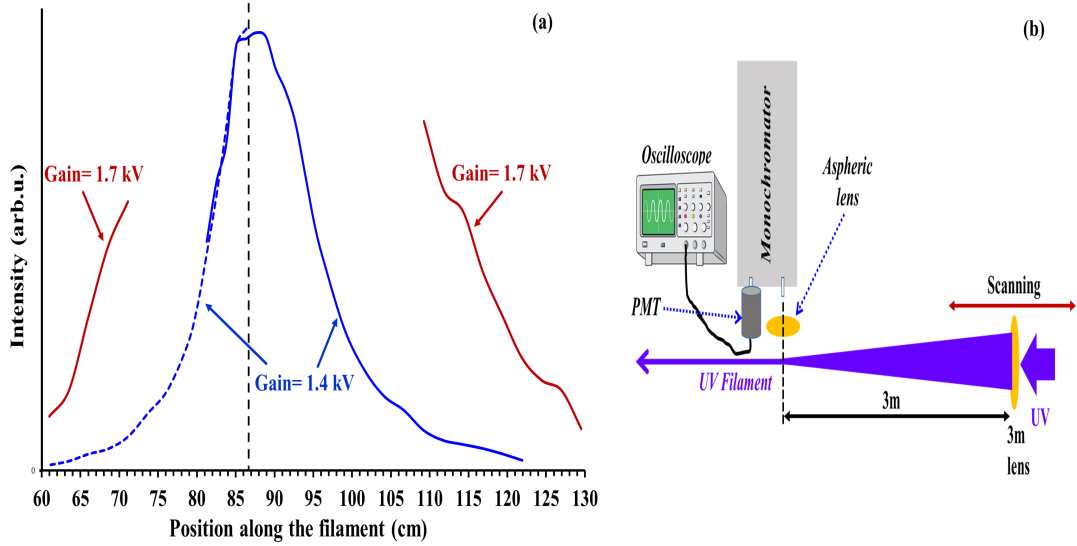


Figure 3.16: The intensity of the 391 nm emission line along the UV filament is measured. The 3 m geometrical focal point of the lens is represented with a black dashed line. In (a) The blue lines correspond to measurements in which 1.4 kV was the applied gain on the PMT. As the standard deviation on the intensity measurements at the beginning and the end of the scan range for this gain was too high, measurements in these respective positions were repeated with a higher gain of 1.7 kV applied to the PMT which is plotted in red. (b) Schematics of the experimental setup.

3.5 Conclusion

Our unique capability of sub-picosecond timing resolution along with absolute timing measurement using the Rayleigh scattering enables us to report accurate measurement in timing and temporal profile of the emission from ($B^2\Sigma_u^+$) to ($X^2\Sigma_g^+ \nu = 0 \ \& \ \nu = 1$) in N_2^+ . It has been observed that these emissions have a delay with respect to the ionizing laser filament. Our study suggests that the fast decay and high peak gain observed in air lasing is due to collective emission introduced by Dicke in 1954 [39]. The temporal behavior of the pulse as a function of density agrees with the predictions of superfluorescence [43, 51]. The presence of a long tail emission at infrared wavelength with no observable delay with respect to the initial pulse suggests the influence of X to A coupling in air lasing. We emphasize that we observe this superfluorescence in the air under ambient

Chapter 3. Measurement of delayed fluorescence in N_2^+ with a streak camera

conditions, making it suitable for practical applications. Our study suggests that collective emission and spatial distribution of the plasma needs to be considered for applications in remote source design using N_2^+ as a gain medium.

Our unique home build UV laser system made it possible to investigate the emission from ($B^2\Sigma_u^+$) to ($X^2\Sigma_g^+ \nu = 0$ & $\nu = 1$) in N_2^+ induced by UV filaments. We concluded that both 391 nm and 428 nm emission lines are present in side measurements. Due to low resolution it was not possible to resolve the rotational bands (P and R branches) of N_2^+ , hence only the envelope can be observed in the measurements. The general shape of the envelopes are in general agreement with previously reported fluorescence emission lines of N_2^+ .

3.6 Future work

A more comprehensive investigation on air lasing induced by UV filaments should be performed. A pump-probe study on the UV filament induced 391 nm and 428 nm fluorescence could be beneficial to investigate the gain mechanism and compare the results with the case of 800 nm filaments [11]. To further investigate the gain mechanism in the case of the UV filaments it is beneficial to perform pump-probe experiments for different air pressures, as it has been shown that the gain has dependencies on the pressure. A new experiment including a streak camera should be performed in which the absolute time measurements for N_2^+ emissions with respect to both 266 nm and 800 nm laser filaments can be performed. With the development of the new 800 nm regen (section 2.6), the effect of the repetition rate of the 800 nm filament on the timing of the 391 nm and 428 nm emission could be also investigated.

References

Acknowledgement

This research has been supported by the Army Research Office (W911NF-19-1-0272), and the Air Force Research Laboratory (FA9451-15-1-0039).

References

- [1] Q. Luo, W. Liu, and S.L. Chin. Lasing action in air induced by ultra-fast laser filamentation. *Applied Physics B*, 76(3):337–340, Mar 2003.
- [2] Helong Li, Danwen Yao, Siqi Wang, Yao Fu, and Huailiang Xu. Air lasing: Phenomena and mechanisms. *Chinese Physics B*, 28(11):114204, nov 2019.
- [3] Jinping Yao, Bin Zeng, Huailiang Xu, Guihua Li, Wei Chu, Jielei Ni, Haisu Zhang, See Leang Chin, Ya Cheng, and Zhizhan Xu. High-brightness switchable multiwavelength remote laser in air. *Phys. Rev. A*, 84:051802, Nov 2011.
- [4] Tie-Jun Wang, Jingjing Ju, Jean-François Daigle, Shuai Yuan, Ruxin Li, and See Leang Chin. Self-seeded forward lasing action from a femtosecond ti:sapphire laser filament in air. *Laser Physics Letters*, 10(12):125401, oct 2013.
- [5] S. L. Chin, A. Talebpour, J. Yang, S. Petit, V. P. Kandidov, O. G. Kosareva, and M. P. Tamarov. Filamentation of femtosecond laser pulses in turbulent air. *Applied Physics Letters*, B74:67–76, 2002.
- [6] R. Salamé, N. Lascoux, E. Salmon, R. Ackermann, J. Kasparian, and J.-P. Wolf. Propagation of laser filaments through an extended turbulent region. *Appl. Phys. Lett.*, 91:171106, 2007.
- [7] Philip R. Hemmer, Richard B. Miles, Pavel Polynkin, Torsten Siebert, Alexei V. Sokolov, Phillip Sprangle, and Marlan O. Scully. Standoff spectroscopy via remote generation of a backward-propagating laser beam. *Proceedings of the National Academy of Sciences*, 108(8):3130–3134, 2011.
- [8] Ali Rastegari, Matthias Lenzner, Jean-Claude Diels, Kristen Peterson, and Ladan Arissian. High-resolution remote spectroscopy and plasma dynamics induced with UV filaments. *Opt. Lett.*, 44(1):147–150, Jan 2019.
- [9] Pengji Ding, Sergey Mitryukovskiy, Aurélien Houard, Eduardo Oliva, Arnaud Couairon, André Mysyrowicz, and Yi Liu. Backward lasing of air plasma pumped by

References

- circularly polarized femtosecond pulses for the sake of remote sensing (black). *Opt. Express*, 22(24):29964–29977, Dec 2014.
- [10] P. N. Malevich, D. Kartashov, Z. Pu, S. Ališauskas, A. Pugžlys, A. Baltuška, L. Giniūnas, R. Danielius, A. A. Lanin, A. M. Zheltikov, M. Marangoni, and G. Cerullo. Ultrafast-laser-induced backward stimulated raman scattering for tracing atmospheric gases. *Opt. Express*, 20(17):18784–18794, Aug 2012.
- [11] Ladan Arissian, Brian Kamer, Ali Rastegari, D. M. Villeneuve, and Jean-Claude Diels. Transient gain from N_2^+ in light filaments. *Phys. Rev. A*, 98:053438, Nov 2018.
- [12] Jinping Yao, Guihua Li, Chenrui Jing, Bin Zeng, Wei Chu, Jielei Ni, Haisu Zhang, Hongqiang Xie, Chaojin Zhang, Helong Li, Huailiang Xu, See Leang Chin, Ya Cheng, and Zhizhan Xu. Remote creation of coherent emissions in air with two-color ultrafast laser pulses. *New Journal of Physics*, 15(2):023046, feb 2013.
- [13] Guihua Li, Chenrui Jing, Bin Zeng, Hongqiang Xie, Jinping Yao, Wei Chu, Jielei Ni, Haisu Zhang, Huailiang Xu, Ya Cheng, and Zhizhan Xu. Signature of superradiance from a nitrogen-gas plasma channel produced by strong-field ionization. *Phys. Rev. A*, 89:033833, Mar 2014.
- [14] R.F. Wuerker, L. Schmitz, T. Fukuchi, and P. Straus. Lifetime measurements of the excited states of N_2 and N_2^+ by laser-induced fluorescence. *Chemical Physics Letters*, 150(6):443 – 446, 1988.
- [15] Ali Rastegari, Jean-Claude Diels, Brian Kamer, Lee R. Liu, and Ladan Arissian. Measurement of delayed fluorescence in N_2^+ with a streak camera. *Opt. Express*, 30(17):31498–31508, Aug 2022.
- [16] Ali Rastegari, Brian Kamer, Jean Claude Diels, and Ladan Arissian. Spatio-temporal measurement of super-fluorescence from light filaments in air. In *Conference on Lasers and Electro-Optics*, page FF2C.4. Optica Publishing Group, 2020.
- [17] Ali Rastegari and Jean-Claude Diels. Investigation of the dynamics of the emission from the N_2^+ cation in light filaments. In *Frontiers in Optics + Laser Science AP-S/DLS*, page JTU3A.35. Optica Publishing Group, 2019.
- [18] H.L. Xu, E. Lötstedt, A. Iwasaki, and K. Yamanouchi. Sub-10-fs population inversion in N_2^+ in air lasing through multiple state coupling. *Nature Communications*, 6:8347, 2015.
- [19] D. Kartashov, S. Haessler, S. Ališauskas, G. Andriukaitis, A. Pugžlys, A. Baltuška, J. Möhring, D. Starukhin, M. Motzkus, A.M. Zheltikov, M. Richter, F. Morales,

References

- O. Smirnova, M. Yu. Ivanov, and M. Spanner. Transient inversion in rotationally aligned nitrogen ions in a femtosecond filament. In *Research in Optical Sciences*, page HTh4B.5. Optical Society of America, 2014.
- [20] A. Mysyrowicz, R. Danylo, A. Houard, V. Tikhonchuk, X. Zhang, Z. Fan, Q. Liang, S. Zhuang, L. Yuan, and Y. Liu. Lasing without inversion in N_2^+ . *APL Photonics*, 4:110807, Aug 2019.
- [21] Yi Liu, Pengji Ding, Guillaume Lambert, Aurélien Houard, Vladimir Tikhonchuk, and André Mysyrowicz. Recollision-induced superradiance of ionized nitrogen molecules. *Phys. Rev. Lett.*, 115:133203, Sep 2015.
- [22] Ali Azarm, Paul Corkum, and Pavel Polynkin. Optical gain in rotationally excited nitrogen molecular ions. *Phys. Rev. A*, 96:051401, Nov 2017.
- [23] B. Kamer, A. Rastegari, M. Rasoulof, and L. Arissian. Nitrogen laser guide star using four wave mixing. In *Conference on Lasers and Electro-Optics*, page JTh2A.80. Optica Publishing Group, 2017.
- [24] Mathew Britton, Patrick Laferrière, Dong Hyuk Ko, Zhengyan Li, Fanqi Kong, Graham Brown, Andrei Naumov, Chunmei Zhang, Ladan Arissian, and P. B. Corkum. Testing the role of recollision in N_2^+ air lasing. *Phys. Rev. Lett.*, 120:133208, Mar 2018.
- [25] Mathew Britton, Marianna Lytova, Patrick Laferrière, Peng Peng, Felipe Morales, Dong Hyuk Ko, Maria Richter, Pavel Polynkin, D. M. Villeneuve, Chunmei Zhang, Misha Ivanov, Michael Spanner, Ladan Arissian, and P. B. Corkum. Short- and long-term gain dynamics in N_2^+ air lasing. *Phys. Rev. A*, 100(4):013406, 2019.
- [26] Hamamtsu. Guide to streak cameras, 2008.
- [27] Harries Muthurajan, Teo Zihao, Robbin Poh Chen Tien, and Ang How Ghee. Simultaneous Streak and Framing imaging for performance evaluation of Composition C-4. In *37th International Pyrotechnic Seminar (EUROPYRO 2011)*. IPS, 2011.
- [28] J Saarela, M Tormanen, and R Myllyla. Three methods for photon migration measurements in pulp. *Optoelectronics Review*, 12(2):193–198, 2004.
- [29] Francis Théberge, Weiwei Liu, Patrick Tr. Simard, Andreas Becker, and See Leang Chin. Plasma density inside a femtosecond laser filament in air: Strong dependence on external focusing. *Phys. Rev. E*, 74:036406, Sep 2006.
- [30] Sergey Mitryukovskiy, Yi Liu, Pengji Ding, Aurélien Houard, and André Mysyrowicz. Backward stimulated radiation from filaments in nitrogen gas and air pumped by

References

- circularly polarized 800 nm femtosecond laser pulses. *Opt. Express*, 22(11):12750–12759, Jun 2014.
- [31] Sergey I Mitryukovskiy, Yi Liu, Aurélien Houard, and André Mysyrowicz. Re-evaluation of the peak intensity inside a femtosecond laser filament in air. *Journal of Physics B: Atomic, Molecular and Optical Physics*, 48(9):094003, apr 2015.
- [32] Andreas Velten, Andreas Schmitt-Sody, Jean-Claude Diels, Shermineh Rostami, Amin Rasoulof, Chengyong Feng, and Ladan Arissian. Videos of light filamentation in air. *Journal of Physics B: Atomic, Molecular and Optical Physics*, 48(9):094020, apr 2015.
- [33] H. C. Bryant and N. Jarmie. The Glory. *Scientific American*, 231:60–71, 1974.
- [34] E. G. Steward. *Fourier optics : an introduction*. Ellis Horwood series in physics. E. Horwood, 1983.
- [35] Joseph W. Goodman. *Introduction to Fourier Optics*. Goodman. Roberts & Co., 3rd edition, 2005.
- [36] Mingwei Lei, Chengyin Wu, Qingqing Liang, An Zhang, Yu Li, Qian Cheng, Shufeng Wang, Hong Yang, Qihuang Gong, and Hongbing Jiang. The fast decay of ionized nitrogen molecules in laser filamentation investigated by a picosecond streak camera. *Journal of Physics B: Atomic, Molecular and Optical Physics*, 50(14):145101, jun 2017.
- [37] N.G. Ivanov, I.A. Zyatikov, V.F. Losev, and V.E. Prokop’ev. Temporal behavior of air lasing by molecular nitrogen ions. *Optics Communications*, 456:124573, 2020.
- [38] N.G. Ivanov, V.F. Losev, V.E. Prokop’ev, K.A. Sitnik, and I.A. Zyatikov. High time-resolved spectroscopy of filament plasma in air. *Optics Communications*, 431:120–125, 2019.
- [39] R. H. Dicke. Coherence in spontaneous radiation processes. *Phys. Rev*, 93(1):99–110, 1954.
- [40] N. B. Delone and V. P. Krainov. Energy and angular electron spectra for the tunnel ionization of atoms by strong low-frequency radiation. *J. Opt. Soc. Am. B*, 8(6):1207–1211, Jun 1991.
- [41] Yukikazu Itikawa. Cross sections for electron collisions with nitrogen molecules. *Journal of Physical and Chemical Reference Data*, 35(1):31, 2006.
- [42] Marlan O. Scully and Anatoly A. Svidzinsky. The super of superradiance. *Science*, 325(5947):1510–1511, 2009.

References

- [43] Mitsuru Nagasono, James R. Harries, Hiroshi Iwayama, Tadashi Togashi, Kensuke Tono, Makina Yabashi, Yasunori Senba, Haruhiko Ohashi, Tetsuya Ishikawa, and Eiji Shigemasa. Observation of free-electron-laser-induced collective spontaneous emission (superfluorescence). *Phys. Rev. Lett.*, 107:193603, Nov 2011.
- [44] N. E. Nefedkin, E. S. Andrianov, A. A. Zyablovsky, A. A. Pukhov, A. P. Vinogradov, and A. A. Lisiansky. Superradiance of non-dicke states. *Opt. Express*, 25(3):2790–2804, Feb 2017.
- [45] Thomas K. Kjeldsen and Lars Bojer. Vibrational excitation of diatomic molecular ions in strong field ionization of diatomic molecules. *Phys. Rev. Lett.*, 95:073004, Aug 2005.
- [46] Ali Rastegari, Brian Kamer, Jean Claude Diels, and Ladan Arissian. Spatio-temporal measurement of super-fluorescence from light filaments in air. In *Conference on Lasers and Electro-Optics*, page FF2C.4. Optica Publishing Group, 2020.
- [47] Chengyong Feng, Xiaozhen Xu, and Jean-Claude Diels. Generation of 300 ps laser pulse with 1.2 J energy by stimulated Brillouin scattering in water at 532 nm. *Opt. Lett.*, 39(12):3367–3370, 2014.
- [48] Ali Rastegari and Jean-Claude Diels. Investigation of UV filaments and their applications. *APL Photonics*, 6(6):060803, 2021.
- [49] Rao S. Mangina, Joseph M. Ajello, Robert A. West, and Dariusz Dziczek. HIGH-RESOLUTION ELECTRON-IMPACT EMISSION SPECTRA AND VIBRATIONAL EMISSION CROSS SECTIONS FROM 330–1100 nm FOR n₂. *The Astrophysical Journal Supplement Series*, 196(1):13, sep 2011.
- [50] Pengxu Ran, Genggeng Li, Tao Liu, Huaming Hou, and Sheng nian Luo. Collision-mediated ultrafast decay of n₂ fluorescence during fs-laser-induced filamentation. *Opt. Express*, 27(14):19177–19187, Jul 2019.
- [51] Guihua Li, Chenrui Jing, Bin Zeng, Hongqiang Xie, Jinping Yao, Wei Chu, Jielei Ni, Haisu Zhang, Huailiang Xu, Ya Cheng, and Zhizhan Xu. Signature of superradiance from a nitrogen-gas plasma channel produced by strong-field ionization. *Phys. Rev. A*, 89:033833, Mar 2014.

Chapter 4

High-resolution spectroscopy and plasma dynamics induced with UV filaments

4.1 Introduction

Laser-Induced Breakdown Spectroscopy (LIBS) is an analytical spectroscopic technique that uses a high-energy laser pulse to create a plasma on the surface of a sample. LIBS has found a broad range of applications in various fields, including space exploration [1], archaeological science [2], environmental monitoring [3], medical diagnosis [4,5], industrial process analysis [6,7], geological exploration [8,9], and remote sensing [10]. In LIBS, a pulsed laser beam is focused on the surface of a sample to create a plasma plume. While typical pulse durations were on the order of nanoseconds, the use of pico- and femtosecond laser pulses has become increasingly prevalent in recent years. The laser pulse heats and vaporizes a small amount of the material, and the resulting plasma contains a mixture of atoms, ions, and free electrons. As the plasma cools, the atoms and ions emit light

Chapter 4. High-resolution spectroscopy induced with UV filaments

which is collected and analyzed by a spectrometer. Each element in the sample emits a unique set of spectral lines or atomic emission lines, which correspond to specific electronic transitions within the atom. The spectral lines are characteristic of the element, and their intensities are proportional to the concentration of the element in the sample. By analyzing the spectral lines, the elemental composition of the sample can be determined. The resulting emission spectra can be used to determine the elemental composition and relative concentrations of the sample [11–13].

A schematic of the laser-induced breakdown process is demonstrated in Fig.4.1 (Left). Firstly, a short laser pulse is directed at the sample surface, and the energy of the beam is absorbed by atoms and molecules of the specimen, causing the vaporization or ablation of a small amount of the material. This process creates a vapor plume above the surface of the sample which is going to be developed into a high-temperature plasma. In the case of LIBS with ns laser pulses, the plasma is created in the first hundreds of ps, and the latter part of the pulse will heat the plasma through the inverse Bremsstrahlung process. In the early stage of plasma expansion, the plume behaves like a supersonic piston, creating an external shock-wave that propagates outward through the ambient gas. As the plasma starts to cool down, it emits light from their excited states due to the spontaneous emission of excited atoms and/or ions. Finally, an optic is used to collect the emitted light, and a spectrometer is used to disperse the light into its constituent wavelengths. The resulting atomic emission peaks in the spectrum can be analyzed quantitatively to identify the elemental constituents of the sample and their relative concentrations. [13–15]

LIBS has several advantages over other analytical techniques, such as its ability to perform in situ analysis without sample preparation, and fast analysis time, with results obtained within a few seconds. LIBS is capable of analyzing a wide range of materials, including solids, liquids, and gases, and can detect most elements in the periodic table. LIBS has a unique advantage in its sensitivity to light elements that are difficult to detect using other spectroscopic techniques. In addition, LIBS is capable of simultaneous multi-

elemental analysis, allowing for comprehensive sample analysis in a single measurement. Furthermore, LIBS is non-destructive and requires only minimal material. [13, 16, 17].

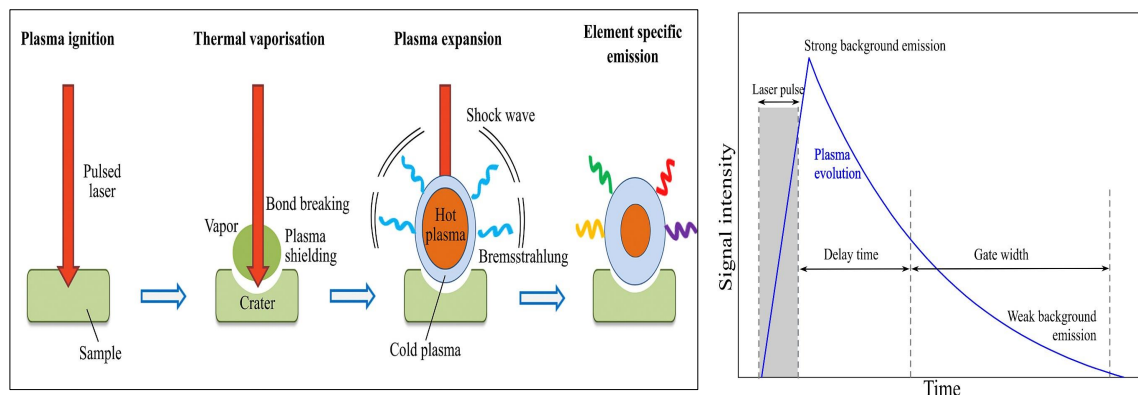


Figure 4.1: Left) Schematic of the laser-induced breakdown process (from [14]). Right) Schematics illustrating the plasma evolution in time, in which the timing of the laser pulse, the intensity of background radiation, delay time, and gate width have been depicted (from [18]).

In Laser-Induced Breakdown Spectroscopy (LIBS), time delay and gate width are important parameters used to control the temporal resolution of the spectral measurements. Time delay refers to the time interval between the laser pulse and the start of the gate, which determines when the spectral measurement begins. Gate width refers to the duration of the gate, which determines the length of time over which the spectral measurement is taken. These two parameters are represented in Fig. 4.1(Right). By adjusting the time delay and gate width, it is possible to optimize the temporal resolution and maximize the accuracy and precision of the elemental analysis. In LIBS, choosing the optimal time delay and gate width requires considering the trade-off between temporal resolution and signal-to-noise ratio. A shorter time delay and gate width offer a higher temporal resolution, which is desirable for accurately determining plasma emission characteristics. However, this can result in a lower signal-to-noise ratio, which can make it challenging to detect and quantify spectral lines accurately. Conversely, a longer time delay and gate width improve the signal-to-noise ratio, making it easier to detect and quantify spectral lines accurately. However, this can come at the cost of reduced temporal resolution, which can

Chapter 4. High-resolution spectroscopy induced with UV filaments

make it harder to distinguish between closely spaced spectral lines. Ultimately, the choice of time delay and gate width should be based on the specific analytical requirements of the application [18, 19].

In Fig. 4.1(Right), there is a schematic representation of the temporal evolution of a LIBS plasma triggered by a single laser pulse. Initially, the plasma light is predominantly composed of a continuous spectrum emission, resulting from the Bremsstrahlung and recombination processes taking place within the plasma. Bremsstrahlung is caused by the acceleration or deceleration of electrons during collisions, leading to the emission of photons. Recombination occurs when a free electron is captured by an ionic or atomic energy level, releasing excess kinetic energy in the form of a photon. As the plasma gradually cools down, emission lines from ions, atoms, and molecules emerge. Integrating plasma emission over its entire evolution time can lead to significant interference of the continuum with the weaker transition emissions, making their detection difficult. Therefore, time-resolved detection is typically employed in LIBS measurements to mitigate this interference.

With the discovery of laser filamentation, researchers have investigated its applications in LIBS [12, 20, 21]. Laser filaments have the unique capability to travel across long distances without experiencing diffraction effects commonly seen during the propagation of nanosecond (ns) laser pulses. This allows for the efficient delivery of laser energy to the sample, even at long distances, without the need for complex optical arrangements to compensate for atmospheric turbulence [22]. Therefore, they have the potential to generate LIBS plumes at considerable standoff distances, providing a more robust and efficient approach for remote sensing applications compared to traditional LIBS methods, especially in challenging atmospheric conditions. Studies have shown that self-guided filaments, with diameters in the order of $100(s) \mu\text{m}$, can be created over distances ranging from hundreds of meters to kilometers¹ [23, 24]. These filaments can be employed

¹It should be mentioned that single laser filaments can not be extended over a few meters. On the other hand multiple filaments generated by very high power lasers, can disappear and reappear

in the detection and identification of various chemical and biological agents in the atmosphere, using LIDAR technology [21, 25, 26]. Also, compared to nanosecond (ns) laser pulses, femtosecond (fs) and picosecond (ps) laser filaments can generate plasma with a higher electron density and lower electron temperature which can lead to enhanced spectroscopic signals. Another advantage that laser filaments have over traditional lasers for LIBS applications is that they have higher precision of sample ablation and they create lower continuum background [20, 27, 28]. A detailed comparison of LIBS performed on lead samples with fs 800 nm filaments and ns pulses has been reported, demonstrating a better signal to noise with the former, because of the higher electron density and the lower plasma temperature [27]. It has been shown that spectral lines from an aluminum target at up to 60 m can be obtained with 800 nm filaments, of which the starting point has been postponed [29].

4.1.1 Self-absorption

Self-absorption occurs when the emitted radiation from the plasma is absorbed by the plasma itself, leading to a decrease in the intensity of the emitted spectral lines. Self-absorption typically affects the entire emission spectrum of a homogeneous laser-induced plasma when the plasma becomes optically thick. Conversely, when the plasma is optically thin, self-absorption is usually negligible. In the case of an inhomogeneous plasma a gradient in both plasma temperature and electron density is present. In fact, the outer layers of the plasma may have a lower temperature than the central region, as shown in Fig. 4.2(b). This results in a higher population of the lower energy level of the transition and therefore leads to strong absorption. Due to the lower electron number density in the outer layers compared to the plasma core, the absorption line profile is narrower than the emission profile, creating an absorption dip in emission line. The self-absorption dip

over very long distances [23]. Or by temporal manipulation of the laser pulses the starting point of laser filaments can be postponed to very large distances [24].

can be referred to as "self-reversal" in some literature. The self-absorption dips are more likely to be present at higher pressures including atmospheric pressures due to the greater confinement of the plasma. [11, 30–34]. An image of a typical spectrum of a uranium sample measured via our setup is illustrated in Fig. 4.2(a). The self-absorption dip is present for both uranium lines of 385.464 nm and 385.957 nm. The experiments were performed at atmospheric pressure with UV filaments created by 266 nm laser pulses of 200 ps duration and with energy of 105 mJ per pulse. The gate width is 500 ns, and the delay is 325 ns.

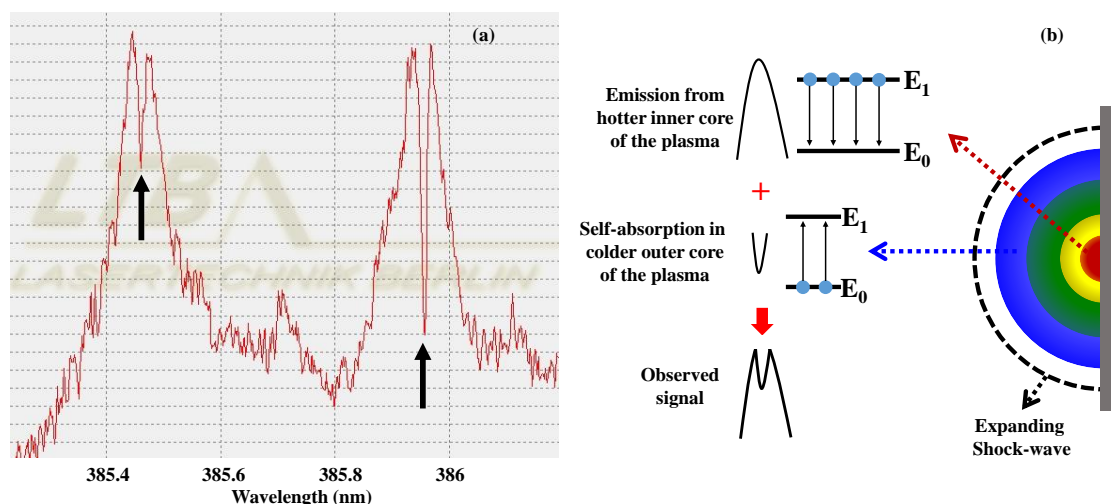


Figure 4.2: (a) An image of a typical spectrum of a uranium sample measured by *DEMON*. The self-absorption dip is present for both uranium lines of 385.464 nm and 385.957 nm. The experiments were performed with UV filaments created by 266 nm laser pulses of 200 ps duration and with energy of 105 mJ per pulse. The gate width is 500 ns, and the delay is 325 ns. (b) A schematic diagram showing the self-absorption mechanism. The temperature gradient is depicted, indicating a hot central region and a colder outer region (inspired by [31]).

Self-absorption is commonly regarded as an undesirable phenomenon in the literature on LIBS, as it distorts the emission lines. Numerous articles have been dedicated to mitigate its impact on the emission line [35–37]. There have been numerous publications attempting to determine the center of the emission line, correcting for the presence of the dip and the Stark shift. Such corrections were reported for the spectrum of

aluminum [31, 38–40] and in chromium [41]. To cite the abstract of a paper: "The self-absorption effect is one of the main bottlenecks for LIBS" [31]. It will be shown in this chapter that these dips are a blessing rather than a curse in high resolution plume spectroscopy.

4.2 Experimental Setup

As sketched in Fig. 4.3, a laser pulse is focused onto a solid target by a 40 cm plano-convex lens, creating a plume that is analyzed by the *DEMON* monochromator (by *Lasertechnik Berlin GmbH*). The *DEMON* is a high spectral resolution Double Echelle MONochromator. It consists of an optomechanically motorized echelle spectrometer in sequence with a prism monochromator that is used for the selection of the inspection range. The echelle grating, derived from the French word "échelle" which means "ladder," is a diffraction grating with a relatively lower groove density but a specialized groove shape that is optimized for high incidence angles and high diffraction orders. This design allows for greater dispersion (spacing) of spectral features at the detector, resulting in enhanced differentiation of these features [42, 43]. Time resolution is realized with a gated ICCD *Andor* camera to record the spectrum. The *Andor* ICCD is triggered by the same delay generator that is used as the master clock for the laser system. The Gate-width and time delay for the measurements were controlled by the ICCD camera. In most of the experiments, the optimum gate width of the *Andor* camera is chosen to be 500 ns as a compromise between the best signal to noise ratio versus the best time resolution. It should be mentioned that the delay times recorded from the ICCD camera needed to be corrected. The delay times reported in all the measurements are the delay time between the arrival of the UV filament on the sample and the time the spectra are measured².

²The earliest time that the UV laser was detectable by *DEMON* was at a delay time equal to 975 ns.

Chapter 4. High-resolution spectroscopy induced with UV filaments

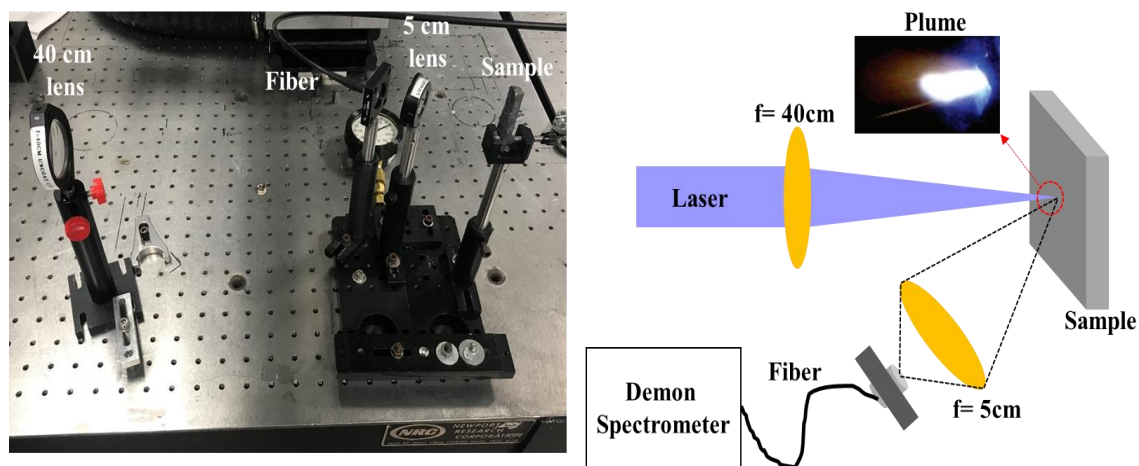


Figure 4.3: Right) Schematics of the LIBS setup. A photograph of the plume produced with natural uranium is shown on top. Different laser sources have been used for the LIBS experiments. Most of the experiments were performed with UV filaments created by 266 nm laser pulses of 200 ps duration and with energies up to 200 mJ. Other sources were: 1. Laser pulses at 1064 nm with 10 ns pulse width, 2. Laser pulses at 532 nm with 240 ps pulse width, and 3. IR filaments created by laser pulses at 800 nm with 50 fs pulse width with 1 mJ energy. The emitted light is collected with a 5 cm aspheric lens and coupled into a fiber. The spectrum is observed with a fiber coupled DEMON spectrometer. Left) The picture of the LIBS setup.

Each measurement is an average of 50-100 images with a spectral resolution of 6 pm at 300 nm to 8 pm at 400 nm. All the data are taken in air at atmospheric pressures (630 torr or 84 kPa at the altitude of Albuquerque, New Mexico). Different laser sources have been used for the LIBS experiments. Most of the experiments were performed with UV filaments created by 266 nm laser pulses of 200 ps duration and with energies up to 200 mJ [44,45]. Other sources were: 1. Laser pulses at 1064 nm with 10 ns pulse width [45], 2. Laser pulses at 532 nm with 240 ps pulse width [45], and 3. IR filaments created by laser pulses at 800 nm with 50 fs pulse width with 1 mJ energy. The best results were achieved with the UV filaments. The solid targets selected are lithium, aluminum, steel, uranium metal, copper, and strontium bromide ($SrBr_2$). In this chapter, the results of experiments including the first 4 elements are presented. Aluminum is selected to emphasize Stark shifts, steel to demonstrate spectral resolution between closely spaced lines, lithium to in-

investigate light atoms, and uranium to highlight the narrow spectral dip. Both the emission and re-absorption linewidths decrease with increasing atomic mass. The emission from the plume is collected with an aspheric lens with a focal length of 5 cm and a diameter of 1". The collected light is then coupled into a fiber which is connected to the spectrometer. It is known that in LIBS experiments on solid samples, the laser-induced crater depth strongly affects the measured signal. The confinement of the plume by the crater walls dramatically influences the laser-induced plasma parameters which will consequently affect the measured LIBS signals [46,47] To avoid this effect the sample holder was placed on a translation stage and was slightly moved after a certain number of shots. The number of shots before each movement was different depending on the sample.

4.3 Experimental Results

4.3.1 Wavelength dependence

The emission spectrum from an aluminum target irradiated by a standard Q-switched Nd:YAG laser pulses of 10 ns duration at 1064 nm and 500 mJ is compared to 266 nm filaments of 200 ps in Fig. 4.4. A small dip at the transition wavelength of 396.152 nm is due to self-absorption effect, where the emission of the excited region of the plume is absorbed by the plume region in the ground state. The time evolution of the two regions is discussed in Section 4.3.3. The self-absorption dip with 1064 nm source appears only after a delay of 5.5 μ s. The dip in emission spectrum is present even at the earliest delay using the 266 nm source. The shorter the delay, the larger the discrepancy between the peak of emission line and the transition wavelength, a discrepancy attributed to a plasma induced Stark shift [48] (see Section 4.3.3). The internal fields in the plasma decrease with the decaying plasma density, resulting in smaller Stark shift at larger delays. Several factors could contribute to the occurrence of self-absorption dips in UV filaments with

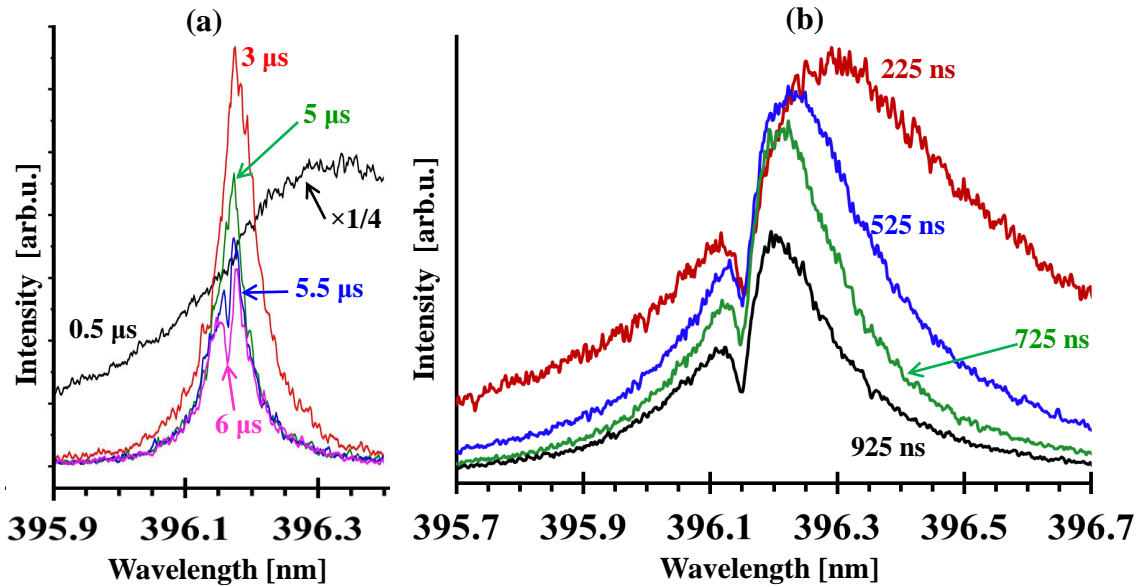


Figure 4.4: (a) The LIBS spectrum of aluminum (Transition from $3s^23p \ J = 3/2$ state to $3s^24s \ J = 1/2$ at 396.152 nm) using a 10 ns pulse at 1064 nm focused by a 40 cm lens is shown for gate delays of 3, 5, 5.5, and 6 μs . The first delay time of 0.5 μs shows the continuum emission rather than emission from the spectral line. The self absorption dip is only recognized at the latest gate delay. (b) LIBS spectrum taken with a 266 nm pulse of 200 ps duration, 200 mJ energy, focused by a 40 cm lens is taken for much shorter delays of 225, 525, 725 and 925 ns.

significantly shorter delays compared to those in 1065 nm and 10 ns laser pulses. The 1064 nm laser pulses have a much longer pulse width (10 ns) compared to the UV filaments (200 ps). Consequently, in the case of 1064 nm laser pulses, most of the trailing part of the laser pulse heats plasma via inverse Bremsstrahlung [11, 12]. It is known that inverse Bremsstrahlung is approximately proportional to λ^3 , making it considerably more favorable for IR than UV wavelengths [12]. Literature reports suggest that shorter pulse widths in LIBS lead to a more pronounced self-absorption effect. This is due to the observed lower plasma temperature and higher ablation efficiency when using shorter laser pulses, leading to an increase in the population density of the ground state species, and consequently enhancing the self-absorption phenomenon [11, 27, 28, 30]. Another factor to take into consideration is that the critical density of a laser-induced plasma is dependent

inversely on the laser wavelength as λ^2 [49]. The critical density refers to the free electron density at which the frequency of plasma oscillation equals that of the laser. As a result, IR light can more easily achieve the critical electron density in the plasma compared to the UV filament. This leads to greater laser-plasma coupling with the IR laser pulse, which reheats the plasma plume and can contribute to a longer delay in the appearance of the self-absorption dip. Conversely, the higher critical density of the UV filament allows it to pass more easily through the plasma, resulting in greater ablation on the sample surface and creating a higher density plasma [50, 51]. Since this chapter is focused on the self-absorption spectrum, all the spectra presented in the sections that follow are taken with UV filaments of 266 nm.

4.3.2 Enhanced resolution through the utilization of self-absorption

In LIBS for remote sensing applications, the goal is to identify the elemental composition of a sample from a distance. This is typically done under atmospheric pressure conditions, as it is difficult to maintain a vacuum in remote sensing scenarios. Therefore, the challenge is to develop LIBS techniques that can provide accurate and precise measurements under ambient conditions. Ambient conditions, such as the pressure of the surrounding gas, are known to play a crucial role in shaping the emission lines in laser-induced plasma. Increasing the ambient pressure results in a more confined plasma, generating more dense plasma and consequently leading to an increase in the LIBS signal intensity. This increase in signal intensity is favorable for improving the signal-to-noise ratio in LIBS measurements. However, increasing the ambient pressure also leads to a decrease in resolution, as the emission lines get broader with the increase in the pressure of the ambient gas [12, 52]. This broadening is due to the fact that emission lines in laser-induced plasma are highly affected by different broadening mechanisms such as Doppler, pressure or collision, and Stark broadening [11, 53].

Chapter 4. High-resolution spectroscopy induced with UV filaments

High-resolution LIBS has been demonstrated at low pressures (0.02 torr) [54]. However, at atmospheric pressures, the broadening of the emission lines makes it difficult to distinguish isotopes or identify the emitter in the presence of a high density of lines [52, 55]. As the surrounding gas pressure increases, the laser-induced plasma becomes more spatially confined, resulting in a denser and hotter plasma [39, 56]. The increased electron and ion densities in the denser plasma intensify both Stark and pressure broadening, leading to even broader emission lines. Stark and pressure broadening are typically the dominant mechanisms that affect the emission lines in most atmospheric conditions [53]. Another characteristic of the emission lines is that they are Stark-shifted due to the presence of charged particles in the laser-induced plasma. This shift is more significant at atmospheric pressures due to the increased electron number density [57, 58]. The Stark shift can affect the accuracy of detection in many spectral lines and can even result in the misinterpretation of elements in automated LIBS systems [59].

As mentioned in section 4.1.1 the self-absorption dips are more likely to be present at higher pressures including atmospheric pressures. In most of the LIBS literature self-absorption is categorized as an undesirable phenomenon in LIBS. We demonstrate that the right approach is to focus on the re-absorption dip seen in transitions from the ground state, which is neither affected by Stark shift nor by spectral broadening providing a higher resolution.

In Fig. 4.5 LIBS spectra obtained from various samples at atmospheric pressure are presented. The LIBS was performed via the UV filament for all these samples. Notably, the self-absorption dips have a considerably narrower full width at half maximum (FWHM) than the emission lines. The emission lines exhibit Stark shifts, while the self-absorption dips occur at the exact wavelengths listed by NIST for the corresponding transitions [60]. This can be realized from the graphs as the self-absorption dip is not symmetrically located at the center of the emission line. Additionally, both the emission lines and self-absorption dips become progressively narrower as the mass of the elements increases.

Chapter 4. High-resolution spectroscopy induced with UV filaments

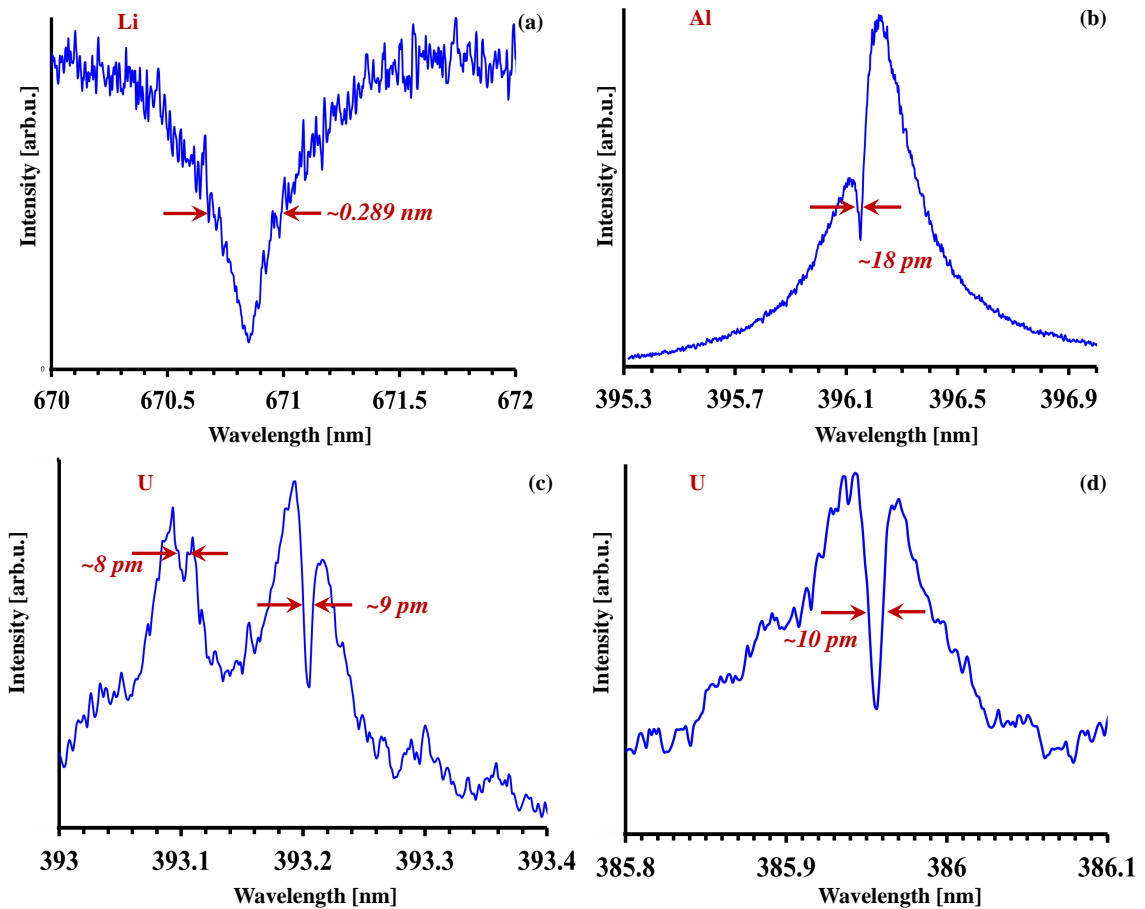


Figure 4.5: The LIBS was performed via the UV filament at atmospheric pressures. (a) The lithium (${}^6\text{Li}$) transition line of 670.791 nm is represented. The gate width for this measurement was 1 μs and the delay time was 25 ns. The self-absorption dip has an FWHM of about 289 pm which is much narrower than the emission line. (b) The Aluminum (${}^{27}\text{Al}$) transition line of 396.152 nm is represented. The gate width for this measurement was 500 ns and the delay time was 725 ns. The self-absorption dip has an FWHM of about 18 pm which is much narrower than the emission line. (c) and (d) show three transition lines of uranium (${}^{238}\text{U}$), with wavelengths of 393.098 and 393.202 nm for (c), and 385.957 nm for (d). The gate width for this measurement was 500 ns and the delay time was 725 ns and 425 ns for (c) and (d) respectively. The self-absorption dips have FWHM values of approximately 8 and 9 pm for (c) and 10 pm for (d) which are much narrower than the emission lines.

The lithium (${}^6\text{Li}$) transition line of 670.791 nm is represented in Fig. 4.5(a). The gate width for this measurement was 1 μs and the delay time was 25 ns. Lithium is a very light atom and its emission line is very broad in atmospheric conditions with approximate

Chapter 4. High-resolution spectroscopy induced with UV filaments

FWHM of $\simeq 9$ nm [54]. This was estimated by performing multiple successive measurements with *DEMON* as the center wavelength of each measurement being shifted by 1.5 nm so that the full emission line can be observed. The self-absorption dip has an FWHM of about 289 pm which is much narrower than the emission line. The center of the self-absorption dip is located at 670.849 nm which is very close to the reported value on NIST which is 670.791 nm. The difference can be attributed to two factors; 1. The *DEMON* spectrometer's resolution is decreased as you approach higher wavelengths, and 2. The broad width of the self-absorption dip.

In Fig. 4.5(b) LIBS spectrum for an Aluminum (^{27}Al) sample for the transition line of 396.152 nm is represented. The gate width for this measurement was 500 ns and the delay time was 725 ns. Compared to the emission line's FWHM of about 200 pm, the self-absorption dip has a much higher resolution, with an FWHM of about 18 pm. The peak of the emission line is estimated to be red-shifted by about 70 pm due to the Stark shift, while the center of the self-absorption dip is located at 396.152 nm, in very good agreement with NIST data [60]. Figures 4.5 (c) and (d) show three transition lines of uranium (^{238}U), with wavelengths of 393.098 and 393.202 nm for (c), and 385.957 nm for (d). The gate width for this measurement was 500 ns and the delay time was 725 ns and 425 ns for (c) and (d) respectively. As seen in Fig. 4.5(c), the self-absorption dips have FWHM values of approximately 8 and 9 pm, which are significantly narrower than the emission line's estimated FWHM of 70 pm. Similarly, the self-absorption dip in Fig. 4.5(d) has an FWHM of about 10 pm, which is much narrower than the estimated FWHM of 125 pm for the emission line. It should be noted that for all uranium spectra, the self-absorption dip is not affected by Stark shift and is located at the exact wavelength values reported by NIST [60]. From these spectra, we can conclude that using self-absorption dips instead of emission lines will increase the accuracy of LIBS measurements. This is because self-absorption dips have much higher resolution compared to emission lines, and they are not affected by Stark shifts. This fact holds true regardless of measurement delay times or gate widths.

Chapter 4. High-resolution spectroscopy induced with UV filaments

To further emphasize that higher resolution is achievable, three chromium (*Cr*) transitions present in the LIBS signal of a steel sample were investigated. The spectrum of steel reproduced in Fig. 4.6(a). Three closely located chromium (*Cr*) lines corresponding to transitions from the ground state ($3d^4 4s^2$ [$J = 1, 2, 3$]) to the upper levels ($3d^4(^5D)4s4p(^1P^o)$ [$J = 2, 3, 0$]) at 301.476 nm (A), 301.491 nm (B), and 301.520 nm (C) [60, 61] are present. Three self-absorption dips corresponding to these lines are labeled A, B, and C in Fig. 4.6(a) and are clearly resolvable. The two emission lines at 301.476 nm (A) and 301.491 nm (B) are only separated by 15 pm and they are embedded in the emission spectrum and are not resolvable. On contrary, the two self-absorption dips labeled A and B are clearly resolved. The dips are only seen in transitions from the ground state. Other transitions, such as the ones labeled D (chromium transition from $3d^4(^3F)4s$ $J = 7/2$ to $3d^4(^3F)4p$ $J = 7/2$ at 301.550 nm) and E (iron (*Fe*) transition from $3d^6 4s^2$ $J = 5$ to $3d^7(^2H)4p$ $J = 4$ at 301.592 nm), do not show a re-absorption dip. Figure 4.6 (a) clearly indicates that lines separated by 15 pm can be resolved, thus providing sufficient resolution for isotopic selectivity [55, 62, 63]. Furthermore, there does not appear to be a Stark shift on these lines, as their wavelengths match the values tabulated by NIST [60].

In another set of experiments, the LIBS spectra from two isotopes of lithium (6Li and 7Li) were investigated. These two transitions correspond to 670.776 nm for 7Li and 670.791 nm for 6Li . The isotopic shift between these two naturally stable isotopes of lithium is 15 pm [60]. As mentioned before in atmospheric pressures the lithium emission lines are very broad and can not be utilized for the detection of this isotopic shift. However as demonstrated in Fig. 4.6(b), by using the self-absorption dips that are much narrower this isotopic shift is resolved. The measured wavelengths for these two lines are 670.830 nm for 7Li and 670.849 nm for 6Li which yields a 19 pm isotopic shift [64]. These measured results are in good agreement with values tabulated by NIST.

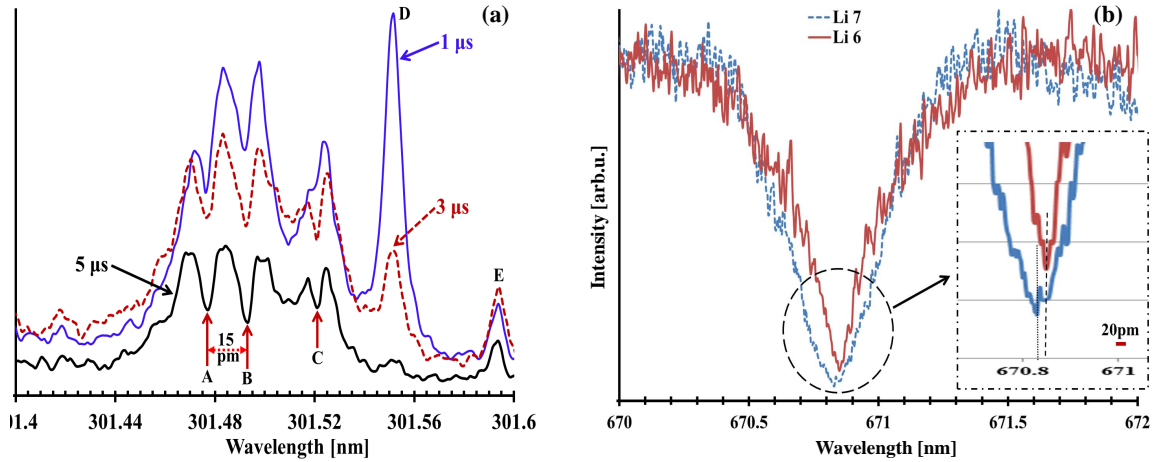


Figure 4.6: Left) LIBS spectrum of steel taken with a 200 ps pulse of 200 mJ energy, focused by a lens of 40 cm focal distance at gate delays of 1, 3, and 5 μ s. A broad emission structure can be seen between 301.44 nm and 301.54 nm, which includes three chromium transitions from the $3d^4 4s^2$ [$J = 1, 2, 3$] ground state to the $3d^4(^5D)4s4p(^1P^o)$ [$J = 2, 3, 0$] levels at 301.476 (A), 301.491 nm (B), and 301.520 nm (C). Emission lines labeled D (chromium transition from $3d^4(a^3F)4s$ $J = 7/2$ to $3d^4(a^3F)4p$ $J = 7/2$ at 301.550 nm) and E (iron transition from $3d^6 4s^2$ $J = 5$ to $3d^7(^2H)4p$ $J = 4$ at 301.592 nm), do not show a re-absorption dip. Right) LIBS spectra of the two isotopes of Lithium. The transition lines for these two isotopes are at 670.830 nm (Li7) and 670.849 nm (Li6) which indicates an isotopic shift of 19 pm. The emission line extends far beyond the boundaries of the figure. Samples are irradiated by a UV filament at atmospheric pressure. UV laser pulse is a 200 ps pulse of 200 mJ energy, focused by a lens of 40 cm focal distance.

4.3.3 Temporal evolution of self absorption and emission profile

In Fig. 4.7, the time evolution of the emission spectra for the 424.166 nm transition line of a uranium (^{238}U) sample is shown for delay times ranging from 25 ns to 1025 ns. For all the spectra the gate width is 500 ns. Initially, at the 25 ns delay, the continuum is dominant, and the emission line is barely noticeable. However, at a very short delay of 225 ns, the emission lines and self-absorption dip become apparent.

By fitting known profiles such as Galatry and Voigt [65] to an emission profile, plasma parameters such as pressure can be deduced. As suggested by several authors [27,65] we fit

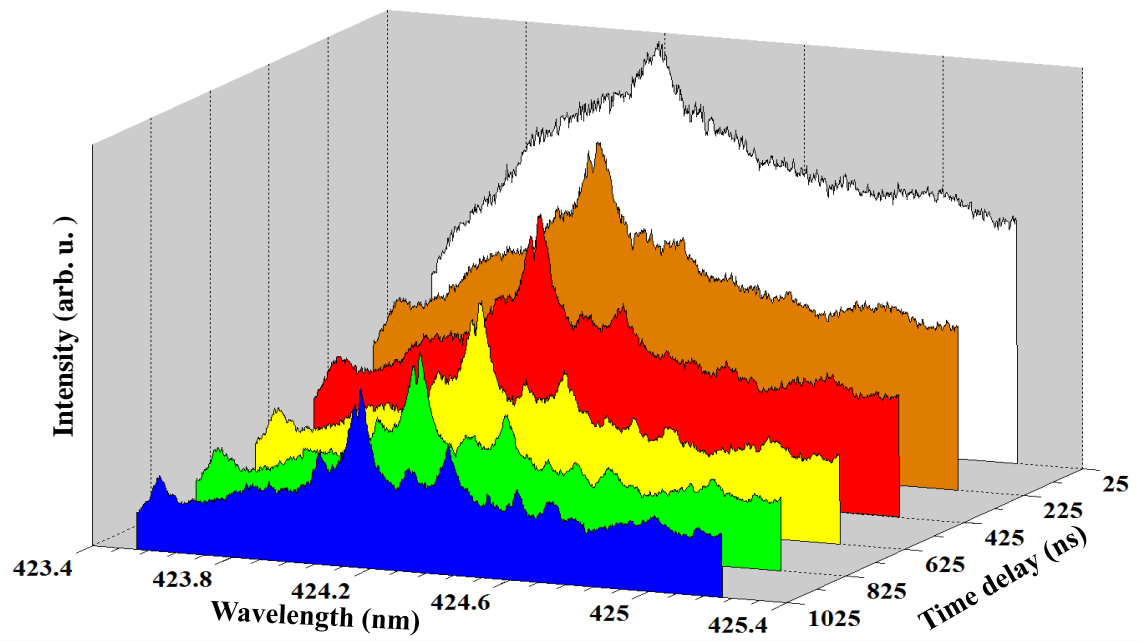


Figure 4.7: The time evolution of the emission spectra for the 424.166 nm transition line of a uranium (^{238}U) sample is shown for delay times ranging from 25 ns to 1025 ns. For all the spectra the gate width is 500 ns.

the emission spectrum to a Lorentzian. The self-absorption is fitted to a Gaussian profile. The center, amplitude, background and width of the profiles are free parameters in the fit. In our method the complete emission spectrum consists of a Lorentzian emission minus a Gaussian absorption. The fitting procedure enables us to determine the line center with a resolution beyond the pixel size. In Fig. 4.8, the best fit to the 385.957 nm uranium line emission spectrum is a Lorentzian, while the absorption dip is seen to be best fit by a Gaussian.

The delay dependent emission from two samples of uranium and aluminum are presented in Fig. 4.9. The fits presented in Fig. 4.9(a) illustrate clearly the fact that the re-absorption dip central wavelength is fixed within a couple of pm, and that its width decreases with delay. The dashed vertical line shows that the absorption dips are perfectly lined up. The center of gravity of the Lorentzian emission spectra however does not match

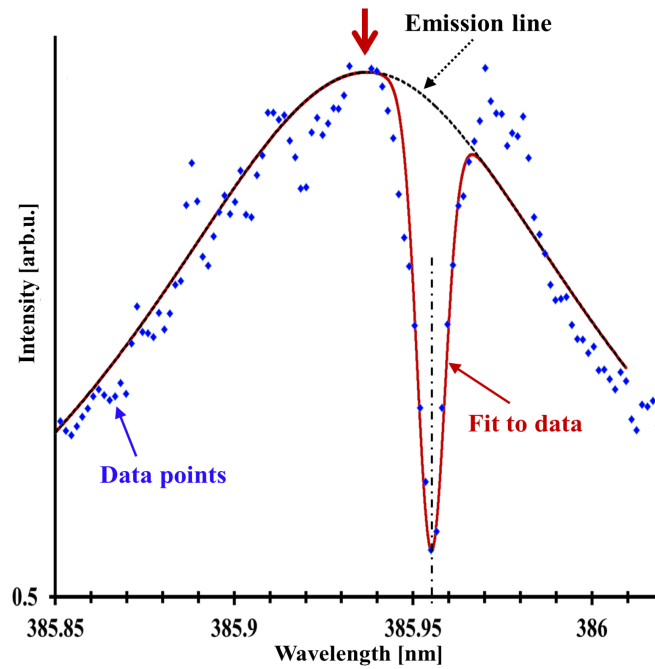


Figure 4.8: LIBS spectrum of the uranium line (Transition from $5f^3(4I^{\circ})6d7s^2$ state to $5f^36d7p$ at 385.957 nm), for gate delay of 425 ns, and 40 cm focalization.. The stars are the data points, the solid green line the fit consisting in a Gaussian line (red dotted line) subtracted from the Lorentzian fit (dashed line).

the transition wavelength and changes with time for both samples. The vertical arrows pointing to the peaks of the Lorentzians in Fig. 4.9(a) show that both linewidth and Stark shift are decreasing with delay. Since the widths of the lines (absorption and emission) decrease with atomic mass of the elements, LIBS spectra for the 396.152 nm transition are shown in Fig. 4.9(b) to better illustrate the wavelength dependence of the emission and absorption peaks. The center emission line at 225 ns delay has 120 pm Stark shift that is reduced to 50 pm at a delay of 1 μ s.

Figure 4.10 summarizes the gate delay dependence of the parameters of the Lorentzian emission and the Gaussian re-absorption, for which some selected lines were presented in Fig. 4.9(a). As shown in Fig. 4.10(a), the peak of the Gaussian re-absorption remains at the same value for all delays within 1.5 pm (well within the 6 pm reported resolution of the

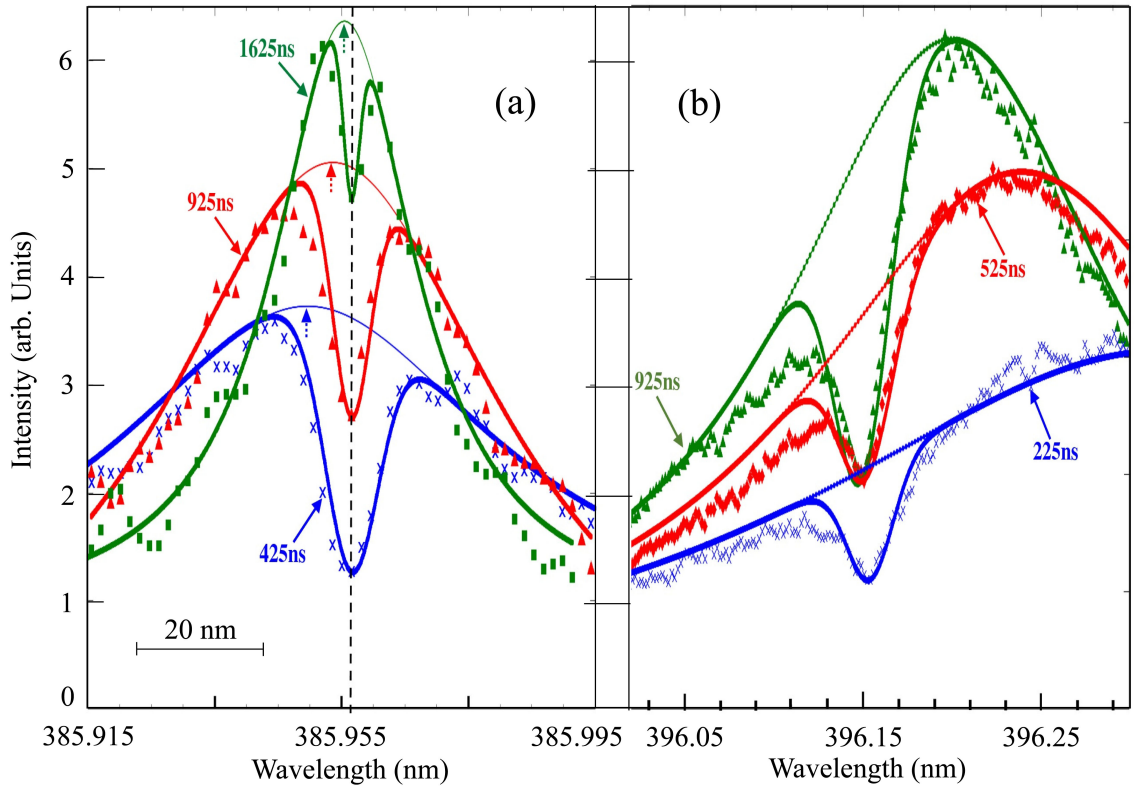


Figure 4.9: (a) LIBS spectra of the uranium line at 385.957 nm, for gate delays of 425, 925 and 1625 ns, and 40 cm focalization. The solid thick lines are the Lorentzian-Gaussian fits to the data. The solid thin lines are the Lorentzian fits. Triangles, squares, and stars are the data point for respective delays. The vertical arrows pointing to the peaks of the Lorentzians fits show a linewidth and Stark shift decreasing with delay. The dashed line shows the center of the re-absorption dips, emphasizing the absence of Stark shift in the absorption feature. (b) LIBS spectra of the aluminum line (transition from $3s^23p \ J = 3/2$ state to $3s^24s \ J = 1/2$ at 396.152 nm), for gate delays of 225, 525, and 925 ns. The stars, diamonds, and triangles are the data points, and the solid thick lines are the complete fits. The dotted lines indicate the Lorentzian parts of the fit.

DEMON at that wavelength), while the peak of the Lorentzian approaches asymptotically the transition wavelength, from an initial Stark shift of 50 pm.

The time evolution of the linewidth of the emission and absorbing features can be correlated to the expansion and collisional cooling of the plasma. A nearly linear decrease in Gaussian linewidth from 12 pm to 5 pm over 1.5 μ s indicates a slower evolution of

Chapter 4. High-resolution spectroscopy induced with UV filaments

the absorbing region (Fig. 4.10(b)). The excited region exhibits a much faster expansion and cooling in Fig. 4.10(c). It should be noted that the emission rides over a continuum background (plasma emission) decaying with time. The continuum emission in our case is due to a plasma, and decays to $1/e^2$ in $1.0 \mu s$, while the much shorter decay reported for a lead sample in reference [27] is that of the filament emission. Even though the continuum emission decays with delay, the specific line emission *increases* with delay as witnessed by the increasing Lorentzian amplitude in Fig. 4.9 and time dependent integrated emission in Fig. 4.10(e). Figures 4.10(d) and (e) pertain to the total energy absorbed (total area of the Gaussian) and emitted (total area under the Lorentzian) plotted as a function of time. The area covered by the Lorentzian Fig. 4.10(e), shows a rise time of the excited state $5f^36d7p$ of approximately 500 ns. The rise of total absorbed energy would have followed the emission if the density of ground state atoms were constant over the range of delays. The slower rise time of the absorbed energy (Fig. 4.10(d)) can be understood as a measure of the increasing density of the re-absorbing region fed by the de-excited Uranium. The ratio of total line absorption to emission plotted in Fig. 4.10(f), varying in the range of 4 to 8%, should correlate to the density of absorbing/emitting particle behind the shock-wave with a peak shifted approximately 200 ns later to the peak of emission.

Best S/N and resolution can be identified using the set of Figs. 4.10. These plots show that the Gaussian width decreases with time while the signal amplitude is maximized at a delay of about 500 ns. Using the fit algorithm to whole spectra, the resolution for centroid detection is better than the width of the Gaussian.

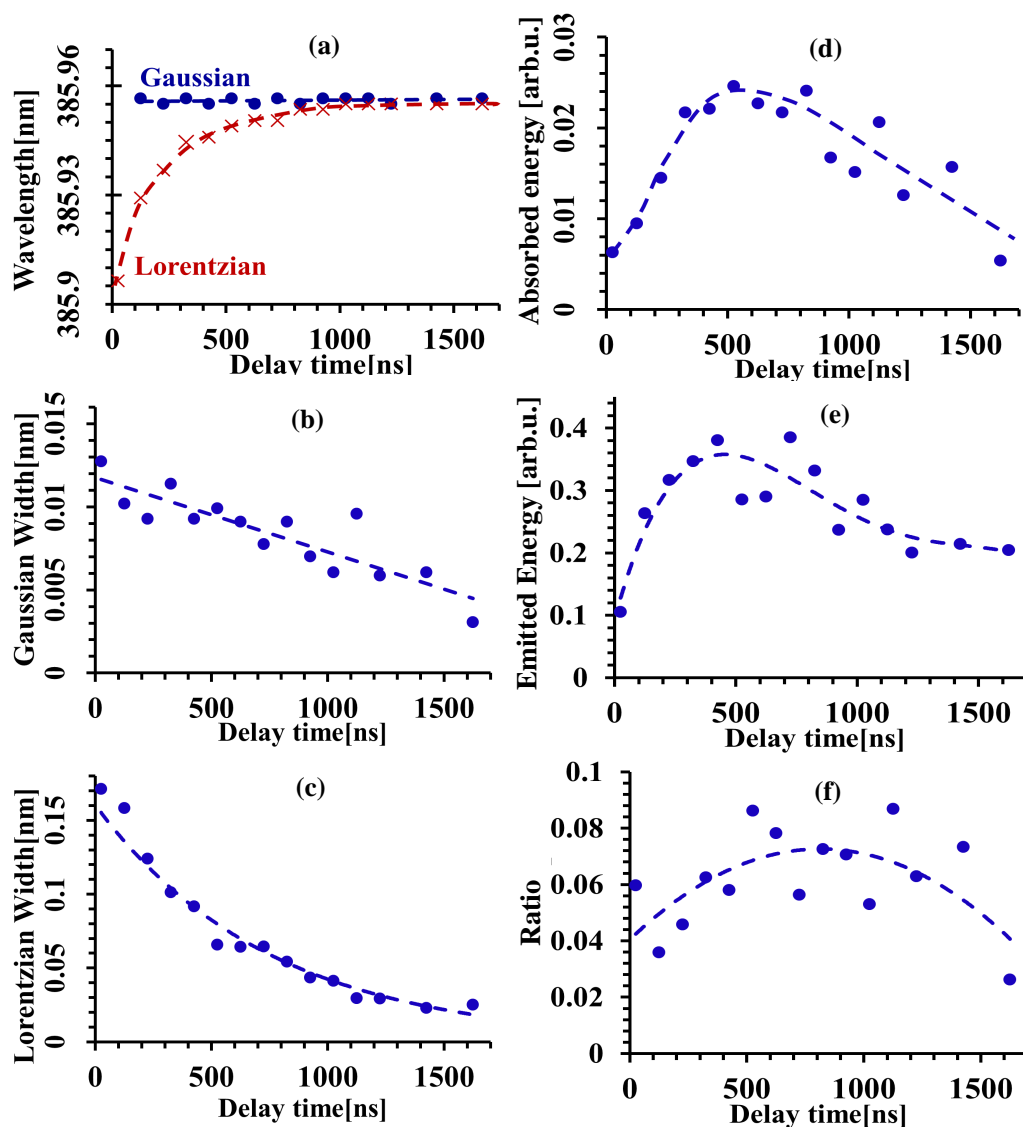


Figure 4.10: Comparison of the emission and re-absorption, as analyzed through the fits of Fig. 4.8 versus gate delay. (a) Wavelength of the emission (at the peak of the Lorentzian) and of the re-absorption (at the peak of the Gaussian fit). The 50 pm stark shift of the emission (solid line) rejoins the absorption dip wavelength (dashed line) for delays in excess of $1 \mu\text{s}$. (b) Decrease of the width of the absorption dip versus delay. (c) The broader width of the emission line exhibits a faster decay rate, indicating a faster cooling/expansion of the excited region. (d) Total integrated absorption (area under the Gaussian) versus delay. (e) Total integrated emission (area under the Lorentzian) versus delay. (f) Ratio of (d) to (e).

4.4 Investigation of the plume generated in LIBS process induced by a ps UV laser

During the LIBS, When the laser pulse interacts with the sample surface, it creates a high-temperature and high-pressure plasma plume. In the presence of ambient gas, this plasma plume rapidly expands into the surrounding environment, which creates a shock-wave in the sample material [50, 66]. Shadowgraphy is used to investigate the characteristics of the laser-induced plume and the created shock-waves [67, 68]. The UV filament is focused using a 40 cm lens onto a piece of aluminum as a target. The probe beam which is a collimated 10 ns 532 nm pulse, is imaging the area of interest on a screen located at a 1m distance from the target (Fig. 4.11). A high-resolution CCD is used to capture the

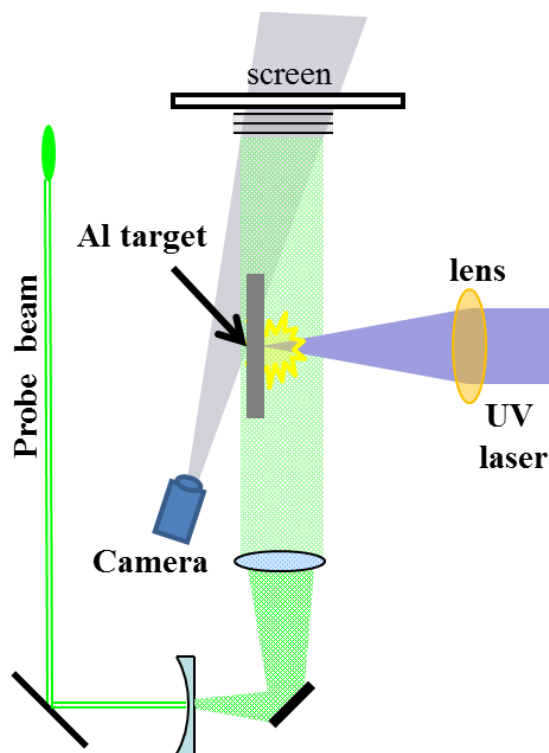


Figure 4.11: Schematics of the shadowgraphy setup.

shadowgrams on the screen. A master clock is used to synchronize the UV laser, the green

Chapter 4. High-resolution spectroscopy induced with UV filaments

laser, and the camera. A delay generator controls the relative delay times between the probe beam and the UV laser, making it possible to investigate the evolution of the plume and the shock-wave in time. The plumes generated by 300 mJ and 185 mJ UV pulse energies are investigated. Two-speed regimes are observed with respect to the propagation of the shock-waves generated by the plume.

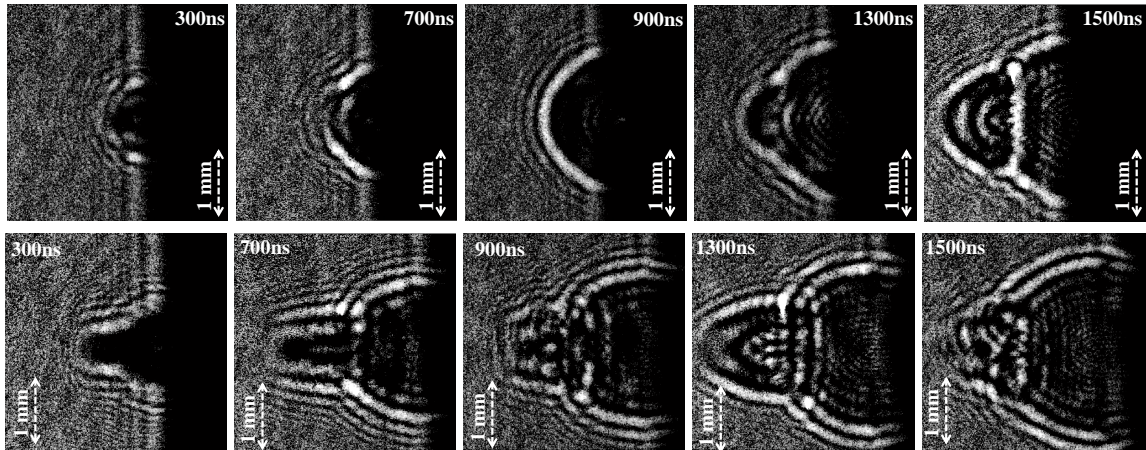


Figure 4.12: Shadowgraphs of the plume for the first regime. Top: 180 mJ Bottom: 300 mJ.

The first regime of the expansion of the plume lasts up to $1.5\mu\text{s}$. The propagation of the related shock-waves vs time in this regime follows the formula which was proposed by Sedov: $R = \left(\frac{E}{\rho}\right)^{\frac{1}{2+d}} t^{\frac{2}{2+d}}$ [50, 69]. In this formula, E is the total energy transferred to the vapor plume, ρ is the air density, and $d=1, 2, 3$ for planar, cylindrical, and spherical propagation respectively. Selected shadowgrams in this regime for different delay times with respect to the UV filament are presented in Fig. 4.12. The second regime starts after the plume is fully expanded and in this regime, the shock-wave propagates with constant speed. Selected shadowgrams of this regime are presented in Fig 4.13. In Fig. 4.14 the radius of the shock-waves in y direction (parallel to the target) vs time for two different regimes is presented. It can be seen that for the first regime, the experimental data points are in good agreement with Sedov equation, with $d = 2.96$ for the 300 mJ filaments, and $d = 2.87$ for the 180 mJ filaments. Similar results have been reported in the literature for

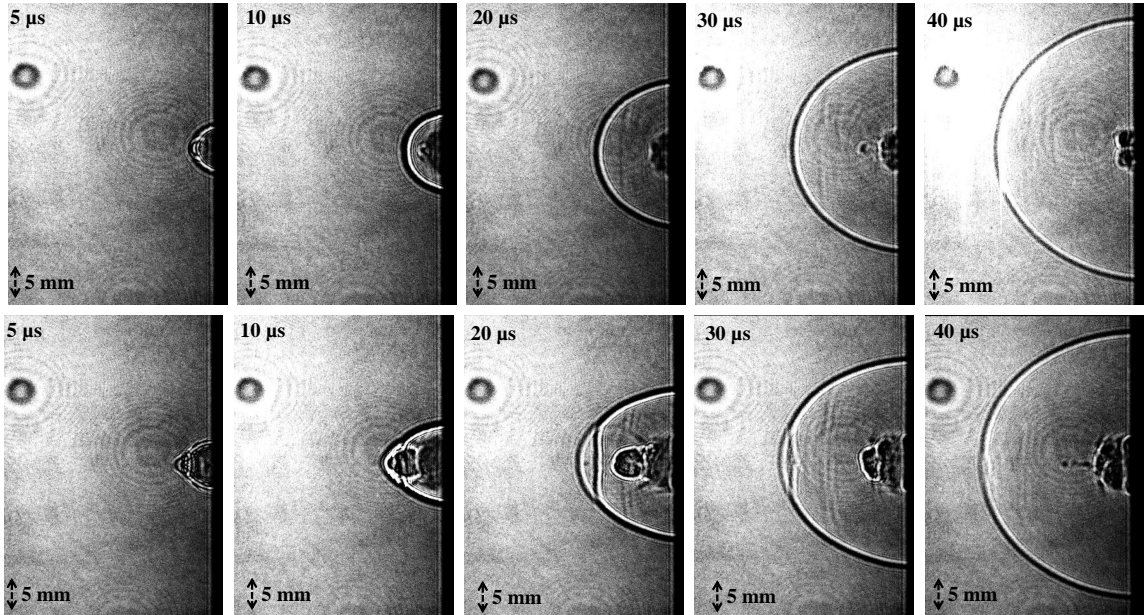


Figure 4.13: Shadowgraphs of the plume for the second regime. Top: 180 mJ Bottom: 300 mJ.

shock-waves generated in LIBS [50, 66]. These values indicate a spherical propagation of the shock-wave. For the second regime, it can be seen that the propagation of the shock-waves is linear with respect to time, and the slope of these lines are 382 m/s and 396 m/s for the 180 mJ and 300 mJ filament, respectively [70]. As in the case of shock-waves created by UV filaments (Section 2.5), the speed of the acoustic disturbance is higher for the higher energy.

4.5 Conclusion

The time-dependent dynamics of emission and absorption profile reveals the expansion and de-excitation of plasma plume in time scales from tens of nanoseconds to up to ms. Shadowgraphy is a technique that provides spatial information on the plasma development at the same time scale [50]. These measurements have not been associated with the appearance of the dip in absorption. Our own shadowgraphy measurement of the plume

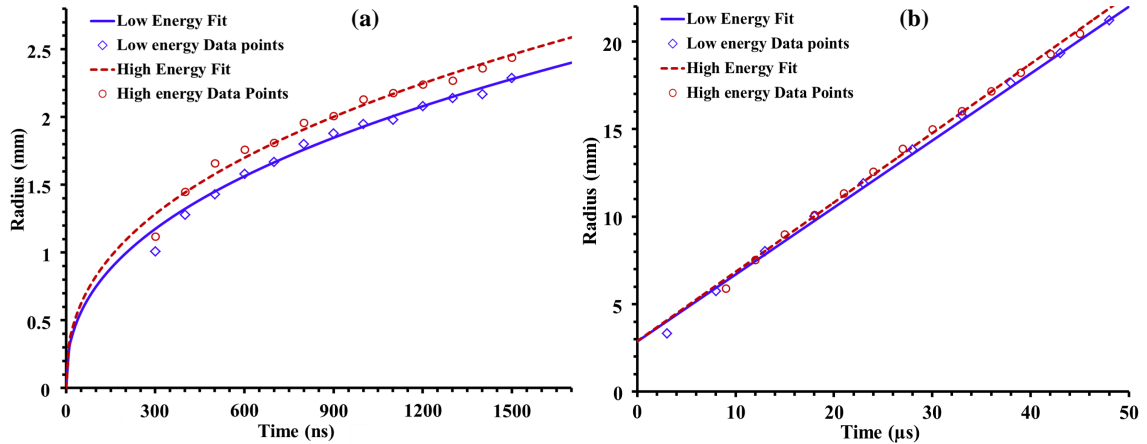


Figure 4.14: a) Shock-wave radius vs time for the first regime. b) Shock-wave radius vs time for the second regime.

associated with the 200 ps UV filaments does not shed any light on the phenomenon because the dip is already fully developed at the shortest delay at which the spectrum can be recorded. At any rate, the shadowgraphy experiment gives only direct information on the position of the shock-wave associated with the plume, and no information of the pressure and temperature behind the shock-wave. As a complement to the shadowgraphy measurement, time-resolved plasma interferometry (wavefront analysis of a plasma probing pulse) was reported [71]. While the wavefront measurements show a region of higher pressure along the shock wave, there is region of very low density and higher temperature along the filament that created the plasma. The same low density should be present in the filament or focused beam creating the plume. But the comparison can only be qualitative, because a much stronger perturbation should be created by the particles and ions expelled from the solid. It is to be expected that the metal particles in the low pressure region absorb the radiation emitted at the surface. The narrowness of the re-absorption dip is attributed to the reduced pressure broadening.

Our study suggests that dynamics of self-absorption and emission can be exploited to understand hydrodynamics of plume expansion and cooling at times below 1 μ s. Self-

absorption with UV filaments can be explored in free space at atmospheric pressure. Further study should involve, in addition to time-resolved spectroscopy, shadowgraphy at the earliest time scale with subnanosecond pulses, combined with plasma interferometry (wavefront analysis of a plasma probe) Quantitative analysis of spectral analysis such as the Stark broadening [27] will reveal the time dependence of electron density in plasma.

4.6 Future Work

A commonly cited claim in the literature is that self-absorption is an unfavorable phenomenon in Laser-Induced Breakdown Spectroscopy (LIBS) measurements, as it can interfere with the direct measurement of emission peak intensity, which is used to determine the concentration of different species in a sample. Further investigation is needed to determine the relationship between the intensity of self-absorption dips and the concentration of species in a sample. Further investigation of the electron density and temperature of the plasma in LIBS via UV filaments is going to be performed.

As mentioned, the shadowgraphy measurement of the plume associated with the 200 ps UV filaments does not provide any insight into the phenomenon because the dip is already fully developed at the shortest delay possible to record the spectrum. To increase the temporal resolution of the shadowgraphy measurements, two essential changes in experimental parameters are required. Firstly, the 10 ns green probe beam needs to be replaced with a shorter laser pulse. Secondly, since the delay between the UV laser and the probe beam is controlled electronically, it has an approximate electronic jitter of 10 ns associated with the delay generators. To resolve both these limitations, we plan to use 200 ps green laser pulses from our UV laser system as the probe beam. These laser pulses are in complete synchronization with the UV laser pulses and have much shorter pulse widths compared to the 10 ns laser pulses. An optical delay line will be used to control the delay between the green laser pulse and the UV pulse. We will use the Schlieren technique in-

References

stead of the shadowgraphy technique to increase the contrast of the shadowgrams [67, 68].

Acknowledgement

This research has been supported by the Army Research office (ARO:W911- NF-1110297) and U.S. Department of Energy (DOE:DESC0011446).

References

- [1] Valerie Payre, Cecile Fabre, Agnes Cousin, Violaine Sautter, Roger Craig Wiens, Olivier Forni, Olivier Gasnault, Nicolas Mangold, P-Y Meslin, Jeremie Lasue, et al. Alkali trace elements in gale crater, mars, with chemcam: Calibration update and geological implications. *Journal of Geophysical Research: Planets*, 122(3):650–679, 2017.
- [2] Peter Vandenaabeele and Mary Kate Donais. Mobile spectroscopic instrumentation in archaeometry research. *Applied Spectroscopy*, 70(1):27–41, 2016.
- [3] Rosalba Gaudiuso, Marcella Dell’Aglia, Olga De Pascale, Giorgio S Senesi, and Alessandro De Giacomo. Laser induced breakdown spectroscopy for elemental analysis in environmental, cultural heritage and space applications: a review of methods and results. *Sensors*, 10(8):7434–7468, 2010.
- [4] Vivek K Singh, Vinay Kumar, Jitendra Sharma, Yugal Khajuria, and Kaushal Kumar. Importance of laser induced breakdown spectroscopy for biomedical applications: a comprehensive review. *Materials Focus*, 3(3):169–182, 2014.
- [5] Vivek Kumar Singh and Awadhesh Kumar Rai. Prospects for laser-induced breakdown spectroscopy for biomedical applications: a review. *Lasers in medical science*, 26:673–687, 2011.
- [6] Ke Liu, Di Tian, Chang Li, Yingchao Li, Guang Yang, and Yu Ding. A review of laser-induced breakdown spectroscopy for plastic analysis. *TrAC Trends in Analytical Chemistry*, 110:327–334, 2019.

References

- [7] Reinhard Noll, Cord Fricke-Begemann, Markus Brunk, Sven Connemann, Christoph Meinhardt, Michael Scharun, Volker Sturm, Joachim Makowe, and Christoph Gehlen. Laser-induced breakdown spectroscopy expands into industrial applications. *Spectrochimica Acta Part B: Atomic Spectroscopy*, 93:41–51, 2014.
- [8] Jesús M Anzano, Mark A Villoria, Antonio Ruíz-Medina, and Roberto J Lasheras. Laser-induced breakdown spectroscopy for quantitative spectrochemical analysis of geological materials: Effects of the matrix and simultaneous determination. *Analytica chimica acta*, 575(2):230–235, 2006.
- [9] James E Barefield II, Elizabeth J Judge, Keri R Campbell, James P Colgan, David P Kilcrease, Heather M Johns, Roger C Wiens, Rhonda E McInroy, Ronald K Martinez, and Samuel M Clegg. Analysis of geological materials containing uranium using laser-induced breakdown spectroscopy. *Spectrochimica Acta Part B: Atomic Spectroscopy*, 120:1–8, 2016.
- [10] Gábor Galbács. A critical review of recent progress in analytical laser-induced breakdown spectroscopy. *Analytical and bioanalytical chemistry*, 407:7537–7562, 2015.
- [11] David A. Cremers and Leon J. Radziemski. *Handbook of Laser-Induced Breakdown Spectroscopy*. Wiley, 2013.
- [12] Jagdish P Singh and Surya Narayan Thakur. *Laser-induced breakdown spectroscopy*. Elsevier, 2020.
- [13] Syed Kifayat Hussain Shah, Javed Iqbal, Pervaiz Ahmad, Mayeen Uddin Khandaker, Sirajul Haq, and Muhammad Naeem. Laser induced breakdown spectroscopy methods and applications: A comprehensive review. *Radiation Physics and Chemistry*, 170:108666, 2020.
- [14] Maria Markiewicz-Keszycka, Xavier Cama-Moncunill, Maria P. Casado-Gavaldà, Yash Dixit, Raquel Cama-Moncunill, Patrick J. Cullen, and Carl Sullivan. Laser-induced breakdown spectroscopy (libs) for food analysis: A review. *Trends in Food Science Technology*, 65:80–93, 2017.
- [15] Andrzej W Miziolek, Vincenzo Palleschi, and Israel Schechter. *Laser induced breakdown spectroscopy*. Cambridge university press, 2006.
- [16] Talib Hussain and MA Gondal. Laser induced breakdown spectroscopy (libs) as a rapid tool for material analysis. In *Journal of Physics: Conference Series*, volume 439, page 012050. IOP Publishing, 2013.

References

- [17] Muhammad Hilal Kabir, Mahamed Lamine Guindo, Rongqin Chen, Alireza Sanaei-far, and Fei Liu. Application of laser-induced breakdown spectroscopy and chemometrics for the quality evaluation of foods with medicinal properties: A review. *Foods*, 11(14):2051, 2022.
- [18] Luís Carlos Leva Borduchi, Débora Marcondes Bastos Pereira Milori, and Paulino Ribeiro Villas-Boas. Study of the effects of detection times in laser-induced breakdown spectroscopy and missed variation of plasma parameters with gate width. *Spectrochimica Acta Part B: Atomic Spectroscopy*, 191:106409, 2022.
- [19] Emanuela Grifoni, Stefano Legnaioli, Marco Lezzerini, Giulia Lorenzetti, Stefano Pagnotta, and Vincenzo Palleschi. Extracting time-resolved information from time-integrated laser-induced breakdown spectra. *Journal of Spectroscopy*, 2014, 2014.
- [20] Huai Liang Xu and See Leang Chin. Femtosecond laser filamentation for atmospheric sensing. *Sensors*, 11(1):32–53, 2010.
- [21] S. Tzortzakis, D. Anglos, and D. Gray. Ultraviolet laser filaments for remote laser-induced breakdown (libs) spectroscopy: Application in cultural heritage monitoring. *Optics Letters*, 31:1139–1141, 2006.
- [22] R. Ackermann, G. Mejean, J. Kasparian, J. Yu, E. Salmon, and J.-P. Wolf. Laser filaments generated and transmitted in highly turbulent air. *Optics Letters*, 31:86–88, 2006.
- [23] Miguel Rodriguez, Riad Bourayou, Guillaume Méjean, Jérôme Kasparian, Jin Yu, Estelle Salmon, Alexander Scholz, Bringfried Stecklum, Jochen Eislöffel, Uwe Laux, Artie P. Hatzes, Roland Sauerbrey, Ludger Wöste, and Jean-Pierre Wolf. Kilometer-range nonlinear propagation of femtosecond laser pulses. *Phys. Rev. E*, 69:036607, Mar 2004.
- [24] Magali Durand, Aurélien Houard, Bernard Prade, André Mysyrowicz, Anne Durécu, Bernard Moreau, Didier Fleury, Olivier Vasseur, Hartmut Borchert, Karsten Diener, Rudiger Schmitt, Francis Théberge, Marc Chateaneuf, Jean-François Daigle, and Jacques Dubois. Kilometer range filamentation. *Opt. Express*, 21(22):26836–26845, Nov 2013.
- [25] S.S. Harilal, P.K. Diwakar, and G. Miloshevsky. Chapter 6 - ultrafast and filament-libs. In Jagdish P. Singh and Surya N. Thakur, editors, *Laser-Induced Breakdown Spectroscopy (Second Edition)*, pages 139–166. Elsevier, Amsterdam, second edition edition, 2020.

References

- [26] S. S. Harilal, B. E. Brumfield, N. L. LaHaye, K. C. Hartig, and M. C. Phillips. Optical spectroscopy of laser-produced plasmas for standoff isotopic analysis. *Applied Physics Reviews*, 5(2):021301, 2018.
- [27] H. L. Xu, J. Bernhardt, P. Mathieu, G. Roy, and S. L. Chin. Understanding the advantage of remote femtosecond laser-induced breakdown spectroscopy of metallic targets. *Journal of Applied Physics*, 101:033124, 2007.
- [28] Kristine L. Eland, Dimitra N. Stratis, David M. Gold, Scott R. Goode, and S. Michael Angel. Energy dependence of emission intensity and temperature in a libs plasma using femtosecond excitation. *Appl. Spectrosc.*, 55(3):286–291, Mar 2001.
- [29] H. L. Xu, P. T. Simard, Kamali, J.F. Daiglea, C. Marceau, Bernhardt, J. Dubois, M. Châteauneuf, F. Théberge, G. Roy, and S. L. Chin. Filament-induced breakdown remote spectroscopy in a polar environment. *Laser Physics*, 22:1767–1770, 2012.
- [30] Fatemeh Rezaei, Gabriele Cristoforetti, Elisabetta Tognoni, Stefano Legnaioli, Vincenzo Palleschi, and Ali Safi. A review of the current analytical approaches for evaluating, compensating and exploiting self-absorption in laser induced breakdown spectroscopy. *Spectrochimica Acta Part B: Atomic Spectroscopy*, 169:105878, 2020.
- [31] J. M. Li, L. B. Guo, C. M. Li, N. Zhao, X. Y. Yang, Z. Q. Hao, X. Y. Li, X. Y. Zeng, and Y. F. Lu. Self-absorption reduction in laser-induced breakdown spectroscopy using laser-stimulated absorption. *Optics Letters*, 40(22):5224–5226, 2015.
- [32] Jiajia HOU, Lei ZHANG, Yang ZHAO, Zhe WANG, Yong ZHANG, Weiguang MA, Lei DONG, Wangbao YIN, Liantuan XIAO, and Suotang JIA. Mechanisms and efficient elimination approaches of self-absorption in libs. *Plasma Science and Technology*, 21(3):034016, jan 2019.
- [33] Rongxing Yi, Lianbo Guo, Changmao Li, Xinyan Yang, Jiaming Li, Xiangyou Li, Xiaoyan Zeng, and Yongfeng Lu. Investigation of the self-absorption effect using spatially resolved laser-induced breakdown spectroscopy. *Journal of Analytical Atomic Spectrometry*, 31(4):961–967, 2016.
- [34] Robert D Cowan and Go H Dieke. Self-absorption of spectrum lines. *Reviews of Modern Physics*, 20(2):418, 1948.
- [35] F. Bredice, F.O. Borges, H. Sobral, M. Villagran-Muniz, H.O. Di Rocco, G. Cristoforetti, S. Legnaioli, V. Palleschi, L. Pardini, A. Salvetti, and E. Tognoni. Evaluation of self-absorption of manganese emission lines in laser induced breakdown spectroscopy measurements. *Spectrochimica Acta*, B61:1294–1303, 2006.

References

- [36] L. Sun and H. Yu. Correction of self-absorption effect in calibration-free laser-induced breakdown spectroscopy by an internal reference method. *Talanta*, 79:388–395, 2009.
- [37] F. Rezaei, P. Karimi, and S. H. Tavassoli. Estimation of self-absorption effect on aluminum emission in the presence of different noble gases: comparison between thin and thick plasma emission. *Applied Optics*, 52:5088–5096, 2013.
- [38] H. Amamou, A. Bois, B. Ferhat, R. Redon, B. Rossetto, and M. Ripert. Correction of the self-absorption for reversed spectral lines: application to two resonance lines of neutral aluminium. *Journal of Quantitative Spectroscopy & Radiative Transfer*, 77(4):365–372, 2003.
- [39] Agnes Nakimana, Haiyan Tao, Xun Gao, Zuoqiang Hao, and Jingquan Lin. Effects of ambient conditions on femtosecond laser-induced breakdown spectroscopy of Al. *J. Phys. D: Appl. Phys.*, 46:285204, 2013.
- [40] J. Hou, L. Zhang, W. Yin, S. Yao, Y. Zhao, W. Ma, L. Dong, L. Xiao, and S. Jia. Development and performance evaluation of self-absorption-free laser-induced breakdown spectroscopy for directly capturing optically thin spectral line and realizing accurate chemical composition measurements. *Optics Express*, 25(19):23024–23034, 2017.
- [41] J. A. Aguilera, C. Aragón, and J. Manrique. Experimental stark widths and shifts of ciii spectral lines. *Monthly Notices of the Royal Astronomical Society*, 438(1):841–845, 2014.
- [42] A. A. Michelson. The Echelon Spectroscope. , 8:37, June 1898.
- [43] Yinxin Zhang, Wanzhuo Li, Wenhao Duan, Zhanhua Huang, and Huaidong Yang. Echelle grating spectroscopic technology for high-resolution and broadband spectral measurement. *Applied Sciences*, 12(21):11042, Oct 2022.
- [44] Ali Rastegari and Jean-Claude Diels. Investigation of UV filaments and their applications. *APL Photonics*, 6(6):060803, 2021.
- [45] Ali Rastegari, Alejandro Aceves, and Jean-Claude Diels. UV filaments. *Light Filaments: Structures, Challenges and Applications*, page 31, 2021.
- [46] M. Corsi, G. Cristoforetti, M. Hidalgo, D. Iriarte, S. Legnaioli, V. Palleschi, A. Salvetti, and E. Tognoni. The effect of laser-induced crater depth in libs analysis and shock wave dynamics. In *Laser Induced Plasma Spectroscopy and Applications*, page FD2. Optica Publishing Group, 2002.

References

- [47] Michela Corsi, Gabriele Cristoforetti, Montserrat Hidalgo, Daniela Iriarte, Stefano Legnaioli, Vincenzo Palleschi, Azenio Salvetti, and Elisabetta Tognoni. Effect of laser-induced crater depth in laser-induced breakdown spectroscopy emission features. *Appl. Spectrosc.*, 59(7):853–860, Jul 2005.
- [48] W. Hübert and G. Ankerhold. Elemental misinterpretation in automated analysis of LIBS spectra. *Analytical and Bioanalytical Chemistry*, 400(10):3273–3278, 2011.
- [49] Chao Gong, Sergei Ya. Tochitsky, Frederico Fiuza, Jeremy J. Pigeon, and Chan Joshi. Plasma dynamics near critical density inferred from direct measurements of laser hole boring. *Phys. Rev. E*, 93:061202, Jun 2016.
- [50] A. E. Hussein, P. K. Diwakar, S. S. Harilal, , and A. Hassanein. The role of laser wavelength on plasma generation and expansion of ablation plumes in air. *Journal of Applied Physics.*, 113:143305, 2013.
- [51] Haohao Cui, Yun Tang, Shixiang Ma, Yiwen Ma, Deng Zhang, Zhenlin Hu, Zhi Wang, and Lianbo Guo. Influence of laser wavelength on self-absorption effect in laser-induced breakdown spectroscopy. *Optik*, 204:164144, 2020.
- [52] Andrew J Effenberger Jr and Jill R Scott. Effect of atmospheric conditions on libs spectra. *Sensors*, 10(5):4907–4925, 2010.
- [53] Xueshi Bai. *Laser-induced plasma as a function of the laser parameters and the ambient gas*. PhD thesis, Lyon 1, 2014.
- [54] D. Cremers, A. Beddingfield, R. Smithwick, R. Chinni, R. Jones, B. Beardsley, and L. Karchd. Monitoring uranium, hydrogen, and lithium and their isotopes using a compact laser-induced breakdown spectroscopy (LIBS) probe and high-resolution spectrometer. *Applied Spectroscopy*, 66:250–261, 2012.
- [55] Ali Rastegari, Matthias Lenzner, Jean-Claude Diels, Kristen Peterson, and Ladan Arissian. High-resolution remote spectroscopy and plasma dynamics induced with UV filaments. *Opt. Lett.*, 44(1):147–150, Jan 2019.
- [56] P. K. Diwakar, S. S. Harilal, M. C. Phillips, and A. Hassanein. Characterization of ultrafast laser-ablation plasma plumes at various ar ambient pressures. *Journal of Applied Physics*, 118(4):043305, 2015.
- [57] M Ivković and N Konjević. Stark width and shift for electron number density diagnostics of low temperature plasma: application to silicon laser induced breakdown spectroscopy. *Spectrochimica Acta Part B: Atomic Spectroscopy*, 131:79–92, 2017.
- [58] Nikola Konjević. Plasma broadening and shifting of non-hydrogenic spectral lines: present status and applications. *Physics reports*, 316(6):339–401, 1999.

References

- [59] Waldemar Hübert and Georg Ankerhold. Elemental misinterpretation in automated analysis of libs spectra. *Analytical and bioanalytical chemistry*, 400:3273–3278, 2011.
- [60] A. Kramida, Yu. Ralchenko, J. Reader, and and NIST ASD Team. NIST Atomic Spectra Database (ver. 5.10), [Online]. Available: <https://physics.nist.gov/asd> [2023, April 9]. National Institute of Standards and Technology, Gaithersburg, MD., 2022.
- [61] Lloyd Wallace and Kenneth Hinkle. The 136.6-5400.0 nm spectrum of Cr I. *The Astrophysical Journal*, 700(1):720, 2009.
- [62] Ali Rastegari, Matthias Lenzner, Ladan Arissian, Jean-Claude Diels, and Kristen Peterson. Utilization of self-absorption for high resolution laser induced breakdown spectroscopy. In *CLEO: 2018*, page SM1O.7, San Jose, CA, 2018. Optical Society of America.
- [63] Ladan Arissian, Ali Rastegari, Brian Kamer, and Jean-Claude Diels. Enhanced resolution in remote sensing using uv filaments with long pulses. In *Frontiers in Optics / Laser Science*, page JW3A.6. Optica Publishing Group, 2018.
- [64] Ali Rastegari, Matthias Lenzner, Chengyong Feng, Ladan Arissian, Jean-Claude Diels, and Kristen Peterson. Exploiting shock wave and self-absorption for high resolution laser induced breakdown spectroscopy. In *Conference on Lasers and Electro-Optics*, page JW2A.77. Optica Publishing Group, 2017.
- [65] P. L. Varghese and R. K. Hanson. Tunable diode laser measurements of spectral parameters of HCN at room temperature. *J. Quant. Spectrosc. Radiat. Transfer*, 31:545–559, 1984.
- [66] Beatrice Campanella, Stefano Legnaioli, Stefano Pagnotta, Francesco Poggialini, and Vincenzo Palleschi. Shock waves in laser-induced plasmas. *Atoms*, 7(2), 2019.
- [67] P. K. Panigrahi and K. Muralidharl. *Schlieren and Shadowgraph methods in heat and mass transfer. Chap.2: Laser Schlieren and Shadowgraph*. Springer, 2012.
- [68] Gary S Settles and Michael J Hargather. A review of recent developments in schlieren and shadowgraph techniques. *Measurement Science and Technology*, 28(4):042001, feb 2017.
- [69] Leonid Ivanovich Sedov and AG Volkovets. *Similarity and dimensional methods in mechanics*. CRC press, 2018.

References

- [70] Ali Rastegari and Jean-Claude Diels. Investigation of the plume generated in lib process induced by a ps uv laser. In *Conference on Lasers and Electro-Optics*, page JTU3A.42. Optica Publishing Group, 2021.
- [71] P. Q. Elias, N. Severac, J.-P. Tobeli, R. Bur, . Houard, Y.-B. Andre, S. Albert, and A. Mysyrowicz. Improving supersonic flights with filamentation. In *COFIL 2018*, page 41, 2018.

Chapter 5

Investigation of laser-induced discharge via UV filaments

5.1 Introduction

Triggering and guiding high voltage electrical discharges can have many applications. Among them, control of lightning has caught attention during the past years [1–6]. Lightning is one of the most lethal and damaging natural phenomena. Between the years 2020 and 2022 lightning has caused more than 19,000 wildfires burning more than 12,000,000 acres in the US at the cost of billions of dollars [7]. The yearly cost of lightning is much higher if one includes the annual loss resulting in damage to electronic systems, buildings, infrastructures, aircrafts, and space rockets [8]. Many believe that the number of lightning strikes is going to be increased due to climate change [9], and considering the incredible destruction and cost of lightning caused damage, there is an urgent and continuing need to provide lightning protection to national forests and other critical assets. The ultimate goal is to create a mobile unit capable of following a storm, trigger lightning reliably and instantaneously, and discharge it to a location where the current/charge could be dissipated

harmlessly.

The first known attempt to manually discharge a cloud has been performed by Benjamin Franklin in 1752. He has tried to send a kite into the stormy sky in order to provide a preferential path for the discharge from clouds to the ground. Since then different approaches have been tried to discharge and control lightning. One of these approaches which is based on the idea of creating an artificial conductive path for lightning is to utilize small rockets trailing a long grounded wire to guide lightning discharges, a technique first used in 1967 [10]. The rockets can not be launched on a semi-continuous basis, hence the success of this method is dependent on the correct firing moment of the rocket as it needs to be launched at the right moment when appropriate lightning conditions are already present. The charges created at the high local field of a sharp point, in this case, the rocket and wire, modify the electric field resulting in the reduction of the effectiveness of this method. ¹ This method has only 60% success rate as reported in [12], requires expendable wires and rockets, and cannot be implemented in urban areas as its falling debris are a danger to buildings and humans. A more reliable, faster method applicable at a higher repetition rate is desirable if the goal is to discharge a cloud rather than capture occasional lightning.

Since the invention of lasers they have been investigated as potential candidates for guiding and triggering lightning discharges, and high power laser beams have been beamed to the sky in multiple attempts to achieve this goal. Attempts in the early 90's with CO₂ lasers [13] failed because the laser produced ionization consisted of discontinuous "plasma beads". On the other hand, ultrashort laser filaments are promising candidates in that regard, because they produce ionized channels over extended distances comparable with atmospheric scales [14–16].

Most of the works to date have focused on near-infrared filaments [17–19], due to the

¹These shielding space charges move with the drift velocity of electrons in air ($2 \cdot 10^5$ m/s [11]), which is much larger than the speed of the rocket.

Chapter 5. Investigation of laser-induced discharge via UV filaments

wide availability of the Ti:Sapphire technology providing 800 nm pulses. More recently, excursions further into the IR [6], and even in the mid-infrared [20], have also shown that the larger filament volume and energy partly balance the low density of free charges related to the less efficient multiphoton ionization for larger wavelengths.

Conversely, the ionization of O_2 only needs three photons at 266 nm instead of eight at 800 nm. The multiphoton ionization is, therefore, more efficient at shorter wavelengths, which results in much higher plasma densities in the case of an ultraviolet laser [21, 22]. Furthermore, they produce a more homogeneous plasma channel than their near-infrared counterparts [23] and can give rise to similar multiple filamentation patterns that provide numerous filaments in parallel, adding up their conductivities [24]. Indeed, the first proposal to guide lightning using ultrashort lasers focused on ultraviolet lasers [25]. However, experimental demonstrations, that were performed over several tens of centimeters in both pure nitrogen and air, relied on tightly focused ($f = 0.3\text{--}1.5$ m) UV lasers rather than on loosely focused, filamenting beams [26–28].

The lifetime of the plasma is in the range of nanoseconds to tens of nanoseconds for the free electrons [29] and in the microsecond range for the ions. The speed of the guided discharge propagation amounts to 10^5 m/s for a leader regime in gaps or 3–7 m [18], and 10^6 m/s in a streamer regime for a shorter gap of 2 m [30]. Although this propagation speed is 10 times faster than that of unguided discharges, it constitutes a clear limitation to the triggering and guiding of discharges on distances in the meter range and above. It can be concluded that the guiding mechanism in filament induced discharges is the air rarefaction caused by the shock-wave (due to recombinations) that creates a preferential path for the discharge [31]. It would be desirable to have the discharge guided by the conductivity of the plasma. Unfortunately, as mentioned the filament created plasma lives only for a few nanoseconds, while it takes microseconds to establish a discharge. Diels and Zhao [25] suggested adding to the main ionizing pulse either longer pulses in the visible range or a train of ultraviolet pulses, in order to photodetach electrons from both O_2^-

Chapter 5. Investigation of laser-induced discharge via UV filaments

and O^- ions, keeping highly mobile free charges, namely electrons, available. Rambo et al [27] quantified this approach, estimating that at least 5 J at 750 nm in about 10 μ s are necessary to maintain the plasma density created by 100 mJ, 800 fs, 248.6 nm laser pulses at a repetition rate of 10 Hz, so as to guide discharges over 10 m.

The objective of the tests presented in this chapter is to:

- Investigate the effectiveness of UV filaments to trigger a discharge
- Investigate the possibility to increase the length and density of the filament created electron plasma by using nanosecond pulses of other wavelengths. 10 ns frequency-doubled Nd:YAG laser at 532 nm was chosen for photodetaching O^- , and a Nd:YAG laser at 1064 nm for plasma heating.

5.2 Experimental setup

5.2.1 High voltage laboratory

The discharge experiments have been performed in the high voltage laboratory located on the roof of CHTM (Center of High Technology Materials). The laser beams are combined in the laboratory and sent via a beam director to HV (High-Voltage) lab. Fig. 5.1 shows the lab and the two mirrors used for redirecting the laser beam(s) into the HV lab. The red arrows show the propagation path for the beam(s). The laser beam(s) enter the HV lab through a hole in the wall of the lab. An optical detector is utilized to monitor the UV filament arrival time (Fig. 5.1(c)). Filters have been located in front of the detector to ensure that only the UV beam is detected by the detector.

An image of the inside of the HV lab is represented in Fig. 5.2(a). Two hollow steel spheres (16 inch diameter) are used as electrodes and the laser beams would pass through

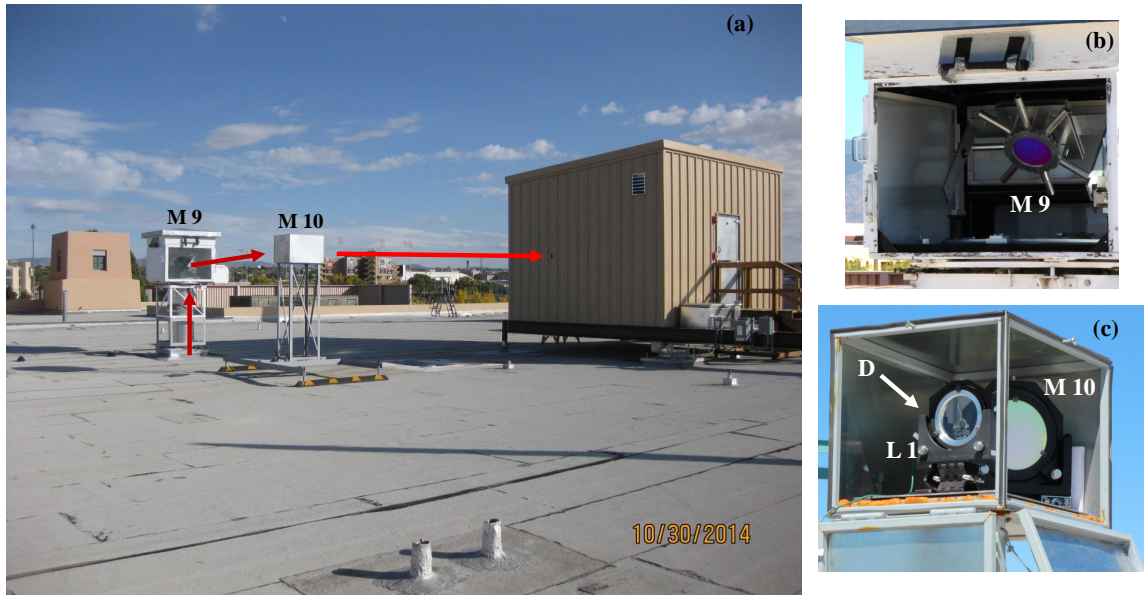


Figure 5.1: (a) High voltage lab and mirrors on the roof. The path of the laser beam(s) is shown by red arrows. (b) and (c) are showing the guiding optics. M9-10: 45° 1064 and 532 and 266 nm HR mirrors; L1: Fused silica Lens with 9 m focal length. For the complete schematics of the optical elements please refer to Fig. 5.4. D: The optical detector which is used to monitor the UV filament arrival time. Filters have been located in front of the detector to ensure that only the UV beam is detected by the detector.

the holes in both the positive and negative electrodes. The propagation path of the laser beam(s) is represented with red arrows. A schematic diagram of the arrangement of the discharge circuit is shown in Fig. 5.2(b). Two capacitor banks each consisting of ten capacitors with an equal capacitance of 0.2 nF were used for charging the electrodes. The capacitor banks were designed for minimum inductance, resulting in a discharge rise time of less than 20 ns. Two high voltage power supplies with opposite polarities (*PTS-300 Hipots* from *High Voltage Inc.*) are used to charge each capacitor bank up to 300 kV. These power supplies were originally designed for insulation resistance testing of dielectric materials, in which case the leakage current is very small. To ensure safety, the controller is equipped with a safety relay that shuts down the 300 kV power supply when the detected current exceeds the rated value of 5 mA. However, the discharge current in our experiments was in the range of hundreds of Amperes. Therefore, additional capacitor banks are necessary to

supply the high current required, instead of using the high voltage power supplies directly.

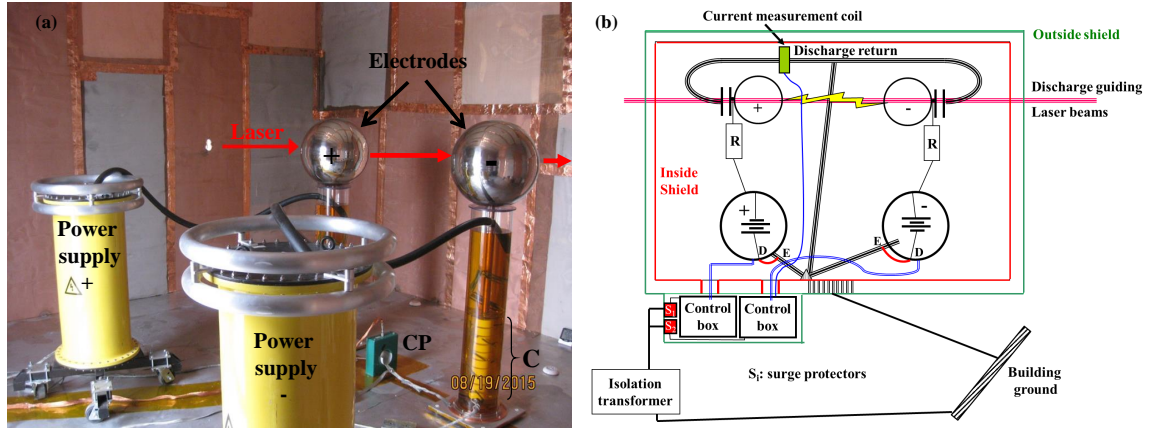


Figure 5.2: a) Experimental setup. (b) Schematic diagram of the circuit.

The discharge current is measured with a current probe (*Pearson* current monitor model 310) connected to an oscilloscope. As mentioned before a photo-detector is positioned after the last turning mirror (Fig. 5.1(c)) in order to monitor the arrival time of the UV filament. The acquisition of the discharge current via the oscilloscope was triggered by the signal from this detector. This made it possible to measure the delay between the laser pulses and the induced discharge. The last charging resistor of each capacitor bank (the last charging resistor of the capacitor bank is the one connected to the ground) consists of a $100\text{ M}\Omega$ and a $136\text{ k}\Omega$ in series. The charging voltage of each capacitor bank is measured by monitoring the voltage across this $136\text{ k}\Omega$. Calibration curves to convert this voltage to the actual charging voltage of the capacitor banks have been acquired before the beginning of the experiments.

A LabVIEW program is used to read different voltage waveforms from the oscilloscope and then save them as text files. For each discharge 4 voltage waveforms are recorded: 1. The voltage from the current probe which is proportional to the discharge current, 2 and 3. The voltage waveform of the two capacitor banks, and 4. the signal from

the photodetector. The high-voltage control boxes as well as the oscilloscope and the laptop used to collect data were set outside of the HV lab and shielded from electromagnetic radiation in a grounded metal box. All the cables inside the HV lab were shielded inside grounded metallic mesh in order to be protected from noise.

For safety purposes, the HV lab at CHTM is not only located on the roof of the building, but it is also built as a Faraday cage to prevent radiated fields from coupling to the structure. The Faraday cage consists of a two-layer shield with a single ground point between the layers. The inside layer is made of wire mesh, while the outside layer is made of solid metallic plates. Additionally, the HV lab has its own separate single-ground return, rather than using the utility or building structure ground. To estimate the electrical field distribution inside the Faraday cage, simulations were performed for the case of applying 300 kV to each electrode ². As shown in Fig. 5.3, the maximum electric field at the walls of the cage is 1 kV/cm, which is significantly lower than the minimum electric field required for breaking down in the air for the proposed distances of high voltage elements in the HV lab. The discharge circuit is also designed in a way that a short circuit inside the cage could be formed in case a discharge happens between the shield and high-voltage sources.

5.2.2 Laser sources

The experiments were performed using three different laser sources:

- A home-designed UV laser delivered 200 ps long pulses with 0.27 J output energy at a central wavelength of 266 nm and 1.25 Hz repetition rate [32, 33].
- *Thales* green laser with a wavelength of 532 nm, pulse energy of 0.85 J, and pulse width of 10 ns.

²Simulations were performed with the assistance of J. Elizondo at Sandia National Lab.

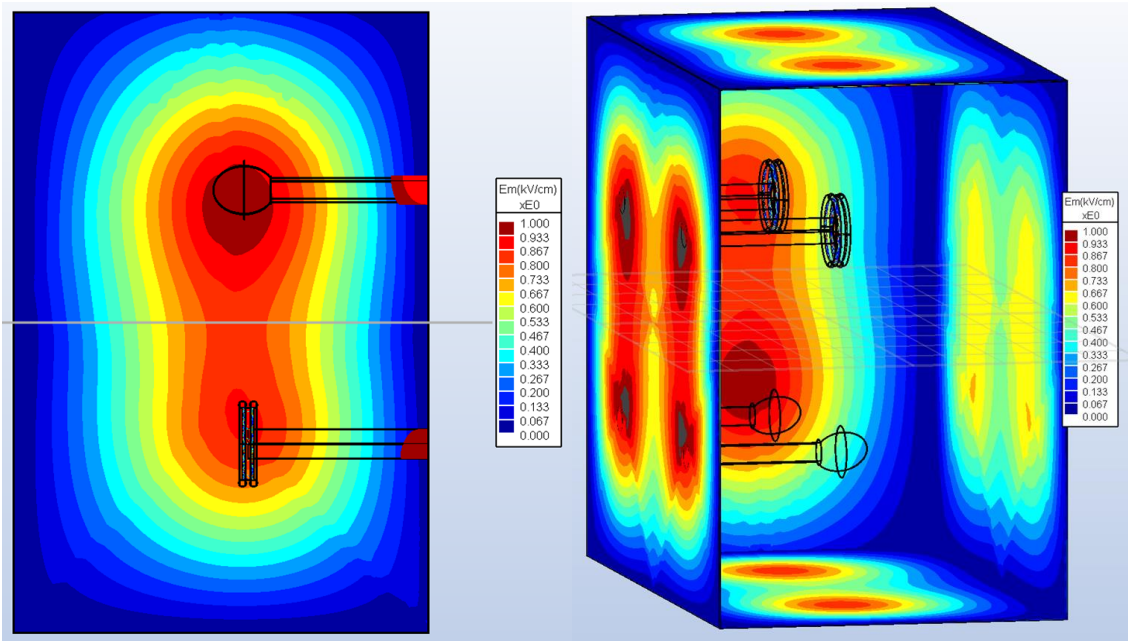


Figure 5.3: Simulation results showing the electric field on the walls of the Faraday cage and also for the electrodes and power supply toroids. Simulations were performed with the assistance of J. Elizondo at Sandia National Lab.

- *Thales* IR laser with a wavelength of 1064 nm, pulse energy of 1.1 J, and pulse width of 10 ns.

These three beams have been expanded and combined in the laboratory before being sent to the roof. Combining three laser beams with different wavelengths requires both spatial and temporal alignment. Achieving temporal alignment is easy: the Q-switches of the three lasers can be fired with the desired timing. However, achieving spatial alignment is more challenging, as the transverse overlap is required even after the beams have propagated for 30 meters. Additionally, longitudinal overlap, or alignment of the beam focus positions, is necessary because high-intensity beams are required for photo-detachment and plasma heating.

Figure 5.4 shows the schematic diagram of the beam combination. The 1064 nm and 532 nm beams are first combined with a mirror labeled as M11 and expanded by the

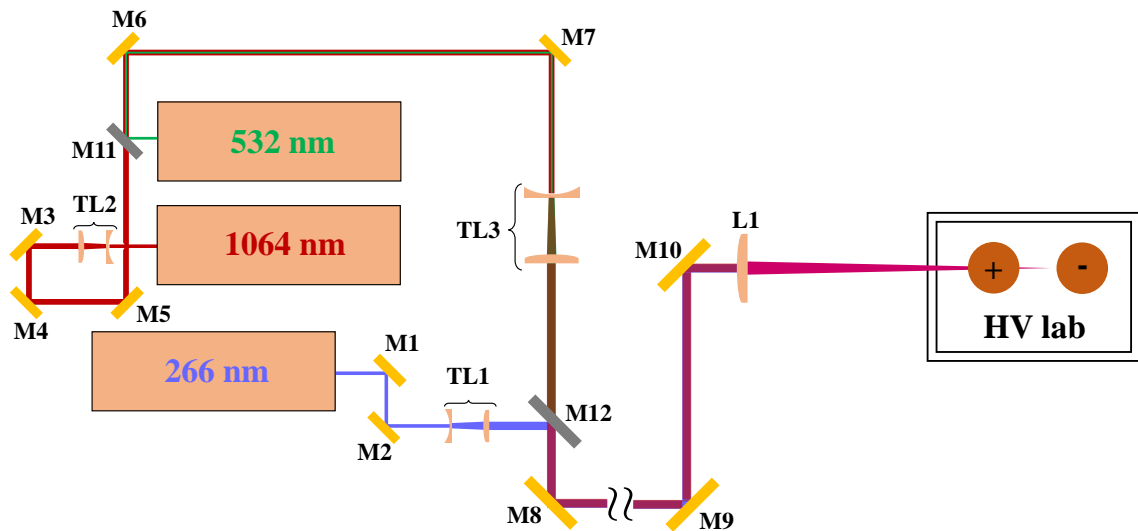


Figure 5.4: Combination and propagation of three laser beams into the high voltage lab on the roof; M1-2: 45° 266 nm HR (High Reflection) mirrors; M3-5: 45° 1064 nm HR mirrors; M6-7: 45° 1064 and 532 nm HR mirrors; M8-10: 45° 1064 and 532 and 266 nm HR mirrors; M11: HR 532 nm and HT (High Transmission) 1064 nm beam combining mirror; M12: HR 266 nm and HT 1064 and 532 nm beam combining mirror; L1: Fused silica Lens with 9 m focal length; TL1: Telescope with a magnification of 2.7; TL2: Near afocal telescope with a magnification of 1.13; TL3: Telescope with a magnification of 7; All the telescope lenses are uncoated fused silica. The propagation distance of the UV laser up to the middle of the two electrodes is approximately 30 meters.

telescope TL3. These two beams are then combined with the expanded UV beam at the mirror labeled as M12. At this point, the three beams have similar diameters of about 3 inches. These 3 beams are reflected by three mirrors M8-10 and are focused to the middle point of two electrodes with a 9 m focusing lens (L1). Mirrors M9 and M10 and the lens L1 are located on the roof as demonstrated in Fig. 5.1. In order to bring the geometric focus of the three beams together, telescopes TL2 and TL3 are used to adjust the divergence of the 1064 nm and 532 nm laser beams, respectively, such that the large chromatic aberration of the focusing lens can be compensated. With these arrangements, it was possible to propagate these 3 beams collinearly over about 30m to the roof. The previously mentioned UV laser energy is measured at the source. The UV beam goes through 3 lenses and is reflected from 6 mirrors, it will have lost energy through all these

optics before reaching the electrodes. We measure a transmission factor of 70% from the source to the middle position between the electrodes. Consequently, the UV pulses have an energy of about 185 mJ at the location of the discharge.

5.3 Experimental results

5.3.1 UV filament induced discharges

In this section, high-voltage discharges induced by only UV filaments are discussed. Different gap distances and electrode configurations were investigated. In Fig. 5.5 images of completely guided discharge (a) and partially guided discharge (b) between the electrodes are presented. The gap distance between the electrodes is 37.3 cm and 186 kV and -186 kV are applied to the positive and negative electrodes. Pictures of the discharge were taken with a camera synchronized with the UV laser pulse. In the case of partially guided discharge, it has been observed that the guided portion always occurs on the negative electrode side (the right side of the image). This phenomenon is similar to what has been observed in long-gap laser-guided discharge [34]. This phenomenon can be explained by the fact that plasmas are more effective at guiding streamers and leaders from a negative electrode than from a positive electrode, and the discharge development from the negative electrode plays an important role in the guidance effect.

For any specific gap distance between the electrodes, the self-breakdown voltage is defined as the voltage at which discharge occurs without the presence of the triggering laser. It has been reported in the literature that by using 800nm filaments to trigger the discharge a 20 to 30% reduction in the breakdown voltage in comparison with the self-breakdown voltage has been reported [17, 19, 35–37]. In our measurements with the UV Filament, we observed a 50% reduction of the breakdown voltage with respect to the self-breakdown voltage which is a significant reduction. The results of these measurements

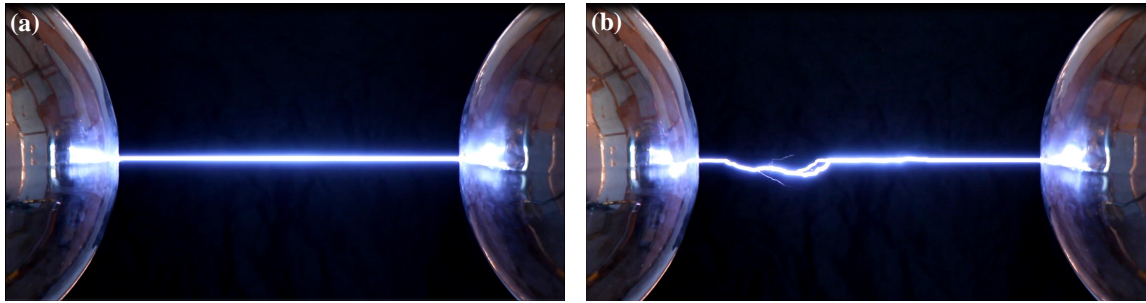


Figure 5.5: (a) Image of a completely guided discharge between the electrodes. (b) Image of a partially guided discharge between the electrodes. For both cases, the gap distance is 37.3 cm and 186 kV and -186 kV are applied to each electrode resulting in an electric field of approximately 997 kV/m. This picture is taken with a camera synchronized with the UV laser pulse from the outside of the HV lab.

for different gap distances are represented in table 5.1. Similar results for UV laser pulses with much tighter focusing have been reported before [27, 28]. This confirms that the UV filament is more suitable for laser-induced discharge compared to the 800 nm laser filaments. It should be mentioned that the same measurements for longer gap distances were not possible, due to the fact that self-breakdown for longer gaps in most cases resulted in a discharge between the negative electrode and the positive charging cable connected to the positive electrode.

d (cm)	V_B (kV)	V_{UV} (kV)	V_{UV}/V_B
5.8	140	76	0.54
10.2	246	124	0.50
11.7	300	148	0.49

Table 5.1: Comparison of the self-breakdown voltage and the breakdown voltage in the presence of the UV filament for different gap distances. d: Gap distance between the electrodes; V_B : Self-breakdown voltage; V_{UV} : Breakdown voltage in the presence of the UV filament.

In Fig. 5.6 we can see two discharge current graphs that are induced by the UV filament only. The left image corresponds to a 37.5 cm gap and applied voltages of 186 kV and -186 kV on the spheres respectively. The peak negative current is 0.605 kA, and the delay

between the laser pulse and discharge for this specific discharge is 650 ns. The right corresponds to a smaller 5cm gap. The voltages on the spheres are 36 kV and -36 kV respectively. The peak negative current is 0.199 kA, which is much smaller than that for the long gap. The delay between the discharge and the laser pulse is about 733 ns for the imaged discharge.

The delay between the UV pulse and the first negative current peak, as presented in Fig. 5.6, is considered as the discharge delay. The delay is typically in the microsecond range. The purpose of the following experimental tests is to see if the delay can be reduced by adding extra laser pulses.

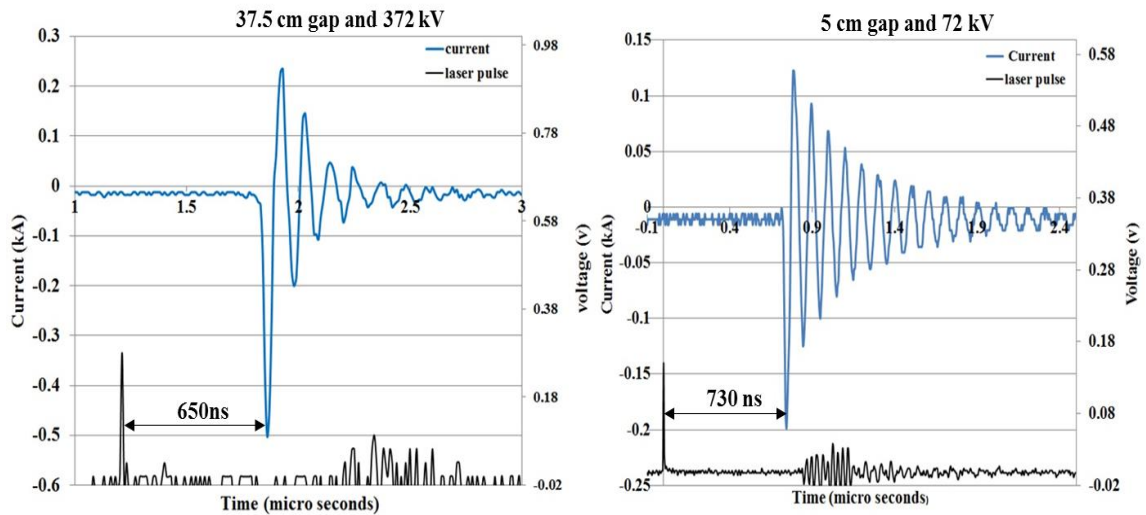


Figure 5.6: Left) The discharge current and laser pulse for 372 kV and a 37.3 cm gap. The maximum negative current is 0.502 kA. The delay is about 650ns. Right) The discharge current and laser pulse for 72 kV and a 5 cm gap. The maximum negative current is 0.199 kA. The delay is about 733 ns.

5.3.2 Combination of the UV filament with two other lasers

As discussed in the introduction the objective is to decrease the discharge threshold and reduce the delay between laser and discharge by adding a green (532nm) laser pulse for

Chapter 5. Investigation of laser-induced discharge via UV filaments

photodetachment of O^- and an IR (1064nm) laser pulse for plasma heating. We investigated different combinations as follows:

- Only UV Filaments
- Combination of UV Filaments and Green laser pulses (532nm). We did various tests for different voltages and also different delay times between the UV Filament and Green laser pulses.
- Combination of UV Filaments and IR laser pulses (1064nm). We did various tests for different voltages and also different delay times between the UV Filament and IR laser pulses.
- Combination of UV Filaments, Green laser pulses (532nm), and IR laser pulses (1064nm). We did various tests for different voltages and also different delay times between the UV Filament, Green laser pulses, and IR laser pulses.
- Green laser pulses, IR laser pulses, and a combination of Green and IR lasers.

Various parameters for each set of data were recorded, such as the temperature inside the HV room, the barometric pressure, the absolute and relative humidity, the laser pulse energies, the discharge shape, the current waveform, the spectrum of the discharge, and the voltage on the electrodes. The temperature and relative humidity in the experimental chamber varied from 27°C to 35°C and 13% to 23%, respectively during the campaign. For each set of data, 100 data points were recorded (in other words 100 laser shots). The probability of discharge, the average delay between the laser pulse and discharge, and the mean square deviation of the delay were the main analyzed data for each set of data. The experimental results can be summarized as follows. No laser induced discharge was observed for the Green laser pulse alone, IR laser pulse alone, or their combination.

One of the main characteristics of the collected data is having a large mean square deviation of typically 30%. As a typical example of data, Fig. 5.7(a) and (c) show plots

of the delay between the laser pulse and the discharge current versus total applied voltage between the electrodes for different beam combinations and delays.

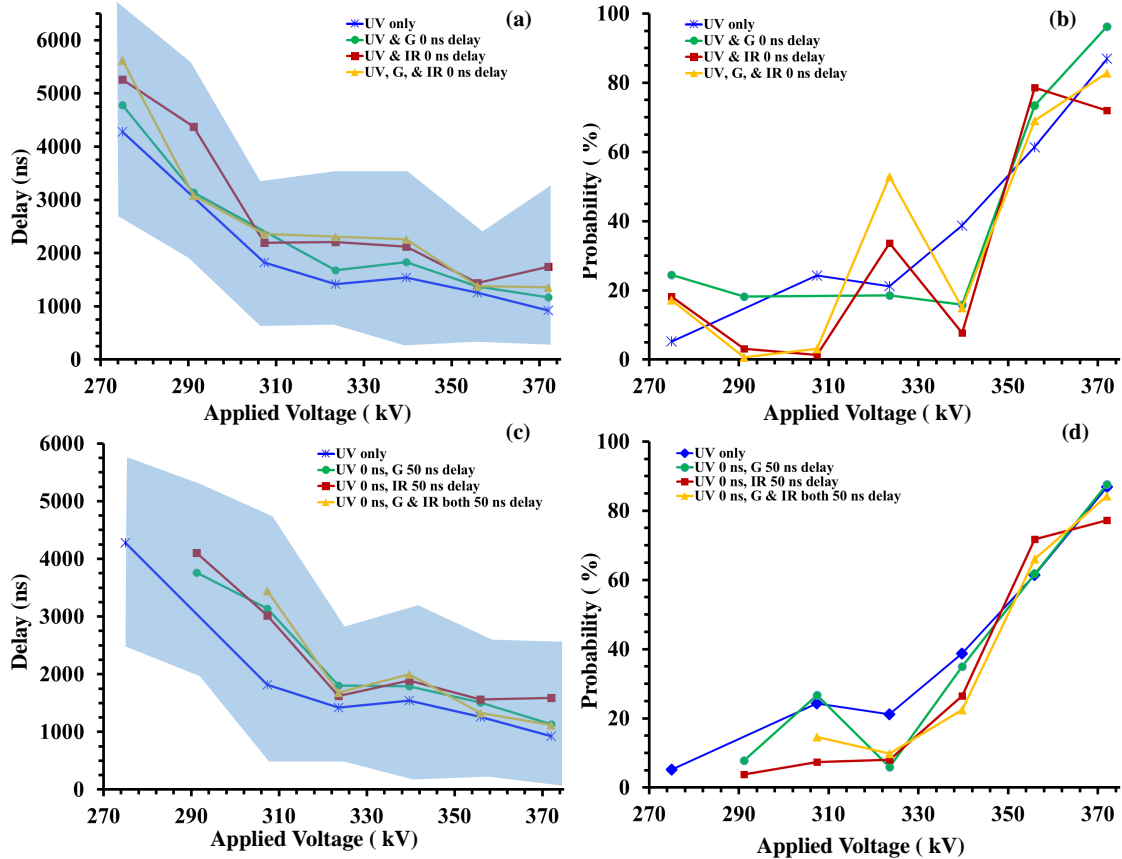


Figure 5.7: Data are taken for a 37.5 cm gap between the electrodes and each point on graph is average of 100 data points. All data points are selected for the same absolute humidity within the range of 0.0093-0.0099 kg/m³. (a) and (c) delay between laser pulse and the discharge versus the voltage applied between the electrodes. The shaded area represents then mean square deviation of the data. (b) and (d) discharge probability versus the voltage applied between the electrodes.

For these sets of data, the gap between the two electrodes (spheres) was 37.3 cm. For each set of data, the average has been taken from 100-250 data points. The blue shaded area is representing the mean square deviation of the data. We have examined different delay times between the UV Filaments and laser pulses and also we have examined different delay times between the Green and IR laser pulses. And we concluded that adding the Green and/or IR 10 ns laser pulses, as can be seen in Fig. 5.7(a) and (c), does not have a

Chapter 5. Investigation of laser-induced discharge via UV filaments

significant effect on the discharge and the delay between the laser pulse and discharge is much longer than the plasma lifetime. In Fig. 5.7(b) and (d) the discharge probability is plotted versus total applied voltages on the electrodes for the same data sets and configuration. As it is expected the discharge probability is increasing as we increase the voltage, but yet it could be seen that the different beam combinations do not have any significant effect on probability. It worth's mentioning that the conditions such as absolute humidity and temperature were varying during the experiments. In Fig. 5.8 we can see the effect of absolute humidity on the discharge probability and delay between the discharge and laser pulse. So we had to be careful to compare the data from the same conditions with respect to each other. All data points in Fig 5.7 have about the same absolute humidity within the range of 0.0093-0.0095 kg/m^3 .

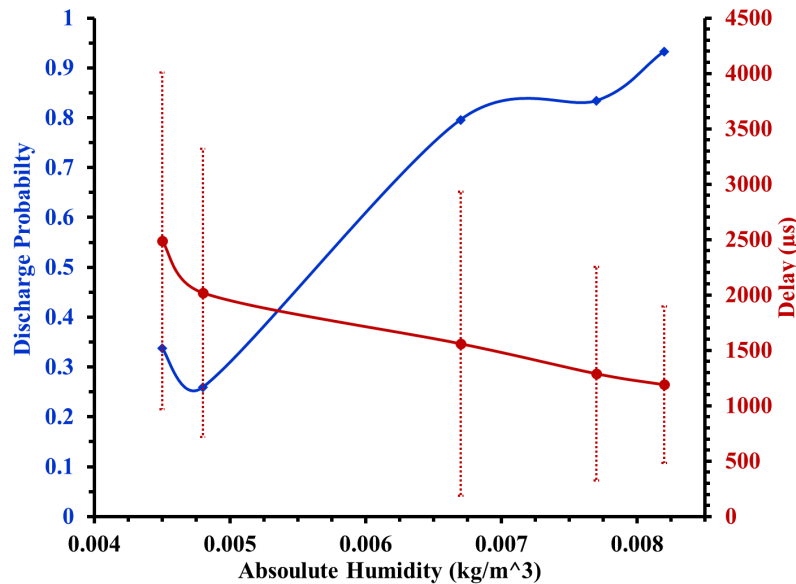


Figure 5.8: Delay (in red) and discharge probability (in blue) versus absolute humidity. Data are taken for a 37.5 cm gap between the electrodes and each point on graph is average of 100 data points. The error bars represent the standard deviation of the measured data. Only UV filaments have been used in these data points

5.3.3 Filament Conductivity Measurements

In Fig. 5.9 two distinct electric circuits that are utilized for measuring the conductivity of the plasma channel created by either a UV filament alone or a UV filament in combination with two other laser beams are illustrated. The first circuit is used to measure the spatially averaged conductivity of the plasma channel over the gap distance between the two electrodes as represented in Fig. 5.9(a). The second circuit (Fig. 5.9(b)) is used to determine the conductivity of the plasma channel along the direction of the filament's propagation. In both circuits, the current waveform is converted to a voltage waveform using a $10\ \Omega$ resistor and recorded by an oscilloscope.

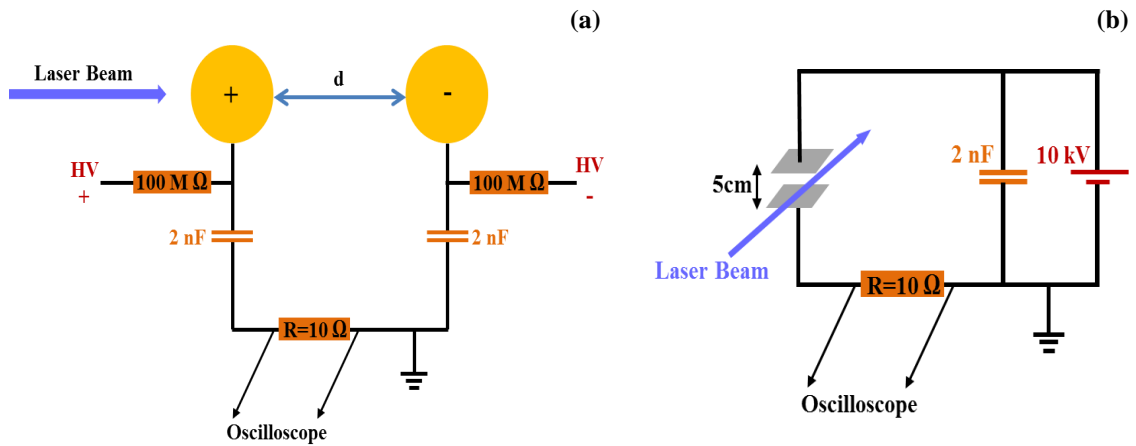


Figure 5.9: Experimental setups for measuring the conductivity of the plasma channel. (a) The circuit that is used to measure the spatially averaged conductivity of the plasma channel over the gap distance between the two electrodes (b) The circuit that is used to determine the conductivity of the plasma channel along the direction of the filament's propagation.

We investigated the spatially averaged conductivity of the plasma channel by varying the gap distance between the electrodes. For each measurement, we recorded the voltage waveform of the $10\ \Omega$ resistor at different applied voltages. The applied voltage represents the total voltage, which is twice the voltage applied on each electrode. Figure 5.10 shows the results of these measurements for a gap distance of $37.3\ \text{cm}$, with an example of the

Chapter 5. Investigation of laser-induced discharge via UV filaments

recorded voltage waveform shown in red in Fig. 5.10(a). The applied voltage to the electrodes was 30 kV. The photodetector's recorded signal corresponding to the arrival time of the UV laser pulse is shown in blue. In contrast to the discharge experiment, where a significant delay was observed, we observed a very small delay (~ 12 ns) between the UV filament and the current in these measurements.

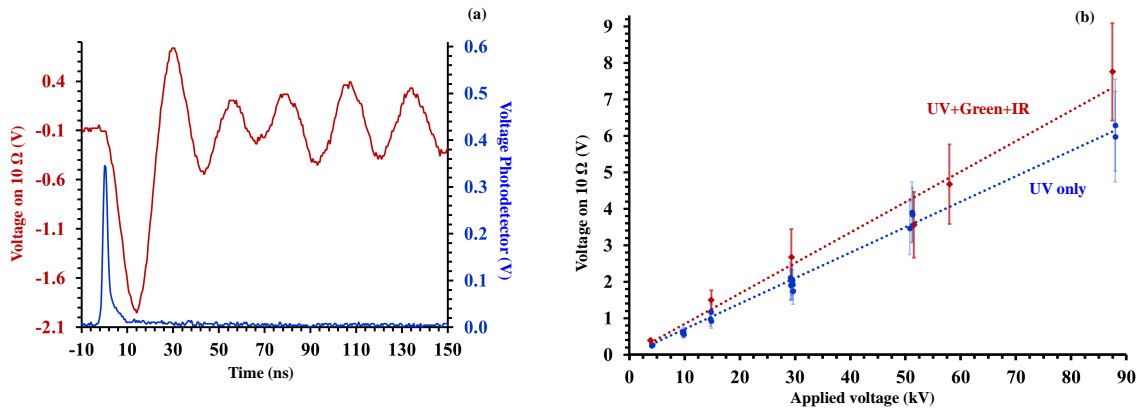


Figure 5.10: Results for the measurement of the spatially averaged conductivity of the plasma channel at the gap distance of 37.3 cm. (a) An example of the recorded voltage waveform across the 10 Ω resistor is plotted in red. The photodetector's recorded signal corresponding to the arrival time of the UV laser pulse is shown in blue. The applied voltage to the electrodes was 30 kV. (b) The peak voltage values across the 10 Ω resistor for different applied voltages on the electrodes are plotted. The blue data points correspond to the plasma induced by only the UV filament, while the red data points represent the recorded voltages when all three lasers were utilized. Each data point is an average of about 100 measurements. Error bars are included on the plots to represent the standard deviation of the measurements.

The peak voltage values across the 10 Ω resistor for different applied voltages on the electrodes are shown in Fig.5.10(b) (It should be noted that these values correspond to the first negative peak, as exemplified in Fig.5.10(a)). The blue data points correspond to the plasma induced by only the UV filament, while the red data points represent the recorded voltages when all three lasers were utilized. It can be seen that the measured signal is linearly proportional to the applied voltage. Each data point is an average of about 100 measurements. In both data sets, error bars are included on the plots to represent the

Chapter 5. Investigation of laser-induced discharge via UV filaments

standard deviation of the measurements. The average resistance of the plasma channel can be estimated by calculating the slope of the fitted line to the data points. For the cases of only UV filaments and all three lasers, the average measured resistance is approximately 3.8 k Ω /cm and 3.2 k Ω /cm, respectively. The conductivity has been slightly improved by adding additional short pulse lasers. However, as can be seen from the measurements, there are very large standard deviations, which make it difficult to definitively conclude the extent of the improvement. However as can be seen the measurements depict very large standard deviations, which makes it difficult to definitively conclude the degree of improvement. Similar measurements were also performed for the case of plasma induced by UV filaments with 11.5 cm gap distances. The average measured resistance was about 5 k Ω /cm.

The resistance per unit length of the plasma channel induced by UV filaments is calculated to be in the range of 3.8-5 k Ω /cm, which is lower than 9 k Ω /cm measured during a recent similar experiment with NIR filaments [37, 38]. Hence, the conductivity of the plasma channel generated by the UV filaments is significantly greater than that of the plasma channel created with the NIR filaments. This finding is in agreement with the findings of Liu et al. [22], who reported that the UV filament has a greater capacity for inducing high-voltage discharges.

As mentioned before the conductivity of the plasma channel along the direction of the filament's propagation is also measured using the circuit illustrated in Fig. 5.9(b). The current waveform is converted to a voltage waveform using a 10 Ω resistor and recorded by an oscilloscope. Two metallic square plane probing electrodes with an area of 4 cm² were placed on either side of the beam and moved along the propagation axis. The distance between the two electrodes was 2 cm and 10 kV was applied to the 2 nF probing capacitance. Figure 5.11 shows the results of these measurements with an example of the recorded voltage waveform shown in red in Fig. 5.11(a). The photodetector's recorded signal corresponding to the arrival time of the UV laser pulse is shown in blue. In contrast

Chapter 5. Investigation of laser-induced discharge via UV filaments

to the discharge experiment, where a significant delay was observed, we observed a very small delay between the UV filament and the current in these measurements.

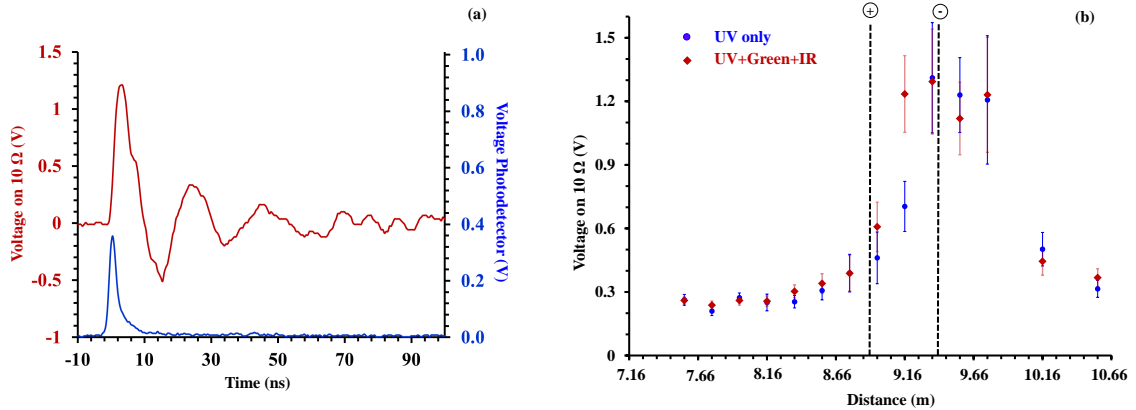


Figure 5.11: Results for the measurement of the conductivity of the plasma channel along the direction of the filament’s propagation. (a) An example of the recorded voltage waveform across the 10 Ω resistor is plotted in red. The photodetector’s recorded signal corresponding to the arrival time of the UV laser pulse is shown in blue. (b) The peak voltage values across the 10 Ω resistor for different locations along the propagation path of the lasers. The blue data points correspond to the plasma induced by only the UV filament, while the red data points represent the recorded voltages when all three lasers were utilized. Each data point is an average of about 100 measurements. Error bars are included on the plots to represent the standard deviation of the measurements.

The peak voltage values across the 10 Ω resistor as a function of the distance from the 9 m lens is shown in Fig. 5.11(b) (It should be noted that these values correspond to the first positive peak, as exemplified in Fig. 5.11(a)). The blue data points correspond to the plasma induced by only the UV filament, while the red data points represent the recorded voltages when all three lasers were utilized. Each data point is an average of about 100 measurements. In both data sets, error bars are included on the plots to represent the standard deviation of the measurements. It’s apparent that adding two more laser beams didn’t result in a noteworthy boost in plasma conductivity. Other combinations of different delays for the two nanosecond pulses have also been tested with similar conclusions. The two black dashed lines in Fig. 5.11(b) represent the position on which the two electrodes were placed for the spatially averaged conductivity measurements shown in Fig. 5.10(b).

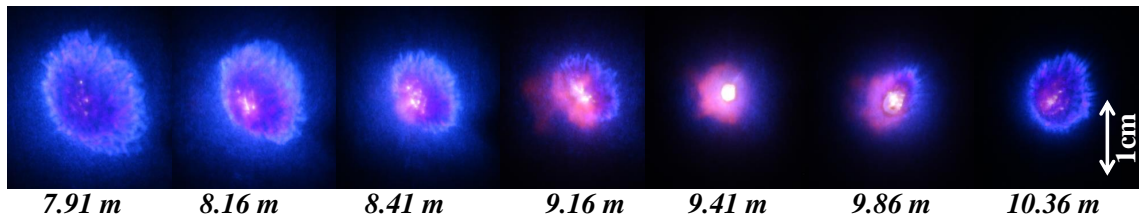


Figure 5.12: The beam profiles of UV filaments at different distances from the 9 m focusing lens. These beam profiles are captured by a digital camera recording the impact of the UV filament on a piece of paper. Different colors correspond to the fluorescent emission from the paper which is changing based on the impacted beam intensity. The white dots in the figure are related to multiple filaments.

It could be beneficial to compare the beam profile of the UV filament along its propagation path with the respective conductivity presented in Fig. 5.10(b). Figure 5.12 shows pictures of successive beam profiles as a function of the distance from the 9 m lens. The initially super-Gaussian profile has diffracted, propagating through turbulent air, until reaching the 9 m focal lens (beam diameter 20 cm). Multiple filaments are generated, as been reported in similar focusing conditions ($f = 10$ m) with near infrared filaments [39]. The distance over which the filaments are observed is about 2 m, which is much longer than the Rayleigh range (approximately 1 mm) for this focusing scheme.

5.3.4 Shadowgraphy measurements

The impulsive heating of air by an electrical discharge creates shock-waves of cylindrical the symmetry which propagates outward from the center line, leaving a low density channel behind. Initially, the shock-waves propagate with velocities much larger than the speed of sound, i.e. supersonic, but their velocity rapidly decreases to the speed of sound as they propagate. The shadowgraphy technique is used to investigate the characteristics of the mentioned low-density tube and shock-waves created by the UV filament induced electrical discharges. Shadowgraphy is an optical technique that can be used for the investigation of small amplitude changes in refractive index in transparent materials, which in

the case of electrical discharges are a consequence of the change in air density [40,41].

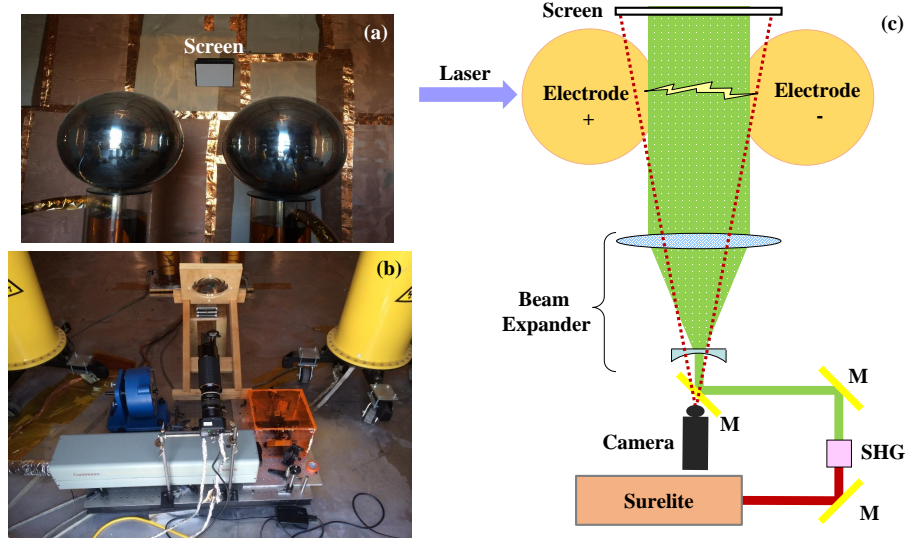


Figure 5.13: (a) The two electrodes are charged at 250 kV and their distance is 16 cm. The filament passes through two 3 mm diameter holes in each electrode. The shadow of the electrical discharge and associated shock-wave is projected onto a screen and recorded by a CCD camera. (b) The *Surelite* laser (Continuum), synchronized with a discharge triggering/guiding UV filament emits a 10 ns 100 mJ pulse, expanded, and aimed at the discharge. (c) Schematic diagram of the shadowgraphy setup; M: 45° mirrors, and SHG: Second Harmonic Generation crystal.

The probe beam is collimated and expanded (about 20 cm) green (532 nm) pulse with 10 ns temporal pulse width. This probe beam is sent perpendicular to the electrical discharge and is imaging the area of interest on a screen located at a 1.5 m distance from the discharge (Fig. 5.13). A CCD camera is used to capture the shadowgrams on the screen. A grid is printed on the screen that provides a reference for the size of shadowgrams. A master clock is used to synchronize the UV laser, the green laser, and the camera. A delay generator controls the relative delay times between the probe beam and the UV laser, making it possible to investigate the temporal evolution of the shock-waves and the low density channel. The distance between the electrodes is 16 cm and the total applied voltage on the electrodes is 250 kV. The electrical discharges are induced by UV filaments with an energy of 185 mJ per pulse. In Fig. 5.14, selected shadowgrams of electrical discharges

Chapter 5. Investigation of laser-induced discharge via UV filaments

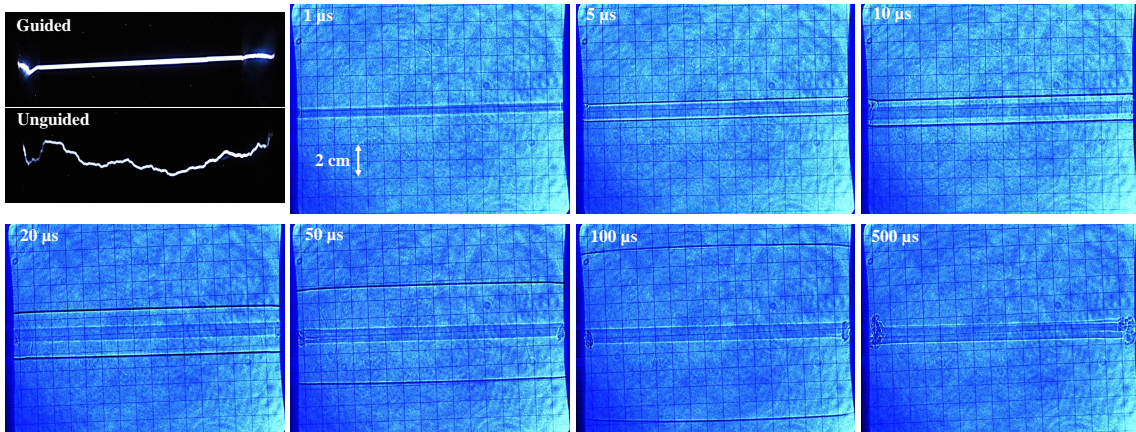


Figure 5.14: Top left: picture of a guided and unguided discharge. In the blue background: shadows of discharge taken at successive times after the UV filament pulse.

are displayed for different time delays between the UV laser and the probe beam. The low density channel left after the discharge has an approximate diameter of 8 mm. The low density channel is present at least up to 5 ms. Quantitative and accurate analysis of shock-wave propagation was challenging due to several factors. Firstly, the probe pulse is triggered and delayed with respect to the arrival time of the UV laser, but as is shown in previous sections the delay time between the discharge and the UV laser exhibits very large standard deviations. Additionally, even at the very high applied voltage on the electrodes, there are cases in which even though the UV laser is present, no discharge occurs.

Two-speed regimes are observed with respect to the propagation of the shock-waves generated by the electrical discharge. The first regime lasts up to 10 μ s. The propagation of the related shock-waves vs time in this regime follows the formula which was proposed by Sedov: $R = \left(\frac{E}{\rho}\right)^{\frac{1}{2+d}} t^{\frac{2}{2+d}}$ [42]. In this formula, E is the total energy transferred to the electrical discharge, ρ is the air density, and d=1, 2, 3 for planar, cylindrical, and spherical propagations respectively. The second regime starts after the plume is fully expanded and in this regime, the shock-wave propagates with constant speed. In Fig 5.15 the propagation distance of the shock-waves vs time for two different regimes is presented. It can

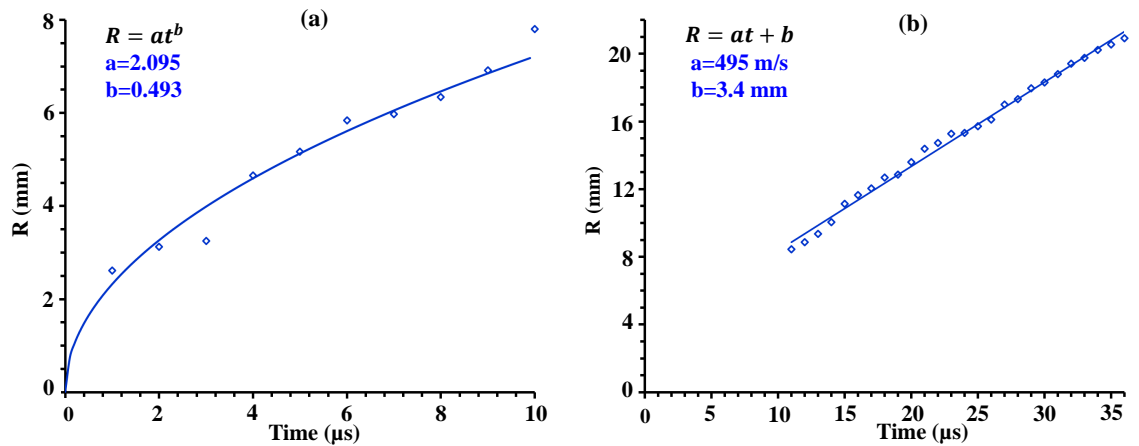


Figure 5.15: a) Shock-wave radius vs time for the first regime. b) Shock-wave radius vs time for the second regime.

be seen that for the first regime (Fig. 5.15(a)), the experimental data points are in good agreement with Sedov equation, with $d = 2.057$ which as expected corresponds to cylindrical propagation. As it is obvious from the Sedov formula the constant a represented in Fig. 5.15(a) is proportional to the deposited energy per length. From this value, the total deposited energy into the electrical discharge can be estimated to be 2.77 J. The air density at Albuquerque is estimated to be 0.9 kg/m^3 for the environmental conditions on the day of the experiment. The total energy stored in the two capacitor banks equals to 3.125 J, which is a close number to the calculated energy. For the second regime, it can be seen that the propagation of the shock-waves is linear with respect to time, and the slope of the slope of the line is 495 m/s.

5.4 Conclusion

Laser induced discharge in air can be achieved at voltages which are less than the half voltage needed for self-breakdown. UV filaments are capable of creating transient conductivity about 200 times bigger than IR (800 nm) filaments. Adding the Green (532 nm)

and/or IR (1064 nm) laser pulses did not have any statistical significant effect on the discharge probability or on the delay between the discharge and laser pulse. This may be due to the fact that these laser pulses are not long enough to have significant effect on discharge. These results are in agreement with measurements of electron density in 800 nm filament reported by A. Zigler [43]. In these measurements, a nanosecond pulse Nd:YAG pulse was delayed with respect to the 800 nm fs pulse. A slight increase in electron density was only recorded for delays less than 10 ns. One can conclude therefore that longer pulses are needed to keep the air ionized for the time needed to establish a discharge. Tests made with an Alexandrite laser were unsuccessful: these pulses could be stretched to 1 μ s, but the energy was limited to 200 mJ, not sufficient for plasma heating. Longer pulses and longer wavelength are desirable, such as could be achieved with atmospheric pressure CO₂ lasers. Better control over the transverse beam profile of the UV pulse is desirable, in order to achieve better confinement of the filament. In the case of 800 nm filaments, a better confinement of filaments has been reported by a combination of collimation and astigmatism control of the beam [43].

5.5 Future work

Another set of measurements that can be beneficial to a better understanding of the discharge mechanism is to study the spatial and temporal profile of electric fields involved in the discharge. Before we simulated the electric field evolution during a discharge. [11]. We believe that the electric field, both in time and space, can be measured by using the nonlinear four-wave mixing process as follows: $E_{2\omega} \sim \chi^{(3)} E_{\omega}^* E_{\omega}^* E_{Electric\ field}$. The schematic of the proposed setup for electric field measurements is illustrated in Fig. 5.16 (b). There are multiple papers in which authors have measured the $\chi^{(3)}$ of air and by knowing the intensity of the probe beam, by measuring the SHG by a detector we will be able to calculate the Electric Field. By using a translation stage to spatially scan the discharge and

References

also by scanning the delay between the probe pulse and discharge, it should be possible to measure the electric field both spatially and temporally. There are two candidates for the probe beam, fs 800 nm laser pulses of 50 mJ energy, and 200 ps 532 nm laser pulses with up to 2 J energy. The first option is going to provide much better temporal resolution, and the second option will provide higher probing energy.

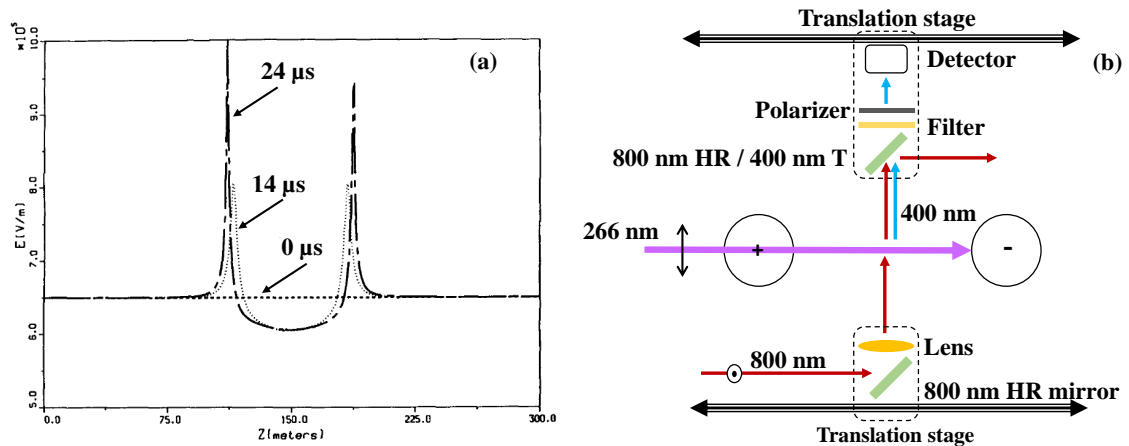


Figure 5.16: a) Electric field evolution in atmospheric pressure air following photoionization by a fs UV pulse. At $t=0$ electrons a(dotted line). The simulation shows the field enhancement at the extremities of the plasma (from ref. [11]). b) The schematic of the proposed setup for electric field measurements.

Acknowledgement

This research has been supported by the grant from Army Research office (ARO:W911-NF-1110297).

References

- [1] Thomas Produit, Pierre Walch, Clemens Herkommer, Amirhossein Mostajabi, Michel Moret, Ugo Andral, Antonio Sunjerga, Mohammad Azadifar, Yves-Bernard

References

- André, Benoît Mahieu, Walter Haas, Bruno Esmiller, Gilles Fournier, Peter Krötz, Thomas Metzger, Knut Michel, André Mysyrowicz, Marcos Rubinstein, Farhad Rachidi, Jérôme Kasparian, Jean-Pierre Wolf, and Aurélien Houard. The laser lightning rod project. *Eur. Phys. J. Appl. Phys.*, 93(1):10504, 2021.
- [2] Francis Théberge, Jean-François Daigle, Jean-Claude Kieffer, François Vidal, and Marc Châteauneuf. Laser-guided energetic discharges over large air gaps by electric-field enhanced plasma filaments. *Scientific Reports*, 7(1):40063, Jan 2017.
- [3] Ali Rastegari, Elise Schubert, Chengyong Feng, Denis Mongin, Brian Kamer, Jerome Kasparian, Jean-Pierre Wolf, Ladan Arissian, and Jean-Claude Diels. Beam control through nonlinear propagation in air and laser induced discharges. In *Laser resonators and beam control XVIII, Photonics West, Conference 9727-51*, pages 9727–51, San Francisco, CA, 2016. SPIE.
- [4] Elise Schubert, Ali Rastegari, Chengyong Feng, Denis Mongin, Brian Kamer, Jerome Kasparian, Jean-Pierre Wolf, Ladan Arissian, and Jean-Claude Diels. HV discharge acceleration by sequences of UV laser filaments with visible and near-infrared pulses. *New Journal of Physics*, 19(12):123040, 2017.
- [5] Thomas Produit, Guillaume Schimmel, Elise Schubert, Denis Mongin, Ali Rastegari, Chengyong Feng, Brian Kamer, Ladan Arissian, Jean-Claude Diels, Pierre Walch, Benoît Mahieu, Yves-Bernard André, Aurélien Houard, Clemens Herkommer, Robert Jung, Thomas Metzger, Knut Michel, André Mysyrowicz, Jean-Pierre Wolf, and Jérôme Kasparian. Multi-wavelength laser control of high-voltage discharges: From the laboratory to Säntis mountain. In *Conference on Lasers and Electro-Optics*, page JM2E.5. Optical Society of America, 2019.
- [6] A. Houard, V. Jukna, G. Point, Y-B. André, S. Klingebiel, M. Schultze, K. Michel, T. Metzger, and A. Mysyrowicz. Study of filamentation with a high power high repetition rate ps laser at 1.03 μm . *Opt. Express*, 24(7):7437–7448, Apr 2016.
- [7] National Interagency Fire Center. Lightning-caused wildfires. <https://www.nifc.gov/fire-information/statistics/lightning-caused>.
- [8] Yoav Yair. Lightning hazards to human societies in a changing climate. *Environmental Research Letters*, 13(12):123002, nov 2018.
- [9] Masson-Delmotte, V. P. Zhai, A. Pirani, S. L. Connors, C. Péan, S. Berger, N. Caud, Y. Chen, L. Goldfarb, M. I. Gomis, M. Huang, K. Leitzell, E. Lonnoy, J. B. R. Matthews, T. K. Maycock, T. Waterfield, O. Yelekçi, R. Yu, and B. Zhou. *IPCC, 2021: Climate Change 2021: The Physical Science Basis. Contribution of Working Group I to the Sixth Assessment Report of the Intergovernmental Panel on Climate Change*, volume in Press. Cambridge University Press, 2021.

References

- [10] M. M. Newman, J. R. Stahmann, J. D. Robb, E. A. Lewis, S. G. Martin, and S. V. Zinn. Triggered lightning strokes at very close range. *J. Geophys. Res.*, 72:4761–4764, 1967.
- [11] Xin Miao Zhao, Jean-Claude Diels, Cai Yi Wang, and Juan Elizondo. Femtosecond ultraviolet laser pulse induced electrical discharges in gases. *IEEE J. Quantum Electr.*, 31:599–612, 1995.
- [12] P. Hubert, P. Laroche, A. Ebert-Berard, and L. Barret. Triggered lightning in New Mexico. *Journal of Geophysical Research*, 89:2511–2521, 1984.
- [13] S. Uchida, Y. Shimada, H. Yasuda, S. Motokoshi, C. Yamanaka, T. Yamanaka, Z. Kawasaki, K. Tsubakimoto, T. Ushio, A. Onuki, M. Adachi, and Y. Ishikubo. Laser triggered lightning experiments in field experiments. In *Proceedings of the 1-st int. workshop on Lightning Protection by Lasers, Journal of Optical Technology*, volume 66, pages 199–202, 1999.
- [14] B La Fontaine, F Vidal, Z Jiang, CY Chien, DI Comtois, A Desparois, TW Johnston, J-C Kieffer, H Pépin, and HP Mercure. Filamentation of ultrashort pulse laser beams resulting from their propagation over long distances in air. *Physics of plasmas*, 6(5):1615–1621, 1999.
- [15] Miguel Rodriguez, Riad Bourayou, Guillaume Méjean, Jérôme Kasparian, Jin Yu, Estelle Salmon, Alexander Scholz, Bringfried Stecklum, Jochen Eisloffel, Uwe Laux, et al. Kilometer-range nonlinear propagation of femtosecond laser pulses. *Physical Review E*, 69(3):036607, 2004.
- [16] G. Mechain, A. Couairon, Y. B. Andre, C. D’Amico, M. Franco, B. Prade, S. Tzortzakis, A. Mysyrowicz, and R. Sauerbrey. Long-range self-channeling of infrared laser pulses in air: a new propagation regime without ionization. *Applied Physics B*, 79:379–382, 2004.
- [17] D Comtois, CY Chien, A Desparois, F Génin, G Jarry, TW Johnston, J-C Kieffer, B La Fontaine, F Martin, R Mawassi, et al. Triggering and guiding leader discharges using a plasma channel created by an ultrashort laser pulse. *Applied Physics Letters*, 76(7):819–821, 2000.
- [18] Bruno La Fontaine, Daniel Comtois, Ching-Yuan Chien, Alain Desparois, Frederic Genin, Genevieve Jarry, Tudor Johnston, Jean-Claude Kieffer, Francois Martin, Raafat Mawassi, et al. Guiding large-scale spark discharges with ultrashort pulse laser filaments. *Journal of Applied Physics*, 88(2):610–615, 2000.
- [19] M. Rodriguez, R. Sauerbrey, H. Wille, L. Woeste, T. Fujii, Y. B. Andre, A. Mysyrowicz, L. Klingbeil, K. Rethmeier, and W. Kalkner; et al. Triggering and guiding

References

- megavolt discharges by use of laser-induced ionized filaments. *Optics Lett.*, 27:772–774, 2002.
- [20] Denis Mongin, Valentina Shumakova, Skirmantas Ališauskas, E Schubert, A Pugžlys, Jérôme Kasparian, Jean-Pierre Wolf, and A Baltuška. Conductivity and discharge guiding properties of mid-ir laser filaments. *Applied Physics B*, 122:1–7, 2016.
- [21] J. Schwarz, P. K. Rambo, J.-C. Diels, M. Kolesik, E. Wright, and J. V. Moloney. UV filamentation in air. *Optics Comm.*, 180:383–390, 2000.
- [22] Xun Liu, Xin Lu, Zhe Zhang, Xiao-Long Liu, Jing-Long Ma, and Jie Zhang. Triggering of high voltage discharge by femtosecond laser filaments on different wavelengths. *Optics Communications*, 284(22):5372–5375, 2011.
- [23] Alexander Alexandrovich Dergachev, Andrei A Ionin, Valeriy Petrovich Kandidov, Leonid Vladimirovich Seleznev, Dmitry Vasil’evich Sinitsyn, Elena Sergeevna Sunchugasheva, and Svyatoslav A Shlenov. Filamentation of ir and uv femtosecond pulses upon focusing in air. *Quantum Electronics*, 43(1):29, 2013.
- [24] V. D. Zvorykin, A. A. Ionin, A. O. Levchenko, L. V. Seleznev, D. V. Sinitsyn, I. V. Smetanin, N. N. Ustinovskii, and A. V. Shutov. Extended plasma channels created by UV laser in air and their application to control electric discharges. *Plasma physics reports*, 41:112–146, 2015.
- [25] J.-C. Diels. Discharge of lightning with ultrashort laser pulses. United States Patent, 1995. Patent number 5,175,664.
- [26] Xin Miao Zhao, Patrick Rambo, and Jean-Claude Diels. Filamentation of femtosecond UV pulses in air. In *QELS, 1995*, volume 16, page 178 (QThD2), Baltimore, MA, 1995. Optical Society of America.
- [27] P. K. Rambo, J. Schwarz, and J. C. Diels. High voltage electrical discharges induced by an ultrashort pulse UV laser system. *Journal of Optics A*, 3:146–158, 2001.
- [28] M. Miki and A. Wada. Guiding of electrical discharges under atmospheric air by ultraviolet laser-produced plasma channel. *J. Appl. Phys.*, 80:3208–3214, 1996.
- [29] Elise Schubert, Jean-Gabriel Brisset, Mary Matthews, Antoine Courjaud, Jérôme Kasparian, and Jean-Pierre Wolf. Optimal laser-pulse energy partitioning for air ionization. *Physical Review A*, 94(3):033824, 2016.

References

- [30] Henri Pépin, D Comtois, F Vidal, CY Chien, A Desparois, TW Johnston, JC Kieffer, B La Fontaine, F Martin, FAM Rizk, et al. Triggering and guiding high-voltage large-scale leader discharges with sub-joule ultrashort laser pulses. *Physics of plasmas*, 8(5):2532–2539, 2001.
- [31] M. Lenzner, J. Yeak, and K. Kremeyer. Femtosecond laser filaments and aerodynamics. In *4th International Symposium on Filamentation COFIL 2012*, Tucson, AZ, 2012.
- [32] Ali Rastegari and Jean-Claude Diels. Investigation of UV filaments and their applications. *APL Photonics*, 6(6):060803, 2021.
- [33] Ali Rastegari, Alejandro Aceves, and Jean-Claude Diels. UV filaments. *Light Filaments: Structures, Challenges and Applications*, page 31, 2021.
- [34] M. Miki, Y. Aihara, and T. Shindo. Development of long gap discharges guided by a pulsed CO₂ laser. *J. Phys. D: Appl. Phys.*, 26:1244–1252, 1993.
- [35] Bruno La Fontaine, Daniel Comtois, Ching-Yuan Chien, Alain Desparois, Frederic Genin, Genevieve Jarry, Tudor Johnston, Jean-Claude Kieffer, Francois Martin, Raafat Mawassi, et al. Guiding large-scale spark discharges with ultrashort pulse laser filaments. *Journal of Applied Physics*, 88(2):610–615, 2000.
- [36] G. Mejean, R. Ackermann, J. Kasparian, E. Salmon, J. Yu, and J. P. Wolf. Improved laser triggering and guiding of megavolt discharge with dual ns pulses. *Applied Physics Letters*, 88:021101, 2006.
- [37] Guillaume Point. *Interferometric study of low density channels and guided electric discharges induces in air by laser filament*. PhD thesis, ENSTA/Université Paris-Saclay, Saclay, France, 2015.
- [38] André Mysyrowicz Guillaume Point, Leonid Arantchouk and Aurélien Houard. Interferometric study of low density channels and guided electric discharges induces in air by laser filament. In *Conference on Laser, Weather, and Climate 2015 (LWC2015)*, Geneva, 2015.
- [39] Takashi Fujii, Megumu Miki, Naohiko Goto, Alexei Zhidkov, Tetsuo Fukuchi, Yuji Oishi, and Koshichi Nemoto. Leader effects on femtosecond-laser-filament-triggered discharges. *Physics of Plasmas*, 15(1):013107, 2008.
- [40] P. K. Panigrahi and K. Muralidharl. *Schlieren and Shadowgraph methods in heat and mass transfer. Chap.2: Laser Schlieren and Shadowgraph*. Springer, 2012.

References

- [41] Gary S Settles and Michael J Hargather. A review of recent developments in schlieren and shadowgraph techniques. *Measurement Science and Technology*, 28(4):042001, feb 2017.
- [42] Leonid Ivanovich Sedov and AG Volkovets. *Similarity and dimensional methods in mechanics*. CRC press, 2018.
- [43] A. Zigler. Long, high density plasma wire generated in air by femto-second laser filamentation. In *Conference on Laser, Weather, and Climate 2015 (LWC2015)*, Geneva, 2015.

Appendix A

Matlab code for data analysis of chapter 3

A.1 Analyzing the data

The following Matlab code has been used to analyze and average the 1000 images for each measurement. The delay is also corrected via this program.

```
1 clear all
2 ROW1=200;
3 ROW2=300;
4 ROWR1=1;
5 ROWR2=100;
6 ROI1=35;
7 ROI2=65;
8 ROJ1=300;
9 ROJ2=500;
10 ROMEAN1=220;
```


Appendix A. Matlab code for data analysis of chapter 3

```
11 ROMEAN2=350;
12 n=5;
13 m=30;
14 k=0;
15 u=0;
16 Threshold=1E6;
17 T=2.8767; %in ps
18 xref=370;
19 path = 'C:\Users\lab_user\Desktop\test2\';
20 pathraw = 'J:\streak\set2\100ps_10cm lens_no filter_full
           p_0.09Exp_1020G\photon on_dark on_jitter
           off_1000images_slit-40';
21 dataFiles = dir(pathraw);
22 %dataFiles = dir('C:\Users\lab_user\Desktop\ali\
           experimental results\He NE aerodynamic window\without
           aerodynamic window\set1n');
23 numfiles = length(dataFiles);
24 %fopen('csvlist.dat');
25 %AVE=zeros(5000);
26 N=0;
27 sizee=0;
28 imageF=0;
29 for K = 3:numfiles
30     str=0;
31     str = sprintf(dataFiles(K).name);
32     size=dataFiles(K).bytes;
33     if size>1000000
34         sizee=sizee+1;
```

Appendix A. Matlab code for data analysis of chapter 3

```
35 fileaddress = fullfile(pathraw, str);
36 %fileaddress = fullfile('C:\Users\lab_user\Desktop\ali\
    experimental results\He NE aerodynamic window\without
    aerodynamic window\setIn', str);
37 headerlinesIn=1;
38 delimiterIn = '\t';
39 %raw=importdata(fileaddress, delimiterIn, headerlinesIn);
40 fid=fopen(fileaddress);
41 c=0;
42 i=0;
43 j=0;
44 clear varname;
45 for pp=1:(length(str)-3)
46     if str(pp) ~= '.' && str(pp) ~= '-'
47         c=c+1;
48         varname(c)=str(pp);
49     end
50 end
51 raw=fread(fid);
52 A=raw(7:end);
53 %version=raw(1:2);
54 height=raw(3)+256*raw(4);
55 width=raw(5)+256*raw(6);
56 % width=raw(3)+256*raw(4);
57 % height=raw(5)+256*raw(6);
58 image1=zeros(height*width, 1);
59 %x=1;
60 %y=1;
```

Appendix A. Matlab code for data analysis of chapter 3

```
61 %for i=7:4:length(raw)-3;
62 %   image(x,y)=typecast(int8(raw(i:i+3)), 'int32');
63   image1=typecast(int8(raw(7:end)), 'int32');
64 %   x=x+1;
65 %   if(x>height)
66 %       x=1;
67 %       y=y+1;
68 %   end
69
70 %end
71 image1=reshape(image1, [height width]);
72 image2=image1';
73 fclose(fid);
74 image2=double(image2);
75 % for i=1:1:520
76 %   for j=1:1:696
77 %       if image2(i,j)>Threshold
78 %           image3(i,j)=Threshold;
79 %       else
80 %           image3(i,j)=image2(i,j);
81 %       end
82 %   end
83 % end
84 image3=image2;
85 % for j=1:1:696
86 %   A(j)=0;
87 %   for i=ROW1:1:ROW2
88 %       A(j)=A(j)+image3(i,j);
```

Appendix A. Matlab code for data analysis of chapter 3

```
89 %     end
90 %     AA(j)=A(j)/(ROW2-ROW1);
91 % end
92 clear M M2 I S;
93 MMM=max(image3(ROI1:ROI2,ROJ1:ROJ2));
94 Maximum=max(MMM);
95 cc=0; JJJ=0; III=0;
96 for i=ROI1:1:ROI2
97     for j=ROJ1:1:ROJ2
98         if image3(i,j)== Maximum
99             III=i+III;
100             JJJ=j+JJJ;
101             cc=cc+1;
102         end
103     end
104 end
105 JJJ=JJJ/cc;
106 III=III/cc;
107 c=0;
108 Z=0;
109 for i=ROI1:1:ROI2
110     for j=ROJ1:1:ROJ2
111         if image3(i,j)== Maximum
112             if (abs(j-JJJ)<=15) && (abs(i-III)<=5)
113                 c=c+1;
114                 M(c)=j; M2(c)=i;
115                 Z=1;
116             end
```

Appendix A. Matlab code for data analysis of chapter 3

```
117         end
118     end
119 end
120 if (Z==1)
121 MM=max(M)-min(M);
122 nx=MM;
123 nx=ceil(0.5*nx);
124 MM=max(M2)-min(M2);
125 ny=MM;
126 ny=ceil(0.5*ny);
127 c=0;
128 for i=ROI1:1:ROI2
129     for j=ROJ1:1:ROJ2
130         c=c+1;
131         S(c)=0;
132         for k=-ny:1:ny
133             for kk=-nx:1:nx
134                 S(c)=image3(i+k,j+kk)+S(c);
135             end
136         end
137         Si(c,:)=[i,j];
138     end
139 end
140 [Smax,ISmax] = max(S);
141 I=Si(ISmax,:);
142 c=0;
143 if (mod(u,100)==0)
144     u
```

Appendix A. Matlab code for data analysis of chapter 3

```
145 end
146 % if N == 0
147 %     xref=I(2);
148 %     u=u+1;
149 %     imageC(u, :, :)=image3;
150 %     image4=image3;
151 % end
152 if (xref < I(2))
153     R=I(2)-xref;
154     u=u+1;
155     c=0;
156     for j=1:1:520
157         for i=R:1:696
158             c=i-R+1;
159             % imageC(u, j, c)=image3(j, i);
160             image4(j, c)=image3(j, i);
161         end
162         for i=1:1:(R-1)
163             c=696-R+1+i;
164             % imageC(u, j, c)=0;
165             image4(j, c)=0;
166         end
167     end
168 end
169 if (xref > I(2))
170     R=xref-I(2);
171     u=u+1;
172     for j=1:1:520
```

Appendix A. Matlab code for data analysis of chapter 3

```
173         c=0;
174         for i=1:1:(696-R)
175             c=i+R;
176             % imageC(u,j,c)=image3(j,i);
177             image4(j,c)=image3(j,i);
178         end
179         for i=1:1:(R-1)
180             c=696-R+1+i;
181             % imageC(u,j,c)=0;
182             image4(j,c)=0;
183         end
184     end
185 end
186 if (xref == I(2)) && (N == 1)
187     u=u+1;
188     % imageC(u, :, :)=image3;
189     image4 = image3;
190 end
191
192 N=1;
193 imwrite(double(image3), [path 'rawframes/frame' sprintf('
194     %03d', u) '.tif'], 'tif');
194 imwrite(double(image4), [path 'corrected/cframe' sprintf('
195     %03d', u) '.tif'], 'tif');
195 imageF=imageF+image4;
196 end
197 end
198 end
```

Appendix A. Matlab code for data analysis of chapter 3

```
199 imageF=imageF./u;
200 imwrite(double(imageF), [path 'data/finalgrey' sprintf('%03
      d', u) '.tif'], 'tif');
201 newmap = parula;
202 imwrite(double(imageF), newmap, [path 'data/final' sprintf(
      '%03d', u) '.tif'], 'tif');
203 figure(1);
204 colormap(gray);
205 imagesc(imageF);
206 colorbar
207 figure(2);
208 colormap(gray);
209 imagesc(imageF);
210 c=0;mean=0;
211 for i=ROMEAN1:1:ROMEAN2
212     mean=mean+imageF(i,:);
213 end
214 mean=mean./(ROMEAN2-ROMEAN1);
215 p=1:1:696;
216 t=p*T;
217 t=t';
218 p=p';
219 mean=mean';
220 filename= 'C:\Users\lab_user\Desktop\test2\data\data.xlsx';
221 C = horzcat(p,t,mean);
222 col_header={'pixel','time(ps)','signal'};
223 data_cells=num2cell(C);
224 output_matrix=[col_header; data_cells];
```


Appendix A. Matlab code for data analysis of chapter 3

```
225 | xlsxwrite(filename,output_matrix);
226 | figure(21);
227 | plot(mean);
228 | figure(22);
229 | plot(t,mean);
230 | meannormalized=mean./(max(mean));
231 | filename= 'C:\Users\lab_user\Desktop\test2\data\
      | data_normalized.xlsx';
232 | C = horzcat(p,t,meannormalized);
233 | col_header={'pixel','time(ps)','signal_normalized'};
234 | data_cells=num2cell(C);
235 | output_matrix=[col_header; data_cells];
236 | xlsxwrite(filename,output_matrix);
237 | figure(23);
238 | plot(meannormalized);
239 | figure(24);
240 | plot(t,meannormalized);
```

```
1 | ROMEAN1=173;
2 | ROMEAN2=362;
3 | n=47;
4 | c=0;mean=0;
5 | for i=ROMEAN1:1:ROMEAN2
6 |     if i ~= 216
7 |         if i ~= 224
8 |             mean=mean+imageF(i,:);
9 |         end
10 |    end
```

Appendix A. Matlab code for data analysis of chapter 3

```
11 end
12 mean=mean./ (ROMEAN2-ROMEAN1+2);
13 %ROMEAN2-ROMEAN1;
14 mean1=0;
15 for i=ROMEAN1:1:(ROMEAN1+n)
16     if i ~= 216
17         if i ~= 224
18             mean1=mean1+imageF(i,:);
19         end
20     end
21 end
22 mean1=mean1./n;
23 mean1=mean1';
24 meannormalized1=mean1./ (max(mean1));
25 mean2=0;
26 for i=(ROMEAN1+n):1:(ROMEAN1+n+n)
27     if i ~= 216
28         if i ~= 224
29             mean2=mean2+imageF(i,:);
30         end
31     end
32 end
33 mean2=mean2./n;
34 mean2=mean2';
35 meannormalized2=mean2./ (max(mean2));
36 mean3=0;
37 for i=(ROMEAN1+n+n):1:(ROMEAN1+n+n+n)
38     if i ~= 216
```

Appendix A. Matlab code for data analysis of chapter 3

```
39         if i ~= 224
40             mean3=mean3+imageF(i,:);
41         end
42     end
43 end
44 mean3=mean3./n;
45 mean3=mean3';
46 meannormalized3=mean3./(max(mean3));
47 mean4=0;
48 for i=(ROMEAN1+n+n+n):1:(ROMEAN2)
49     if i ~= 216
50         if i ~= 224
51             mean4=mean4+imageF(i,:);
52         end
53     end
54 end
55 mean4=mean4./(n+2);
56 mean4=mean4';
57 meannormalized4=mean4./(max(mean4));
58 p=1:1:696;
59 t=p*T;
60 t=t';
61 p=p';
62 mean=mean';
63 filename= 'C:\Users\lab_user\Desktop\test2\data\data.xlsx';
64 C = horzcat(p,t,mean);
65 col_header={'pixel','time(ps)','signal'};
66 data_cells=num2cell(C);
```

Appendix A. Matlab code for data analysis of chapter 3

```
67 output_matrix=[col_header; data_cells];
68 xlswrite(filename,output_matrix);
69 figure(21);
70 plot(mean);
71 xlabel('t (pixels) ');
72 xlim([0 400]);
73 title('PIXEL');
74 print('C:\Users\lab_user\Desktop\test2\data\pixel','-djpeg'
      , '-r1000');
75 figure(22);
76 plot(t,mean);
77 xlabel('t (ps) ');
78 xlim([0 1500]);
79 title('TIME (ps) ');
80 meannormalized=mean./(max(mean));
81 filename= 'C:\Users\lab_user\Desktop\test2\data\
      data_normalized.xlsx';
82 C = horzcat(p,t,meannormalized);
83 col_header={'pixel', 'time (ps)', 'signal_normalized'};
84 data_cells=num2cell(C);
85 output_matrix=[col_header; data_cells];
86 xlswrite(filename,output_matrix);
87 figure(23);
88 plot(meannormalized, 'LineWidth', 1);
89 xlabel('pixel (ps) ');
90 xlim([0 400]);
91 ylim([0 1.1]);
92 grid on
```

Appendix A. Matlab code for data analysis of chapter 3

```
93 grid minor
94 title('normalized PIXEL');
95 print('C:\Users\lab_user\Desktop\test2\data\
    normalized_pixel', '-djpeg', '-r1000');
96 figure(24);
97 plot(t, meannormalized);
98 xlabel('t (ps)');
99 xlim([0 2000]);
100 title('normalized TIME (ps)');
101 figure(25)
102 plot(t, mean1, 'r', t, mean2, 'g', t, mean3, 'b', t, mean4, 'y');
103 figure(26)
104 plot(t, meannormalized1, 'r', t, meannormalized2, 'g', t,
    meannormalized3, 'b', t, meannormalized, 'y');
```

A.2 De-convolution

The following Matlab code has been utilized for the de-convolution process.

```
1 clear GT1 GTX GTY GTY2 GFY GFY2 x i MMM atg RRRR SFY STY
    STY2
2 %parameters:
3 N=(2^10);
4 MAX=200; %3500
5 shift=160; % 14 : 16700 160
6 Threshold=1;
7
8
```

Appendix A. Matlab code for data analysis of chapter 3

```
9  %the raw signal in time
10 GT1=GT0';
11 GTY0=GT1(2,:);
12 GTX0=GT1(1,:);
13
14 % defining x:
15 dx=MAX/N;
16
17 for i=1:1:(N*2)+1
18     x(i)=- (N*dx) + ((i-1)*dx);
19     GTX(i)=x(i);
20 end
21
22 % defining omega
23
24 Span_omega = 2*pi/(dx); %span of omega = 2*pi/dt
25 domega=Span_omega/(2*N+1);
26 omega =linspace(-Span_omega/2,Span_omega/2,2*N+1); %after
    fftshift
27 omega1 =linspace(0,Span_omega,2*N+1); %before fftshift
28
29
30 % The fit to the raw signal in time done in origin; only
    including the fast decay to zero
31 XX1=5.11107
32 XX2=31.35344
33 t1=1.41716
34 t2=9.90939
```

Appendix A. Matlab code for data analysis of chapter 3

```
35 C=0.41766
36 F=1./ (C*[exp((sqrt(x)-XX1)/t1)+exp(-(x-XX2)/t2)]);
37 GTY=F;           %for normalized data
38
39
40 %Gaussian reference (the fitted data to signal from
    diffuser)
41
42
43 xc=0; %-0.79928
44 w=25.64768;
45 %w=25.9041568;
46 A=40.98652;
47 y0=-0.01177;
48 RTY = y0 + (2*A/pi)*(w./(4*(x-xc).^2 + w^2));
49 RTX=x;
50
51
52 %RT1=RT0';
53 %RTY=RT1(2,:);
54 %RTX=RT1(1,:);
55
56
57 %Taking the Fourier transform of the fit data to the raw
    signal
58
59
60 figure(1);
```

Appendix A. Matlab code for data analysis of chapter 3

```
61 plot(x,GTY,'r',GTX0,GTY0,'x','MarkerSize',9,'
    MarkerEdgeColor','blue');
62 title('Data fit and data points');
63 GTYS = circshift(GTY,-shift);      %shifting the data before
    taking the Fourier transform
64 %GTYS=fftshift(GTYS);
65 figure(11)
66 plot(x,GTYS,'r',x,GTY,'b');
67 title('Original fitted signal(blue) and shifted(red)');
68 GFY = fft(GTYS);
69 figure(12);
70 plot(omega1,(GFY));
71 title('Fourier transform of fitted signal before fftshift')
    ;
72 GFY2=fftshift(GFY);
73 figure(13);
74 plot(omega,(GFY2));
75 title('Fourier transform of the fitted signal after
    fftshift');
76 xlim([-1 1]);
77 GTY2=ifft(GFY);
78 %GTY2=ifftshift(GTY2);
79 figure(14);
80 plot(x,GTY2);
81 title('Fitted signal after inverse Fourier');
82 % xlim([0 1400]);
83 % ylim([-0.2 1.2]);
84 figure(15);
```


Appendix A. Matlab code for data analysis of chapter 3

```
85 plot(x,GTYS,'r',x,GTY2,'x');
86 title('Compare original fitted signal with fitted signal
      after inverse Fourier');
87 % xlim([-200 1400]);
88 % ylim([-0.2 1.2]);
89
90 %Taking the Fourier transform of the reference pulse
91
92 figure(2)
93 %plot(RTX,RTY);
94 plot(RTX,RTY,'r',GTX,GTYS,'b');
95 title('Reference pulse (red) and fitted signal after shift(
      blue)');
96 RTY2=fftshift(RTY);
97 RFY = fft(RTY2);
98 figure(21);
99 plot(omega,RFY);
100 title('Fourier transform of the reference pulse before
      shift');
101 RFY2=fftshift(RFY);
102 figure(22);
103 plotyy(omega,(RFY2),omega,angle(RFY2));
104 title('Fourier of reference after shift');
105 %xlim([-1 1]);
106 RTY2=ifft(RFY);
107 RTY2=fftshift(RTY2);
108 figure(23);
109 plotyy(RTX,(RTY2),RTX,angle(RTY2));
```

Appendix A. Matlab code for data analysis of chapter 3

```
110 title('Inverse Fourier of reference after shift')
111
112
113
114 %GFY2=RFY2;
115
116 %
117 % GFY2=GFY2./max(abs(GFY2));
118 % RFY2=RFY2./max(abs(RFY2));
119
120 for i=1:length(RFY2)
121     if RFY2(i) < Threshold
122         SFY(i)=0;
123     else
124         SFY(i)=(GFY2(i))./(RFY2(i));
125     end
126 end
127 %SFY=(GFY2)./(RFY2);
128
129 figure(5)
130 plot(omega,((SFY)));
131 title('The final signal in Fourier domain')
132 ylim([0 2]);
133
134
135 %SFY=abs(SFY)
136 %SFY=fftshift(SFY);
137 STY=ifft(SFY);
```

Appendix A. Matlab code for data analysis of chapter 3

```
138 %STY=fftshift(STY);
139 STY2=STY./max(STY);
140 % GTYY=GTY./max(GTY);
141 %STY2=circshift(STY2,-10200);
142 figure(61)
143 plot(x,abs(STY2),'b',x,GTYS,'r');
144 title('The final signal(blue) versus the original data fit(
      red)')
145 %xlim([0 1400]);
146 figure(51)
147 plot(omega,(GFY2),'b',omega,(RFY2),'r')
148 title('The reference signal in Fourier domain(red) vs The
      data in Fourier domain(blue) ')
149 xlim([-0.3 0.3]);
```

Appendix B

Matlab code for data analysis of chapter 4

```
1 clear all
2 close all
3
4
5 %%%%%%%%%%%%%%%%%%%%%%%%%%%%%%%%%%%%%%%%%
6 aa=csvread('U_385_paper2.csv');
7 times=[125,525,925,1625];
8 laurentz_correction=[1 1.048 1.04 1.02];
9 gausstau_correction=[1.12 1.09 0.77 1.01];
10 gauscenter_correction=[-0.0005 -0.0005 -0.0007 0];
11 tot_scan=length(times);
12 mycolors=['b','g','r','k'];
13
14 myend=size(aa,1);
15 figure(1)
```

Appendix B. Matlab code for data analysis of chapter 4

```
16 %xlim=([395.403 397.007]);
17 %ylim=([0 397.007]);
18 xregion=[520 690 540 660 588 640 582 638];
19 %spec_cut=zeros(1,6);
20 %y_cut=zeros(max(xregion)-min(xregion),6);
21 for i_scan=2:2
22     %i_scan=i_scan+4;
23 spec=aa(:,i_scan*2-1);
24 amp=aa(:,i_scan*2);
25 xstart=xregion(1,i_scan*2-1);
26 xend=xregion(1,i_scan*2);
27
28 % Connect a line between the beginning and end of the
    spectrum
29 first=mean(amp(2:4,1));
30 last=mean(amp(end-4:end-2,1));
31 % first=mean(amp(xstart-1:xstart+1,1));
32 % last=mean(amp(xend-4:xend-2,1));
33 % Connect a line between the beginning and end of PART of
    the spectrum
34 % first=(amp(610,1));
35 % last=(amp(680+50,1));
36 %%%%%%%%%%%%%%%%%%%%%%%%%%%%%%%%%%%%%%%%%
37 slope=(last-first)/(spec(myend-2,1)-spec(1,1));
38 myline1=slope.*(spec-spec(1,1))+first;
39 % Fit a line to the spectrum
40 [a,b]=polyfit(spec,amp,1);
41 myline=a(1,1).*spec+a(1,2);
```

Appendix B. Matlab code for data analysis of chapter 4

```
42 %plot(spec',myline','r',spec',myline1','b',spec',amp','+')
43 difcurve=amp-myline1;
44 mycurve=difcurve./mean(difcurve);
45 % plot(spec',(mycurve)')
46 % hold on
47 x=spec(xstart:xend,1);
48 y=mycurve(xstart:xend,1);
49 spec_cut(xstart:xend,i_scan)=x;
50 y_cut(xstart:xend,i_scan)=y;
51 param = [0.2106    0.0592   385.957 1 (y(end,1)-y(1,1))./(x(
    end,1)-x(1,1))];
52 ytofit=y;
53 for ii=1:3
54
55
56 % plot(spec(xstart:xend,1)',mycurve(xstart:xend,1)')
57 % hold on
58 %param2 = [0.2106    0.0592   393.1993 0.05 0.5 393.3,1.2];
59     for ik=1:9
60
61         [par0,resnorm]= lsqcurvefit(@lorentzpline,real(param),
            x,ytofit);
62         %[par,resnorm]= lsqcurvefit(@lorentz2,real(param2),spec
            (xstart:xend,1),mycurve(xstart:xend,1));
63         param=par0;
64         % param2=par;
65     end
66
```

Appendix B. Matlab code for data analysis of chapter 4

```
67     % Lets see what lorentzian function fit to the data
68     y_f0=lorentzpline(par0,x);
69     y_f0=y_f0.*laurentz_correction(i_scan);
70     % This is to fit absorption for a peak we need to have
       an opposite sign
71     y2=y_f0-y;
72
73     % take the weight and width of difference
74
75     xavg=sum((y2.*x).*(y2>0))./sum(y2.*(y2>0));
76
77     taucal=sqrt(sum(y2.*x.^2.*(y2>0))./sum(y2.*(y2>0))-xavg
       .^2);
78
79
80     % Bandwidth of the pulse is calculated as \Sigma (
       lambda^2*Y(lambda))/
81     % \Sigma(Ylambda)-lambda(mean)^2....The square root
       is taken
82
83     %plot(spec(xstart:xend,1),mycurve(xstart:xend,1),spec(
       xstart:xend,1),y_f,'--')
84     %hold on
85     [a,b]=max(y2);
86     [cc index]=min(abs(y2-a/2));
87     cond=abs(y2(index)-a/2);
88     epsilon=0;%(cond)*abs(x(index)-(x(index+1)))/abs(y2(
       index)-y2(index+1))); % epsilon correction of FWHM
```

Appendix B. Matlab code for data analysis of chapter 4

```
89     if(y(index)>a/2) %
90         xhalf=abs(x(index)-x(b))-epsilon*sign(x(index)-x(b)
91             );
92     else(y(index)<a/2) %
93         xhalf=abs(x(index)-x(b))+epsilon*sign(x(index)-x(b)
94             );
95     end
96     tau=xhalf/(sqrt(log(2)));
97     m=x(b)+gausscenter_correction(i_scan);
98     tau=tau*gausstau_correction(i_scan);
99     mypar=[a tau m 0];
100    mygauss=gauss(mypar ,x);
101    tFWHM_Gauss=2*sqrt(log(2))*tau;
102    param_g = [a tau x(b,1) 1]; %0.0592
103    ytofit=y+mygauss;
104    end%a is the peak value , x(b,1) is the x for the peak
105    % [par_g,resnorm]= lsqcurvefit(@gauss,real(param_g),x(b
106        -5:b+5,1),smooth(y2(b-5:b+5,1)));
107    % [par,resnorm]= lsqcurvefit(@lorentz,real(param),x(b-5:
108        b+5,1),smooth(y2(b-5:b+5,1)));
109    % x_dip=393.15:0.002:393.23;
110    % y_dip=gauss(par_g,x_dip);
111    % y_l=lorentz(par,x_dip);
112    [par_g,resnorm]= lsqcurvefit(@lorentz,real(param_g),x,y2);
113    gaussfit=gauss(par_g,x);
114    r1=[mycolors(i_scan),'*'];
115    r2=[mycolors(i_scan),'+'];
```


Appendix B. Matlab code for data analysis of chapter 4

```
113 r3=[mycolors(i_scan), '--'];
114 r4=[mycolors(i_scan)];
115 mygauss1=mygauss./max(mygauss);
116 y1=y./max(y);
117
118 y_f01=y_f0./max(y_f0);
119 fit=y_f0-(mygauss);
120 fit1=fit./max(fit);
121 c=1;
122 for q=min(x):0.000015:max(x)
123     xx(c)=q;
124     c=c+1;
125 end
126 [n,nn]=max(mygauss);
127 mypar2=[a tau x(nn) 0];
128 mygauss_new=gauss(mypar2,xx);
129
130 plot(x,y,r1,x,y_f0,r2,xx,mygauss_new,r3,x,fit,r4)
131 xlim=( [395 396] );
132 ylim=( [0 6] );
133 sum_gauss=sum(mygauss);
134 sum_yf0=sum(y_f0);
135 sum_ysim=sum(y_f0-mygauss);
136 sum_y=sum(y);
137 [n,nn]=max(mygauss);
138 [m,mm]=max(y_f0);
139 M=m-min(y_f0);
```

Appendix B. Matlab code for data analysis of chapter 4

```
140 res(i_scan,:)=[times(i_scan),xavg,taucal,a,x(b,1), tau,
    param,sum_gauss,sum_yf0,sum_ysim,sum_y,x(nn),n,x(mm),M,
    tFWHM_Gauss];
141
142 data(i_scan,:)=[times(i_scan),xavg,tau,sum_gauss,sum_yf0,
    sum_ysim,sum_y,x(nn),n,x(mm),M,tFWHM_Gauss];
143 %legend('data','lorentzfit','gaussian abs','fit to data')
144 % plot (x,y_f0)
145 %plot(x,smooth(y2),'+',x,gaussfit)
146 hold on
147
148 %legend(num2str(times(1,i_scan)));
149
150 end
151 csvwrite('Ures.csv',res)
152 filename= 'E:\matlab_ladan_libs code\total_data_U_paper2.
    xlsx';
153 C = horzcat(res);
154 col_header={'delay time','xavg','taucal','a','x(b,1)','tau
    gaussian','param1','param2','param3','param4','param5','
    sum_gauss','sum_yf0','sum_ysim','sum_y','wavelength
    gaussian center','max gauss','wavelength lorentzian
    center','max lorentzian','tFWHM_Gauss'};
155 data_cells=num2cell(C);
156 output_matrix=[col_header; data_cells];
157 xlswrite(filename,output_matrix);
158
```

Appendix B. Matlab code for data analysis of chapter 4

```
159 filename= 'E:\matlab_ladan_libs code\data_fio_figure_U.xlsx
      ';
160 C = horzcat(res);
161 col_header={'Delay time','gaussian_x','Gaussian_y','
      lorentzian_x','lorentzian_y','fit_x','fit_y','data
      points_x','data points_y'};
162 data_cells=num2cell(C);
163 output_matrix=[col_header; data_cells];
164 xlswrite(filename,output_matrix);
165
166 filename2= 'E:\matlab_ladan_libs code\data_U_paper2.xlsx';
167 C = horzcat(data);
168 col_header={'delay time','xavg','tau gaussian','sum_gauss',
      'sum_yf0','sum_ysim','sum_y','wavelength gaussian center
      ','max gauss','wavelength lorentzian center','max
      lorentzian','tFWHM_Gauss'};
169 data_cells=num2cell(C);
170 output_matrix=[col_header; data_cells];
171 xlswrite(filename2,output_matrix);
172
173 filename3='LIBS_U.mat';
174 save(filename3);
175
176 h=zeros(tot_scan,1);
177 h(1)=plot(NaN,NaN,mycolors(1,1));
178 h(2)=plot(NaN,NaN,mycolors(1,2));
179 h(3)=plot(NaN,NaN,mycolors(1,3));
180 h(4)=plot(NaN,NaN,mycolors(1,4));
```

Appendix B. Matlab code for data analysis of chapter 4

```
181 %h(5)=plot(NaN,NaN,mycolors(1,5));
182
183 legend(h,num2str(times(1,1)),num2str(times(1,2)),num2str(
    times(1,3)),num2str(times(1,4)));% ,num2str(times(1,5))
184 %legend(num2str(times(1,1)),num2str(times(1,2)),num2str(
    times(1,3)),num2str(times(1,4)),num2str(times(1,5)))
185
186
187
188 %legend(num2str(times(1,1)),num2str(times(1,2)),num2str(
    times(1,3)),num2str(times(1,4)),num2str(times(1,5)))
189 % figure(2)
190 % plot(aa(:,3),aa(:,4))
191 %
```

```
%%%%%%%%%%%%%%%%%%%%%%%%%%%%%%%%%%%%%%%%%%%%%%%%%%%%%%%%%
```

Appendix C

Matlab code for data analysis of chapter 5

```
1 clear all
2 %A=xlsread('C:\Users\ali\Desktop\
   Discharge_Geneva_albuquerque\ALburquerque\27072015\
   current\New folder\uv 31 cm sep 23vlt 29hum 31dot6 c.
   xlsx'
3
4 %%%%%%%%% Reading files
5 CC=0;
6
7 dataFiles = dir('C:\Users\ali\Desktop\
   Discharge_Geneva_albuquerque\ALburquerque\07082015\
   current\a');
8 numfiles = length(dataFiles);
9 fileID = fopen('C:\Users\ali\Desktop\
   Discharge_Geneva_albuquerque\ALburquerque\07082015\
```

Appendix C. Matlab code for data analysis of chapter 5

```
    current\csvlist8test.csv', 'wt');
10 fprintf(fileID, '%s', 'description', ',', 'date', ',', 'voltage',
    ',', 'No.of discharges', ',', 'No. of Shots', ',', '
    Probability', ',', 'Delay Ave.', ',', 'Standard Deviation', '
    ,', 'Corrected Delay Ave.', ',', ');
11 fprintf(fileID, '%s\n', 'Corrected Standard Dev.');
```

```
12 for k = 3:numfiles
13     str = sprintf(dataFiles(k).name);
14     str2 = sprintf(dataFiles(k).date);
15     fileaddress = fullfile('C:\Users\ali\Desktop\
    Discharge_Geneva_albuquerque\ALburquerque\07082015\
    current\a', str)
16     headerlinesIn=1;
17     delimiterIn = '\t';
18     A =importdata(fileaddress, delimiterIn, headerlinesIn);
19     for pp=1:(length(str))-4
20         if str(pp) ~= ' '
21             varname(pp)=str(pp);
22         else
23             varname(pp)='_';
24         end
25         if pp>5
26             if str(pp)=='v'
27                 STRVOLTAGE=str(pp-2:pp-1);
28             end
29         end
30     end
31     AA=A(1).data;
```

Appendix C. Matlab code for data analysis of chapter 5

```
32 assignin('base' , varname , AA);
33 %clear varname;
34
35 %%%Data Analysis
36 %%%finding the number of discharges
37 Ndisccharge(k-2)=0;
38 clear indexofdischarge;
39 for i=1:length(AA(:,1))/5
40     m=0;
41     for j=1:1000
42         if (AA(((5*i)-3),j)<-2)
43             m=m+1;
44         end
45     end
46     if m>0
47         Ndisccharge(k-2)=Ndisccharge(k-2)+1;
48         indexofdischarge(Ndisccharge(k-2))=((5*i)-3);
49     end
50 end
51 D=strcat('N__',varname);
52 NDISCHARGEandNSHOTSandRATIO=[Ndisccharge(k-2),0.2*length(
    AA(:,1)),5*Ndisccharge(k-2)/length(AA(:,1))];
53 assignin('base' , D , NDISCHARGEandNSHOTSandRATIO);
54 D=strcat('Dis_index_',varname);
55 if Ndisccharge(k-2)>0
56     assignin('base' , D , indexofdischarge);
57 %%%finding the delay
58 for l=1:length(AA(:,1))/5
```

Appendix C. Matlab code for data analysis of chapter 5

```
59     peakofallshots(1)=max(AA(((5*1)-4),1:110));
60 end
61 DD=strcat('Peak_of_all_',varname);
62 assignin('base' , DD , peakofallshots);
63 clear peakofallshots;
64 delayaverage=0;
65 c=0;
66 for i=1:length(indexofdischarge)
67     %dischargenumber=0;
68     dischargenumber=indexofdischarge(i);
69     [dischargepeak, dischargepeakindexnumber]= min(AA(
70         dischargenumber,:));
71     [shotpeak, shotpeakindexnumber]= max(AA((
72         dischargenumber-1),1:110));
73     if shotpeak >= 0.02
74         c=c+1;
75         delay(c)=(dischargepeakindexnumber-shotpeakindexnumber
76             )*10^-8;
77         delayaverage=delayaverage+delay(c);
78     end
79 end
80 delayaverage=(10^9*delayaverage)/c; %% (length(
81     indexofdischarge));
82 DD=strcat('Delay__',varname);
83 assignin('base' , DD , delay);
84 DD=strcat('Delay_Ave__',varname);
85 assignin('base' , DD , delayaverage);
```


Appendix C. Matlab code for data analysis of chapter 5

```
83 std=0;
84 for i=1:c
85     std=std+(delay(i)-(delayaverage*10^-9))^2;
86 end
87 std=std/c;
88 std=(std)^0.5;
89 std=std*10^9;
90 DD=strcat('STD___',varname);
91 assignin('base' , DD , std);
92 AVE=0;
93 C=0;
94 for i=1:c
95     if delay(i)<((1.5*std)+(delayaverage))*10^-9 && delay(i)
96         >(delayaverage-(1.5*std))*10^-9
97         AVE=AVE+delay(i);
98         C=C+1;
99     end
100 end
101 AVE=AVE;
102 AVE=(10^9*AVE)/C;
103 DD=strcat('D_Ave_Corrected___',varname);
104 assignin('base' , DD , AVE);
105 std1=0;
106 for i=1:c
107     if delay(i)<((1.5*std)+delayaverage)*10^-9 && delay(i)
108         >(delayaverage-(1.5*std))*10^-9
109         std1=std1+(delay(i)-AVE*10^-9)^2;
110     end
```

Appendix C. Matlab code for data analysis of chapter 5

```
109 end
110 std1=std1/C;
111 std1=(std1)^0.5;
112 std1=std1*10^9;
113 CC=CC+1;
114 MM(1,CC)=AVE;
115 MM(2,CC)=std;
116 MM(3,CC)=1.5*std;
117 MM(4,CC)=(AVE-std);
118 x=str2num(STRVOLTAGE);
119 fprintf(fileID, '%s', varname);
120 fprintf(fileID, '%s', ', ');
121 fprintf(fileID, '%s', str2);
122 fprintf(fileID, '%s', ', ');
123 fprintf(fileID, '%d', x);
124 fprintf(fileID, '%s', ', ');
125 fprintf(fileID, '%d', NDISCHARGEandNSHOTSandRATIO(1));
126 fprintf(fileID, '%s', ', ');
127 fprintf(fileID, '%d', NDISCHARGEandNSHOTSandRATIO(2));
128 fprintf(fileID, '%s', ', ');
129 fprintf(fileID, '%d', NDISCHARGEandNSHOTSandRATIO(3));
130 fprintf(fileID, '%s', ', ');
131 fprintf(fileID, '%d', delayaverage);
132 fprintf(fileID, '%s', ', ');
133 fprintf(fileID, '%d', std);
134 fprintf(fileID, '%s', ', ');
135 fprintf(fileID, '%d', AVE);
136 fprintf(fileID, '%s', ', ');
```

Appendix C. Matlab code for data analysis of chapter 5

```
137 fprintf(fileID, '%d\n', std1);  
138     end  
139 clear delay;  
140 clear varname;  
141 end  
142 fclose(fileID);  
143 clear AA A headerlinesIn delimiterIn varname fileaddress pp  
    str numfiles c NDISCHARGEandNSHOTSandRATIO Ndisccharge  
    ;
```